Hydromorphology of ecological deep pool habitats

Zur Erlangung des akademischen Grades einer

DOKTORIN DER INGENIEURWISSENSCHAFTEN (Dr.-Ing.)

von der KIT Fakultät für

Bauingenieur-, Geo- und Umweltwissenschaften

des Karlsruher Instituts für Technologie (KIT)

genehmigte

DISSERTATION

von

Christin Kannen

Tag der mündlichen Prüfung: 19.04.2024

Referent: Prof. Dr.-Ing. Dr.h.c. mult. Franz Nestmann
Korreferenten: Prof. Dr.-Ing. habil. Boris Lehmann

                              Prof. Dr. Mário Jorge Rodrigues Pereira da Franca

Karlsruhe (2024)

Abstract

The hydromorphological quality of rivers around the world is deteriorating due to human intervention, making sustainable measures to revitalize rivers necessary. Artificial deep pools are intended to improve the resilience of rivers, especially in the context of climate-related extreme weather events such as droughts and heat waves. This dissertation establishes fundamental knowledge regarding hydromorphological processes for the creation of deep pool habitats and develops a concept for the investigation of various measures for implementation in practice. The habitat preferences of the barbel (*Barbus Barbus*) are taken into account; however, the ecological effects go beyond the exclusive benefit for this species. To tackle the challenge of defining hydromorphological boundary conditions, this dissertation explores the suitability of mean flow velocities and discusses on incorporating additional parameters related to turbulence characteristics. A hybrid modeling approach combining physical model experiments and 3D HN simulations was developed to investigate six selected in-stream structures. The importance of different scour mechanisms was emphasized using three kinds of structures, pier-, stone- and dam-like structures, which exhibit different flow types and were defined within this work. The bed morphology and flow field within the scour are described in detail, highlighting prominent vortex structures and helices that play a crucial role in the efficient entrainment and transport of sediment. The triangular pier proved to be the most effective structure and was selected for further investigation. Deeper analyses focused on the influence of natural materials, debris accumulations and the combination of deep pools with shelters. The subsequent hydromorphological assessment considered target values for scour depth and area for bed morphology, and uses a traffic light rating system for the mean flow velocity field, vortex strength assessments based on streamlines and specific power density as an integral approach to hydrodynamics. In summary, this dissertation develops measures that create favorable ecological and hydromorphological conditions for deep pools, which contribute to improving beta diversity in river ecosystems. Along with the predictability of hydromorphological development and the quantification of water level rises during flood events, this work presents a significant improvement in the planning process for revitalization projects.

Zusammenfassung

Weltweit verschlechtert sich die hydromorphologische Qualität von Flüssen aufgrund menschlicher Eingriffe, was nachhaltige Maßnahmen zur Revitalisierung von Flüssen erforderlich macht. Durch tiefe Kolke soll die Resilienz von Flüssen, insbesondere im Zusammenhang mit klimabedingten Extremwetterereignissen wie Dürreperioden und Hitzewellen, verbessert werden. Diese Dissertation befasst sich mit den hydromorphologischen Grundlagen zur Schaffung von tiefen Kolken und entwickelt ein Konzept zur Untersuchung verschiedener Maßnahmen für die Umsetzung in der Praxis. Hierbei wurden die Habitatanforderungen der Barbe (*Barbus Barbus*) herangezogen; die ökologische Wirkung geht jedoch über den ausschließlichen Nutzen für diese Art hinaus. Im Rahmen der Festlegung der hydromorphologischen Randbedingungen wurde die Eignung der mittleren Fließgeschwindigkeit als Bewertungskriterium kritisch diskutiert und zusätzliche Parameter zur Berücksichtigung der turbulenten Strömungseigenschaften integriert. Es wurde ein hybrider Modellansatz entwickelt, der physikalische Modellversuche und 3D-HN-Simulationen kombiniert, um sechs ausgewählte in-stream Strukturen zu untersuchen. Die Bedeutung verschiedener Kolkmechanismen wurde durch die Definition von drei verschiedenen Strukturtypen hervorgehoben: pfeiler-, stein- und dammartige Strukturen, die jeweils einen anderen Strömungstyp erzeugen. Die Sohlmorphologie und das Strömungsfeld innerhalb des Kolks werden detailliert beschrieben, wobei markante Wirbelstrukturen und Helices hervorgehoben werden, die eine entscheidende Rolle bei der effizienten Mobilisierung und dem Transport von Sediment spielen. Der dreieckige Pfeiler wurde als vielversprechendste Variante für weitere Untersuchungen ausgewählt. Tiefergehende Analysen befassen sich mit dem Einfluss von natürlichen Materialien, Geschwemmselansammlungen und der Kombination von tiefen Kolken mit Unterständen. Die anschließende hydromorphologische Bewertung berücksichtigt Zielwerte für die Kolktiefe und -fläche für die Sohlmorphologie und verwendet ein Ampel-Bewertungssystem für das mittlere Strömungsgeschwindigkeitsfeld, Wirbelstärkenbewertungen anhand von Stromlinien und die spezifische Leistungsdichte als integralen Ansatz für die Hydrodynamik. Zusammenfassend wurden in dieser Dissertation Maßnahmen entwickelt, die günstige ökologische und hydromorphologische Bedingungen für tiefe Kolke schaffen, was zu einer Verbesserung der Betadiversität in Fließgewässern beiträgt. Die Vorhersagbarkeit der hydromorphologischen Entwicklung und die Sicherheit hinsichtlich der Wasserspiegellagen im Hochwasserfall werden quantifiziert und stellen damit eine deutliche Verbesserung der Planungsgrundlage für Revitalisierungsprojekte dar.

Acknowledgements

Contents

Symbol directory

A	area	[m²]
$A_{r(e)}$	blockage ratio (at time t_e of the experiment)	[-]
A_0	area in initial depth	[m²]
A_{target}	area in target depth	[m²]
A_p	projected area	[m²]
$A_{s(0,e)}$	solid area of the in-stream structure (at time t_0 and t_e of the experiment)	[m²]
$A_{f(0,e)}$	total flown through area (at time t_0 and t_e of the experiment)	[m²]
C_D	drag coefficient	[-]
C_r	contraction ratio w_s/w	[-]
D	hydraulically significant length	[m]
d	length of the porous medium	[m]
d_{se}	maximum scour depth at equilibrium	[m]
d_s	scour depth	[m]
d_{10}	10 % of the grains are smaller than this size	[m]
d_{50}	50 % of the grains are smaller than this size (considered as mean grain diameter)	[m]
d_{60}	60 % of the grains are smaller than this size	[m]
d_{equ}	equivalent diameter	[m]
D_e	equivalent width of the debris	[m]
Fr	Froude number	[-]
$Fr_{0,1,2}$	Froude number in the approach flow (0), upstream (1) and downstream (2) of the structure	[-]
Fr^*	grain related Froude number	[-]
F_D	drag force	[kg m/s²]
F_f	friction force	[kg m/s²]
F_w	force due to gravity	[kg m/s²]
g	gravitation	[m/s²]
h_d	height of the dune	[m]
h_d/h_0	submergence of the debris	[-]
$HQ2$	discharge of a flood with return period of 2 years	[m³/s]
h_s	height of the structure	[m]
Δh	water level difference between upstream and downstream water level = $h_1 - h_2$	[m]
h_0	approach flow water depth for uniform flow	[m]
h_1	upstream water level	[m]
h_2	downstream water level, also tailwater depth of Kdam	[m]
$h_{ü}$	overflow height	[m]
h_v	local loss	[m]

CONTENTS

I	turbulence intensity	[%]
I_0	bottom slope	[-]
K	pier shape factor K according to Yarnell	[-]
K	permeability	[m²]
k_f	hydraulic conductivity	[m/s]
$K_{d_{50}}$	correction factor for relative grain size	[-]
k_{st}	Strickler coefficient	$[m^{1/3}/s]$
k_s	equivalent sand roughness	[m]
l_{ds}	length of the scour hole	[m]
l_{dune}	distance of the dune	[m]
l_{dam}	length of the dam	[m]
l_v	viscous length scale	[m]
L_g	length of the groyne	[m]
L_f	distance between two groynes	[m]
$L_{d(u,d)}$	upstream and downstream length of the debris	[m]
MNQ	average of lowest annual discharge	[m³/s]
MQ	average of annual discharge	[m³/s]
n	manning roughness value	$[s/m^{1/3}]$
p	pressure	[N/m²]
$p_{stat,dyn,luv,lee}$	static, dynamic pressure; pressure in luv and lee	[N/m²]
P_D	specific power density	[W/m³]
P_{vol}	porosity of the synthetic wadding material	[%]
Q	discharge	[m³/s]
Q	Q-criterion	[1/s²]
Re	Reynolds number	[-]
Re_d	obstacle Reynolds number	[-]
Re^*	grain related Reynolds number	[-]
R_{hy}	hydraulic radius = A/U	[m]
S	submergence ratio h_s/h_0	[-]
SVF	solid volume fraction $= 1 - \Phi$	[-]
t	time	[s]
t_e	equilibrium time	[s]
$TKE, \kappa_{(T)}$	turbulent kinetic energy	[m²/s²]
T_D	thickness of the debris	[m]
U	wetted perimeter	[m]
U_0	approach flow velocity	[m/s]
U_C	critical flow velocity	[m/s]
u, v, w	fluid velocity components in x-, y-, z-direction	[m/s]
$\overline{u}, \overline{v}, \overline{w}$	mean component of flow velocity in x-, y- and z-direction	[m/s]
u', v', w'	velocity fluctuation component of flow velocity in x-, y- and z-direction	[m/s]
u_{rms}	root of the squared velocity fluctuation	[m/s]
u^*	shear velocity	[m/s]
V	volume	[m³]
V_{tot}	total scour volume	[m³]
V_{target}	scour volume below target depth	[m³]
V_{cum}	cumulated volume	[m³]
w	width of the channel	[m]
w_d	width of the debris	[m]
w_s	width of the structure	[m]
x, y, z	coordinate system	[m]

α	inclination angle of the groyne	[º]
β, μ	correction factors to accommodate varying pier shapes	[-]
δ	boundary layer thickness	[m]
ζ	local loss coefficient	[-]
λ	pressure loss coefficient	[1/m]
μ	dynamic viscosity of the fluid	[N s/m²]
$\nu_{(t)}$	(turbulent) kinematic viscosity of the fluid	[m²/s]
ρ	fluid density of water	[kg/m³]
ρ_s	density of the sediment	[kg/m³]
ρ'	specific density $= \frac{\rho_s - \rho}{\rho}$	[kg/m³]
σ_g	uniformity of the sediment d_{60}/d_{10}	[-]
τ_{ij}	Reynolds shear stresses	[N/m²]
τ	shear stress	[N/m²]
Φ	void fraction	[-]
ω	vorticity	[1/s]
Ω	vorticity tensor	[1/s]
∇	nabla operator	[-]

CP	Circular Pier
RP	Rectangular Pier
TP	Triangular Pier
DWD	Double Wing Deflector
DG	Deflected Groyne
Kdam	Kdam

Chapter 1

Introduction

1.1 Context

Over the past centuries, river systems worldwide have lost large parts of their hydromorphological quality due to human activities such as rectifications and channelizations (Wohl, 2019; Lane & Richards, 1997; WFD, 2014). Natural rivers were characterized by a variable riverbed that could change with each major flood, resulting in significant variations of depth and flow velocities. Further, the presence of deadwood was much higher in their natural state, allowing for the promotion of self-sustaining morphological processes in the river (Wohl et al., 2019). Human interventions, ranging from channelization to full rectification of riverbeds, levee construction for flood protection and construction of groynes for navigation, have significantly altered the natural dynamics of river systems. Further, river maintenance tasks, such as the systematic removal of deadwood from the river to enhance flood safety, disrupt the natural dynamics of the river system. Consequently, nowadays rivers in Western Europe often exhibit predetermined, straightened, and monotonous characteristics in the prealpine to flatland region, with a largely flat riverbed, leading to the loss of a significant portion of depth and flow variation.

The aforementioned factors contribute to a deterioration in the hydromorphological quality of the river, creating an increasingly inhospitable environment for fish: The absence of depth variability becomes particularly problematic during droughts, where insufficient water depth hinders fish movement between habitats. Moreover, low water levels and high air temperatures during heatwaves lead to increased water temperatures and consequently to reduced oxygen concentrations (Becker et al., 2022; Roberts, Promny, & Vollmers, 2014; Zscheischler et al., 2020), which are a threat especially to temperature sensitive fish species. Among other reasons, this resulted in a decline of population and diversity of fish species over the past decades (Baras & Cherry, 1990; Peňáz et al., 2002; Gründler & Baier, 2018; Gründler, Schläppi, & Philipp, 2019).

The severity of this problem is exemplified by two extreme hot and dry periods in southern Germany during the summers of 2018 and 2022, resulting in a significant drop in water levels in some rivers. In addition, high water temperatures surpassing critical levels led to a sub-

stantial decrease in oxygen concentration (LUBW, 2019). Fish species particularly sensitive to temperature, such as the common barbel (*Barbus barbus*), faced an increasing threat due to the lack of suitabl e habitats. To prevent high fish mortality rates, local river managers undertook emergency measures: They initiated the dredging of holes into the riverbanks that were filled with cold water by local firefighter teams. To enhance the effectiveness of the measure, additional shading was installed to minimize solar radiation, thereby stabilizing water temperature, and nets were employed to deter terrestrial predators from exploiting the situation. While these improvised measures proved remarkably effective and helped the fish to endure droughts and heatwaves, the holes were re-filled with sediment during the subsequent floods. This experience underscores the necessity for sustainable and predictable engineering measures to create stable and suitable habitats during heat waves, and hereby improving the resilience of river systems, especially considering that climate projections predict increasing severity of extreme weather events (Roberts, Promny, & Vollmers, 2014).

This issue has been acknowledged by the relevant authorities and has been established as an objective in various programs. For instance, the implementation of the Water Framework Directive (WFD) in 2000, has initiated a significant transition towards balancing flood protection requirements with considerations for aquatic ecology. In response, European member states have launched national programs aimed at improving the resilience of river systems. Consequently, river managers are actively seeking measures that can be implemented to enhance a river's ability to withstand the impacts of heatwaves and droughts.

A promising strategy to increase resilience against droughts in the context of fish habitats is the creation of deep pool habitats. Their significant water depth creates a favorable environment for fish due to the larger volume with consequently lower water temperatures (with possible temperature differences of up to 8°C, as indicated by Kurylyk et al. (2015)) and ultimately larger oxygen concentrations (Magoulick & Kobza, 2003). Beyond that, they act as flow shelters outside the main flow path during flood events, offer refuge during the wintering season, especially when coupled with suitable structures, and provide visual shelter to protect fish populations from aerial predators such as cormorants (Magoulick & Kobza, 2003). In essence, deep pool habitats are multi functional aquatic structures with vital importance for sustaining fish populations. Due to the large variability of water depth, flow velocities, turbulence and also sediment sorting, deep pool habitats are supposed to create diverse habitats and have a positive impact on the beta diversity (Whittaker, 1960; Tuomisto, 2010; Heino & Tolonen, 2017).

In river restoration, two distinct approaches to enhance flow velocity and depth variability and hence the resilience of rivers are recognized. The first involves implementing measures to restore natural morphodynamic processes, known as "Eigendynamik" (self-development) which includes actions like dismantling bank reinforcements and altering the river course to enhance flow variability - an approach that relies on a largely natural sediment balance (Becker & Ortlepp, 2022). However, in urbanized areas with side constrictions and mostly disturbed hy-

dromorphological regimes (Leibundgut et al., 2002), achieving self-development cannot be realized in most cases. The second approach is based on the creation of depth and flow variability through engineered replacement structures. Those measures become necessary in restricted urbanized areas, aiming for predictable hydromorphological development, encompassing changes in depth, flow velocities, and backwater rise. In-stream measures emerge as the preferred means of intervention as replacement structures. Valuable insights into possible in-stream measures can be derived from deep sections in rivers, commonly observed around hydraulic structures like bridge piers and downstream of weirs where scours naturally form. Drawing from this knowledge, there is an opportunity to develop a systematic approach for utilizing local scours as intentional deep pool habitats, providing a predictable and sustainable solution for maintaining aquatic ecosystems.

Previous studies have examined individual structures, such as micro groynes (Mende, 2014; Müller, Seidel, & Nestmann, 2020), and their impact on bed morphology and flow velocities and subsequently characterized possible habitat types that evolve around the structures. This study follows a novel focus: rather than focusing on one specific structure type and its geometric parameterization and optimization, the emphasis in this work is on the intended use and comparison of different structures to create the habitat type "deep pool". This broader perspective is expected to enhance our understanding of the ecological implications of various engineering measures in fostering fish habitats.

The present dissertation has been developed within the scope of the project "Hydraulics and morphodynamics for the initiation of sustainable deep sections" in collaboration with the Fisheries Authority of the Regional Council Karlsruhe in the Water Engineering and Water Management research group of the Institute of Water and Environment of the Karlsruhe Institute of Technology. Consequently, this work possesses a pronounced interdisciplinary orientation.

1.2 Research objectives

This dissertation explores various engineering measures aimed at creating scour holes and assesses their ecological potential as deep pool habitats. Within this framework, the following objectives are addressed:

- Identification and development of different measures for the sustainable creation of scours in rivers in prealpine to flatland conditions that provide a deep pool habitat for the fish based on physical and ecological parameters.

    – Defining a deep pool habitat regarding physical parameters relevant for a hydromorphological dimensioning that are based on biological needs of fish.

    – Selection and conceptualization of measures to create local scours to be used as deep pool habitat. Literature from both disciplines biology and hydromorphology shall be reviewed here.

- Development of a hydromorphological model approach for the representation of scour processes for ecological questions.

- Investigation of additional considerations such as the influence of natural materials, debris accumulations and combination of a deep pool habitat with a shelter, to derive recommendations for the implementation in practice.

Note that the measures developed in this work are intended for urbanized areas where a self-dynamic development of the river cannot be initiated due to local restrictions. The measures could be implemented in river restoration projects with focus on self-development as well, even though other engineering measures for the initiation should be favoured in those cases.

1.3   Report structure

Chapter 2 bridges the gap between fish biological questions and hydromorphological dimensioning of structures. The relevant life cycle stages of the indicator fish species are shown and physical parameters are derived to describe a deep pool habitat. Additional information is given on potential hydromorphological parameters for the characterization of a deep pool habitat.

Chapter 3 reviews literature of local scouring processes including the flow fields for different scour mechanisms as well as parameters influencing maximum scour depth.

Chapter 4 outlines the experimental configuration and the instrumentation. This setup is modified in the subsequent chapters based on the specific research objectives, and described therein accordingly. Additionally, a short description of the numerical model applied in chapter 5 is given in chapter 4.

Chapter 5 analyses the equilibrium bed morphology, the flow field and the backwater rise of six selected structures in an idealized setup based on a physical model experiment and 3D-HN simulations.

Chapter 6 contains all further considerations that have been made to implement the favourable structures in practice.

Chapter 7 starts with a comprehensive overview of all investigated variants, followed by an hydromorphological evaluation of the different structures. The focus is on the selected hydromorphological parameters from Chapter 2 and incorporating perspectives that have evolved throughout the analysis in chapter 5. The chapter concludes with an outlook on further considerations required for practical implementation.

Chapter 8 presents the primary conclusions of this work.

Additional data, graphs and images, not included in the main document, can be found in the Appendix.
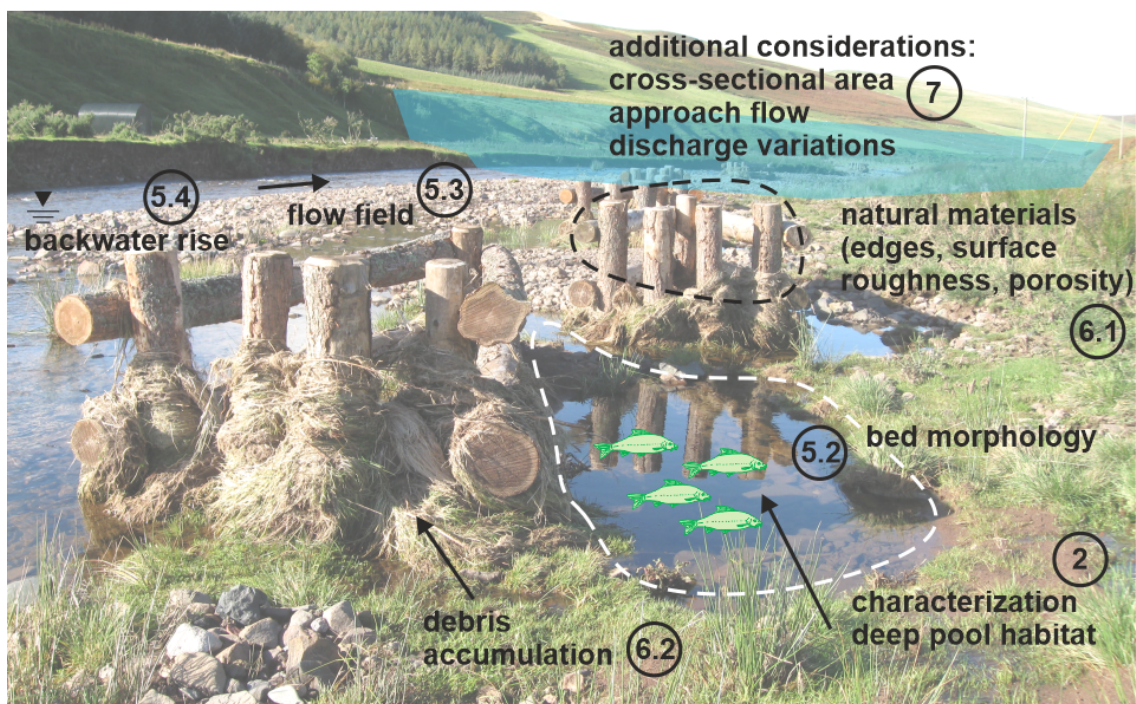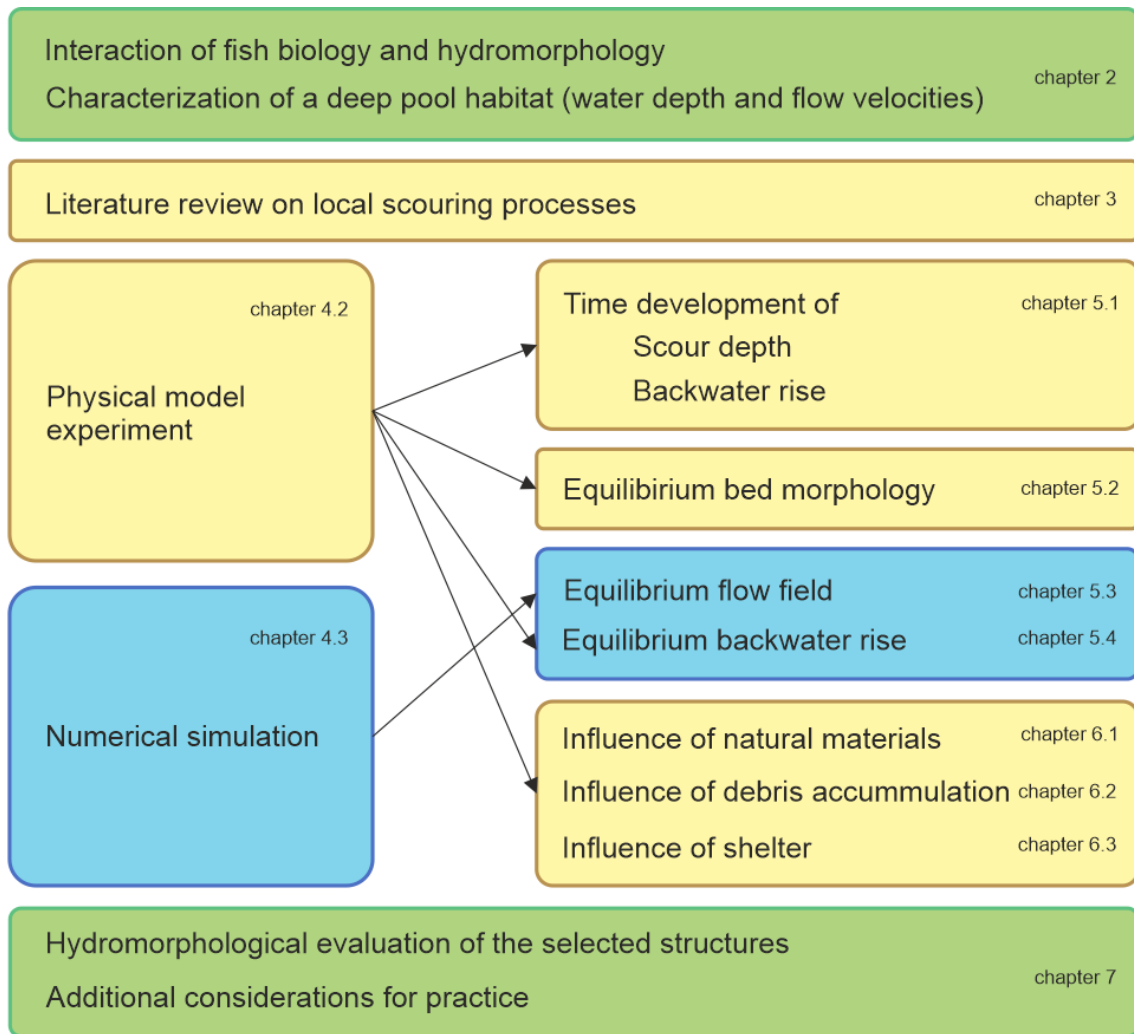
Figure 1.1: A representative view of the report structure (background: engineered log jam structures in a gravel-bed river, image courtesy of Stephen Addy).

Chapter 2

Hydromorphological and ecological requirements of deep pool habitats

River systems are often altered by humans for flood protection through methods such as rectification, channelization, and hydraulic optimization (Lane & Richards, 1997; WFD, 2014), which results, among other consequences, in a loss of habitat diversity characterized by reduced flow and water depth variability (Wohl, 2019). Habitat restoration efforts have identified deep pool habitats as a key factor in promoting diversity (Kurylyk et al., 2015; Labbe & Fausch, 2000), especially in the project region of the tributaries of the Upper Rhine valley (Gründler & Baier, 2018; Gründler, Schläppi, & Philipp, 2019). This study aims to create deep pool habitats through the implementation of in-stream structures. Within this dissertation possible in-stream measures are selected and developed. On this basis a generalizable model approach for the investigation of bed morphology, flow velocities and backwater rise is developed. The applied methodology differs from previous studies, where mostly one type of in-stream structure (see chapter 3.2) was investigated and the resulting bed morphology and flow field was evaluated for ecological functionality (e.g. Mende (2014) and Müller, Seidel, and Nestmann (2020)). The new approach defines the ecological requirements of the deep pool habitat first and only after this different in-stream structures are designed especially for those requirements. The outcomes aim to a) provide quantitative values essential for flood risk assessment and b) establish a robust dataset for subsequent biological evaluations. It is crucial to establish clear hydromorphological target values at the outset of the process to guide and inform the investigation effectively. The lack of clarity surrounding the target values prompts a more thorough exploration in this chapter.

The habitat under investigation is the deep pool habitat which is sometimes called the "barbel holes" (german: "Barben-Löcher"), in colloquial language of fishermen in the Upper Rhine Valley in Germany, France and Switzerland. This already gives a hint that the species barbel (*Barbus barbus*) is one of the inhabitants of deep pool habitats. The common barbel also gave name to the barbel zone according to Aarts and Nienhuis (2003). The barbel is a good indicator for structural diversity and fish passage, due to specific habitat needs during their life stages and different seasonal preferences (Britton & Pegg, 2011). For this reason, the species *Barbus barbus* (common barbel) was selected as the "Fokusart" (german for focus or

target species, a representative fish species based on their habitat requirements, also indicator species) for the study. It is crucial to emphasize that although the analysis in this dissertation exemplifies improvements for the barbel, the enhancement of deep pool habitat extends beyond the exclusive benefit to this species. Augmenting variability in water depth, flow velocities, turbulence, and potentially substrate composition contributes to an overall improvement in the beta diversity of the river section. As defined by Whittaker (1960) beta diversity is a measure of the difference in species diversity between different, spatially distributed communities within a landscape (Heino & Tolonen, 2017; Tuomisto, 2010).

Defining the hydromorphological boundary conditions of a deep pool habitat is crucial but to the authors knowledge there is no universal hydromorphological characterization of this habitat type available. Hence, this chapter starts with two approaches that were considered to find a hydromorphological characterization of a deep pool habitat. The first examines natural pool sequences and forced pools in the field to derive the hydromorphological boundary conditions. The second considers the habitat preferences of the focus species barbel. Based on the species selection the deep pool is characterized with parameters for water depth, flow velocity and substrate type. Water depth and substrate type can be commonly defined, whereas suitable description of flow velocities for biological evaluation is still a highly discussed question. For instance in the fish pass community it is still a remaining open questions whether mean flow velocities are able to give a sufficient insight into the hydrodynamics to undergo a biological evaluation (Henning & Weichert, 2020; Sokoray-Varga & Weichert, 2020). Therefore, an excursion to turbulence statistics and hydrodynamic parameters that can be used to evaluate habitats is presented subsequently to link the hydrodynamics to an ecological evaluation. Additionally, the importance of habitat availability throughout the yearly cycle and shelters is explained.

It is important to consider that this study does not aim to evaluate the deep pool habitat in its biological functionality but to make the first step towards a functioning habitat by ensuring suitable hydromorphological boundary conditions. So, the focus of this dissertation is the characterization and comparison of the bed morphology pattern and the flow field around different in-stream structures to reach the ecological requirements. This chapter shall help to define the metrics that are needed to design the hydromorphology and identify the research gap. In the complexity of the interdisciplinary field this needs a more profound explanation. In this context, the term local scour is mostly used in the hydraulic engineering community and describes the river bed incision around an in-stream structure. The term deep pool habitat describes an ecological functionality of a deep section in a river that is used by certain species in particular life-, seasonal- and day cycles and is mostly used in the fishbiological community. Both terms describe a similar hydromorphological pattern in a river. The second part, the biological evaluation needs to be performed by a fish biologist subsequent to this work. Due to their complexity, all questions related to temperature are excluded in this work and are upon further research, the focus is on the hydromorphology.

2.1 The common barbel (*Barbus barbus*)

Barbus barbus is a species of fish found in the entire North Atlantic region, including North Spain, France, Germany, the entire Baltic region, Scandinavia, and North Russia. It is a rheophilic, bottom dwelling cyprinid with a preference for relatively deep water, and generally requires lotic river sections. Despite being a well-studied species, the biology of the barbel is still insufficiently understood. This fish species was facing a decline in numerous European rivers (Peňáz et al., 2002) and was classified as threatened or endangered in most of the studies conducted in the early eighties in Western Europe as cited in Baras and Cherry (1990). More recently, the common barbel was classified as "least concern (LC)" by the IUCN Red List of Threatened Species" in 2010 (IUCN, 2016).

2.1.1 Lifecycle and need of habitats

Spawning

The spawning migration, which is directed in upstream river direction into the tributary river to reach suitable gravel bars (Panchan et al., 2022), is triggered by water temperature (13-17°C, Ebel (1996), Ebel (2002), and Ovidio et al. (2007)) and increasing discharge, so the spawning season in our latitudes usually falls in the months of May and June (Ebel, 2002). Photoperiod may also play an important regulator of spawning time, with evidence of a daily rhythm of photosensitivity (Poncin, 1992). Barbels are a diurnal spawning cyprinids, however, nocturnal spawning activity was observed, too (Baras, 1992). Barbel spawn in groups on gravel beds with a grain size 1-3 cm (Ebel, 1996; Ebel, 2002). The slightly sticky eggs (diameter 2 mm; 3000-9000 eggs) are washed into the hyporheic interstitial, were they develop until hatching (Ebel, 1996; Ebel, 2002).

Larvae and Juvenile

The larvae live in the hyporheic interstitial for 8-19 days and feed on the yolk sac. With a body length of 10-14 mm, they emerge and drift down with the current. In flat, well-structured shore areas with low flow velocities, they start with the first food intake. Shallow depths are also used where they prefer the dead water zone behind boulders (Ebel, 2002). With increasing age and size, they move to places with greater flow velocities and water depths (Ebel, 2002). With length above 50 mm barbels begin to avoid water velocities below 10 cm/s (Bischoff & Freyhof, 1999). Differences in microhabitat use are correspondingly apparent between age 0+ and > 1+ barbel, with lentic, shallow, littoral environments important for 0+ fish, and deeper, faster areas in mid-channel important for >1+ fish (Watkins, Doherty, & Copp, 1997). The sexual maturity of *Barbus barbus* varies between genders, with males reaching maturity at 4-5 years and females at 5-6 years.

Adult

Adult barbels need a well-structured river bed, with low and high flow velocities, as well as shallow and deep areas. Average summer water temperatures of around 20°C are typical for

the barbel zone (Ebel, 2002). In large rivers in France (> 50 m wide), the highest abundance of barbel were in stretches of highest heterogeneity in the benthic habitat (Lelek & Lusk, 1965). The barbel is a potamodromic migratory fish. Migrations are observed over a seasonal cycle. In the course of the spawning migration, distances of between 50 and 300 km were observed (Steinmann, Koch, & Scheuring, 1937). During the course of the day, migrations between 20 and 500 m (Baras, 1992; Pelz & Kästle, 1989), and even up to 10 km for individual barbels (Gerstmeier & Romig, 2003) between the resting habitat and the feeding habitat were recorded during summer. In winter, fish movements and activities tend to cease in accordance with their thermal activity limits being reached (4 °C; Baras (1992)). As barbels are vagile with a lifecycle incorporating relatively large spawning migration, even small blockages arising through river engineering that disrupt longitudinal connectivity may impede their movements and have large ecological consequences (Lucas & Batley, 1996). The habitats inhabited by an adult barbel throughout the daily and seasonal cycle are summarized in table 2.1.

Table 2.1: Adult habitats of *Barbus barbus* during different daily, monthly and yearly cycles.

habitat in the daytime:	Differences in microhabitat use are correspondingly apparent between age 0+ and > 1+ barbel, with lentic, shallow, littoral environments important for 0+ fish, and deeper, faster areas in mid-channel important for > 1+ fish (Watkins, Doherty, & Copp, 1997). Adult barbels rest during daytime at the bottom of deeper river sections (mid-channel). Preferred water depth are deeper than 1 m and sections with shadow through overhanging vegetation or undercut banks are inhabited by adult barbels (Blohm, Gaumert, & Kämmereit, 1994).
habitat in the nighttime:	At dusk, older barbels seek out areas with shallower water and higher flow velocities (riffles) (Ebel, 2002), where they track down and eat all kinds of small animals such as insect larvae, snails and mussels, but also graze on algae.
habitat for feeding:	Barbels are usually in search of food in small swarms at dusk. The feeding habitats are characterized by water depths of 0.13 to 0.5 m and flow velocities of 0.13 to 0.60 m/s (Becker & Ortlepp, 2022).
habitat during winter season:	In winter, mean daily activity was less than 20 % of peak summer levels and fish are relatively dormant (Lucas & Batley, 1996). During that period of the year, barbels inhabit deep pool habitats where they stay close together. These are the barbel holes mentioned above.

2.2 Hydromorphological analysis of natural riffle-pool-sequences and forced pools

Deep pool habitats are known from classical riffle-pool-sequences that naturally form in gravel bed rivers with limited transport capacity and a river bed slope < 0.02 (Thompson, 2018). According to the review of Thompson (2018) free-formed pools are mostly associated with channel narrowing, confluences or meandering, where pools mostly form due to helical flow and sediment routing. In ecology, besides natural riffle-pool sequences also forced pools are known which are related to natural obstructions in the flow, like boulders or large wood obstructions (Thompson, 2018). Local constriction and separation of the flow, as well as dead water zones, locally increased water-surface slope and high turbulence are associated with

forced pools.

2.2.1 Hydrodynamics of natural riffle-pool-sequences and forced pools

Venditti et al. (2014) analyzed *natural* riffle pool sequences and found repeating flow structures for the majority of sequences as shown in figure 2.1. As the water approaches the pool, high flow velocities were detected. While entering the pool a velocity inversion was observed which means high velocities at the bed and low velocities at the surface. This leads to negative vertical velocities along the channel centreline. The water then plunges into the pool causing an up-welling along the canyon walls and two vortex cells that form boils at the water surface. This flow structure leads to a deep scour and an undercutting of the channel walls as well as cleaning off of debris, as the walls stay nearly vertical. The high flow velocity reduces along the distance of the pool but gets reactivated with every narrowing of the channel. This pattern of multiple plunging pools was observed at several places.
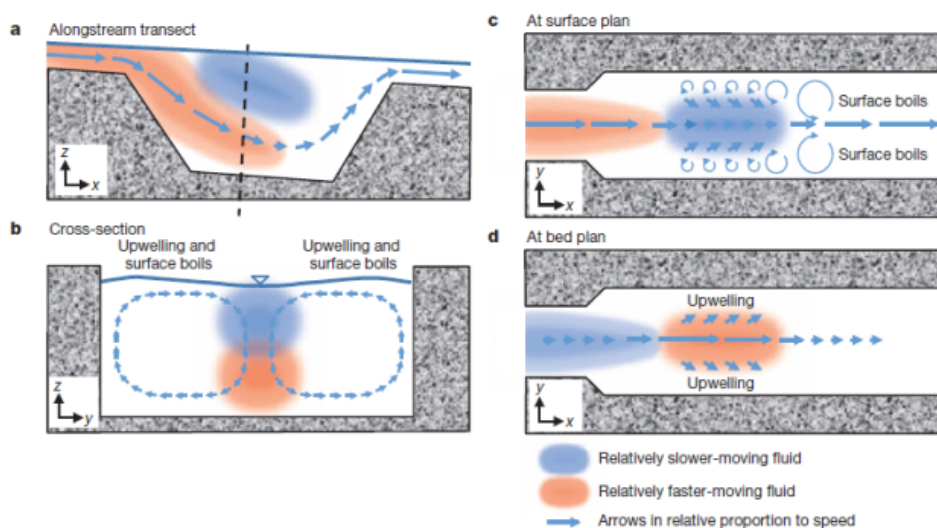
Figure 2.1: Conceptual model of the flow in a riffle-pool-unit of a bedrock canyon in Fraser River (Venditti et al., 2014).

Dashtpeyma (2019) idealized the riffle-pool-sequence to a ramp with an angle as a riffle and a pool as shown in figures 2.2 and 2.3. The ramp entrance to the pool is characterized as a convective decelerating flow (CDF) and the pool tail as a convective accelerating flow (CAF) zone. The turbulent structures of three types of sequences were tested: a simplified riffle-pool unit (a), with linear (b) and concave constriction (b). The riffle-pool unit is dominated by the generation and dissipation of turbulent structures in the adverse pressure gradient region (CDF). The turbulent structures are described as ramp or bed roller, corner eddies, axial tails and surface turbulence. Horseshoe vortices are generated in the favourable pressure gradient zone (CAF). Dashtpeyma (2019) concludes that these vortices exert an additional resistance to the flow by increasing mixing effects and changing the pressure domain and describe this as the vortex resistance hypothesis.
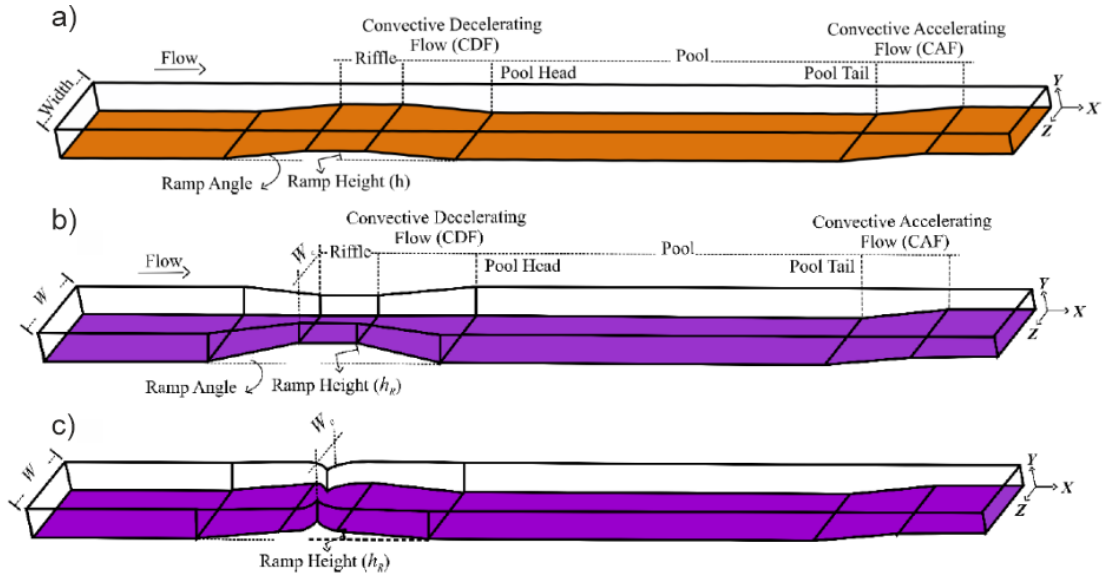
Figure 2.2: Idealization of a riffle-pool unit with a) simple, b) linear constriction and c) concave constriction as presented in Dashtpeyma (2019).
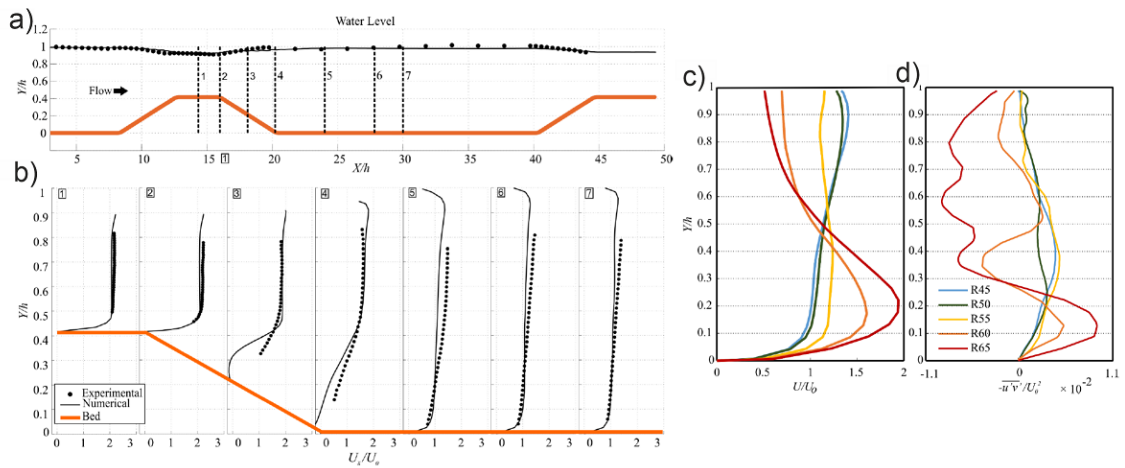
Figure 2.3: a) and b) Velocity profiles and water surface profile along the centerline of the riffle-pool-unit. c) and d) Velocity profile at the center of the pool for different riffle heights (Dashtpeyma, 2019).

A conceptual model of the hydrodynamics of *forced* riffle-pool-sequences has been presented by MacVicar and Roy (2007) and MacVicar and Roy (2011). It consists of a run, a pool-head, a constriction, a mid-pool and a pool tail (see figure 2.4). They name two main characteristics of the riffle-pool-sequence. A change in velocity distribution can be observed due to a lateral convergence and divergence zone with secondary flows and flow separations. The second characteristic is the generation of turbulence as a consequence of the beforementioned perturbations and can be observed in the lateral shear zones and high turbulence intensities close to the bed.
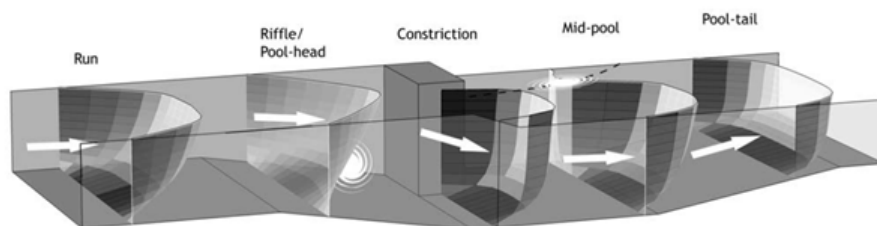
Figure 2.4: Conceptual model of the hydrodynamics of forced riffle-pool sequences as presented in MacVicar and Roy (2007)

2.2.2 Morphology of natural riffle-pool-sequences and forced pools

MacVicar and Roy (2011) link the hydrodynamics inside a pool unit with the sediment dynamics. They found that the head of the pool is characterized by full mobility due to high levels of turbulence that are a consequence of a deceleration of the flow. The entrance slope shows partial mobility and lateral gradients indicate that the majority of the sediment is routed over the side bar. The center of the pool shows full mobility again. The exit slope is characterized by high near bed velocities and shear stress due to the constriction and hence acceleration of the flow which leads to full mobility in this area. The lateral constriction of the channel and the topographic forcing by the pool exit slope induce a convective acceleration of the flow which increases the time-averaged, near-bed shear stress. This is the dominant mechanism for pool scour and induces local full mobility and is necessary for the maintenance of pool depth. Cycles of deposition and erosion can be observed in the deep pool unit and are associated with different discharges and sediment supply from upstream. Dashtpeyma (2019) could show that the Shields threshold for sediment motion does not explain sediment motion in deep pool cases as it does not consider the pulsation and variability in shear stress. In zones with higher mean and standard deviations of shear stress Dashtpeyma (2019) detect higher entrainment rates. In accordance with MacVicar and Roy (2011), the downsloping ramp at the entrance of the pool is associated with lower shear stress and higher pulsation and hence low sediment entrainment and acts as a deposition zone and prevents sediment from entering the pool.

2.3 Ecological specifications of deep pool habitats

In the previous chapter natural riffle-pool sequences and forced pools due to natural obstructions (e.g. trees) as observed in the field were analyzed regarding hydromorphological aspects. Due to human intervention those natural pools mostly vanished from rivers, especially in urbanized areas. Therefore, in the present case deep pool habitats are intended to be created by inducing a local scour hole with an in-stream structure. For the design and dimensioning of the in-stream structure target values that specify the conditions for the deep pool habitat need to be defined. As explained above, the deep pool habitat has a complex set of boundary conditions. First there are the hydromorphological boundary conditions that include water depth, flow velocities and substrate type. Another group of boundary conditions is the water chemistry which includes e.g. water temperature and dissolved oxygen concentration. A more diverse group is the surrounding factors which include shelters (flow and visual shelters)

and connectivity to other habitats. This work will focus on the hydromorphological parameters water depth and flow velocity. Some words on shelters and the availability throughout the year due to changing discharge, flow velocities, water depth and sediment supply are given at the end of this chapter but will not be the focus of this investigation.

Before evaluating the importance of the parameters mentioned above, it needs to be said that even though the barbel is one of the most studied fish species in Western Europe, further specifications on the habitat use, in particular deep pool habitat, are rare in literature (Melcher & Schmutz, 2010; Peňáz et al., 2002). For the purpose of designing a deep pool habitat further specification of water depth and flow velocities is needed. It is important to know, that the values presented in this chapter do not claim to reflect the absolute truth from an ecological point of view, but are to be interpreted as appropriate target values for the hydromorphological design of an in-stream structure that can provide a deep pool habitat for a barbel.

The specifications are based on several sources and upon best knowledge:

- Observation of existing deep pools in nature without reference to the species barbel (e.g. Capone and Kushlan (1991) (Sulphur River, Texas USA), McIntosh et al. (2000) (Columbia River Basin, USA))

- Observation of barbel preferences in relation to deep pool habitats, but also other habitat types that they use throughout their lifecycle (Panchan et al. (2022), Danube, Austria; Baras and Cherry (1990), Ourthe, Southern Belgium; Cismaș, Bănăduc, and Bănăduc (2018), Târnava River, Romania; Melcher and Schmutz (2010), Pielach River, Danube system, Austria; Peňáz et al. (2002), Jihlava river, Czech Republic; Pouilly and Souchon (1994), Ain, Ardeche, Rhône, France).

- Species preferences and design parameters given in statal directives:
  Landesstudie Gewässerökologie - Fischökologisch funktionsfähige Strukturen in Fließgewässern (Becker & Ortlepp, 2022)
  Mindestwasserabflüsse in Ausleitungsstrecken (LfU, 2005)
  Vollzugshinweise zum Schutz von Fischarten in Niedersachsen (LAVES, 2011)

- Expert talk with Regierungspräsidium Karlsruhe (Dr. Frank Hartmann and Stephan Hüsgen) on the need of deep pool habitats as summer and winter habitat as derived from practical work at rivers in Baden - Württemberg and Fischereiforschungsstelle Baden-Württemberg (Dr. Jan Baer and Dr. Andreas Brinkmann) especially regarding barbel preferences in Baden - Württemberg and review and evaluation of the above-mentioned resources

For the water depth a few values can be found in literature for deep pool habitats and are also specified for barbels, whereas quantifications for flow velocities are rare to find in literature as shown in chapter 2.3.1. Especially ecological studies often do not specify where velocity was measured and how it was averaged (mean velocity, nose-tip velocity, surface velocity).

However, it is questionable whether a mean flow velocity can reflect the needs of a fish in a habitat in an adequate extent. Research on fishways, particularly slot passes, has shown that not only mean flow velocity but also velocity fluctuations and eddies determine the likelihood of fish residing in the pools and slots (Henning & Weichert, 2020; Sokoray-Varga & Weichert, 2020). Therefore, a short excursion on hydrodynamic parameters for the biological evaluation of flow conditions is given subsequently, followed by a short description of the movement of fish bodies in turbulent flows and existing studies on the probability of residence of fish in the flow around in-stream structures. These preliminary remarks shall give a background on the complexity of the definition of the boundary conditions for the deep pool habitat. The subchapter concludes with specific values for water depth and flow velocities of deep pool habitats for barbels.

Hydrodynamic parameters for the biological evaluation of flow conditions

Several attempts have been made to find a characterization of flow properties that is suitable for a biological evaluation of hydrodynamics. First an introduction into statistical evaluation of hydrodynamic flow data is given. Then, several basic concepts, ideas and applications of hydrodynamic parameters are presented in the following paragraphs.

The most commonly used parameter to describe flow conditions is the time-averaged flow velocity $\overline{u}$ (e.g. Pope (2011)):

$$\overline{u} = \frac{1}{T} \int_{t}^{t+T} u \, dt \tag{2.1}$$

where t equals the time and T the total observed time period. Often it is referred to as mean flow velocity, which can be the above-mentioned time-averaged flow velocity or a space-averaged flow velocity. Space averaged flow velocities are often built as depth-averaged or cross-sectional-averaged flow velocities.

The magnitude of velocity $\overline{U}$ refers to the three-dimensional vector of the time-averaged flow velocity at a point:

$$\overline{U} = \sqrt{\overline{u}^2 + \overline{v}^2 + \overline{w}^2} \tag{2.2}$$

The Reynolds decomposition decomposes the instantaneous flow velocity u into a mean flow velocity part $\overline{u}$ and a flow velocity fluctuation part u'.

$$u(t) = \overline{u} + u'(t) \tag{2.3}$$
$$v(t) = \overline{v} + v'(t) \tag{2.4}$$
$$w(t) = \overline{w} + w'(t) \tag{2.5}$$

The root-mean square velocity u_{rms} is the root of the squared velocity fluctuation. It gives a first impression on turbulence characteristics of the flow.

$$u_{rms} = \sqrt{\overline{u'(t)^2}} \qquad (2.6)$$

$$v_{rms} = \sqrt{\overline{v'(t)^2}} \qquad (2.7)$$

$$w_{rms} = \sqrt{\overline{w'(t)^2}} \qquad (2.8)$$

The turbulent characteristics of the flow can also be evaluated by several other statistical parameters that are introduced briefly here. The Reynolds shear stresses $\tau_{xy}, \tau_{xz}, \tau_{yz}$ are obtained by time-averaging of the Navier-Stokes-equations with Reynolds decomposition of the velocity fluctuations.

$$\tau_{xy} = |\rho\,\overline{u'v'}| \qquad (2.9)$$

$$\tau_{xz} = |\rho\,\overline{u'w'}| \qquad (2.10)$$

$$\tau_{yz} = |\rho\,\overline{v'w'}| \qquad (2.11)$$

The turbulent kinetic energy κ_T (TKE) is characterized by the root-mean-square velocity fluctuations in the three dimensions. TKE is the mean kinetic energy per unit mass that is associated with vortices in turbulent flow. Zones of high TKE are zones with high shear, friction or buoyancy forces.

$$\kappa_T = 0.5 \left(\overline{(u')^2} + \overline{(v')^2} + \overline{(w')^2} \right) \qquad (2.12)$$

The turbulence intensity I relates the velocity fluctuations to the mean value of the flow velocity and hence is a measure of how significant the fluctuations are to the flow. It can give a measure on how large the turbulence is, but is not considering the scale or structure of turbulence. It is defined as follows:

$$I = \frac{U_{rms}}{\overline{U}} \qquad (2.13)$$

In statistically averaged numerical models such as RANS models (see chapter 4.3.5), the velocity fluctuations are not always calculated. Considering the definition of turbulent kinetic energy in equation 2.12, the magnitude of root-mean square velocity U_{rms} can also be calculated with:

$$U_{rms} = \sqrt{\frac{2}{3}\kappa_T} \qquad (2.14)$$

The turbulence intensity used within the numerical model applied in this work is also based on the turbulent kinetic energy approach and is defined in equation 4.22.

The vorticity of the flow ω describes the spinning motion around a point in the flow. This value could easily be misinterpreted as the strength of a vortex. The unit of vorticity 1/s shows that it is a frequency. To characterize the strength of the vortex other types of analysis need to be taken as shown in chapter 7.3.

$$\omega_x = \frac{\partial w}{\partial y} - \frac{\partial y}{\partial z} \tag{2.15}$$

$$\omega_y = \frac{\partial u}{\partial z} - \frac{\partial w}{\partial x} \tag{2.16}$$

$$\omega_z = \frac{\partial v}{\partial x} - \frac{\partial u}{\partial y} \tag{2.17}$$

The above-mentioned vorticity is often used to visualize vortex structures but is not able to capture all coherent turbulent structures. Another method to show turbulent structures is the Q-criterion. Therefore, the velocity gradient tensor is divided in two parts:

$$\frac{\partial u_i}{\partial x_j} = 0.5 \left(\frac{\partial u_i}{\partial x_j} + \frac{\partial u_j}{\partial x_i} \right) + 0.5 \left(\frac{\partial u_i}{\partial x_j} - \frac{\partial u_j}{\partial x_i} \right) \tag{2.18}$$

The symmetric part is the strain rate tensor:

$$S = 0.5 \left(\frac{\partial u_i}{\partial x_j} + \frac{\partial u_j}{\partial x_i} \right) \tag{2.19}$$

The antisymmetric part is the vorticity tensor

$$\Omega = 0.5 \left(\frac{\partial u_i}{\partial x_j} - \frac{\partial u_j}{\partial x_i} \right) \tag{2.20}$$

It is to be noted that the strain rate is a specific function of the viscous stresses

$$\tau = \mu \left(\frac{\partial u_i}{\partial x_j} + \frac{\partial u_j}{\partial x_i} \right) \tag{2.21}$$

The Q-criterion is then defined as the second invariant of the velocity gradient tensor

$$Q = 0.5 \left(||\Omega||^2 - ||S||^2 \right) \tag{2.22}$$

Positive values of Q indicate areas where the rotation term exceeds the strain rate and indicates that the flow field is dominated by vorticity and the presence of rotational flow. Negative values of Q show that the area is dominated by strain rate or viscous stresses. This criterion was used e.g. by Dashtpeyma (2019) to visualize turbulent flow structures in an isolated riffle pool unit and refers to several other studies that visualize vortices in channel confluences groynes and channel bends (Beheshti, Ataie-Ashtiani, & Dashtpeyma, 2017; Ettema, Constantinescu, & Melville, 2017; Guillén-Ludeña et al., 2017; Keylock, Constantinescu, & Hardy, 2012; Keylock, Chang, & Constantinescu, 2016; Zeng & Constantinescu, 2017). The before mentioned fundamental hydrodynamic parameters were combined and applied in several studies and are shown on the example of selected studies.

IPOS as proposed by Lacey et al. (2012) is a framework that enables a generalization of turbulent flow characteristics in laboratory and field studies (see quantities in Table 2.2). The framework is based on four characteristics: intensity, periodicity, orientation and scale. *Intensity* covers parameters that describe turbulence characteristics of the flow such as turbulence intensity, turbulent kinetic energy, Reynolds shear stresses and vorticity. It is important to consider maximum turbulence levels for the comparison of laboratory and field studies as the absolute turbulence values experienced by the fish are an important criterion. Low vorticity has shown no measurable effect on swim stability of fish whereas high vorticity lead to rapid body rotations of fish as shown in Tritico and Cotel (2010). *Periodicity* of the flow is known to be important to fish swimming behavior as a predictable vortex shedding with a single dominant frequency is tolerated by adjustment of the fish's gait whereas the swimming pattern in randomly generated pulse flow is difficult to predict. A spectral analysis can give insights into the shedding frequency. The *orientation* of eddies plays a role for fish swim stability. Eddies with vertical axis are more likely to be tolerated whereas horizontal eddies can disorient fish to lose position. The last component is the *scale of turbulence*, which is often considered by looking at the eddy length scale in comparison to the fish length. In the presence of small eddies, the fish is not affected due to the lack of momentum. Trinci et al. (2017, 2023) concretize and apply the approach of Lacey et al. (2012) to three different rivers and can show that the selected parameters are able to capture different regimes in the different systems.

After the short excursus on hydrodynamic parameters the second important factor is the reaction of the fish to the flow. Therefore, the basic moving mechanisms of fish in turbulent flows are explained.

Fish bodies in turbulent flow

Rheophilic fishes use two main mechanisms to move in turbulent flows. The first mechanism is hiding in zones with reduced flow velocities e.g. downstream of boulders. Some fish species are able to reduce energy consumption by tilting their body in an angle to the mean flow direction and need nearly no body corrective or fin motion to hold their position (Trinci et al., 2017). The fins motion generates vortices that help the fish to stabilize their position in the flow. The second mechanism is taking advantage of discrete vortices with a certain vortex to fish size ratio. Under the condition that the incoming vortices are in a predictable pattern the fish is able to anticipate the flow structure and use the vortices to maintain position. This type of motion is often called Kármán gait as it is associated with the defined frequency of vortex shedding of a von-Kármán vortex street. By the anticipation of vortices, the fish needs only the anterior axial muscle to stabilize the body in the flow and requires a lower tail-beat frequency (Trinci et al., 2017). Not only the strength and size of vortices is important, but also the orientation of the vortices. Vortices with axis of rotation in main flow direction causes rolling, horizontal vortices with pitching and vertical vortices with yawing (Trinci et al., 2017). Subsequently, the flow structure and the fish movement are connected in studies about the probability of residence of fish in the flow around idealized in-stream structures.

Table 2.2: Parametrization of the IPOS Framework and absolute values available from literature

Group	Parameter	Absolute values
intensity	turbulence intensity	
	turbulent kinetic energy	mentioned in Lacey et al. (2012) Smith, Brannon, and Odeh (2005): 0.016 m²/s² (lab) Tritico and Hotchkiss (2005): >0.08 m²/s² (field, behind a boulder) Lacey and Roy (2008): >0.06 m²/s² (field, submerged pebble cluster)
	Reynolds shear stresses	as mentioned in Lacey et al. (2012): Smith, Brannon, and Odeh (2005): $-\rho\overline{u'v'}$= 4.9 N/m² $-\rho\overline{u'w'}$ = 2. N/m²
	vorticity	as mentioned in Lacey et al. (2012): Tritico, Cotel, and Clarke (2007): up to 9 1/s (field) White, Somandepalli, and Mungal (2004): 40 1/s
periodicity	predictability (kurtosis of the turbulent fluctuations)	
	energy spectra (Fourier analysis or wavelet analysis)	
orientation	skewness of the turbulent fluctuations	
	event structure	
	direction of the dominant fluctuation	
	Reynolds shear stresses	
scale	eddy length scale	
	fish momentum to wedge momentum ratio	
	eddy diameter	Tritico & Cotel (2010): for 75% of fish length → fish showed stability problems Lupandin (2005) and Pavlov, Lupandin, and Skorobogatov (2000): vortices reach two third of the fish length, swimming performance begins to decrease

Probability of residence of fish in the flow around in-stream structures based on hydrodynamic parameters

Little is known about quantitative numbers of flow velocity preferences of habitat use in natural conditions. Tests for several species were conducted under laboratory conditions.
Hockley et al. (2014) tested the fish response to micro habitats downstream of hemisphere boulders. They classified regions downstream of the boulder as high- ($\overline{u} = 14.5 \pm 2.26\,cm/s$) and low-velocity ($\overline{u} = 6.46 \pm 6.97\,cm/s$) with low- ($k = 3.56 \pm 6.09\,cm^2/s^2$) and high-turbulence

($k = 25.28 \pm 27.92\,cm^2/s^2$) regions. Microhabitat preferences were dependent on size, sex and parasite load. Large guppies preferred high velocity and low turbulence regions, male guppies preferred low-velocity regions and guppies with parasite load spent most time in regions with moderate velocity and low turbulence.

A similar approach was applied by Muhawenimana et al. (2019). They investigated the influence of a spanwise cylinder wake flow on *Nile tilapia*. Therefore, they classified the wake structure behind the cylinder into 9 regions, a bedwater, a midwater and a topwater column in the near, center and far wake zone (see figure 2.5 a)-c)). Fish avoided zones close to the cylinder, zones with lowest magnitudes of turbulence intensity, TKE, Reynolds stresses and vorticity and preferred the zone far-bed with about 55 % of time they spent there (figure 2.5 d)). Fish showed significant stability loss for eddy length of 45 % to 50 % of the fish length. The study showed that direction and orientation of the flow structure is important for swimming stability.
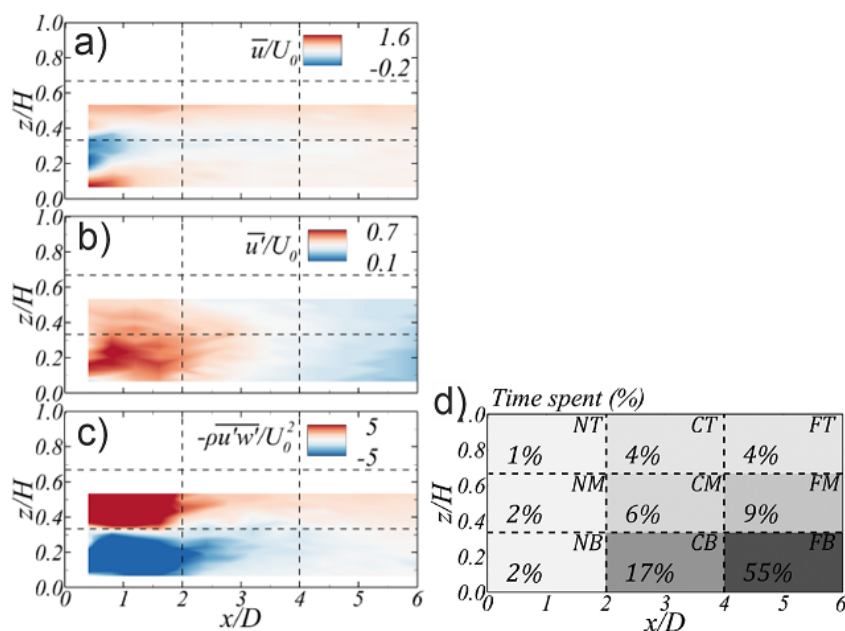
Figure 2.5: a) Time-averaged streamwise velocity $\overline{u}$, b) streamwise turbulence intensity u', c) principal Reynolds stress $-\rho u'w'$ and d) Time percentage spent in the different zones. Image adapted from Muhawenimana et al. (2019)

Tritico and Cotel (2010) could show significant differences of swimming stability for different orientations of eddy vortices for Creek chubs (*Semotilus atromaculatus*) as shown in figure 2.6. Swimming stability could be kept steady until an eddy diameter of 76 % of the body length was reached. For these conditions fish adapted to the flow and changed orientation. Fish were more sensitive to horizontal eddies than to vertical eddies of the same size. For streamwise flow velocities < 25 cm/s fish preferred the gap region between the cylinders for both vertical and horizontal arrangement. For velocities > 25 cm/s the preference shifts to the recirculation zone for horizontal cylinder and to the shear layer zone for vertical cylinder, but the preference is not as clear (> 70 %) than for low flow velocities.
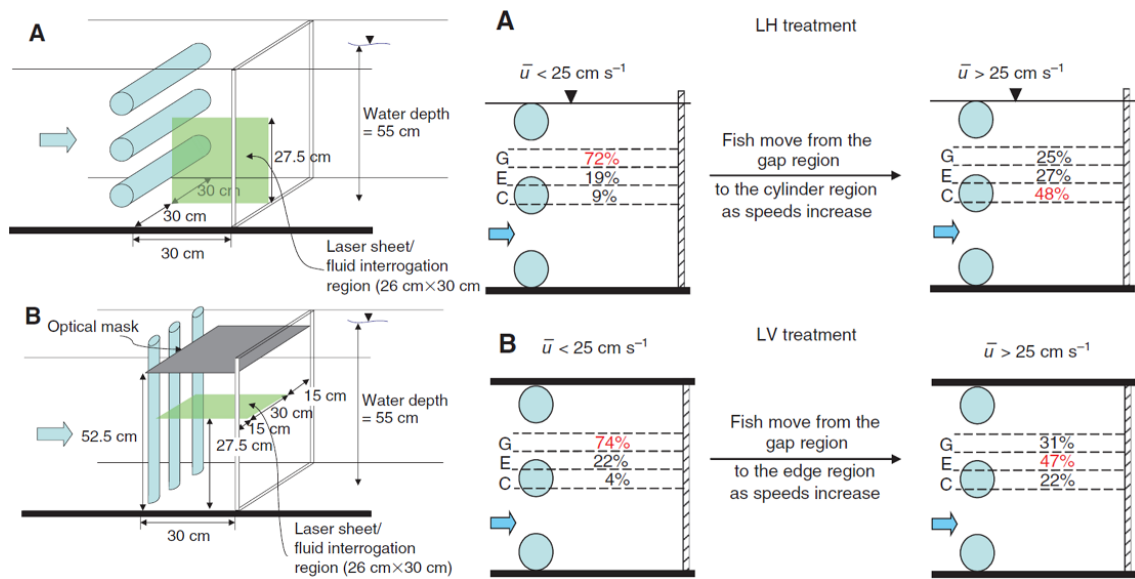
Figure 2.6: Left: configuration of horizontal (LH) and vertical (LV) arrangement of a group of cylinders. Right: probability of residence of fish in the different regions.

Przybilla et al. (2010) investigated the entrainment behaviour of trouts in the presence of the wake structure of a hemisphere as shown in figure 2.7. The flow field around the hemisphere was sectioned into 3 zones. The bow zone upstream of the cylinder (blue), the entraining zone at the sides of the cylinder where vortex formation is present (red) and the Kármán gait zone downstream of the cylinder in the midline of the cylinder wake with reduced flow velocities (green). The trouts spent 28.3 ± 36.3 %, 27.7 ± 31.0 % and 7.9 ± 17.2 % in the respective zone. There was no preference in the two entraining zones with 13.6 ± 22.6 % of the observation time entraining on the right and 14.2 ± 25.0 % entraining on the left side of the cylinder. In general the trout spent significantly more time the defined zones than in the random distribution.
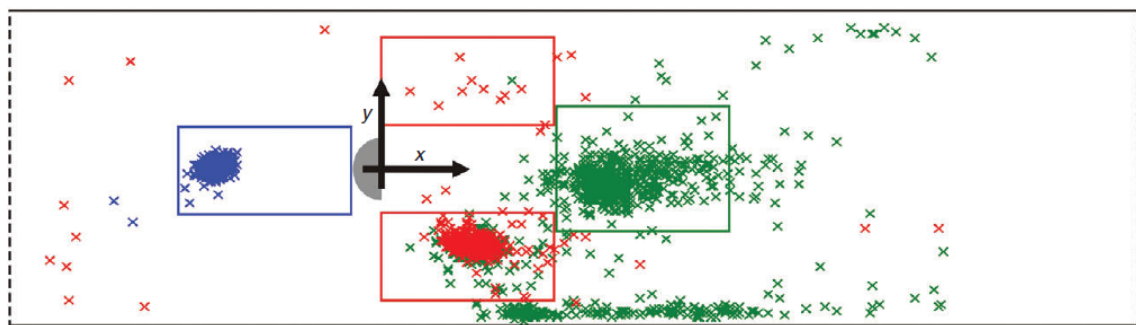
Figure 2.7: Entrainment behaviour of trouts in the presence of the wake structure of a hemisphere according to Przybilla et al. (2010)

21

2.3.1 Hydromorphological parameters of deep pool habitats with reference to the barbel

Flow velocity preferences of barbels in deep pool habitats

Details on preferences regarding flow velocities or turbulence characteristics with reference to the barbel is very scarce in literature (referring to the Iberian barbel, Silva et al. (2011)). Silva et al. (2011) investigated the preference of the Iberian barbel and state that TKE and Reynolds shear stress are two interdependent turbulence descriptors that influence the fish's body. They could show that eddies that are approximately of the body size of the barbel affect the balance of the fish in the turbulent flow. Especially the horizontal Reynolds shear stress component seems to be an important parameter for the hydraulic habitat selection of the Iberian barbel. The statal directive LSGÖ (Becker & Ortlepp, 2022) recommends a mean surface flow velocity of < 0.3 m/s. Peňáz et al. (2002) and Pouilly and Souchon (1994) observed mean flow velocities of deep pool habitats in a range of 0 - 0.6 m/s. The results of the literature review are summarized in table 2.3.

Table 2.3: Flow velocity preference with reference to the barbel.

Flow velocity (specification of measurement if available)	Source
Observation with reference to barbel	
0 – 0.4 m/s (mean flow velocity)	Peňáz et al. (2002)
0.075 – 0.6 m/s	Pouilly and Souchon (1994)
< 0.30 m/s	Artensteckbrief [1]
< 0.3 m/s (mean flow velocity)	Landesstudie Gewässerökologie Becker and Ortlepp (2022)

[1] http://www.artensteckbrief.de/Print.aspx?ID_Art=32&ID_Bundesland=20012)

Water depth and surface area preferences of barbels in deep pool habitats

The water depth is known to be the second crucial parameter for habitat preference of barbels (Panchan et al., 2022). Preferred water depths are given in table 2.4 and visually in figure 2.8 for different literature resources. Panchan et al. (2022) is an exception in the list as they show data from a regulated river of first order, but the authors mention that it remains an open question whether this habitat preference would correspond equally to an unregulated river. The comparison of the different literature values shows that the mean water depth for deep pool habitats lays around 2 m. This value is also taken as a target value as the project area lays within southern Germany and the qualitative depth specification given in the directive Landesstudie Gewässerökologie (LSGÖ) (Becker & Ortlepp, 2022) are of high importance in this context.

Data on the area of deep pool habitats was only presented in the observations of Capone and Kushlan (1991) with an estimation of 12-4324 m². The Landesstudie Gewässerökologie gives the advice to plan deep pool habitats with an area of at least 15 m² to show a significant effect (Becker & Ortlepp, 2022).

Table 2.4: Overview of water depths of deep pool habitats with and without reference to the barbel.

Water Depth	Source
Observations without reference to barbel	
0.032 – 2.35 m	Capone and Kushlan (1991)
large pools: $\geq 20\,m^2$ area and $\geq 0.9\,m$ depth deep pools: $\geq 20\,m^2$ area and $\geq 1.8\,m$ depth	McIntosh et al. (2000)
Observations with reference to barbel	
>1 m	Blohm, Gaumert, and Kämmereit (1994)
2 – 6 m	Bănărescu and Bogutskaya (2003)
0.6 – 2.0 m Preference curve	Pouilly and Souchon (1994)
0.5 – 1.8 m	Peňáz et al. (2002)
4.2 m mean values with a range of 2.5 to 8 m in a large regulated river system	Panchan et al. (2022)
Statal directives	
>0.40 m	Artensteckbrief [1]
>2 m	Landesstudie Gewässerökologie (Becker & Ortlepp, 2022)

[1] http://www.artensteckbrief.de/Print.aspx?ID_Art=32&ID_Bundesland=20012
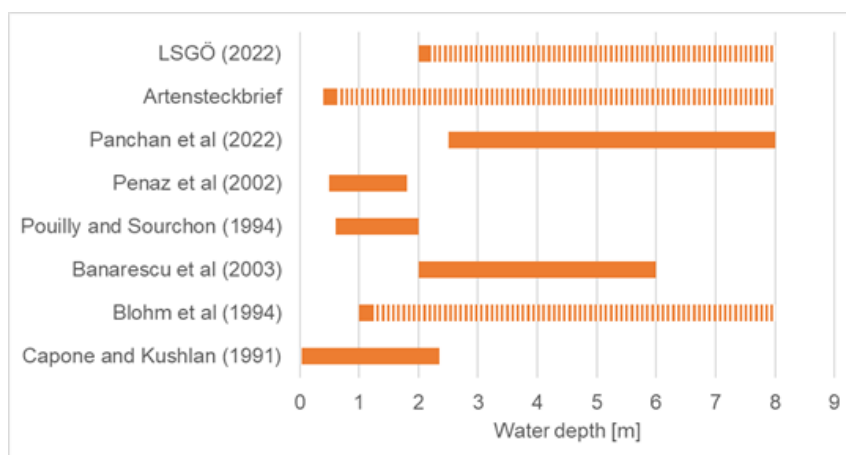
Figure 2.8: Water depths of deep pool habitats according to different literature resources. The dashed lines indicate that the water depth is provided as a value greater than.

2.3.2 Availability throughout the yearly cycle

The availability throughout the yearly cycle is essential for the biological functionality of the deep pool habitat. Availability refers to the mean flow velocities as well as the bed morphology indicating a possible redeposition process during low flow periods. The variances of riffle-pool-sequences has been studied by many researchers and several hypotheses have been discussed over the years. The two most common hypothesis are explained briefly. The velocity reverse hypothesis was introduced by Keller (1971). This hypothesis states that with changing discharge a velocity reverse takes place for the riffle and the pool sequence. For low flow conditions the bottom velocity is lower in the pool than in the riffle, for high flow the conditions

reverse to high bottom velocities in the pool and lower bottom velocities in the riffle. The hypothesis was later widened to a reversal in hydraulic conditions. Booker, Sear, and Payne (2001) summarizes various hydraulic parameters that were suggested for the reversal such as water surface slope (Keller, 1971), mean velocity, near-bed velocity and mean boundary shear stress. According to the flow convergence and sediment routing theory proposed by MacWilliams et al. (2006), the maintenance of riffle-pool-sequences is primarily influenced by the constriction of the upstream flow and the flow's routing through the system, rather than the presence of a mean flow velocity reversal. Both theories support the fact, that a maintenance of riffle-pool-sequences can be achieved by naturally varying discharges throughout the year. Therefore, it is hypothesized that the planned deep pool habitats can keep themselves free of sediments with the condition of varying discharges throughout the year. Floods are to be evaluated as an essential part of the maintenance of deep pool habitat. If there are years with only low floods a maintenance may be needed. The hypothesis needs to be verified in field experiments. Besides the maintenance effect, floods have the ambivalence to reduce local fish population on a seasonal or annual time frame. Even though they are crucial for the creation and maintenance of deep pool that are needed during summer droughts and freezing in winter (Labbe & Fausch, 2000).

2.3.3   Combination with shelter (flow shelter, visual shelter)

Deep pool habitats play a crucial role during drought seasons due to their large water depth, surface area and volume. The reduction in available habitats during drought periods due to lower water depth can result in a concentration effect, leading to an increased fish density (Magoulick & Kobza, 2003). It may arise the concern that the creation of relatively few fixed deep pool habitats with high fish density would make it easy for terrestrial predators to learn where they can find fish. Thus, the deep pool habitat could increase the risk of terrestrial predation.

To account for this problem the deep pool habitat can be coupled with appropriate structures such as rootwads or deadwood to provide visual cover to protect fish from predatory birds like cormorants (Magoulick & Kobza, 2003). A study from Greece shows that deadwood inside of deep pools can increase species diversity (in this case, chub and spirlin), but depth and the connectivity of the deep pool to other habitat types seem to be more important (Kalogianni et al., 2020). A study in Portugal concluded that shaded deep pools host the most species, but as well species abundance depends on various other factors (location, substrate, etc.) (Vardakas et al., 2017). When considering the entire fish community of a river, the specific characteristics of the deep pool habitats (presence or absence of deadwood, substrate size, etc.) seem to be of relatively minor importance, as long as they are present and accessible (Matthews, Harvey, & Power, 1994).

2.4 The research gap – local scours as deep pool habitats

Human interaction in river systems through rectification, channelization and optimization for flood protection lead to a significant loss in habitat diversity (flow and water depth variability). Deep pool habitats have been identified to play a key role in habitat restoration. This work aims to design in-stream structures that create a deep pool habitat for barbels. The novelty in this approach lays in defining the ecological requirements for the deep pool habitat prior to the design of the in-stream structure. Formerly, in-stream structures were investigated and possible habitat uses were defined afterwards. The used approach requests a definition of the hydro-morphological boundary conditions of a deep pool habitat. To the authors knowledge there is no universal description of a deep pool habitat available. Therefore, two different approaches for the definition of the deep pool habitat were considered. The first approach investigates natural riffle-pool sequences and forced pools in the field and derives hydromorphological boundary conditions from there. The second approach looks at the habitat preferences of the indicator species barbel. From the combination of both approaches a selection of suitable parameters is derived. The literature review on the indicator species barbel revealed that even though the barbel is one of the most studied species, the habitat preferences of the barbel remain mostly unclear. Literature values from Germany, France, Belgium and Czech Republic seem to represent a deep pool habitat for a barbel in a sufficient accuracy for hydromorphological engineering design. For the evaluation of habitat suitability water depth and velocity are equally important. A water depth of around 2 m and mean flow velocities <0.3 m/s preferably and between 0.3 and 0.6 m/s tolerable were identified as suitable hydromorphological boundary conditions of a deep pool habitat.

The analysis of natural riffle-pool-sequences and forced pools showed that the flow inside the pool is highly three-dimensional and dominated by turbulence. Therefore, it is questionable whether the mean flow velocity, that was identified as significant parameter for habitat preference for the barbel, is a suitable hydrodynamic parameter to evaluate the conditions inside a deep pool. Turbulence statistics, such as the analysis of root-mean-square velocities, vorticity, Reynolds shear stresses, TKE and Q-criterion can give an insight into the turbulent characteristics of the flow. On the other hand, when using turbulence statistics for the biological evaluation of the habitat, one needs to be careful to not raise the impression of an accuracy that is not based on biological knowledge.

In an expert assessment with the Fischereiforschungsstelle Baden-Württemberg the following variables for the hydromorphological evaluation of the barbel habitat were selected:

- scour depth [m]

- area in target depth [m²]

- volume below target depth [m³]

- Mean flow velocity with velocity vector field [m/s]

- Velocity fluctuations [m/s]

- strength of the whirl (for this parameter a parametrization needs to be found within this work)

Nevertheless, it needs to be kept in mind, that a single in-stream structure has a limited biological impact. The habitat diversity is dependent on many more factors, as mentioned above. Even though, the deep pool habitat is one step to a more diverse river. In conclusion, this dissertation can provide the first step to a functioning habitat by creating the hydromorphological boundary conditions for a deep pool habitat. In a further step the derived structures have to be implemented and after an initial time need to be evaluated whether (I) the conditions measured in this research project can be validated in natural surroundings and (II) the conditions are accepted by fish, in this case barbel, and are really inhabited throughout the yearly cycle. In case condition (I) fails the in-stream structures need to be adapted. In case condition (II) fails the biological boundary conditions need the be reevaluated.

Chapter 3

Local scour around in-stream structures - A state of the art review

Parts of this chapter were already published previous to this dissertation. The respective subchapters are indicated.

3.1 Definition of a local scouring

Scouring is a hydromorphological process where sediment is removed around an obstacle, such as the erosion of soil around a bridge pier due to steady flow of a river or due to tidal forces. Scouring occurs due to a change of the sediment transport capacity in a limited area, which is mainly provoked by

- Higher flow velocities,

- Three-dimensional turbulence,

- Secondary currents

and combinations of the latter (Zanke, 1982).

There are several ways how to classify scouring. The most convenient ways are presented as follows. The general scour is defined by hydromorphological changes in the river due to changes in flow characteristics and considers rather long-term changes in the river bed elevation such as scours due to constrictions, scours in bends and scours at confluences. Local scouring occurs in the vicinity of hydraulic structures like bridge piers, spur dikes and abutments and due to jets at high and low head structures.

According to their conditions of transport scours can be divided in clear-water scours and live-bed scours. In clear-water scour conditions there is no general sediment transport and only local scouring in the vicinity of the hydraulic structure is present. Live-bed scour conditions are characterized by constant sediment supply from upstream.

3.2   Selection and conceptualization of measures for local scours as deep pool habitats

In a comprehensive literature study, approximately 400 resources were explored, ranging from classical scour depth predictions around bridge piers (e.g. Melville (2008)) to practical experiences documented in river restoration handbooks by statal authorities (e.g. Seehorn (1992)). The study yielded a list of 35 potential measures that could be suitable to create a deep pool habitat. This list does not claim to be complete, but offers a broad overview of hydromorphological situations where local scour was observed. The scours were formed due to natural morphological situations (e.g. confluences, vegetation), hydraulic engineering structures (e.g. dams, gates, bridge piers) and intentionally planned within river restoration projects. The structures were categorized into different groups, including classical bodies, in-stream structures, vegetation, riffle-pool-sequences, jets, technical hydraulic structures and river course as depicted in figure 3.1. For the specific research question, emphasis was placed on the group of in-stream structures due to the limitations posed by restricted urbanized areas.

3.2.1   Flow types in the context of local scouring

For the analysis of governing parameters and influences on scour depths, three groups of flow types are defined according to their interference with the open channel flow. The classification is dependent on the relation of the flow depth h_0 to height of the structure h_s and to the relation width of the channel w to width of the structure w_s:

- **pier-like structures** are emergent ($h_s > h_0$) and are flown around laterally on both sides ($w_s < w$),

- **stone-like structures** are submerged ($h_s < h_0$) and are flown around laterally on both sides and are overflown ($w_s < w$) and

- **dam-like structures** are submerged ($h_s < h_0$) and cover the whole river width ($w_s = w$) and are only overflown.

The concept of the three flow types is displayed in figure 3.2.
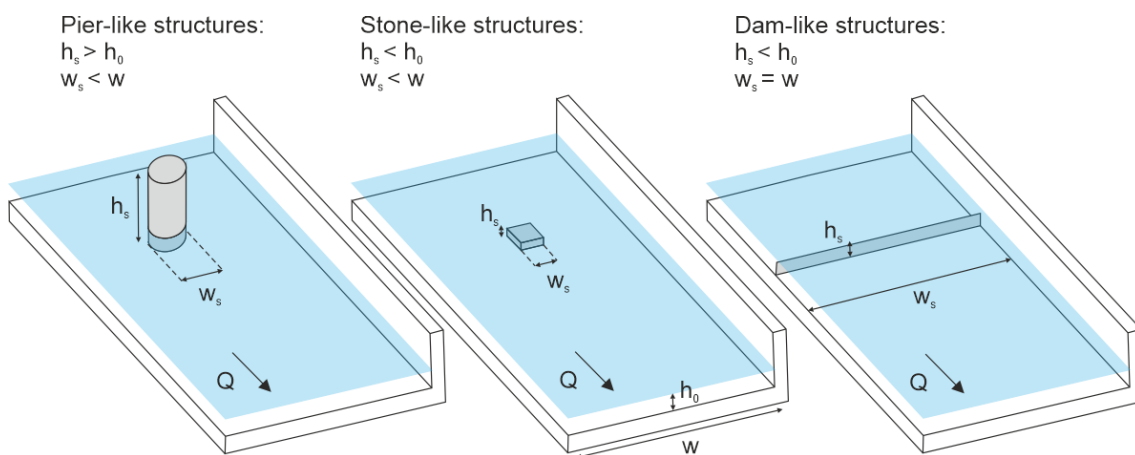
Figure 3.2: Definition of flow types for different in-stream structures.
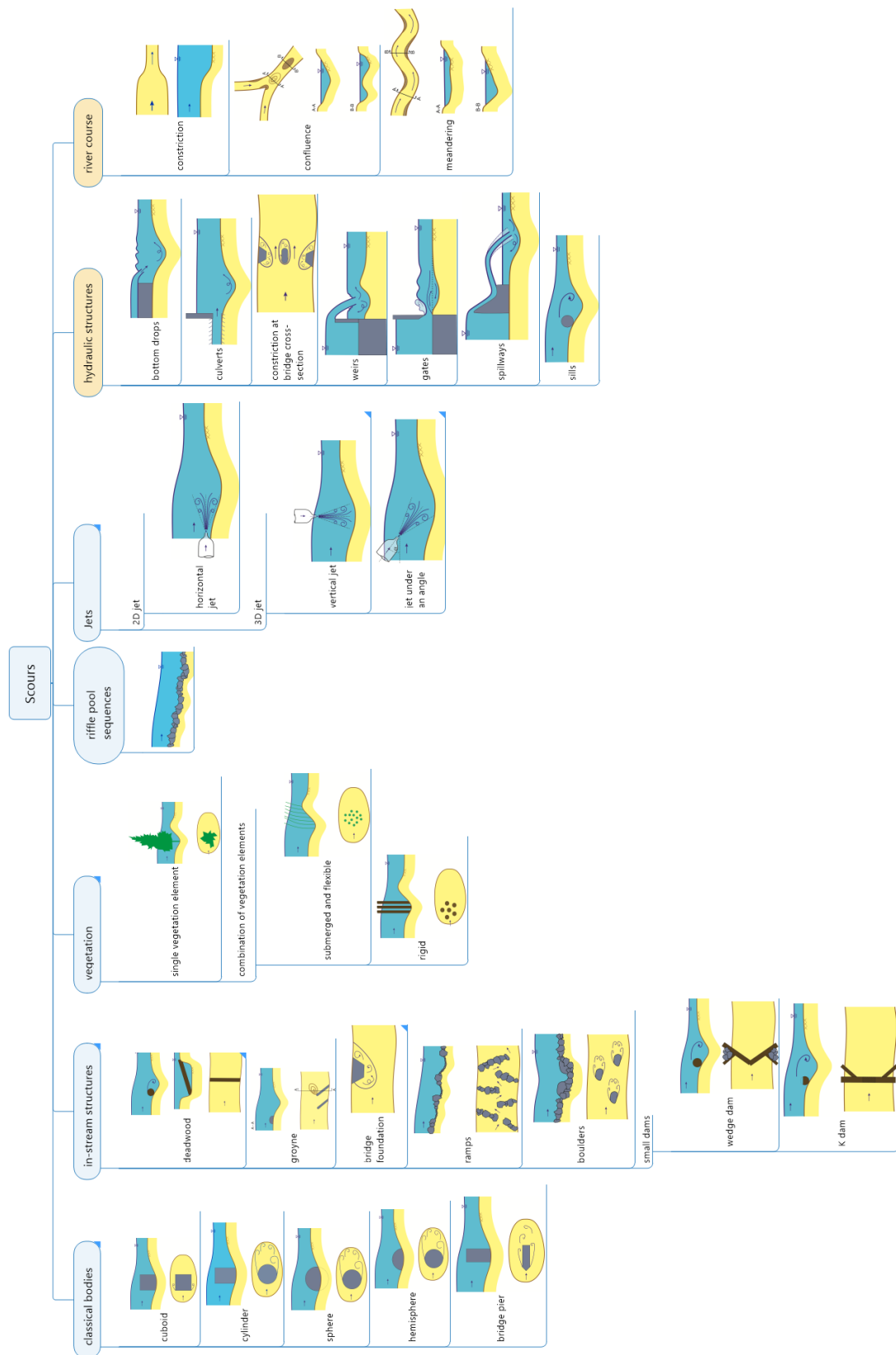
Figure 3.1: Overview of different scour mechanisms.

3.2.2   Conceptualization of the measures

Six structures were selected from the 35 identified measures, representing different flow types such as pier-, stone-, and dam-like structures as previously defined in chapter 3.2.1. Each flow type should contain at least one structure. Figure 3.3 shows an overview of the selected structures and their respective geometrical specifications. The criteria for the selection of these structures is given subsequently:

- Pier-like structures:

  - Circular Pier (CP): The CP is the most complete studied in-stream structure among literature and was selected as a benchmark to compare with other studies. The structure is emergent and has a width of 0.2 w.

  - Rectangular Pier (RP): The RP is examined to understand the influence of sharp edges at the pier while maintaining the same blockage ratio as for the CP. The structure is emergent and has a width of 0.2 w.

  - Triangular Pier (TP): The TP was a new invention within this dissertation and was inspired by previous works in the institute, where triangular piers were investigated as coastal protection measure in ocean engineering. The structure is emergent and has a width of 0.2 w.

- Stone-like structures:

  - Double Wing Deflector (DWD): The Double Wing Deflector was inspired by the measures presented in the stream management handbook of Seehorn (Seehorn, 1992). Two single wings, positioned on opposing streambanks, are designed to constrict the flow to 80 % and thereby create a midchannel pool through scouring. The height of the structure is selected to the waterlevel reached at MQ. The anticipated outcome includes the formation of a scour pool, with a scour depth of 0.6 to 0.9 m in gravel and small rubble bed rivers with low-gradient bottom slopes.

  - Deflected groyne (DG): The DG was inspired by the work of Bundesanstalt für Wasserbau (BAW), where alternatives for classical middle water groynes for navigation were tested (Anlauf & Hentschel, 2007; Hentschel, Henning, & Hüsener, 2012). In particular, the impact on ecological quality was evaluated and showed good results for the DG. The DG spans 1/3 w and is installed at the water level of MQ as well.

- Dam-like structures:

  - Kdam (Kdam): The Kdam was also inspired by the measures presented in the stream management handbook of Seehorn (Seehorn, 1992). The structure is supposed to create pools or deeper sections through scouring. It is mentioned that they are best suitable for rivers with a width < 4.5 m. This limits the applicability but enables the comparison as a dam-like structure. The Kdam spans the whole width w and is installed at a height of MQ. The notch in the center of the log is installed at a height of MNQ.
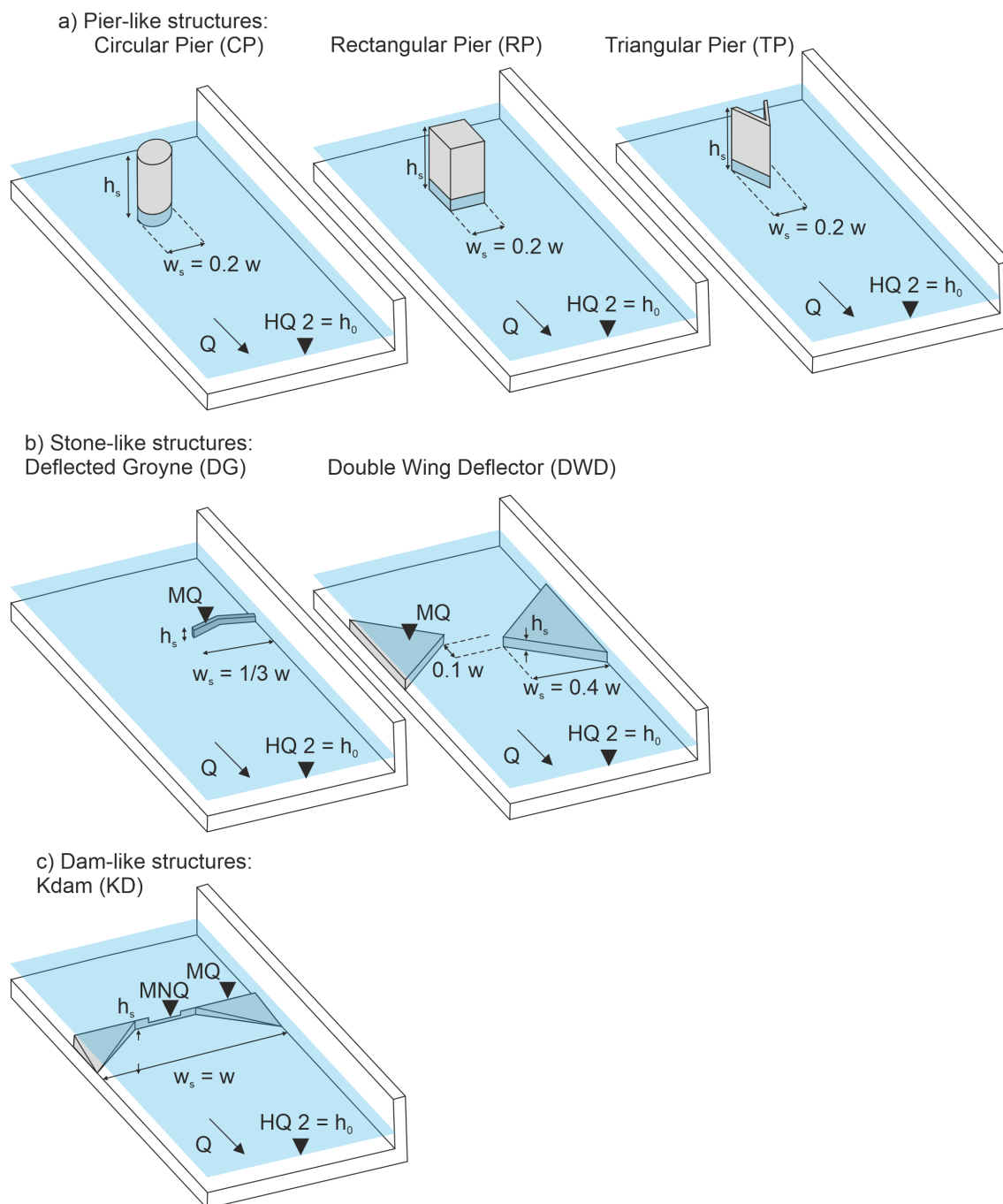
Figure 3.3: Overview of different in-stream structures and corresponding flow types. a) Pier-like structures: Circular Pier (CP), Rectangular Pier (RP) and Triangular Pier (TP), b) Stone-like structures: Deflected Groyne (DG), Double Wing Deflector (DWD) and c) Dam-like structures: Kdam (Kdam).

3.3 Flow field and scour process around different in-stream structures

The flow field and scour mechanisms around the beforementioned in-stream structures is different for each flow type. The subsequent chapters are therefore divided according to this classification. A few geometric dimensions of the scour hole are necessary to follow the

chapter, which are defined in figure 3.4.
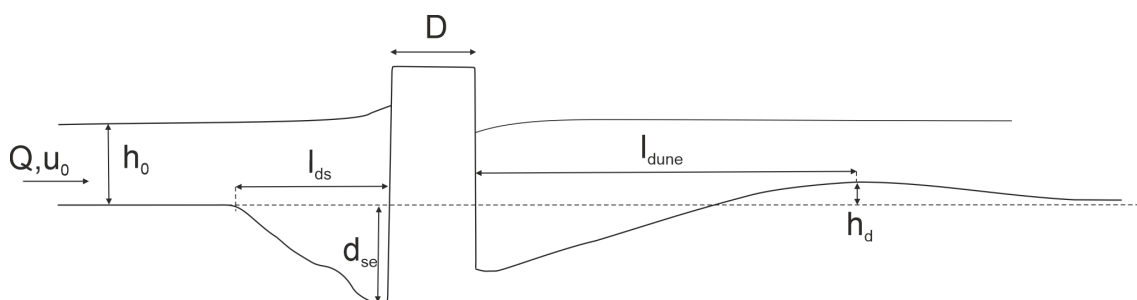
Figure 3.4: Definition of hydraulic conditions: discharge Q, approach flow velocity U_o, approach flow depth h_0 for uniform flow. Geometric dimensions of the scour hole: maximum end scour depth d_{se}, length of the upstream scour hole l_{ds}, height of the dune h_d and distance of the dune l_{dune}

3.3.1   Flow field and scour process around pier-like structures

The flow pattern around a cylindrical pier is well known (see e.g. Breusers and Raudkivi (1991)). Four different flow phenomena can be observed in figure 3.5. At the upstream side of the pier the approach flow velocity goes to zero and the stagnation pressure increases. As a result, a backwater rise in the vicinity of the circular pier can be observed and a backwards rotating surface roller forms at the water surface. As a consequence of the pressure gradient upstream of the circular pier a strong downflow in front of the circular pier is induced. The velocities in the downflow can reach a maximum of 0.6-0.8 U_0 (Raudkivi, 1986; Dey & Raikar, 2007). The downflow acts like a vertical jet and erodes sediment upstream of the circular pier (Akhlaghi et al., 2020). This is the starting point of the horseshoe vortex that separates here and is characterized by a spiral movement that evolves at both sides of the circular pier. It is the main driver of scouring as this spiral movement is able to transport high capacities of sediment. Downstream of the circular pier the horseshoe vortex becomes part of the general wake vortices. Nevertheless, the horseshoe vortex system forms as a result of the scour hole and is not the cause of the scour hole. The wake vortices form due to a separation of the flow on both sides of the circular pier and form backwards rotating whirls and a dead water zone until they get part of the general turbulence. The flow separation occurs alternating on both sides and is not stable, therefore the wake vortices are not essential for scour formation (Breusers, Nicollet, & Shen, 1977; Akhlaghi et al., 2020).
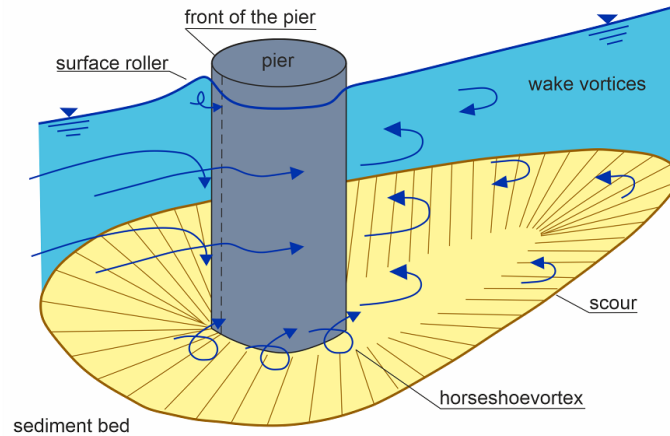
Figure 3.5: Flow field around a circular pier with surface roller, downflow, horseshoe vortex, wake vortices and the scour hole. Adapted from Breusers and Raudkivi (1991).

Due to this vortex system a complex bed morphology is formed. The scour pattern around pier-like structures such as circular and rectangular piers were investigated in numerous works (Dey & Raikar, 2007; Khosronejad, Kang, & Sotiropoulos, 2012). The circular (CP) develops the point with the maximum scour depth d_{se} directly upstream of the structure and the scour hole spreads radially with decreasing depth as shown in figure 3.6. The maximum relative scour depth d_{se}/D is -1.3 for Dey and Raikar (2007) and -0.36 for Khosronejad, Kang, and Sotiropoulos (2012). The eroded sediment deposits in a dune downstream of the pier that lays in a distance of l_{dune} = 6.7 (Dey & Raikar, 2007) or is transported further downstream. Changing the shape of the pier from a circular to a rectangular pier shows similar scour pattern as for the circular pier, with the deepest point of the scour upstream of the pier and a radially spread scour hole and a dune downstream of the pier. Faster time development and the deeper scour hole, are due to greater flow, turbulence and shear stresses around the rectangular pier in comparison with the circular pier (Dey & Raikar, 2007).
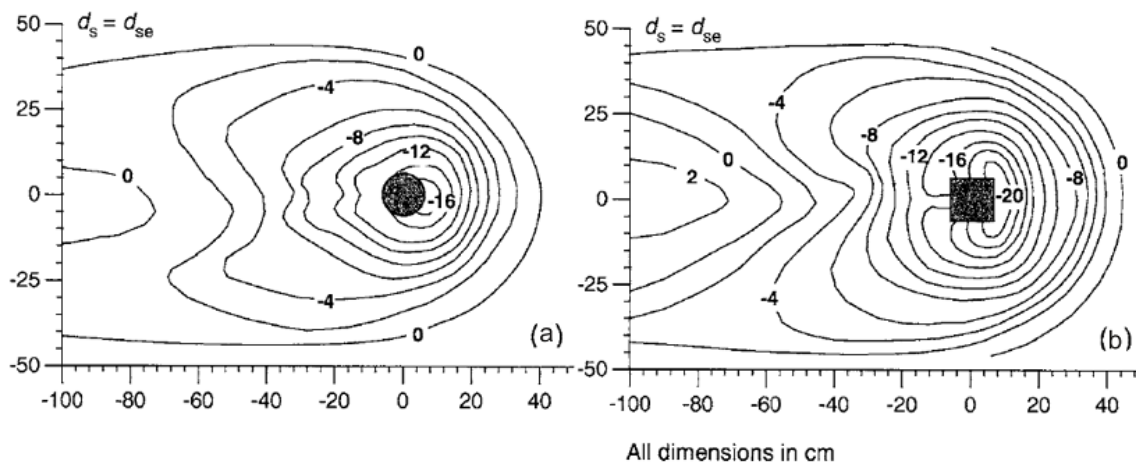
Figure 3.6: Scour depth around a circular (left) and a rectangular (right) pier. Adapted from Dey and Raikar (2007).

A diamond shaped pier creates the deepest scour hole in comparison with a circular and rectangular pier (Khosronejad, Kang, & Sotiropoulos, 2012). The authors attributed this to the different physical phenomena taking place around the different shapes of piers. The scouring process around the circular and the rectangular pier are dominated by a turbulent horseshoe vortex system whereas the diamond shaped pier leads to a diversion of the flow and hence higher bed shear stresses. To the authors knowledge triangular piers, in the geometric form shown in figure 3.3, have not been investigated systematically yet. Addy and Wilkinson (2016) investigated porous triangular engineered log jams in a field study. Pools and scours were expected upstream and on both sides of the log jams. After a flood event the predicted bed morphology could not be detected in the full extent which the authors traced back to the porous structure and the location within the cross-section of the river, which is later addressed in chapter 6.1.3. The relevant parameters of scour formation and scour depth can be divided into the groups of fluid properties, flow parameters, sediment parameters and structural parameters, which are explained in chapter 3.4 (Raudkivi, 1986; Melville, 2008; Akhlaghi et al., 2020).

3.3.2 Flow field and scour process around stone-like structures

In comparison with pier-like structures, stone-like structures are submerged and have an additional overflow component. The group of stone-like structures can be divided into two subgroups: (I) submerged boulders or cobbles that are symmetrical to the centerline of the channel and are investigated in a simplified version as submerged circular piers (Dey, Raikar, & Roy, 2008), hemispheres (Shamloo, 1997) or arbitrary shape (Shamloo, 1997; Fisher & Klingeman, 1984) and (II) groynes, which are non-symmetrical to the centerline of the channel and are laterally installed. The dominating parameter on the scouring process are the same as for pier-like structures with additional parameters for (I) bluff bodies (boulders) such as obstacle Reynolds number, blockage ratio including obstacle height and width as well as projected frontal area (Euler et al., 2017; Euler & Herget, 2012), the volume of the boulder (Fisher & Klingeman, 1984) and the width of the structure (hemisphere (Shamloo, 1997) and cube (Huang, 1991)) and (II) groynes such as relative submergence, shape of the structure, angle of attack, length of the groyne, tailwater depth and position in the river cross section (Armanini et al., 2010; Breusers & Raudkivi, 1991; Ishigaki & Baba, 2004; Möws & Koll, 2014; Pagliara & Kurdistani, 2013; Pagliara, Hassanabadi, & Kurdistani, 2015). The subgroups are characterized by different flow and scour processes, that are explained as follows.

Bluff bodies (hemispheres, cubes and natural rocks) show four different flow regimes as shown in figure 3.7 (Shamloo, 1997). In regime 1 ($h_0/h_s > 4$) the effect of the structure cannot be detected in the upper layer of the wake of the structure. Regime 2 ($h_0/h_s = 1.3$ -4) is characterized by a recirculation zone, a free shear layer and first surface waves. Regime 3 ($h_0/h_s = 1.1$-1.3) shows a mixing through the whole depth of the flow and a recirculation zone downstream of the structure as well as the appearance of surface waves in the wake. The first three regimes are surface flow regimes where a jet stays at the surface even downstream of the obstacle. Regime 4 ($h_0/h_s < 1$) is characterized by a Kármán vortex street and a strong

recirculation zone downstream of the structure. In contrast to the previous regimes it is an impinging jet regime.
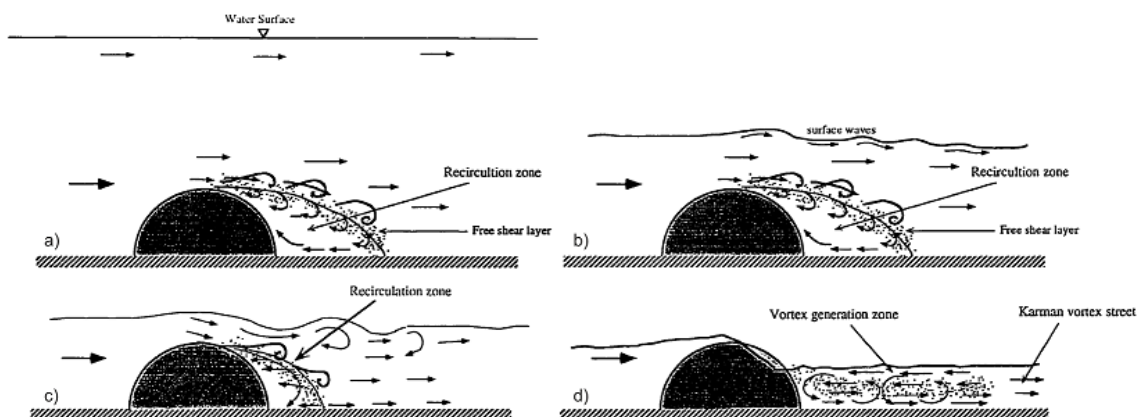
Figure 3.7: Flow regime around a submerged hemisphere: a) regime 1 ($h_0/h_s > 4$), b) regime 2 ($h_0/h_s = 1.3 - 4$), c) regime 3 ($h_0/h_s = 1.1 - 1.3$), d) regime 4 ($h_0/h_s < 1$). Adapted from Shamloo (1997).

In comparison with the emergent pier where a significant downward velocity component is upstream of the pier, the submergence of a circular pier leads to a flow deviation above the pier and separates at the top as shown in figure 3.8 (Dey, Raikar, & Roy, 2008). The submerged pier shows a similar horseshoe vortex upstream of the pier as the emergent one and has a less coherent and smaller secondary horseshoe vortex upstream of it (Euler & Herget, 2012; Kirkil, Constantinescu, & Ettema, 2008). Downstream of the obstacle an arch vortex, hairpin vortices and trailing vortices develop. Further research showed that the same flow patterns can not only be observed for submerged circular piers but also for cobbles (Euler et al., 2017).

The primary horseshoe vortex is still the main driver of the erosion process at a submerged structure (Euler & Herget, 2012; Euler et al., 2017). The deepest point of the scour is reached upstream of the structure and spreads radially, comparable to the emergent piers. The inner and outer scour hole can be observed in gradually changing slopes upstream of the obstacle from less steep to a steeper slope (Dey, Raikar, & Roy, 2008; Euler & Herget, 2012; Euler et al., 2017). Downstream of the obstacle a symmetrical dune is created (Burkow & Griebel, 2016). With increasing submergence the dimension and strength of the horseshoe vortex decreases and results in a decrease in scour depth (Dey, Raikar, & Roy, 2008).
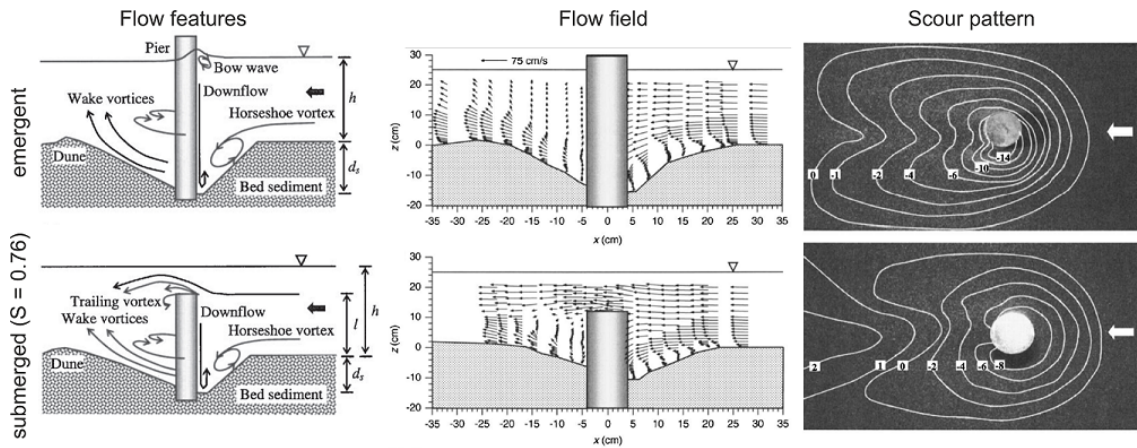
Figure 3.8: Comparison of flow features, flow field and scour pattern of an emergent and submerged circular pier. Adapted from Dey, Raikar, and Roy (2008).

The second subgroup, the groynes, are investigated widely for water level management in navigation channels, but it has been detected that they also cause scouring especially at the head of the groyne, which has shown ecological benefits (Anlauf & Hentschel, 2007; Hentschel, Henning, & Hüsener, 2012). Emergent groynes show a mostly two-dimensional flow field with different size and orientation of recirculation pattern depending on width to length ratio of the groyne field (Sukhodolov, Uijttewaal, & Engelhardt, 2002; Weitbrecht, 2004) and the inclination of the groyne (Weitbrecht, 2004) as shown in figure 3.9.
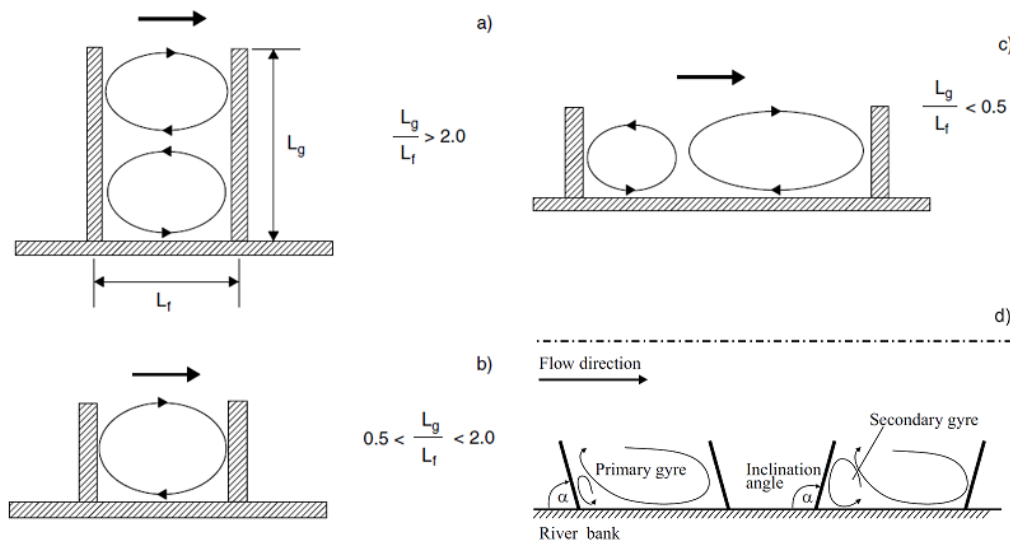
Figure 3.9: Flow features around an emergent groyne in dependence on a), b), c) length of the groyne L_g to distance of the groynes L_f ratio (Sukhodolov, Uijttewaal, & Engelhardt, 2002) and d) inclination angle (Weitbrecht, 2004).

As the groyne is submerged, the additional flow component of the overflow leads to a three-dimensional flow field inside of the groyne field as depicted in figure 3.10 (McCoy, Constantinescu, & Weber, 2007; Ambagts, 2019). The surface flow velocities in Hentschel, Henning, and Hüsener (2012) show that this behavior not only accounts for straight groynes (90° to the main flow direction) but also for kink groynes (later called deflected groyne in this work).
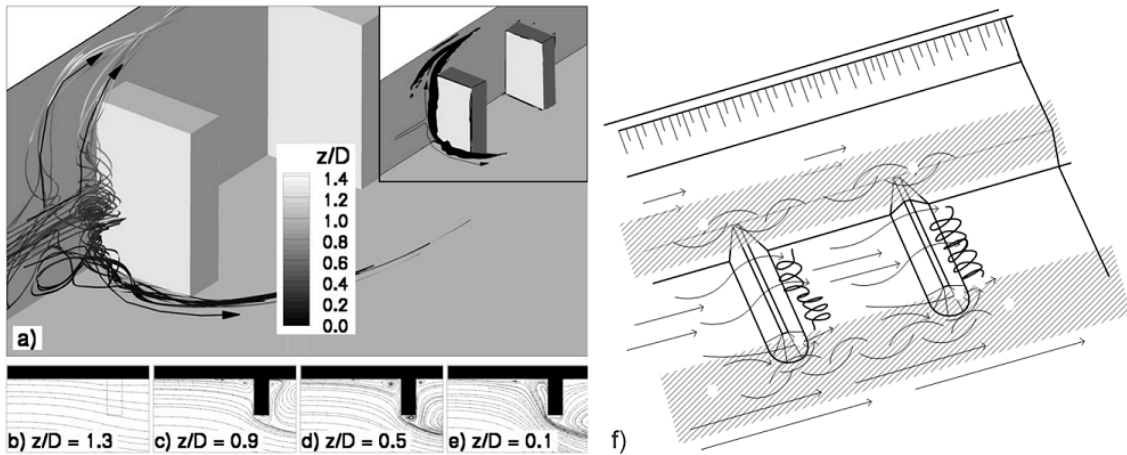
Figure 3.10: a) 3D mean velocity streamlines and Q-criterion to visualize the vortex system around a submerged groyne, as well as b) to e) 2D streamlines at different depth of the groyne (McCoy, Constantinescu, & Weber, 2007) f) Flow features around a submerged groyne according to Ambagts (2019).

A scour develops around the head of the groyne and the eroded sediment deposits in a dune downstream of the groyne as shown in figure 3.11. The maximum scour depth increases with decreasing submergence ratio reaching a maximum for the emergent case (Ishigaki & Baba, 2004) and with increasing inclination angle (Harada et al., 2013).
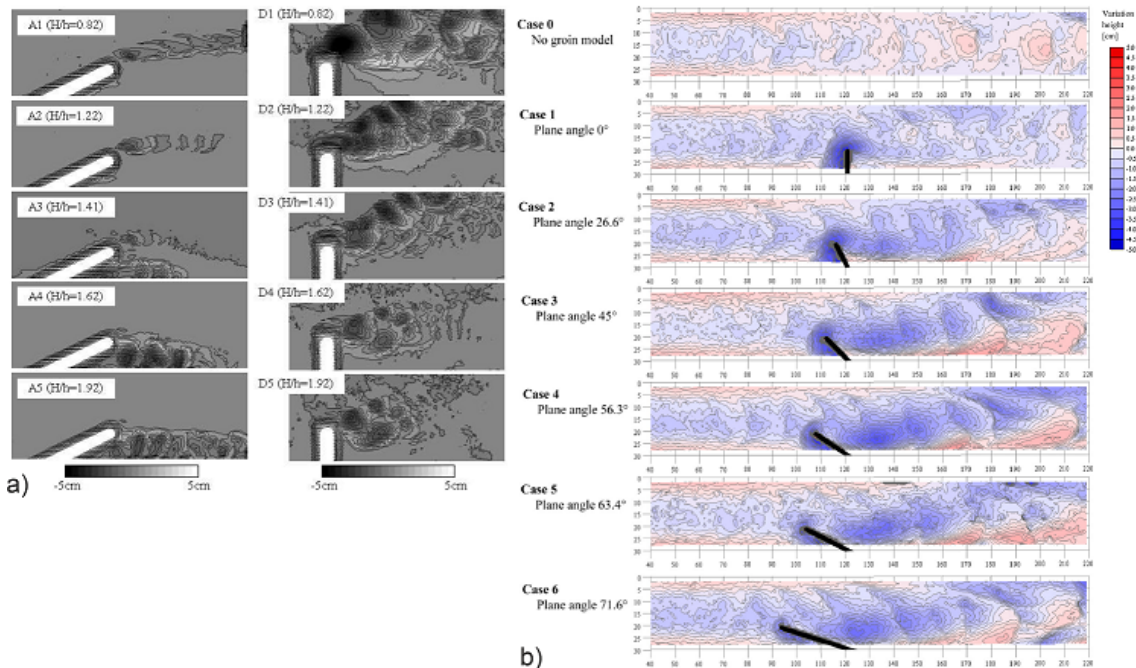
Figure 3.11: a) Scour process around emergent and submerged groynes for different inclination angles (Ishigaki & Baba, 2004) and b) Scour process around submerged groynes for different inclination angles (Harada et al., 2013).

37

3.3.3 Flow field and scour process around dam-like structures

The flow field of a dam-like structure was described in detail by Guan, Melville, and Friedrich (2014) and Wu and Rajaratnam (1996) who performed laboratory experiments with sharp crested fully submerged sills in a rectangular flume as shown in figure 3.12. According to their findings the flow regimes can be classified as: (1) surface jet, (2) surface wave, (3) breaking wave (or surface jump) and (4) impinging jet (Wu & Rajaratnam, 1996). Regime 1 – 3 can be summarized as surface-flow regimes as the flow remains as a jet at the surface. The fourth regime is an impinging jet regime. The flow regimes are dependent on the water level differences upstream and downstream of the sill and the approach flow rate (Wu & Rajaratnam, 1996). Figure 3.13 shows that the approach flow accelerates at the crest of the weir and a dead water zone forms immediately downstream of the sill (Guan, Melville, & Friedrich, 2014). Moreover, secondary currents lead to rotating cells at the sides of the channel downstream of the sill. In upward motion areas ridges build and in downward motion areas erosion occurs as shown in figure 3.13 (Meftah & Mossa, 2004; Guan, Melville, & Friedrich, 2014).
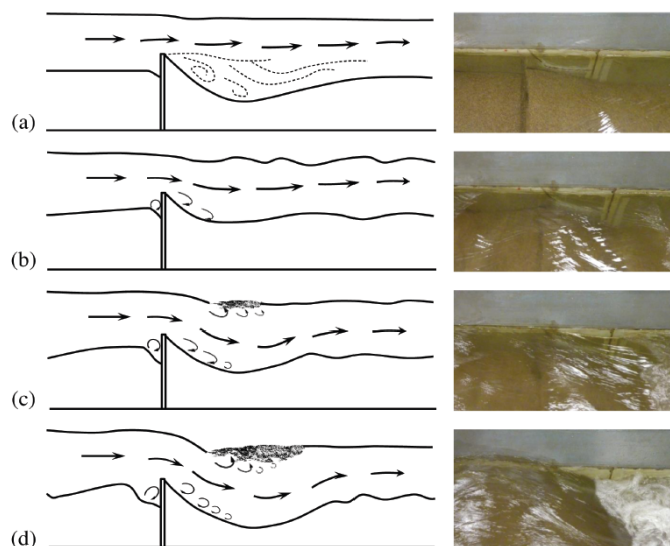
Figure 3.12: Flow regimes at a weir with movable bed: a) surface jet, b) surface wave, c) transition stage d) impinging jet. Adapted from Guan, Melville, and Friedrich (2015).

The resulting scour pattern shows a small scour hole upstream and a large scour hole downstream of the dam. The scour depth gradually increases until a maximum scour depth is reached at 2.5 w downstream of the dam (Guan, Melville, & Friedrich, 2014). A U-shaped dam leads to a flow concentration in the middle of the flume where the deepest point of the scour develops (Scurlock, Thornton, & Abt, 2012; Kurdistani, 2013). Dams installed in channels with trapezoidal cross section lead to increased side scours and a central ridge (Mueller & Kobus, 1981). Additional governing parameters of the scour process to the one from the pier-like structures are Δh (difference between upstream h_1 and downstream h_2 water level), the tailwater depth h_2 for flow parameters and the overflow height $h_{\ddot{u}}$, the height of the structure h_s and the length of structure for U-shaped dam for geometrical parameters (Meftah & Mossa, 2004; Pagliara & Kurdistani, 2013; Wang et al., 2019).
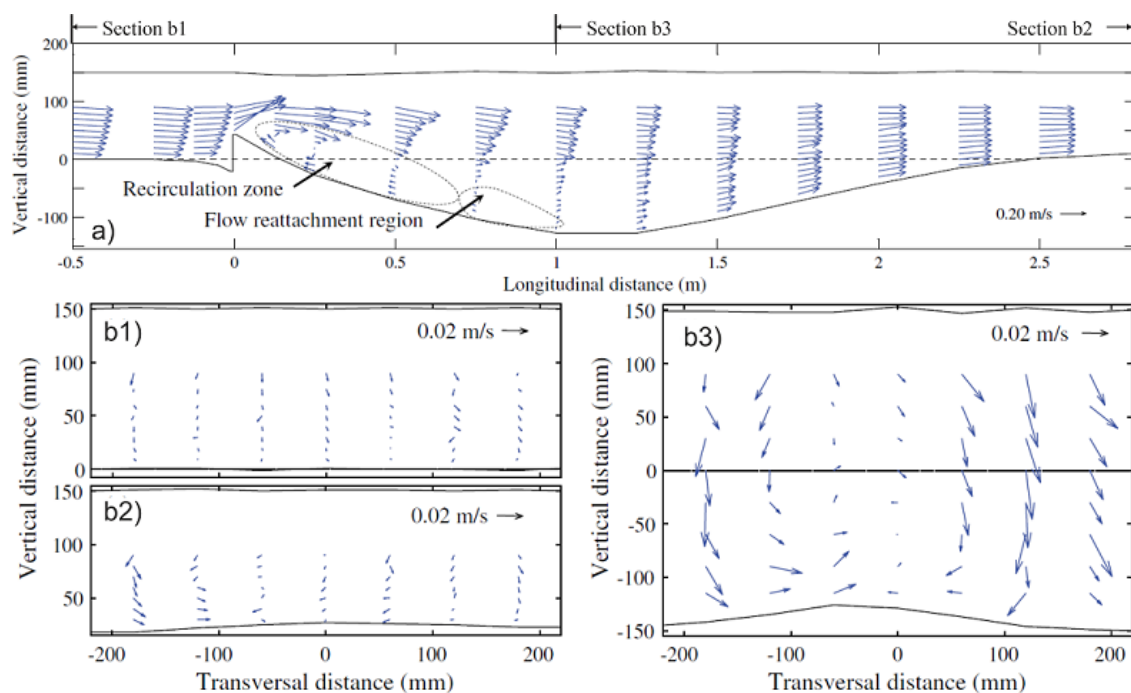
Figure 3.13: Flow features around a dam-like structure in a) sideview and b) cross-sectional view. Adapted from Guan, Melville, and Friedrich (2014).

The general flow features and scour patterns that evolve due to the three different flow types were explained up to this point. As local scouring is the result of the interaction of the water flow with the river bed sediment, it is important to know the main parameters influencing maximum scour depth, which are explained in the following chapter.

3.4 Influencing parameters on maximum scour depth

According to Breusers and Raudkivi (1991) and Melville (2008), the most influencing parameters on scour depth can be categorized into the following groups. The categories are also displayed in figure 3.14.

- Fluid parameters: density of the fluid ρ, kinematic viscosity of the fluid ν

- Flow parameters: approach flow depth h_o, approach flow velocity U_o, gravitation g

- Sediment parameters: mean grain diameter d_{50}, uniformity of the sediment σ_g, density of the sediment ρ_s, critical flow velocity U_c

- Structural parameters: shape, width, submergence, etc.

Fluid density, kinematic viscosity, gravitation and density of sediment are considered constant in this case and are therefore not further mentioned.
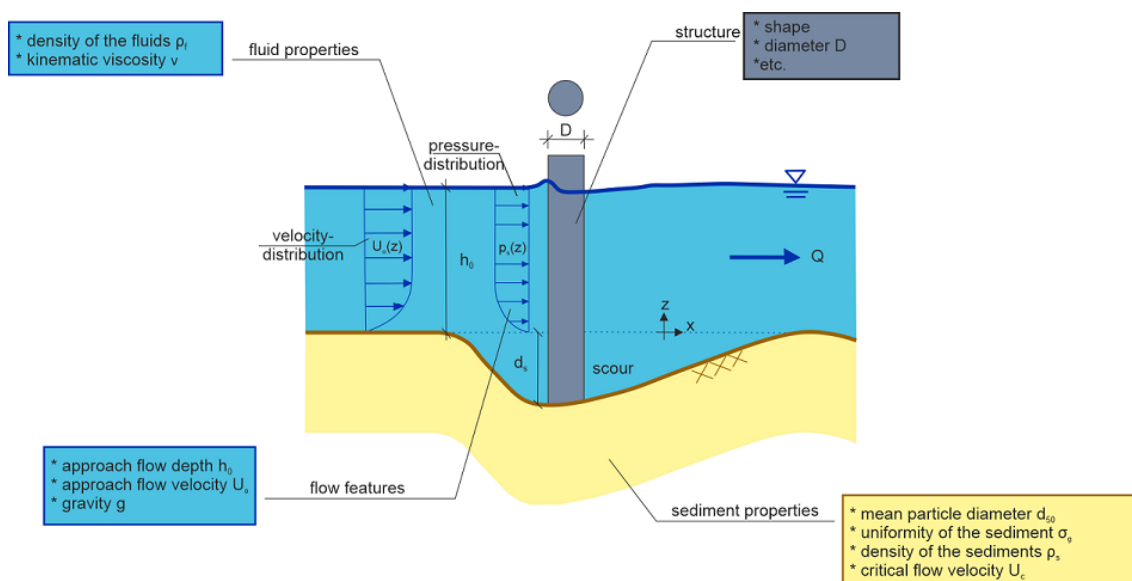
Figure 3.14: Parameters influencing scour depth according to Breusers and Raudkivi (1991) and Melville (2008).

Comprehensive works that sum up the research of the last 100 years identified the following non-dimensional parameters as the most influencing regarding the maximum scour depth d_{se} of local scours around in-stream structures:

- Flow intensity U_0/U_c, which is the relation of the approach flow velocity U_0 and the critical velocity of the bed sediment U_c.

- Flow shallowness h_0/D, which is the relation of approach flow depth h_0 to the hydraulically significant length D, e.g. the width of a circular pier D.

- Relative grain size D/d_{50}, which is the relation of the hydraulically significant length D to the mean diameter of the sediment d_{50}.

- Sediment non-uniformity σ_g which equals d_{60}/d_{10}.

- Relative time t/t_e, which indicates the scour process to be a time dependent process where t is the time and t_e is the time where equilibrium conditions are reached.

- The structural parameters that influence scour depth are diverse. An example would be the submergence h_s/h_0 of a submerged groyne. The details regarding the investigated structures within this work are explained in the following chapter.

The hydraulically significant length D is further explained in chapter 4.2.5. The maximum scour depth is named as d_s during the whole process of scouring and the maximum scour depth reached at equilibrium conditions is named as d_{se}.

3.4.1 Influence of flow intensity U_0/U_c

The relation of approach flow velocity U_0 to the critical flow velocity of the sediment U_c is named the flow intensity. With regard to scour processes this relation classifies whether clear water scour conditions ($U_0/U_c < 1$), threshold conditions (U_0/U_c =1) or live-bed scour conditions ($U_0/U_c > 1$) are present.

Pier-like structures

Under clear-water conditions relative scour depth d_s/D increases almost linearly with increasing U_0/U_c until it reaches a peak at the threshold velocity as shown in figure 3.15. After passing the threshold peak, live-bed conditions are reached and the local scour depth decreases firstly and then increases again until the live-bed peak (Melville, 2008; Akhlaghi et al., 2020; Breusers & Raudkivi, 1991). According to Raudkivi and Ettema (1983) it is feasible to assume clear-water conditions in most cases even though a flood event passes the structure. During a flood event a flood wave passes the structure and live-bed conditions are present. After the passage of the peak flow smaller flow rates that lie within clear-water conditions pass the structure. If the time span with clear-water scour conditions is long enough it is convenient to assume clear-water conditions in most cases. This aspect is further highlighted in chapter 7.4.3.
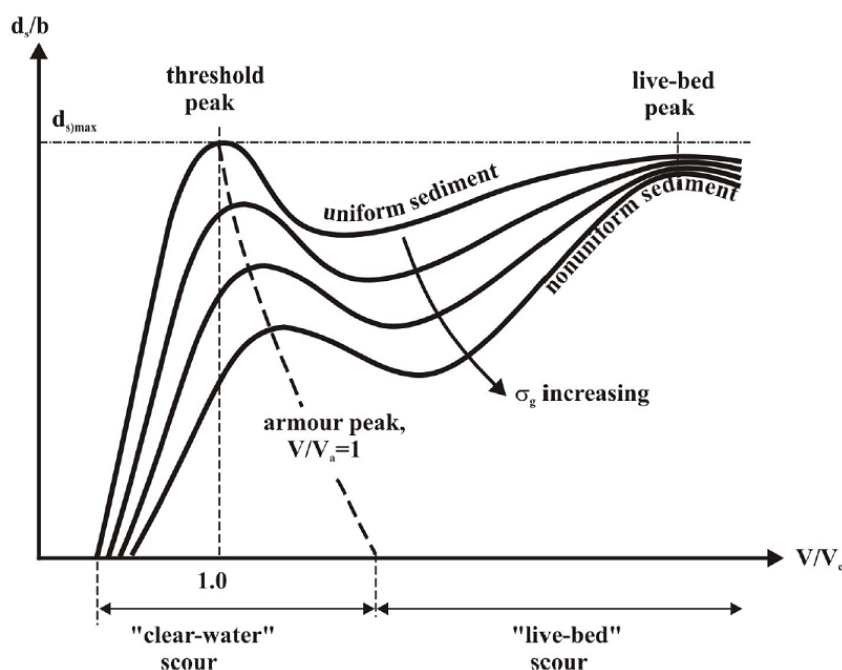
Figure 3.15: Influence of flow intensity on the relative scour depth on pier-like structures. b equals the pier width D and V/V_c equals U_0/U_c. Adapted from Melville (2008).

Stone-like Structures

To the authors knowledge the aspect of flow intensity has not been investigated separately for submerged structures yet. The author expects a similar behavior for submerged structures as for pier-like structures.

Dam-like structures

A similar trend for the influence of flow intensity on the scour development downstream of dam-like structures was observed in the studies of Guan, Melville, and Friedrich (2015), Guan, Melville, and Friedrich (2016), and Wang et al. (2019) as shown in figure 3.16. For U_0/U_c = 0.5 - 1 an increase in relative scour depth d_s/h_2 could be observed and a peak value is reached for U_0/U_c = 1. Until U_0/U_c = 1.5 - 2 a decrease can be observed. For higher U_0/U_c the relative scour depth increases again. Guan, Melville, and Friedrich (2015) state that it remains unclear whether a live-bed peak is reached at higher flow intensities as for pier-like structures. They hypothesize a shift of the possible live-bed peak to be due to the different scour mechanisms in pier-like and dam-like structures. It is to be noted that the scour depth is normalized with the tailwater depth h_2 instead of the pier diameter D in the pier-like structure cases.
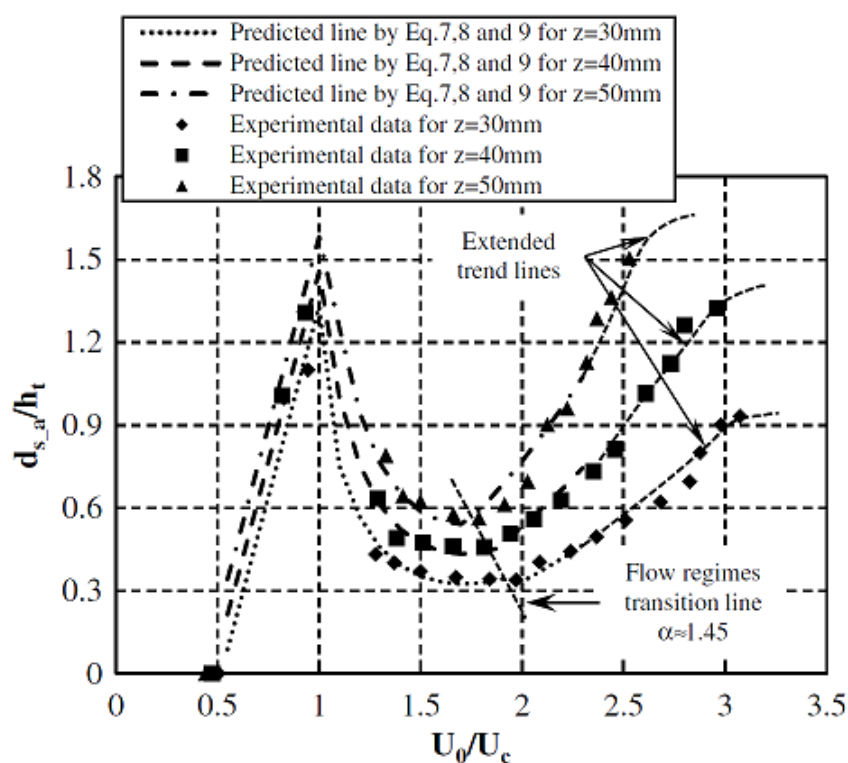
Figure 3.16: Influence of flow intensity on the relative scour depth on dam-like structures. h_t in this graph equals h_2 in this work. Adapted from Guan, Melville, and Friedrich (2015).

3.4.2 Influence of flow depth h_0/D

The relation of the approach flow depth h_0 and the pier diameter D characterizes whether the flow is characterized as so called deep flow ($h_0/D > 1.4$), intermediate flow ($0.2 < h_0/D \leq 1.4$) or shallow flow ($h_0/D \leq 0.2$) and is known to influence the local scour depth.

Pier-like structures

For deep flows ($h_0/D > 1.4$) the scour depth increases proportionally with the pier diameter D and is independent of flow depth as shown in figure 3.17 (Melville, 2008; Raudkivi & Ettema,

1983). Intermediate flow depths depend on both flow depth h_0 and pier diameter D. For shallow flows scour depth increases with flow depth h_0 and is independent of pier diameter D. For intermediate flow depths the horseshoe vortex is affected by the surface roller which rotates in opposite direction. As long as the two whirls do not interfere with each other local scour depth is independent from flow depth. In shallow flows the surface roller is becoming relatively more dominant and reduces the horseshoe vortex. This leads to a reduced scour depth. For further detail the reader is referred to the summaries of Melville (2008) and Raudkivi and Ettema (1983).
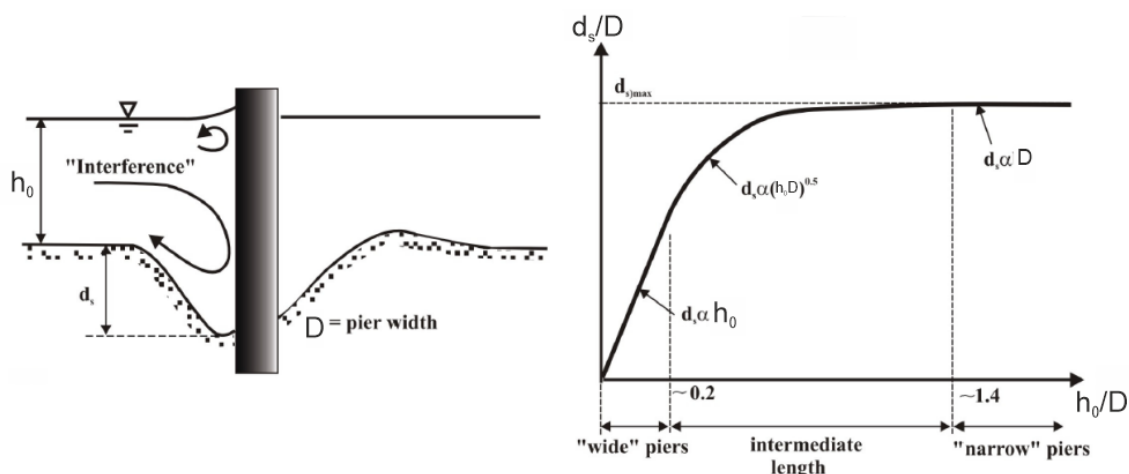
Figure 3.17: Influence of flow shallowness on the relative scour depth on pier-like structures. Adapted from Melville and Dongol (1992) and Melville (2008).

To the authors knowledge the influence of flow depth has not been investigated systematically for stone- and dam-like structures.

3.4.3   Influence of relative grain size D/d_{50}

The mean grain size diameter d_{50} has an influence on the scour depth in the vicinity of in-stream structures and is classified into fine and coarse sediment. The normalization is done via the hydraulically significant length D, which is explained in chapter 4.2.5.

Pier-like structures

In older literature such as Raudkivi and Ettema (1983) the influence of relative grain size is divided into 4 groups. For $D/d_{50} < 8$ the sediment is relatively large and scouring only happens at the flanks of the pier. For $30 > D/d_{50} \geq 8$ large parts of the energy of the downflow is dissipated in the coarse sediment at the bed of the scour hole. Intermediate sized sediment ($130 > D/d_{50} \geq 30$) is entrained from the ground of the scour hole with a limited horseshoe vortex. Sediment slides down the upstream slope and guarantees a sediment supply to the scour hole. For $D/d_{50} > 130$ Raudkivi and Ettema (1983) lack of sufficient laboratory data but formulate the hypothesis that the sediment is relatively fine and the scour depth is independent of the relative grain size. The maximum value of D/d_{50} in Raudkivi and Ettema (1983) experiments is at approximately 250. More recent data by Sheppard, Odeh,

and Glasser (2004) extended local scour data to larger D/d_{50} ratios up to approximately 4000. As a result, they could show that the hypothesis of a constant relative scour depth for relative grain sizes $D/d_{50} > 130$ is not correct. A significant decrease in local scour depth for $D/d_{50} > 130$ could be identified as shown in figure 3.18.
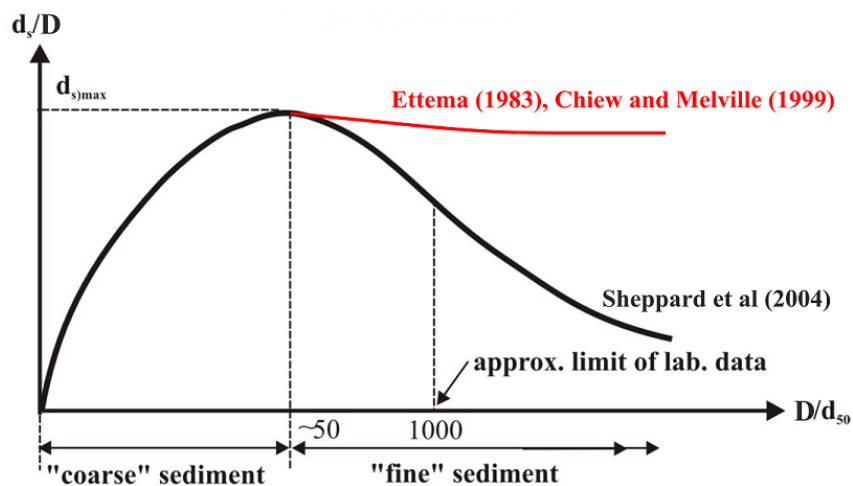
Figure 3.18: Influence of relative grain size on the relative scour depth on pier-like structures. Adapted from Melville (2008).

Stone-like structures

Euler and Herget (2011), Euler and Herget (2012), and Euler et al. (2017) consider the influence of relative grain size w_s/d_{50} on scour development around three-dimensional obstacles with a correction factor $K_{d_{50}}$, which is shown in figure 3.19. In this case, the normalization of the mean grain diameter is via the width of the obstacle w_s. The correction factor shows a similar trend to the phenomena observed at pier-like structures. A maximum value is reached at around w_s/d_{50} = 50 with decreasing trends for smaller and higher values of w_s/d_{50}.
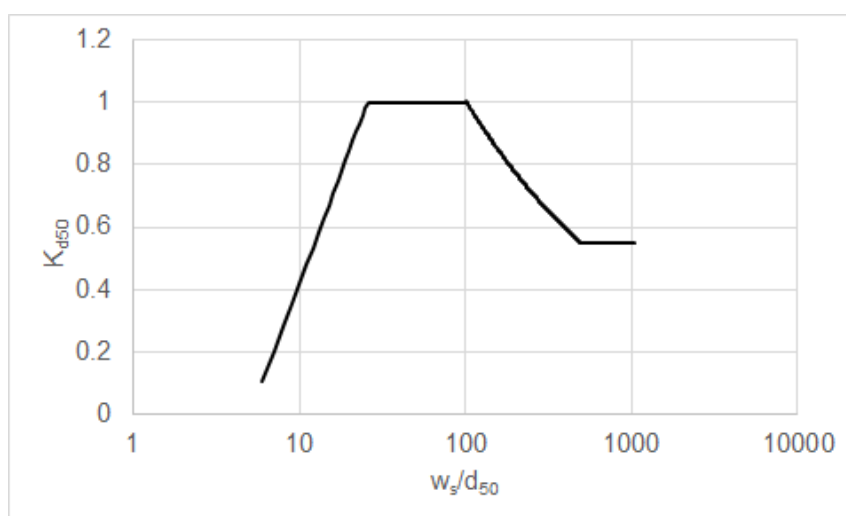
Figure 3.19: Influence of relative grain size on the relative scour depth on stone-like structures. Adapted from Euler et al. (2017).

Dam-like structures

For dam-like structures, the scour depth increases with increasing h_2/d_{50} until a value of 40 then decreases again as shown in figure 3.20 (Wang et al., 2019). The hydraulically significant length is the tailwater depth h_2 in this case. For $h_2/d_{50} < 40$ the energy dissipation is dominated by particle pores, means that fine sediment dissipates less energy than coarse sediment. For $h_2/d_{50} > 40$ the dominant process is the dissipation of flow energy through the downflow (Wang et al., 2019; Guan, Melville, & Friedrich, 2016).
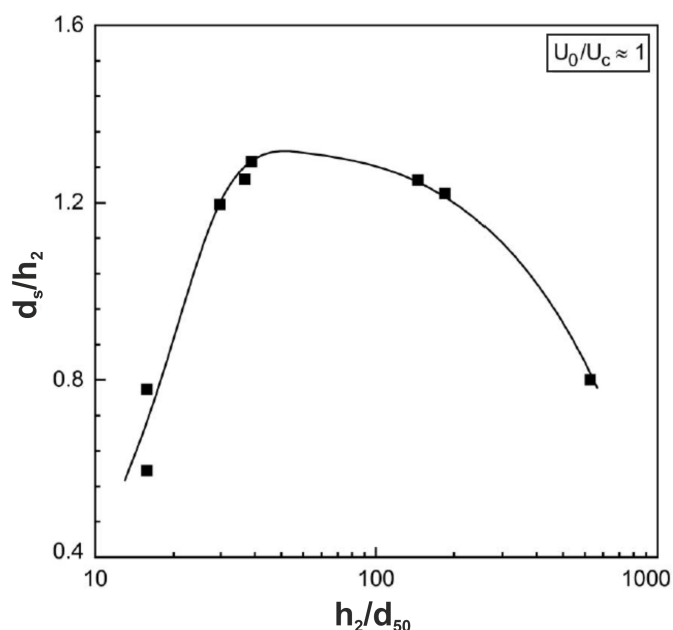
Figure 3.20: Influence of relative grain size on the relative scour depth on dam-like structures. Adapted from Wang et al. (2019).

3.4.4 Influence of uniformity of grainsize curve

Sediment grading is known to have an influence on morphological processes and often shows a sediment sorting due to varying flow velocities. The uniformity of the sediment also has an influence on the local scour depth in the vicinity of in-stream structures.

Pier-like structures

Melville (2008) summarizes the results of the studies of Ettema (1976), Ettema (1980), Chiew and Melville (1987), and Baker (1986) on the influence of uniformity of grainsize curves which are also stated in Raudkivi and Ettema (1983). At threshold condition ($U_0/U_c \sim 1$) an armouring effect can be observed at the upstream sediment bed and also in the scour hole (see figure 3.21). The armouring effect leads to a significant reduction in relative scour depth at threshold conditions. For live-bed conditions ($U_0/U_c > 1$) the armouring effect decreases until the live-bed peak. At the live-bed peak nearly all grain sizes are in motion and the non-uniformity has less impact on scour depth. To the authors knowledge no studies on this specific parameter were done for stone- and dam-like structures, but it can be expected to find the same dependency.

Zone I: Armour Layer Formation
Zone II: Progressive Break-up of Armour
Zone III: All Particle Sizes in Motion
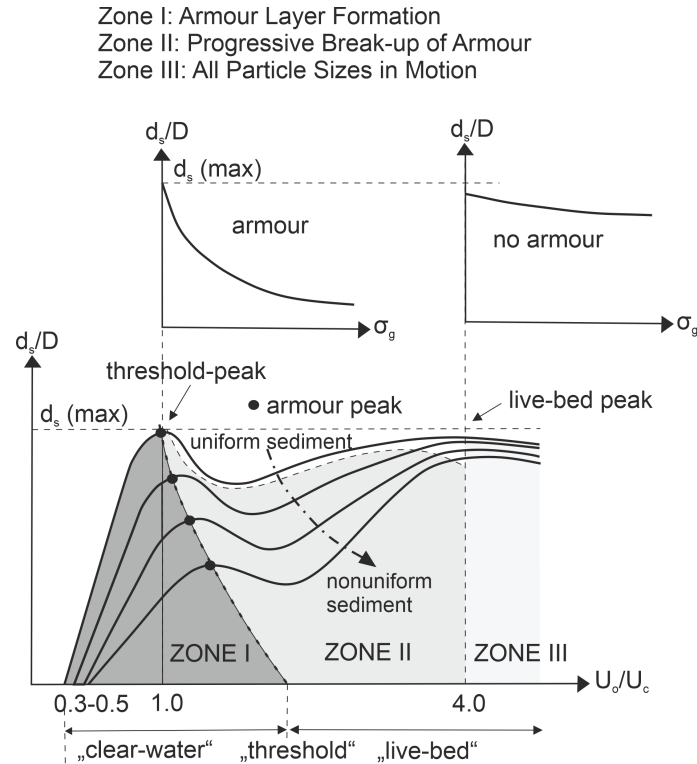
Figure 3.21: Influence of uniformity of sediment grain size curve on the relative scour depth on pier-like structures. Adapted from Melville (2008).

3.4.5 Influence of time

Parts of this chapter were already published in Kannen, Seidel, and Franca (2022).

Scouring is a time-dependent process. The progression of scour development can be categorized into distinct stages, as outlined by Ettema (1980) and Hoffmans and Verheij (1997) (see figure 3.22). Both models identify an initial phase, marked by a rapid scour rate due to the downflow at the pier front. This is followed by a principal phase, dominated by the horseshoe vortex. In Hoffmans and Verheij's model, this phase is further divided into development and stabilization stages. The models culminate in an equilibrium phase, where negligible changes in scour depth occur. Despite the widespread recognition of these models, the debate continues regarding whether scour development eventually stabilizes after a specific time (Cardoso & Bettess, 1999), or continues indefinitely (Bertoldi & Jones, 1998; Franzetti, Larcan, & Mignosa, 1982; Oliveto & Hager, 2002).

Even though there is no consensus between scientist on this topic yet, it is necessary to define a certain time limit for stopping experiments that allow a comparison of different structure types. Three different approaches are presented in literature: equilibrium criteria, time development formulas and predictor equations as summarized in Lança, Fael, and Cardoso (2010). An overview of the criteria is given in table 3.1.
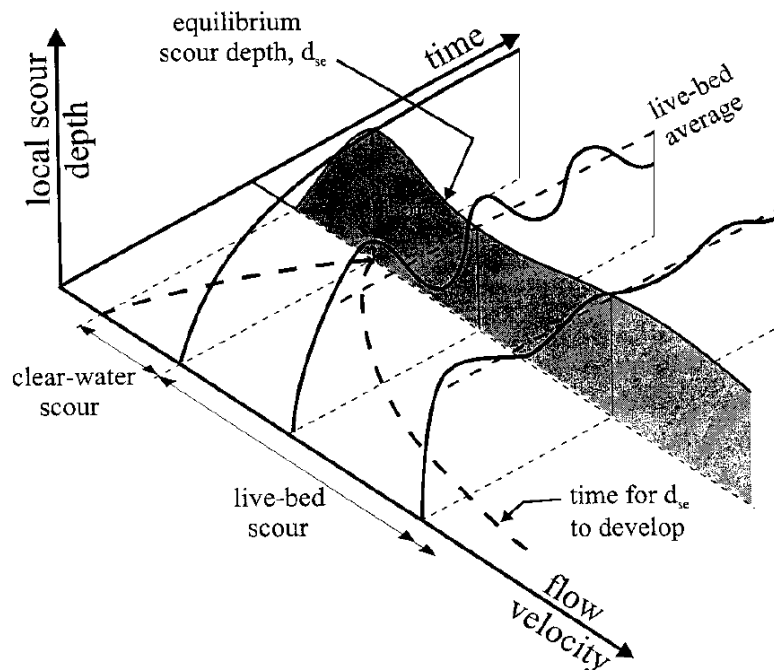
Figure 3.22: Time development of local scour around pier-like structures for different flow intensities. Adapted from Melville and Chiew (1999).

Equilibrium criteria are determined by the equilibrium time t_e to achieve stable conditions during scouring. As shown in Table 3.1, this could represent a scouring rate that is beneath a specified threshold, which might be based on geometrical references, as mentioned in studies by Melville and Chiew (1999), Coleman, Lauchlan, and Melville (2003), and Grimaldi et al. (2009), or visual criteria, as noted in the work by Cardoso and Bettess (1999). Time development formulas predict this equilibrium duration using past recorded data and then project a stable value. Typically, recordings cease once they reach 95% of the anticipated maximum scour depth. For approximation purposes, various functions like logarithmic (referenced by Ettema (1980)), exponential (cited in studies by Melville and Chiew (1999), Lança, Fael, and Cardoso (2010), and Franzetti, Larcan, and Mignosa (1982)), and polynomial (as seen in Bertoldi and Jones (1998) and Lança et al. (2013)) are utilized. In addition, several research works, including those by Cardoso and Bettess (1999), Melville and Chiew (1999), Chang, Lai, and Yen (2004), and Lança, Fael, and Cardoso (2010), have introduced predictor equations to estimate the necessary duration to reach equilibrium conditions. However, Lança, Fael, and Cardoso (2010) pointed out potential inaccuracies in predicting both the time to equilibrium t_e and the equilibrium scour depth d_{se}, since these predictions rely on how measurement data fits the curve.

The observations above highlight the ongoing challenge: there hasn't been a universally accepted standard for determining the equilibrium time in scour experiments, irrespective of the structure's type. In chapter 4.2.5 the author therefore derives a criterion that allows comparison of different structures.

Table 3.1: Summary of selected equilibrium criteria, predictor equations and time development formulas as shown in Kannen, Seidel, and Franca (2022).

Criterion from	Description or formula
EQUILIBRIUM CRITERIA BASED ON SCOUR RATES	
Melville and Chiew, 1999	time when the rate of scour reduces to 5% of the pier diameter in a 24-hour period
Coleman, Lauchlan, and Melville, 2003	time at which the rate of scour reduces to 5% of the smaller of the foundation length (pier diameter or abutment length) or the flow depth in the succeeding 24-hour period
Grimaldi et al., 2009	1) Estimation according to Franzetti (1994) 2) Estimation according to Cardoso and Bettess (1999) 3) Reduction of the scour rate to less than 0.05 D/3 in 24 hours
Umeda, Yamazaki, and Ishida, 2008	The tests were run for 10.3 hours until the variation in the scour depth was less than 1 mm in 1 hour.
EQUILIBRIUM CRITERIA BASED ON VISUAL PARAMETERS	
Cardoso and Bettess, 1999	time where the slope of plots of the scour depth versus the logarithm of time changes and tends to zero
PREDICTOR EQUATIONS	
Coleman, Lauchlan, and Melville, 2003	$t_e = 10^6 \left(\frac{L}{U_o}\right)\left(\frac{U_o}{U_c}\right)^3 \left(\frac{y}{L}\right)\left\{3 - \left[1.2\left(\frac{y}{L}\right)\right]\right\}$ for $\left(\frac{y}{L}\right) < 1$ $t_e = 1.8 \cdot 10^6 \left(\frac{L}{U_o}\right)\left(\frac{U_o}{U_c}\right)^3$ for $\left(\frac{y}{L}\right) \geq 1$
Melville and Chiew, 1999	$t_e(days) = 48.26\frac{D}{U_o}\left(\frac{U_o}{U_c} - 0.4\right)$ for $\frac{y}{D} > 6$ $t_e(days) = 30.89\frac{D}{U_o}\left(\frac{U_o}{U_c} - 0.4\right)\left(\frac{y}{D}\right)^{0.25}$ for $\frac{y}{D} \leq 6$
Chang, Lai, and Yen, 2004	$t_e(days) = AK'_\sigma \frac{D}{U_o}\left(\frac{U_o}{U_c} - 0.4\right)\left(\frac{d_{50}}{D}\right)^k \left(\frac{y}{D}\right)^m$ for coefficients see Chang, Lai, and Yen, 2004 Table 4
Franzetti (1994)	$U_o \cdot \frac{t}{D} > 2 \cdot 10^6$ (as cited in Lança, Fael, and Cardoso, 2010)
TIME DEVELOPMENT FORMULAS	
Melville and Chiew, 1999	$\frac{d_s}{d_{se}} = exp\left(-0.03\left\|\frac{U_c}{U_o}ln\left(\frac{t}{t_e}\right)\right\|^{1.6}\right)$
Ettema, 1980	$\frac{d_s}{D} = K_1 log\left[\left(\frac{d_{50}}{D}\right)\left(\frac{u_* t}{D}\right)\left(\frac{\nu}{u_* D}\right)\right] + log K_2$ for coefficients K_1 and K_2 see Ettema, 1980
Bertoldi and Jones, 1998	$d_s = p_1\left(1 - \frac{1}{1+p_1 p_2 t}\right) + p_3\left(1 - \frac{1}{1+p_3 p_4 t}\right)$ p_i = parameters of polynom
Lança, Fael, and Cardoso, 2010	$d_s = p_1\left(1 - \frac{1}{1+p_1 p_2 t}\right) + p_3\left(1 - \frac{1}{1+p_3 p_4 t}\right) + p_5\left(1 - \frac{1}{1+p_5 p_6 t}\right)$
Lança et al., 2013	$\frac{d_s}{d_{se}} = 1 - exp\left[-1.22\left(\frac{D}{d_{50}}\right)^{-0.764}\left(\frac{U_o t}{D}\right)^{0.09\left(\frac{D}{d_{50}}\right)^{0.244}}\right]$
Franzetti, Larcan, and Mignosa, 1982	$\frac{d_s}{d_{se}} = 1 - exp\left[-0.028\left(\frac{U_o t}{D}\right)^{1/3}\right]$
Kothyari, Hager, and Oliveto, 2007	$log T = 4.8 F_d^{1/5}$ where T = dimensionless time; $F_d = U_o/(g' d_{50})^{1/2}$
Oliveto and Hager, 2002	$Z = 0.068\sigma^{-1/2}F_d^{1.5}log(T)$ where Z = dimensionless scour depth

where L = abutment length; U_o = approach flow velocity; U_c = critical flow velocity; d_{50} = mean diameter of sediment; d_{se} = end (maximum) scour depth; y = water depth

Pier-like structures

The initiation of the scour process occurs at the front of the pier, triggered by the downflow. This causes a gradual expansion of the scour hole upstream and laterally as shown in figure 3.23. The eroded sediment accumulates in a central dune downstream from the pier, which continues to grow in height until the scour hole reaches its maximum size (Raudkivi & Ettema, 1983; Umeda, Yamazaki, & Ishida, 2008). It's important to note that the dune hasn't achieved its equilibrium state when the scour hole has reached its deepest point. The dune's development continues, marked by a reduction in both height and width until it, too, attains a state of equilibrium.
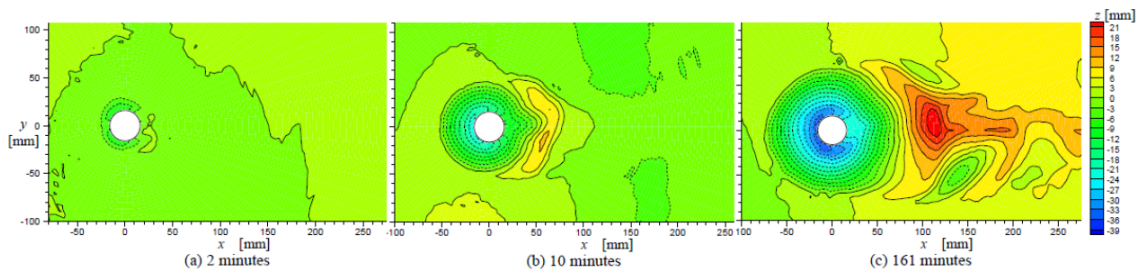
Figure 3.23: Progression of the local scour around a pier-like structure. Adapted from Umeda, Yamazaki, and Ishida (2008).

Stone-like structures

Euler and Herget (2012) detected a similar non-linear temporal development for submerged piers as for emergent piers, as shown in figure 3.24. As for pier-like structures, the length of the dune continued to grow, even when the sediment movement in the scour hole had considerably decelerated (Euler et al., 2017).
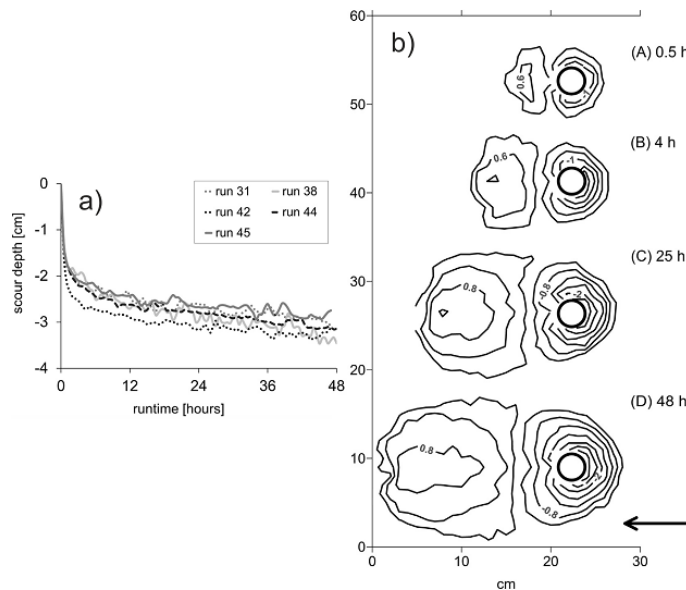
Figure 3.24: a) Time development of the deepest point and b) Top view of progression of the local scour around a submerged circular pier. Adapted from Euler et al. (2017)).

Different types of submerged groynes showed a similar behavior for the time development of the deepest point in the scour hole at the groyne head (Figure 3.25, h_s/h_0 = 0.33, Rashak and Khassaf (2020)).
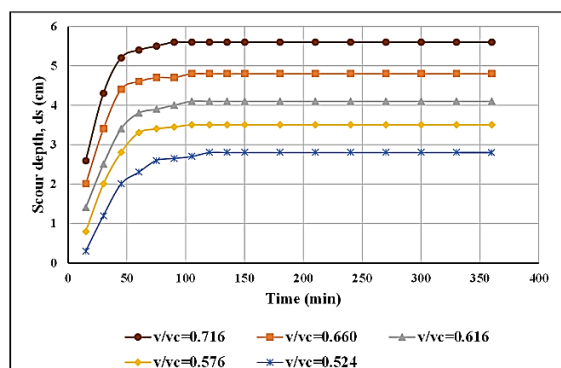
Figure 3.25: Time development of the deepest point in the vicinity of a submerged groyne, v/v_c equals U_0/U_c. Adapted from Rashak and Khassaf (2020).

Dam-like structures

Dam-like structures like submerged weirs show a similar asymptotical behavior as the previous in-stream structures. The development is divided into three stages as shown in figures 3.26 and 3.27: (1) initial fast stage, (2) progressing stage, and (3) equilibrium stage (Guan, Melville, & Friedrich, 2014; Meftah & Mossa, 2006). The initial phase shows high rates of erosion which is due to the high bed shear stresses that are exerted on the sediment (Meftah & Mossa, 2004). 65 % of the maximum scour depth is reached in less than 10 % of the equilibrium time (Meftah & Mossa, 2004). In the second stage the scour rate slows down with about 25 % scour depth increase in 30 % of the equilibrium time (Meftah & Mossa, 2004). Hence, the bed shear stresses reduce significantly in this stage (Meftah & Mossa, 2004). In the final stage equilibrium is reached (Meftah & Mossa, 2004).
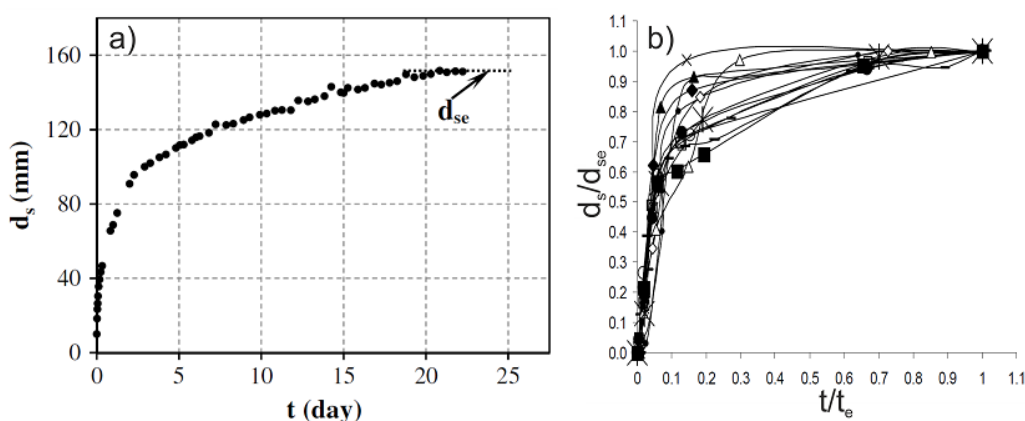
Figure 3.26: Time development of the deepest point in the vicinity of a dam-like structure according to a) Guan, Melville, and Friedrich (2014) and b) Meftah and Mossa (2004).
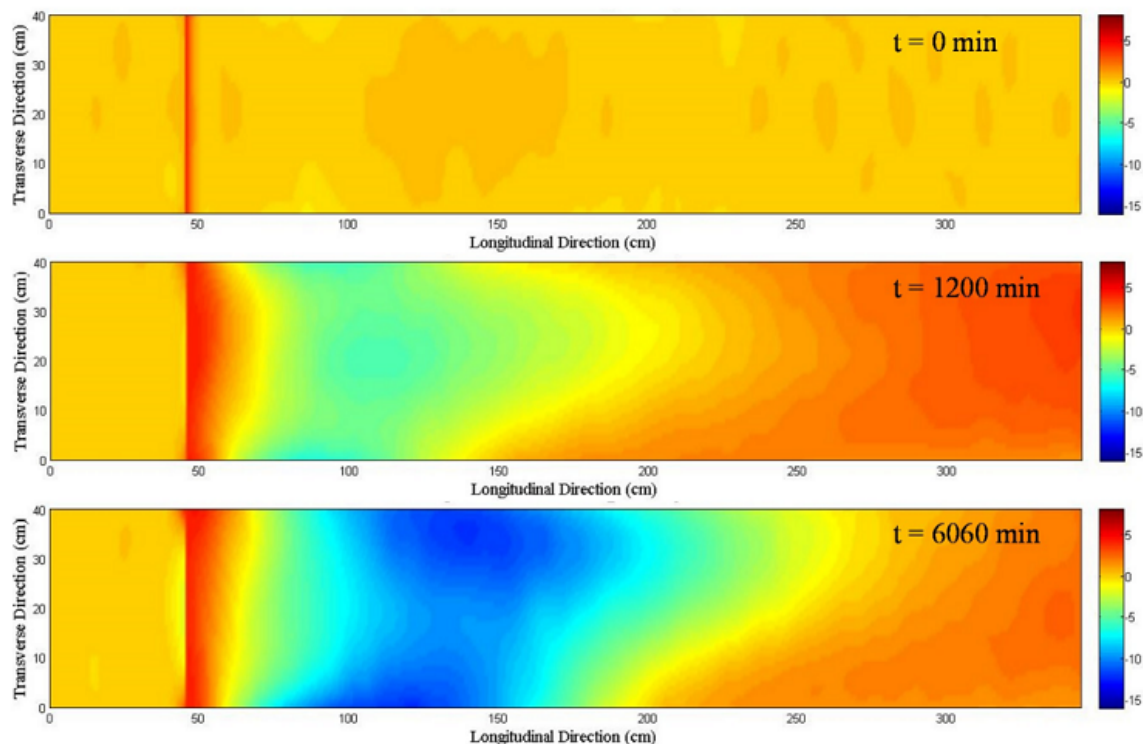
Figure 3.27: Top view of progression of the local scour around a dam-like structure. Adapted from Guan et al. (2019).

3.4.6 Influence of structural parameters

The factor that distinguishes the three flow types are the geometrical dimensions of the in-stream structure. For each flow type the influence of different geometrical dimensions is important and they are explained subsequently.

Pier-like structures

Two factors of pier-like structures influence the maximum scour depth that evolves around them: the pier shape and the pier alignment. Streamlined pier shapes lead to a reduction of scour depth and sharp edged piers such as rectangular piers lead to an increase of maximum scour depth in comparison with the reference of a circular pier. The shape of the pier is considered in a shape factor which is shown in table 3.2.

Table 3.2: Shape factors for different pier shapes according to Breusers and Raudkivi (1991).

shape	shapefactor
streamlined pier	0.8
cylindrical pier	1.0
rectangular pier	1.22

The influence of pier alignment was investigated by Laursen and Toch (1956). Figure 3.28 shows a strong dependence of the alignment factor on the angle of attack.
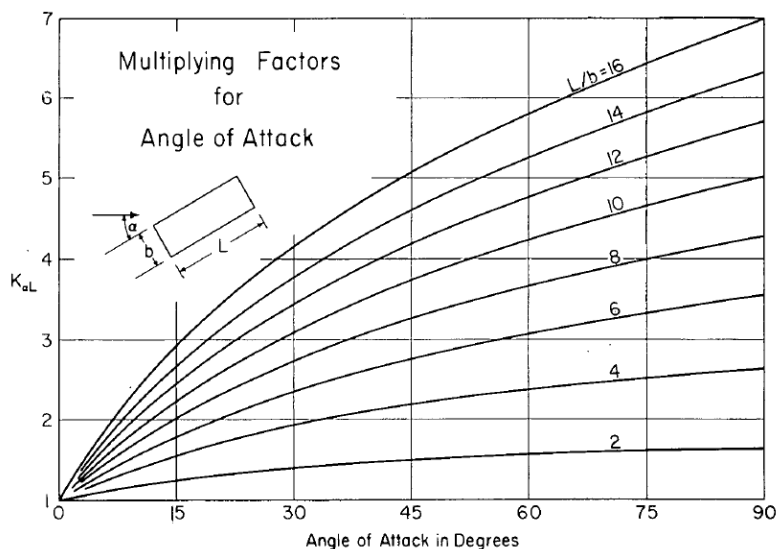
Figure 3.28: Influence of angle of attack on the scour depth around a pier-like structure. Adapted from Laursen and Toch (1956).

Stone-like structure

For submerged circular piers a considerable reduction in the non-dimensional scour depth $\hat{d}_s$ was detected with increasing submergence ratio S as shown in figure 3.29 (Dey, Raikar, & Roy, 2008; Huang, 1991). This is due to the decrease in size and strength of the horseshoe vortex with an increase in submergence ratio S. Moreover, zones of high vorticity are concentrated within the scour hole for the emergent circular piers whereas a vorticity zone also is present at the trailing vortex at the top of the circular pier.
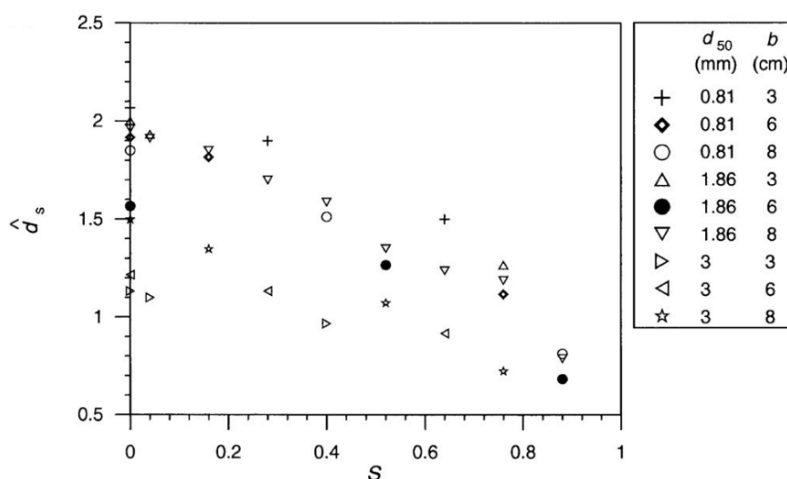
Figure 3.29: Influence of submergence S on the maximum non-dimensional scour depth $\hat{d}_s$ at a submerged circular pier. Adapted from Dey, Raikar, and Roy (2008).

The shape of the submerged structure can be considered with a correction factor for scour depth for different obstacle shapes as shown in figure 3.30.

52

width		height	
●	1.0	◗	0.85
⬬	0.8	▬	1.0
◼	1.1		

Figure 3.30: Correction factors for obstacle shapes of height and width to account the influence of the obstacles shape. Adapted from Euler et al. (2017).

Ishigaki and Baba (2004) showed for 90° groynes that the maximum scour depth at the groyne head decreases with increasing submergence. This also accounts for inclined groynes (see figure 3.11). Harada et al. (2013) analyzed how the angle of attack impacts submerged groynes. When the angle was 90° to the flow, it resulted in a scour hole that was both deepest and shortest. As the angle of attack increased (while maintaining a constant blockage ratio, leading to a longer groyne), there was a noticeable decrease in scour depth and an increase in the length of the scour hole.

Dam-like structures

Structural parameters of dams that influence the scour depth are the curvature, the dam height and the upstream or downstream sloping of the dam. The standard dam is rectangular to the main flow direction and has no sloping. In a trapezoidal channel two deep scour holes at the riverbanks and a shallower but larger scour hole in the centerline form (Mueller & Kobus, 1981) (see figure 3.31). Changing the curvature to a V- or U-shaped dam (the V is pointing in upstream direction) leads to a concentration of the flow in the middle of the channel, hence a larger and deeper scour in the middle and two small scours at the riverbanks (Mueller & Kobus, 1981). If the V-shaped dam points in downstream direction the flow is diverted to the sides and scours at the riverbanks and a dune in the centerline form (Mueller & Kobus, 1981; Pagliara & Carnacina, 2013). Pagliara and Carnacina (2013) could show that U-shaped dams show a dependency on the relation of length of the dam l_{dam} to the channel width w. With increasing l_{dam}/w the maximum scour depth increases and the location of the deepest point moves towards the dam. W-shaped dams lead to two scour holes (Scurlock, Thornton, & Abt, 2012).
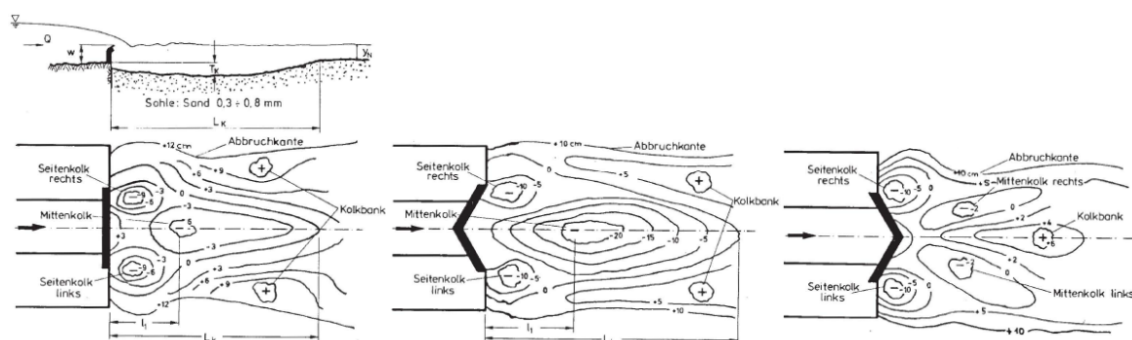
Figure 3.31: Influence of curvature on the scour pattern downstream of a dam-like structure. Adapted from Mueller and Kobus (1981).

With increasing dam height h_s, the maximum scour depth increases as shown in figure 3.32. This is due to a constriction of the flow which causes a higher impact on the downstream bed (Wang et al., 2019). Downstream and upstream sloped dams have no influence on the maximum scour depth downstream of the dam (Wang et al., 2018; Wang, Melville, & Guan, 2018).
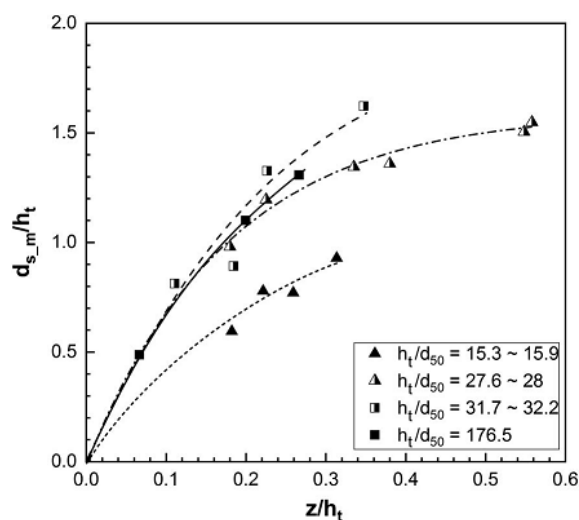
Figure 3.32: Influence of weir height on the scour depth downstream of dam-like structures. h_t equals h_2 and z equals h_s in this work. Adapted from Wang et al. (2019)

3.4.7 Influence of surface roughness

Some basic considerations on the influence of surface roughness on the scour development have been made by Shamloo (1997). In his work he compared hemispheres and natural rocks of the same approximate size under the same hydromorphological conditions. The results showed a significant reduction in scour depth for the natural materials as shown in figure 3.33. The significance of the investigation for this work is limited as not only the surface roughness but also the shape of the structure (hemisphere, cube and ellipsoid) was different. The author assumes that the influence of the shape of the structure is of higher order of magnitude for the scour process than the surface roughness for this study. Therefore, a general meaning cannot be drawn from this investigation. Further investigation on the influence of surface roughness is given in chapter 6.1.2.
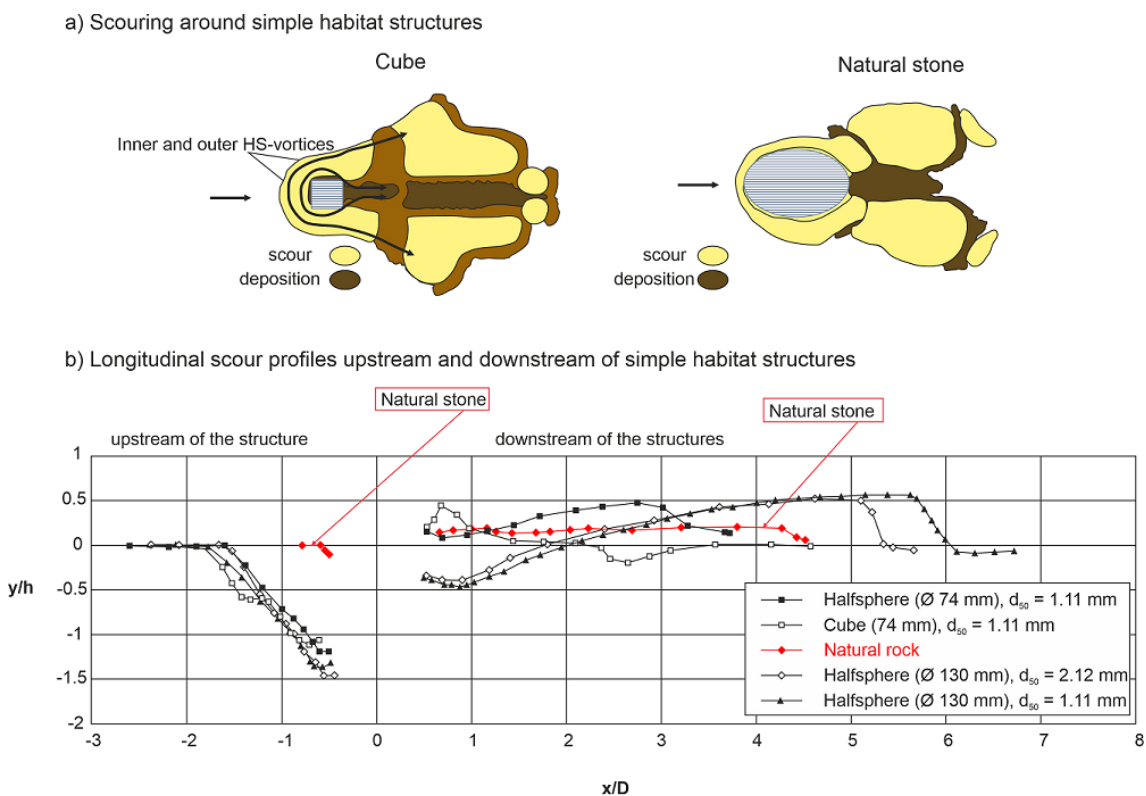
Figure 3.33: Scouring around simple habitat structures. a) Scour pattern around a cube and a natural stone (ellipsoid) and b) Longitudinal scour profiles upstream and downstream of simple habitat structures. Adapted from Shamloo (1997).

3.4.8 Influence of foundation

Experiences with large boulders as in-stream structures from recent river restoration projects showed the phenomenon of "self-burial". This means that large boulders that are placed on the river bed without adequate foundation start to form an upstream scour hole and roll backwards into the scour hole as shown in figures 3.34 and 3.35. After some time, this leads to a complete burial of the large boulder (Euler et al., 2017; Huang, 1991). Another factor that influences the tilting movement is the obstacle shape. Elliptical objects dropped into the scour hole and did not move further whereas round objects dropped once and continued with moving upstream. This especially accounts for riverbeds with fine sediments.
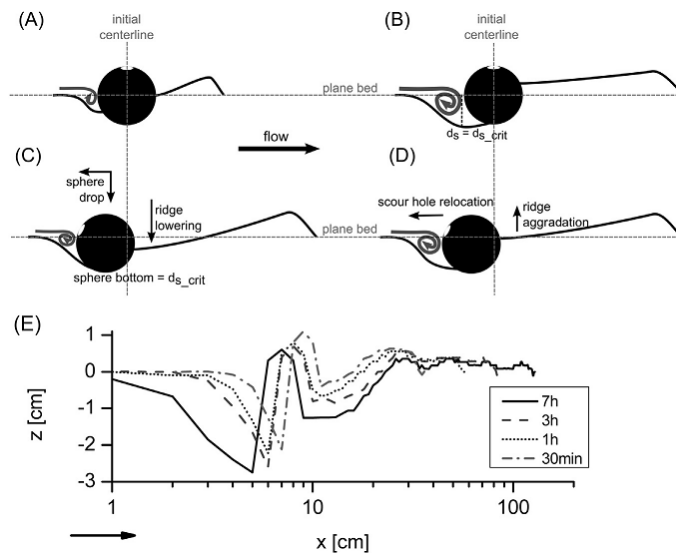
Figure 3.34: Process of burial of a large boulder. Adapted from Euler et al. (2017).
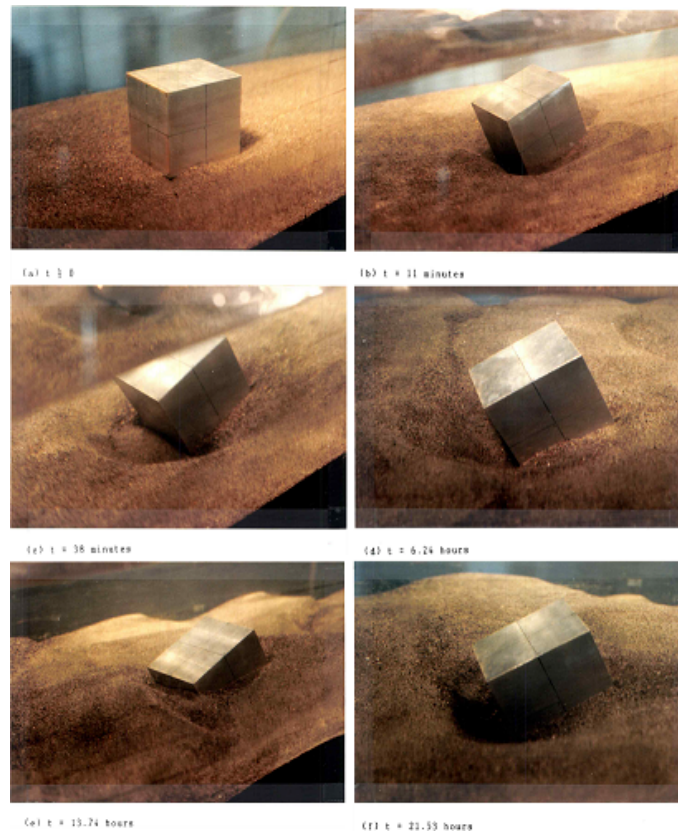
Figure 3.35: Process of burial of a cube in a physical model experiment of Huang (1991).

All of the beforementioned structures cause a scour hole and are possible measures to create a deep pool. On the other side the structures obstruct the flow and cause resistance which leads to a backwater rise which can increase the risk of inundations during flood events. Therefore, knowledge about the influence of the structures on backwater rise is of interest, which is given in the subsequent chapter.

3.5 Influence of in-stream structures on the backwater rise

The cumulative drag caused by in-stream structures is predominantly due to flow separation, vortices, turbulence, overfalling jets (in the case of submerged structures) and hydraulic jumps. Under free surface conditions, energy loss leads to a rise in water surface elevation, subsequently causing backwater rise. Various approaches to address the backwater rise of in-stream structures are explored in existing literature. The backwater rise can be attributed in different ways. Δh is defined as the difference between the upstream flow depth h_1 and the downstream flow depth h_2 as shown in figure 3.36. The ratios $\Delta h/h_2$ and h_1/h_0 are common in literature to characterize the backwater rise (e.g. Azinfar and Kells (2009) and Gebhardt et al. (2012)). But also drag coefficients C_D are used to describe the resistance that a structure imposes on a flow.
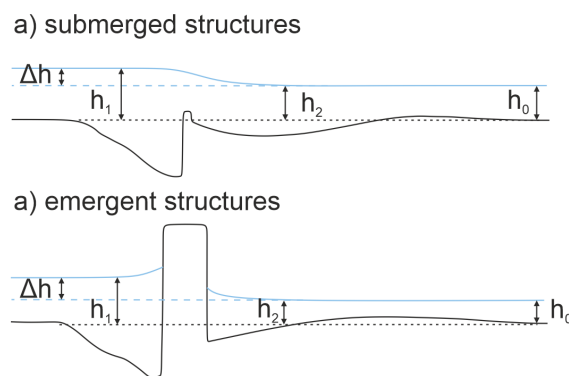
Figure 3.36: Definition of water levels for the backwater rise.

.

3.5.1 Backwater rise on the basis of energy approaches

The energy approach interprets resistance as a local loss h_v, incorporating it through a local loss coefficient $h_v = \zeta \cdot U_2^2/2g$. First the Bernoulli equation is employed to the cross sections up- and downstream of the structure as shown in figure 3.37, where friction loss is already subtracted. Employing the definition of the Froude number and the continuity equation leads to

$$\frac{\Delta h}{h_2} = \frac{Fr_2^2}{2} - \frac{Fr_2^2}{2}\left(\frac{h_2}{h_1}\right)^2 + \frac{\Delta H}{h_2} \tag{3.1}$$
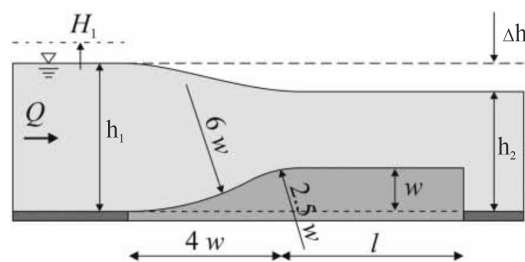
Figure 3.37: Application of the energy approach on the example of a Jambor weir sill. Adapted from Gebhardt et al. (2012).

Gebhardt et al. (2012) employed this method to characterize the energy loss at a structure known as a Jambor weir sill. Here, the loss coefficient was substituted by $\zeta = C_D \cdot w/h_2$, leading to

$$\frac{\Delta h}{h_2} = \frac{Fr_2^2}{2} \cdot \left(1 - \left(\frac{h_2}{h_1} \right)^2 + C_D \cdot \frac{w}{h_2} \cdot \left(\frac{h_2}{h_1} \right)^2 \right) \tag{3.2}$$

3.5.2 Backwater rise on the basis of empirical approaches

Schalko et al. (2018) adopted an empirical approach to explore the backwater rise caused by large accumulations of wood. Drawing from prior research and methodical experimental work, they were able to identify the governing parameters (approach Froude number Fr_0, bulk factor (relating to porosity), length of logs, diameter of logs and percentage of fine material FM). Through dimensional analysis and non-linear regression analysis an empirical formula on backwater rise was derived

$$\frac{\Delta h}{h_0} = 5.4 \, \frac{Fr_0 \, u^{1/3} \, (9FM + 1)}{a^{4/3}} \tag{3.3}$$

3.5.3 Backwater rise on the basis of momentum approaches

The momentum approach associates the resistance of the in-stream structure with a drag force acting on the flow. By utilizing a control volume, this approach bypasses the need to quantify individual energy losses, making it the most commonly used method for describing backwater rise (Suribabu et al., 2011). Azinfar and Kells (2008) formulated an equation for backwater rise based on the momentum and continuity equation for a spur dike as shown in figure 3.38. The control volume shows the forces acting here: F_1 and F_2 are hydrostatic pressures, F_D is the drag force due to the spur, F_f are forces due to friction, F_w is the force due to gravity.
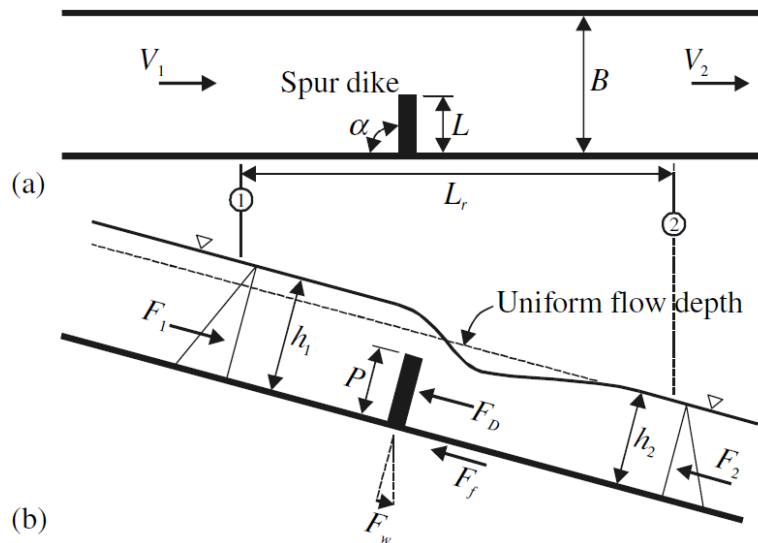
Figure 3.38: Application of the momentum approach on the example of a spur dike. V_1 equals the approach flow velocity U_0 in this work. Adapted from Azinfar and Kells (2009).

The drag force F_D is defined as:

$$F_D = C_D \cdot A_p \cdot \rho \cdot \frac{U_0^2}{2} \tag{3.4}$$

where C_D is the dimensionless drag coefficient, which is dependent on various parameters as outlined below. A_p is the projected cross-sectional area (i.e., the maximum cross-sectional area normal to the flow direction) of the body. With the momentum and continuity equation as well as the equation for the drag force the following equation was derived by Azinfar and Kells (2009):

$$2Fr_1^2 \left(\frac{h_1}{h_1}\right)^3 - \left(2Fr_1^2 - C_D A_r Fr_1^2 + 1\right) \left(\frac{h_1}{h_2}\right)^2 + 1 = 0 \tag{3.5}$$

C_D values have been derived e.g. for spur dikes (Azinfar & Kells, 2008; Azinfar & Kells, 2009; Oak, 1992) and for piers (Roberson & Crowe, 1993; Hoerner, 1965; Aksel et al., 2021; Naudascher, 1992). An overview is given in table 3.3. The values given in the table distinguish whether the drag coefficient was measured in flat or scoured bed conditions, as the scouring is supposed to change the drag of the in-stream structure. This point is further addressed in chapter 5.4.2. Additionally, the boundary conditions of the experiments are given. A lot of studies were performed in air flows where the structure is typically placed horizontally between two walls to measure the drag force on the body. With this setup a 2D C_D value is measured. Studies like Naudascher (1992), Azinfar and Kells (2009), and Aksel et al. (2021) investigate free surface flows with water as the fluid phase. In those setups the structure is placed vertically into a flume and the water is under the influence of gravity and the free surface. Hence, additionally a Froude number dependency can be expected. The overview shows that the shape of the pier has an influence on the drag coefficient and a triangular shaped pier has a higher drag than a rectangular and a circular pier (Hoerner, 1965). Moreover, the openness of the upstream front face plays a role for the drag. Open front faces, e.g. for a circular pier this means a half-cylinder that is open in upstream direction, lead to a higher drag coefficient (Hoerner, 1965).

Table 3.3: Summary of drag coefficients obtained from literature study around different types of structures.

	flat bed					scoured bed
	in between walls		free surface flow			
	Roberson and Crowe (1993) Re $>10^4$	Hoerner (1965) 10^4<Re<10^6	Naudauscher (1992) $2 \cdot 10^3$<Re<$7 \cdot 10^3$ Fr=0.1-1	Azinfar and Kells (2009) Fr=0.15-0.58	Aksel et al (2021) Re=52800 Fr=0.19	Aksel et al (2021) Re=52800 Fr=0.19
CP	1.1	1.17 [1] 2.3 [2]	1-1.3		1.65	0.78
RP	2	2.05 [1]				
TP		2.00 [1] 2.2 [2]				
DG				6.73 [3]		

[1] full body with closed upstream front face

[2] body with open upstream front face

[3] calculated for the case of this work based on formula 3.5

3.5.4 Backwater rise formulas for pier-like structures

The backwater rise at piers is influenced by factors such as the type of the flow, the discharge, the geometric parameters of the cross section, and the shape of the pier (Charbeneau & Holley, 2001; El-Alfy, 2006; Suribabu et al., 2011; Yarnell, 1934).

Yarnell (1934) formulated an equation for the backwater rise at bridge piers. Suribabu et al. (2011) further refined Yarnell's equation by introducing a correction factor, μ, to accommodate varying pier shapes and blockage ratios A_r. For instance, for square piers, μ values were set at 0.2 and 0.18, while for circular piers, μ values were 0.24 and 0.2 for blockage ratios A_r of 0.33 and 0.4, respectively.

$$\frac{\Delta h}{h_0} = \mu \, K(K + 5Fr^2 - 0.6)(A_r + 15A_r^4) \; Fr^2$$

pier shape factor K according to Yarnell: circular nose = 0.9,

triangular nose = 1.05, square nose = 1.25. (3.6)

Charbeneau and Holley (2001) performed hydraulic experiments and adjusted the formula of Yarnell (1934) with two additional parameters μ and β.

$$\frac{\Delta h}{h_0} = \beta \, K \left(K + \mu \, 5Fr^2 - 0.6 \right) \left(A_r + 15A_r^4 \right) \; Fr^2$$

For circular pier β = 1.24 and μ = 0.4. (3.7)

In numerical applications the backwater rise of in-stream structures is often considered by altering the roughness value n. Charbeneau and Holley (2001) derived a formula for the backwater rise at a pier by alteration of the Manning equation, which is valid for shallow flows

$$\frac{\Delta n}{n} = \sqrt{1 + \frac{K \, h_0^{\frac{4}{3}}}{g \, L \, n^2}(K + 5Fr^2 - 0.6)(A_r + 15A_r^4)} - 1$$

where L is the characteristic length (normally flow length under the bridge). (3.8)

El-Alfy (2006) conducted research on various pier shapes and determined that the primary factors influencing backwater rise are the blockage ratio and the Fr_2/Fr_{2c} ratio. The backwater rise can be calculated using the subsequent equations:

$$\text{Rectangular Pier:} \quad \frac{\Delta h}{h_2} = 0.217 - 0.367 \, C_r + 0.389 \, Fr_2 \tag{3.9}$$

$$\text{Triangular Pier:} \quad \frac{\Delta h}{h_2} = 0.205 - 0.338 \, C_r + 0.322 \, Fr_2 \tag{3.10}$$

$$\text{Circular Pier:} \quad \frac{\Delta h}{h_2} = 0.178 - 0.315 \, C_r + 0.314 \, Fr_2 \tag{3.11}$$

C_r is the contraction ratio w_s/w and application range of Fr_2 = 0.2-0.62, C_r = 0.42-0.9 and pier length-width 5:1 to 30:1. It is to be noted, that the pier length-width ratio lays outside of the piers used in this study.

3.5.5 Backwater rise formulas for stone-like structures

Azinfar and Kells (2008) and Azinfar and Kells (2009) explored the backwater rise associated with spur dikes, identifying five main influencing factors: the approach Froude number Fr_0, blockage ratio A_r, aspect ratio (specifically height to length), submergence and angle of attack. They found that an increased drag coefficient C_D was a result of a surge in negative pressure downstream of the structure when the blockage ratios were larger. Experiments conducted under fixed-bed conditions revealed that the impact of the blockage ratio was ten times more significant than the other factors.

$$C_D = 1.62 \left(1 - A_r\right)^{-2.40} \left(\frac{P}{L}\right)^{-0.32} \left(\frac{h_1}{P}\right)^{-0.19}$$

(3.12)

<div align="center">definitions see figure 3.38</div>

The peak drag coefficient is observed when the submergence ratio falls between 1 and 1.5. When the angle is at a 90° angle to the direction of the approaching flow, the drag coefficient is at its maximum, but it diminishes at both smaller and larger angles. In the context of emergent conditions, the drag coefficient exhibits a marked increase as the blockage ratio rises.

3.5.6 Backwater rise formulas for dam-like structures

Gebhardt et al. (2012) found the governing parameters of the backwater rise in the vicinity of dam-like structures to be the downstream Froude number, defined as $U_2/\sqrt{gh_2}$, and the ratio h_2/w. They derived a design chart to identify the $\Delta h/h_2$ dependent on Fr_2 which is shown in figure 3.39.
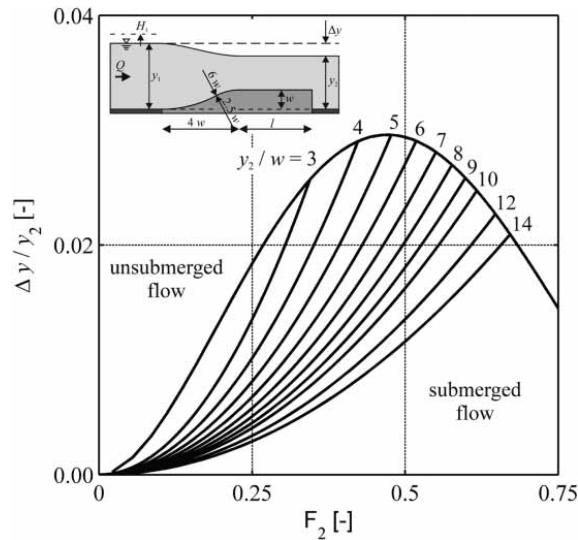
Figure 3.39: Design chart to estimate the backwater rise $\Delta h/h_2$ (here: $\Delta y/y_2$) at a Jambor weir sill from the Froude number Fr_2 (here F_2) and the dimensionless sill height h_2/w_S (here: y_2/w) according to Gebhardt et al. (2012).

3.5.7 Influence of scour on backwater rise

Previous research on backwater rise has typically been carried out under fixed bed conditions. As such, the impact of the scouring process around in-stream structures on backwater rise has not been considered in the studies thus far. The scouring process causes an expansion of the flown through area, resulting in decreased flow velocities around the structure. This change in the flow field modifies the structure's drag, which can subsequently lead to a decrease in backwater rise under movable bed conditions.

Schalko et al. (2019) conducted a series of tests under both fixed and movable bed conditions to examine the effect of a movable bed on backwater rise. They found that the movable bed condition led to a decrease in the backwater rise $\Delta h/h_0$ by 25 %. It was accounted in formula 3.3 by introducing the accumulation type factor f_A that is 0.55 for fixed bed conditions and 0.3 for movable bed conditions.

$$\frac{\Delta h}{h_0} = 5.4 \; f_A \; LW_A \tag{3.13}$$

Aksel et al. (2021) analysed the influence of scour on the drag of a circular pier and found, that the drag coefficient decreased from an average of 1.65 for a circular pier on flat bed to around 0.78 for a pier with scoured bed (see table 3.3), which marks a reduction of about 50%. As a reason they state, that the scour hole leads to a streamlining of the pier which reduces the drag on the pier.

Chapter 4

Methods

Parts of this chapter were already published previous to this dissertation. The respective subchapters are indicated.

4.1 Conceptual design and selection of boundary conditions

4.1.1 Conceptual design

As shown in the preceding chapters, this dissertation centers on comparing the hydromorphology of in-stream structures for generating local scours to create deep pool habitats. The literature review highlighted crucial aspects for consideration in the conceptual design of the model approach.

I. Deep pool habitats play an important role in enhancing river resilience during low water periods and high temperatures. Current revitalization measures, largely guided by ecologists' experience, often rely on trial and error. Especially in this sector profound hydromorphological studies on the different structures were not performed.

II. The in-stream structures identified in the literature review showed that the structures can be classified in three groups: pier-like emergent structures, stone-like submerged structures and dam-like submerged structures. As there are fundamentally different scour mechanisms associated with the three groups it is necessary to investigate at least one representative of each group to provide a profound comparison.

III. Local scours are primarily studied through physical model experiments, as numerical models for local scours are still in the research stage and provide reliable results only for specific cases. This suggests the benefit of conducting morphodynamic investigations of local scours through physical model experiments.

To address the research question, a hybrid model approach was chosen, as illustrated in figure 4.1. The purpose of the physical model with movable bed was mainly the acquisition of the bed morphology (see chapter 4.2) and it was selected due to its better reliability across different scenarios compared to numerical models with movable beds. This physical model experiment also characterized backwater rise by measuring water levels upstream and downstream of the

structures. As morphodynamics and hydraulics are always interdependent, it is necessary to not only measure the bed morphology around the in-stream structure but also to investigate the flow velocity field. A high spatial resolution of the flow velocity field was crucial to capture all flow phenomena such as vortices. Furthermore, turbulence plays a significant role in local erosion phenomena, therefore it is also necessary to have a high temporal resolution of the velocity field. While in physical modeling velocity measurements are time-intensive, a 3D numerical model was employed on the equilibrium state bed morphology from the physical model to simulate hydraulics at high spatial resolution (see chapter 4.3). Mean flow velocities were investigated with an RNG approach, while an LES approach provided insights into the turbulent fluctuations of the flow velocity field. The numerical model was verified with sparse 2D flow velocity measurements from the physical model, that were acquired in high temporal resolution to capture the turbulence.
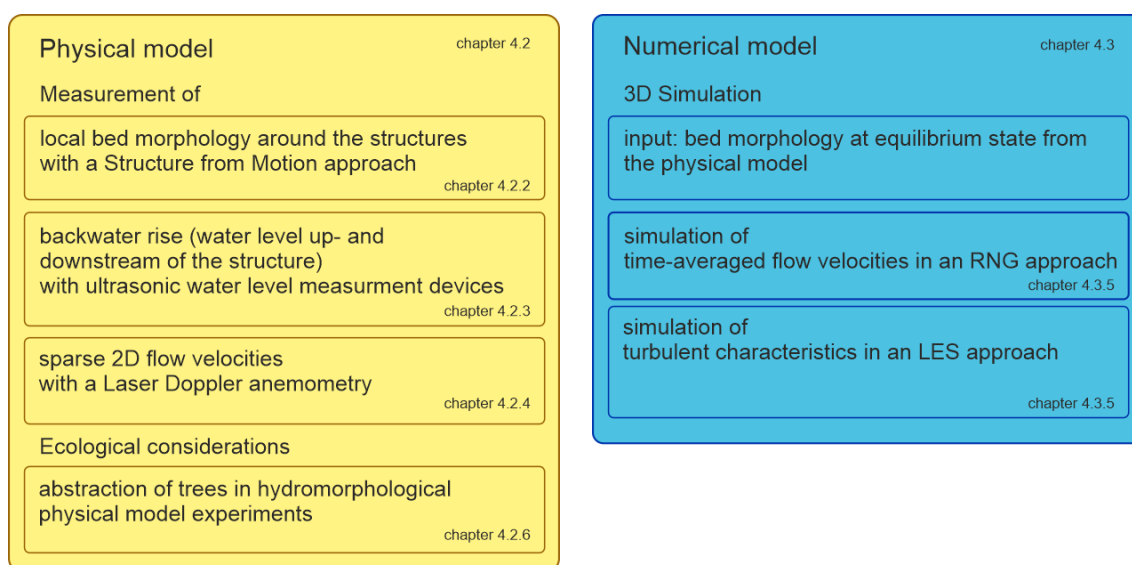
Figure 4.1: Conceptual design of the hybrid approach for the investigation of hydraulics and morphodynamics of local scours as deep pool habitats.

Based on the literature review, six different in-stream structures were selected for investigation. Within this selection, three belong to pier-like structures (Circular Pier, Rectangular Pier, Triangular Pier), two to stone-like structures (Double Wing Deflector, Deflected Groyne), and one to dam-like structures (Kdam). The pier-like structures, which are emergent, have a width w_s of 15.8 cm, constituting 20 % of the total flume width w. The CP serves as a benchmark for comparison with existing studies. The DWD comprises two triangular submerged groynes with a width of 0.4 w each and an initial offset of 0.1 w. The DG covers 1/3 of the flume width. The Kdam spans the entire flume width with a notch in the middle. The last three structures are submerged, and the height of the structure h_s above the initial bed is $0.41\, h_0 = 2.8\, cm$, corresponding to the water level reached at mean discharge (MQ).

4.1.2 Selection of boundary conditions

The project associated with this dissertation aims to develop measures for river boundary conditions in the state of Baden-Württemberg, Germany. To achieve this, two representative rivers in the region were chosen as references for the hydromorphological boundary conditions. These rivers are situated in the South German Scarplands, characterized by steep escarpments. The first river, the Murg, originating from the Black Forest, is classified as a silicate low mountain range river according to the LAWA classification (Umweltbundesamt, 2016). It encompasses sediment ranging from fine to coarse. The second river, the Kocher, is a large river within the low mountain range and originates from the Swabian Jura. Both rivers are part of the Rhine river catchment. The region is known for disrupted hydrological patterns (Leibundgut et al., 2002), disturbed sediment balance, and colmated river beds (Seitz, 2020). Morphological changes in these rivers typically occur at bankful discharge, often corresponding to HQ2 (two-year return period), as observed in previous projects at IWU. The dissertation primarily focuses on comparing various in-stream structures for creating deep scours. To streamline the study, the hydromorphological boundary conditions were kept constant within a single setup, primarily due to the time-intensive nature of morphodynamic experiments and the requirement for multiple replications to ensure reliability. The hydraulic boundary conditions were selected to be at HQ2, which is often associated with bankful discharge and the highest bed shear stresses and morphodynamically active conditions. Moreover, a return period of two years could minimize the maintenance efforts as the flow can erode additional sediment every two years. Specifically, clear-water scour conditions were chosen for morphodynamic conditions, with the sediment size determined accordingly. The derivation of the boundary conditions is explained subsequently.

The hydraulic boundary conditions were derived upon the above mentioned rivers at the gauging stations Schwarzenberg (Murg) and Kocherstetten (Kocher) as detailed in table 4.1. Discharge-water level curves for these stations were obtained from HVZ BW (`https://www.hvz.baden-wuerttemberg.de/`) and are illustrated in figure 4.2. For both the experimental and numerical model, hydraulics were scaled by 1:25 according to Froude similitude law. This scale was chosen to align with the capabilities of the laboratory's experimental facilities and to ensure the hydraulic conditions remain within the limits of hydromorphological similitude. The flume width is 79 cm, allowing the representation of the river Murg with 71% of its 28 m width and the river Kocher at 100% of its 19 m width. The slope was selected as 0.003, an average value derived from both river sections.

Table 4.1: Examples of two representative rivers in the South German Scarplands.

	Murg (Schwarzenbach)	Kocher (Kocherstetten)
river width	28 m	19 m
flume width	0.79 m	0.79 m
river width (1:25)	1.12 m	0.76 m
displayed width	71 %	100 %
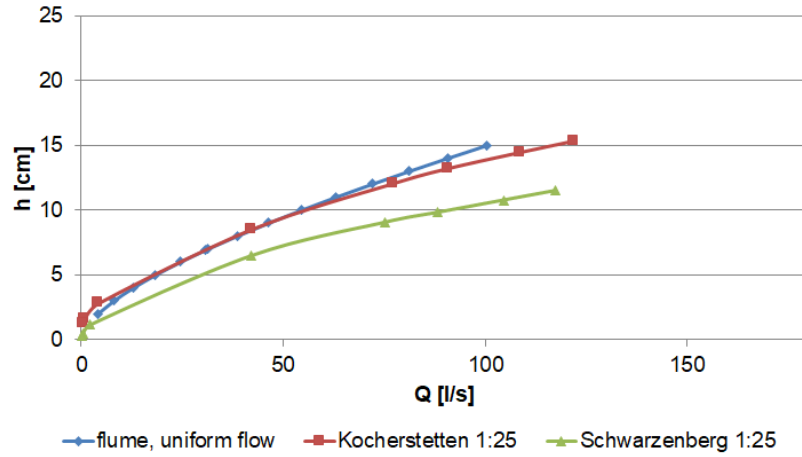
Figure 4.2: Scaled discharge-waterlevel curves for the gauging stations Schwarzenberg and Kocherstetten and uniform flow in the flume.

Assuming uniform flow conditions, the discharge, water level, and size of the uniform sediment in the flume were iteratively calculated according to Froude similitude. Assuming a d_{50} of 3.13 mm and a d_{90} of 3.2 mm, and applying the Strickler formula, a k_{st} value can be determined as follows:

$$k_{st} = 26/d_{90}^{1/6} = 26/0.0032^{1/6} = 68 \tag{4.1}$$

Hence, the mean flow velocity is as well iteratively calculated, here assuming a flow depth of 6.9 cm:

$$u_0 = k_{st} \cdot R_h^{2/3} \cdot I_o^{1/2} = 68 \, m^{1/3} \cdot (0.059 \, m)^{2/3} \cdot 0.003^{1/2} = 0.56 \, m/s$$
where
$$R_{hy} = \frac{b \cdot h}{b + 2h} = \frac{0.79 \cdot 0.069}{0.79 + 2 \cdot 0.069} = 0.059 \, m$$
$$I_o = 0.003 \tag{4.2}$$

The discharge is then:

$$Q = u_0 \cdot A = 0.56 \, m/s \cdot 0.79 \, m \cdot 0.069 \, m = 30.7 \, m^3/s \tag{4.3}$$

To achieve clear-water scour conditions a common assumption is:

$$U_0/U_c \approx 0.9 \tag{4.4}$$

But most formulas for critical velocity do not cover all relevant parameters and they can only be seen as a first approximation (Gehrig, 1954). Therefore, the Shields diagram based on a shear stress approach was used to ensure conditions with no movement. First, the bed shear stress is calculated as:

$$\tau = \rho_w \cdot g \cdot R_{hy} \cdot I_0 = 1000 \, kg/m^3 \cdot 9.81 \, m/s^2 \cdot 0.059 \, m \cdot 0.003 = 1.72 \, N/m^2 \tag{4.5}$$

The shear velocity u^* is then calculated as:

$$u^* = \sqrt{\frac{\tau}{\rho_w}} = 0.042 \; m/s \tag{4.6}$$

The beginning of sediment transport can then be derived from the Shields diagram with the grain-related Reynolds number Re^*

$$Re^* = \frac{u^* \cdot d_m}{\nu} = \frac{0.042 \, m/s \cdot 0.00313 \, m}{10^{-6} \, m^2/s} = 130 \tag{4.7}$$

and the grain-related Froude number Fr^*

$$Fr^* = \frac{u^{*2}}{\rho' \cdot g \cdot d_m} = \frac{(0.042 \, m/s)^2}{\left(\frac{2650 kg/m^3 - 1000 kg/m^3}{1000 kg/m^3}\right) \cdot 9.81 \, m/s^2 \cdot 0.00313 \, m} = 0.034 \tag{4.8}$$

The Shields diagram shows that under the taken assumptions, no movement is to be expected. This was also confirmed by visual observations in preliminary experiments in the physical model. Consequently, the hydraulic and morphodynamic boundary conditions are selected as follows:

Table 4.2: Hydraulic Boundary conditions of the physical model experiments

	Q	h_0	u	Fr	Re
Murg (HQ2)	127 m^3/s	1.62 m	2.8 m/s		
Murg 1:25	40.5 l/s	6.48 cm			
Murg total width	42.3 l/s	6.48 cm	0.82 m/s		
Kocher (HQ2)	186 m^3/s	2.12 m	4.62 m/s		
Kocher 1:25	59.5 l/s	8.48 cm			
Kocher total width %	42.3 l/s	8.48 cm	0.63 m/s		
this dissertation	30.7 l/s	6.9 cm	0.56 m/s	0.68	132160

To achieve the morphodynamic boundary conditions a uniform sediment (σ_g = 1.3) with a d_{50} of 3.13 mm and ρ_s of 2.65 g/cm^3 was selected. The sediment grading curve is shown in figure 4.3.
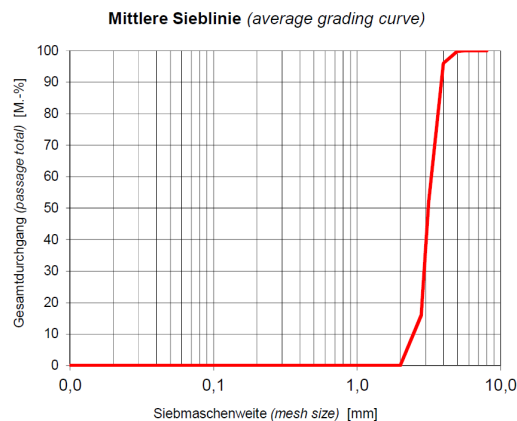
Figure 4.3: Average sediment grading curve of the used sediment of Holcim (Süddeutschland) GmbH.

4.2 Physical Model experiment

4.2.1 Experimental setup and procedure

The physical model experiments were conducted in a 8 m long and 0.79 m wide flume with a slope of 0.003, at the Theodor-Rehbock-Laboratory (TRL) of Karlsruhe Institute of Technology (KIT). This flume is divided into three parts: an upstream fixed and flat bed, a sediment pit with movable bed that contains the measurement section, and a downstream fixed and flat bed (see figure 4.4). The discharge originates from an upstream tank, passes through a flow straightener and surface waves are calmed using a wave board. The sediment pit, which is located at 3.7 m downstream of the flume entrance, is equipped with three ultrasonic sensors for continuous water level measurement. On the opposite side of the visualization window, markers and a camera are shown as part of the Structure from Motion setup. To ensure equal roughness conditions, the fixed bed is coated with sediment of the same size as in the sediment pit. At the downstream end of the flume a liftable tailgate is installed to control the flow at the beginning and the end of the experiments. Sediment is collected in a tank downstream of the flume.
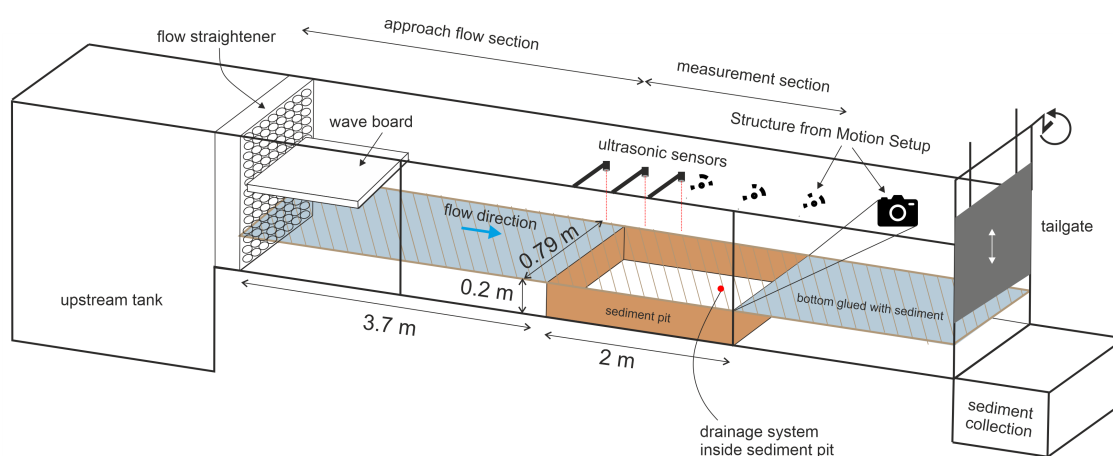
Figure 4.4: Experimental setup of the clear-water scour experiments.

A detailed experimental procedure was implemented to ensure consistent starting and ending conditions for each experiment. Dry sediment was initially introduced into the flume to achieve uniform packing density at the experiment's start. Using a sprinkling machine, the sediment was gradually moistened until saturation. A protection plate covered the saturated sediment, and the water level was slowly raised until reaching the target value without activating the pump. Subsequently, the inflow rate was gradually increased, and the tailgate was simultaneously lifted to maintain the water level. Subsequently, vertical lamellas positioned at the downstream end of the flume assumed the role of maintaining the downstream water level at the specified target value. The inflow rate was measured with an electromagnetic flow meter with an accuracy of +/- 0.1 l/s. When the desired discharge and water level was reached, the protection plates were removed carefully. Upon reaching the hydraulic boundary conditions, the experiment formally started and the scouring process was documented. Once equilib-

rium was reached and the experiment was stopped, the pump was slowly shut down and to maintain the water level the tailgate gradually closed. The water was drained out of the flume through a drainage system in the bottom of the flume over several hours to prevent any more sediment motion and preserve the existing bed morphology.

The physical model experiments focus on the measurement of the bed morphology (chapter 4.2.2) and the water level (chapter 4.2.3), but also sparse 2D velocities (chapter 4.2.4) were measured for later comparison with the numerical results.

4.2.2   Measurement of the bed morphology: Structure from motion (SfM)

For capturing the bed morphology, a Structure from Motion approach in combination with a MATLAB analysis was used as shown in figure 4.5.
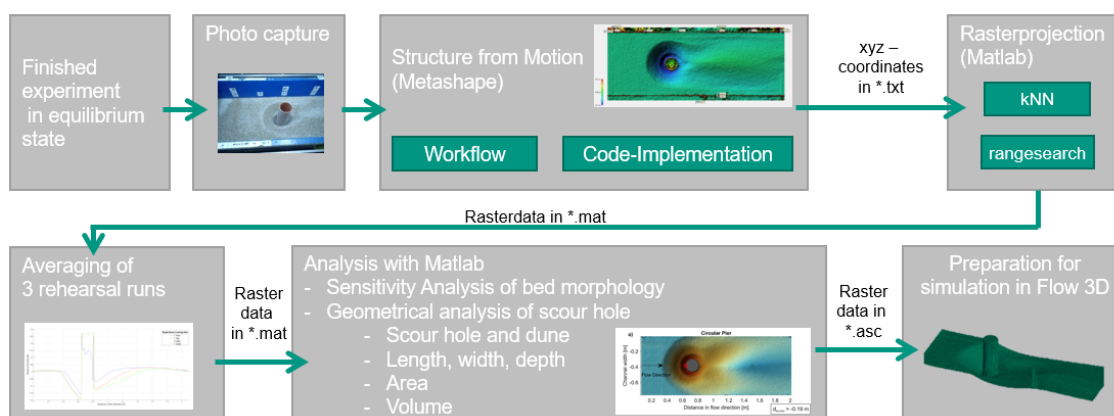
Figure 4.5: Workflow of the analysis of the bed morphology data.

Structure from Motion (SfM) is a photogrammetric technique capable of deriving a three-dimensional topography from two-dimensional images (Morgan, Brogan, & Nelson, 2016). The measurement of the bed morphology was conducted under equilibrium conditions by stopping the flume experiment and slowly draining the water through holes in the flume bottom. This drainage process, lasting approximately 2 hours, was designed to prevent additional sediment movement. It was also tested whether the sediment settles due to the drainage, but could be excluded. The measurement area was illuminated from above with two LED spots with diffusive lights. The lights were installed in opposite directions at both ends of the measurement area and positioned to reduce shadowing of the structures on the bed. This is especially important to improve the accuracy of the SfM algorithm. The sediment consisted of materials of different color, which is optimal for the detection by the SfM algorithm. The implemented structures were made of grey, smooth PVC that produced reflections when illuminated with a light. The SfM algorithm was not able to detect the parts where reflections were visible and moreover showed problems detecting surfaces that are vertical to the bed. Therefore, the surface of the structures was sanded and a square pattern was sprayed onto the surface as shown in figure 4.6, which significantly improved the detection of the structures in the SfM procedure.
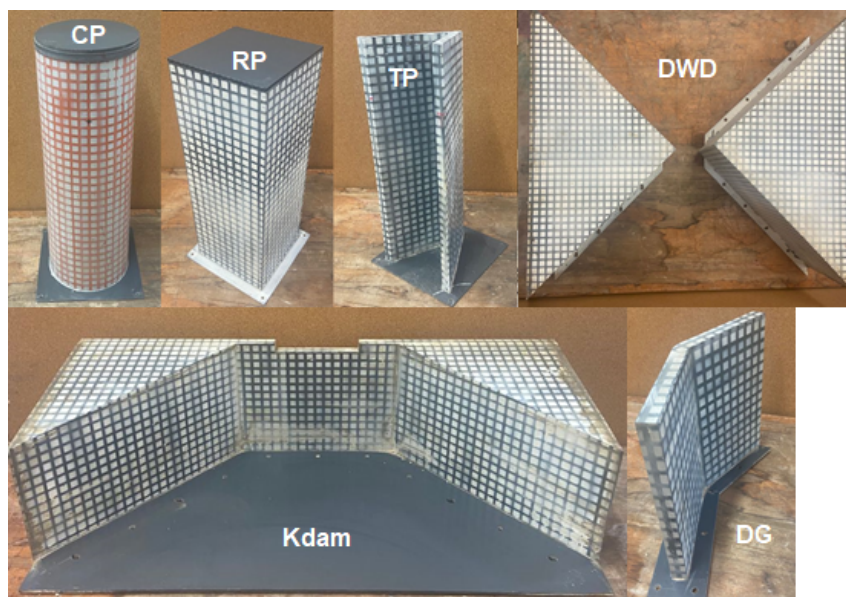
Figure 4.6: Investigated structures with sanded surface and a sprayed square pattern for the improvement of the detection of the Structure from Motion algorithm.

Between 250 to 300 photographs were systematically taken, following a prescribed procedure. The first set captured images from directly above, at a 90° angle to the bed surface, with an 80% overlap in three rows across the entire measurement area. This procedure was repeated at a 45° angle to the bed surface. Additionally, circular photos were taken around the structures, varying the distance from the bed. Some photos providing an overview of the flume were also taken. Ten markers were placed inside the flume to ensure visibility in various photos, enabling the algorithm to detect their positions. The left side of the flume at the beginning of the measurement area served as the origin of the coordinate system (x|y|z = 0|0|0).

The Agisoft Metashape software was employed to transform the images into a 3D point cloud (Metashape, 2020). The first step in the post-processing of the data in Agisoft was loading in the images. A local coordinate system was implemented within the 3D model of the flume. Subsequently, markers in the flume were detected and used to calibrate the orientation and distances of the 3D point cloud. A bounding box set the limits of the measurement section and defined the data for export. An additional algorithm densified the sparse 3D points into a dense 3D point cloud, exportable in *.xyz format or convertible into a Digital Elevation Model (DEM). For streamlined analysis in Agisoft Metashape, a Python script was programmed to execute all the aforementioned steps automatically. Around 2.1 billion points could be detected in the measurement section of 2.1 m x 0.79 m. Agisoft Metashape provides an internal sensitivity analysis where the mismatches between the markers and the 3D point cloud after transformation is shown. An accuracy of +/- 1 mm could be achieved. Three experimental runs were done for each investigated structure to be able to quantify the sensitivity of the experimental setup, which is discussed in chapter 5.2.1.

The data was further processed in Matlab. The 3D point cloud showed an arbitrary distribution of x-y points, so the first step was to interpolate the z-points on a designated raster of 1 mm.

Two different algorithms were tested for this transformation. The first algorithm employed a rangesearch approach, which searched for point data around every raster point within a radius of 0.7 mm. It then averaged all points detected within this range, projecting the mean value onto the prescribed raster. The second algorithm was a kNN (k-nearest neighbors) approach, which identified the k nearest neighbors of a raster point and calculated their mean value. Both algorithms exhibited only marginal differences, with slightly higher variations observed in regions with steep slopes, such as the slopes inside the scour holes as shown in figure 4.7 a). The absolute distances were below 0.5 mm, significantly smaller than the d_{50}. Consequently, both algorithms were deemed suitably accurate. The rangesearch algorithm was ultimately chosen for its superior representation of the slopes within the scour holes, as demonstrated in figure 4.7 b).
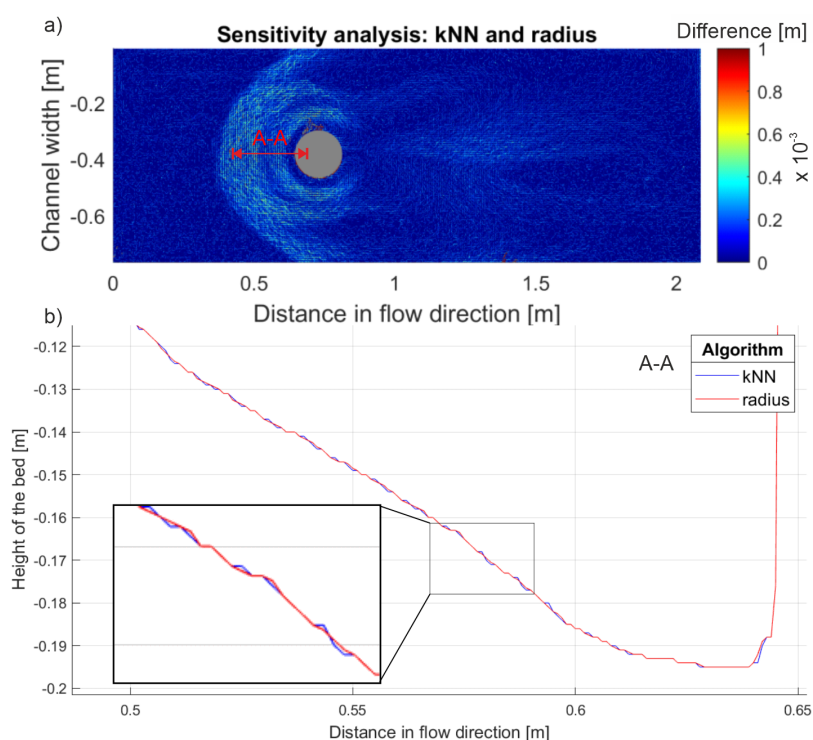
Figure 4.7: Comparison of the kNN and rangesearch algorithm for the translation of an arbitrary 3D point cloud to a raster.

The created data was used to compare the three different experiments and a sensitivity analysis could be done (see chapter 5.2.1). The geometrical characteristics of the scour hole such as scour hole length, width and depth, as well as the area and volume were retrieved through Matlab. The data was further transformed into a raster data set in ASCII format that could be used as a simulation basis for the numerical simulations (see chapter 4.3).

4.2.3 Measurement of the water level: ultrasonic measurement

The water level was measured using ultrasonic sensors UM18-212 produced by Sick AG. The sensors' working principle is based on a sound transit time measurement. Each of them emits an ultrasonic sound pulse and measures the time it takes for that pulse to travel from

the sensor to a sound-reflecting object and back. From this transit time the distance to the object can be derived by calculation (distance = speed of sound * transit time/2). This kind of sensors was originally developed to measure the distance to solid objects. However, with the sensor oriented perpendicularly to a flat water surface, this surface behaves comparable to a solid object in terms of sound reflection because no reflection losses are generated (angle of incidence = angle of reflection). A wavy and turbulent water surface can cause scattering of the reflected pulse which may therefore not reach the receiver at all, hence decreasing quality and confidence of the measurements. The accuracy of the sensors is given in the data sheet as +/- 1 % of the measured value. The sensors were located 5 h_0 and 8.8 h_0 upstream and 5 h_0 downstream of the structure.

4.2.4 Measurement of the flow velocity: Laser Doppler Anemometry (LDA)

The flow velocities were measured with Laser-Doppler-Anemometry (LDA). The LDA is a non-intrusive, optical measurement system for the measurement of flow velocities in fluids. In comparison with other flow velocity measurement devices the LDA has a high temporal resolution. The measurement principle is based on the characteristics of laser light. A laser delivers monochromatic light with a coherent phase relationship. The wavelength is precisely defined and the properties of light allow stationary interference phenomena. A laser beam is split into two beams, which are guided so that they cross at a point in the fluid to be measured. This intersection area represents the measurement volume. Through overlapping of the two coherent laser beams an interference pattern is created. When a particle enters the measurement volume and travels through the bright and dark areas of the interference pattern, it reflects and scatters the emerging light. The receiver detects changes of the light intensity and the velocity of the particle can be calculated on the basis of the distance between the interference pattern. The velocities are measured normal to the interference pattern. For the measurement of the second velocity component a second laser beam with another wave length is used and is then converted 90° to the previous orientation.

The LDA was mounted on a carriage on top of the flume, that could be driven to a specific point (x|y|z) inside the measurement section. With this setup the streamwise and lateral velocity components could be measured. As the water surface was wavy and the laser cannot measure through an inclined water surface as the laser beams do not intersect anymore, a small glass plate was used to create a flat and transparent surface at the phase transition of air to water as shown in figure 4.8. This glass plate modifies the angle of incidence and reflection at two points: the phase transition from air to the glass plate and from the glass plate to the water. The refraction at the two phase transitions changes the distance between the laser lens and the measurement volume. The real distance can be calculated using Snellius' law:

$$n_1 \cdot sin\,\delta_1 = n_2 \cdot sin\,\delta_2 \qquad (4.9)$$

where δ_1 is the angle of incidence and δ_2 the angle of refraction. n_1 and n_2 are the refractive indices, which are dependent on the medium.
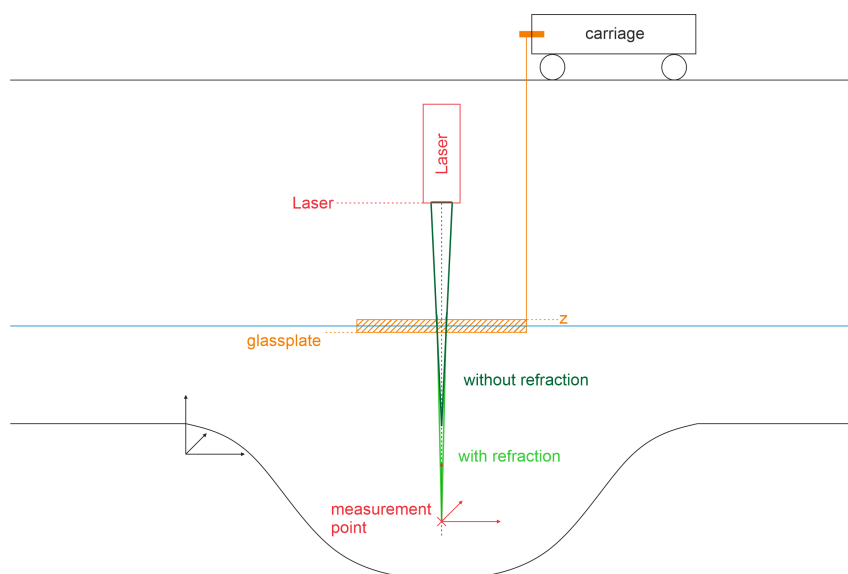
Figure 4.8: Laser mounted on a movable carriage looking through a glass plate into the water column with indicated refraction of light at the glass plate.

The Laser used in this setup was a FlowExplorer by Dantec Dynamics with the technical specifications given in table 4.3. Further details are given in the manual (*BSA Flow Software Version 4.10. Installation and User's Guide*, 2006).

Table 4.3: Technical specifications of the FlowExplorer by Dantec Dynamics.

Light wavelength	red component: 61 nm
	green component: 532 nm
laser output power	red component: 148 mW
	green component: 111 mW
focal length of the length	300 nm
measurement volume	0.1 mm * 1 mm * 1 mm

The laser beam is reflected at small particles inside the fluid and send back to the receiver. The fresh water in the flume did not have enough particles, therefore an artificial seeding was applied. It consists of a mixture of glass flour and glass microspheres and is applied directly upstream of the measurement point, with a point dispenser. The velocity data can be acquired in two different modi: a maximum acquisition time or a maximum number of samples. Pretests showed that especially inside the scour hole where the velocity magnitude is around zero, the data rate was significantly lower. This is due to the fact that particles spread slower here and pass the measurement volume. Therefore a constant sample number was selected instead of a constant measurement time. The LDA manual suggests 1000-2000 samples per position. This suggestion was verified by own measurements. After 2000 samples the average value does not change more than 2 %.

4.2.5 Determination of equilibrium scour depth

The results of this subchapter were already published in Kannen, Seidel, and Franca (2022).

As described in chapter 3.4.5, there has not been a universally accepted standard for determining the equilibrium time in scour experiments, irrespective of the structure's type. The choice of the presented criterion depends mainly on the research question. In the design of a scour protection for a bridge pier, time development formulas and predictor equations are suitable, as a guideline for engineers in practice. When comparing hydraulic structures in rivers the effect of different geometrical characteristics needs to be considered, therefore an equilibrium criterion is an obvious choice. Here within, the selection of the correct geometrical characteristics of the structure remains a challenge. The pier diameter is usually the geometrical parameter for piers as used in Melville and Chiew (1999). The foundation length was used by Coleman, Lauchlan, and Melville (2003) to characterize an abutment. Both structures are emergent and the blocked width of the structure is used as a geometric parameter. Submerged structures have not been investigated with this criterion yet.

Derivation of an equilibrium criterion

As this research focuses on the comparison of different structures a generally applicable equilibrium for all types of structures is needed. Therefore a new criterion is derived in this chapter and tested for the structures within in this work. An equilibrium criterion is derived on the basis of the definition of a hydraulically significant length D, that describes the geometric characteristics of the respective structure. In literature there are several definitions available that account for length scales to describe a hydraulically significant length of a structure. Some approaches are based on area metrics (like wetted area, frontal area, and planform area) while others utilize length measures (such as wetted perimeter and hydraulic radius). A more recent advancement was proposed by Euler and Herget (2012) who introduced the equivalent diameter D_{equ}, calculated as $D_{equ} = \sqrt{2(w_s \cdot h_s)/\pi}$, which accounts for an obstacle's width w_s and height h_s. The newly derived concept includes the idea of the different flow types (see figure 3.3). The width of the structure w_s is included to account for the blocked area for emergent structures. Additionally, the formula is extended by a factor to account for the submergence of the structure which consists of the relation of height of structure h_s to the water depth h_0. The hydraulically significant length scale D is then defined as:

$$D = w_s \cdot \frac{h_s}{h_0} \tag{4.10}$$

The criterion for time to equilibrium t_e is then based on the criterion of Melville and Chiew (1999) who define equilibrium time as the time when the rate of scour reduces to 5 % of the pier diameter in a 24 h period. The pier diameter is replaced by the newly derived hydraulically significant length scale D and leads to:

$$\frac{d(d_{se})}{dt} \geq \frac{0.05 \, w_s \cdot \frac{h_s}{h_0}}{24h} \tag{4.11}$$

For pier-like structures h_s equals h_0 and hence $D = w_s$, leading to the criterion proposed by Melville and Chiew (1999). The selection of 5 % of the hydraulically significant length still stays an arbitrary choice but has the advantage that the accordance of this criterion and Melville and Chiew (1999) enables a comparison to literature studies that use this criterion. The equilibrium criteria for the different structures in this study are summarized in table 4.4. To determine the equilibrium time of the experiment preliminary tests were performed where the scour depth was measured over time at the deepest point with a point gauge.

Table 4.4: Equilibrium criteria for the structures used in this study.

	$w_s[cm]$	$h_s[cm]$	$h_0[cm]$	D	equilibrium criterion $[mm/24h]$
CP	15.8	6.9	6.9	15.8	7.9
RP	15.8	6.9	6.9	15.8	7.9
TP	15.8	6.9	6.9	15.8	7.9
DWD	31.6	2.8	6.9	25.6	12.8
DG	26.9	2.8	6.9	10.9	5.5
Kdam	79	2.8	6.9	32.1	16.0

4.2.6   Abstraction of trees in hydromorphological physical model experiments

To expand the biological functionality of the deep pool the addition of a shelter was tested. The purpose of this shelter is further explained in chapter 6.3.1 and this chapter shall focus on the abstraction of the shelter in the physical model experiment. A deceased tree served as the shelter in this study. Various methods exist for modeling vegetation in physical model experiments, with the approach varying based on the specific case (examples for atmospheric flows: Chen, Chan, and Li (2012), Aubrun et al. (2005), and Gromke and Ruck (2018); examples for water flows: Ricardo, Franca, and Ferreira (2016), Juez et al. (2019), and Curran and Hession (2013)). Two aspects needed to be considered for the current case:

- When a tree, complete with trunk, large and small branches and leaves, falls into a river, continuous water flow and periodic flooding strip the tree off its leaves and minor branches, leaving behind only its main trunk and larger branches. This transformation is similar to a living tree with and without foliage. Therefore, approaches for trees with and without foliage are taken into account.

  - For plants with foliage, the flow around them is largely influenced by viscous drag occurring at their leaves and minor branches, as outlined by Järvelä (2004). Such dynamics can be emulated using methods designed for bushy vegetation. In contrast, the flow dynamics around plants without foliage are dominated by form drag at the main stem and larger branches, as highlighted by Nepf (1999).

  - Common representations for vegetation with foliage include arrays or clusters of tiny cylinders (as seen in López and García (2001) and Bennett, Pirim, and Barkdoll (2002), porous panels (Ventres-Pake et al., 2020), glass plates (Eiff et al., 2019), or actual plants (Wunder, Lehmann, & Nestmann, 2011). However, key processes like the streamlining or reshaping of vegetation when subjected to flow are challenging to capture using these methods (Järvelä, 2004).

- Acrylic tubes and brass rods to simulate mangrove trees (Maza et al., 2017) and combinations of PVC tubes for the representation of emergent trees (Ricardo, Franca, & Ferreira, 2016; Zhang, Rutherfurd, & Ghisalberti, 2020) are common for vegetation without foliage. Friedrich et al. (2022) noted that in most studies, large wood elements are typically simulated with smooth cylinders crafted from metal or wood, and these models often assume a static bed condition.

- Transition from rigid bed setting to movable bed setting

  - Many of the existing hydrodynamic models for vegetation do not align well with morphological experiment needs. Given the changing bed morphology, it is challenging to anchor vegetation patches securely, either from the base or the top, as they must adapt to the bed's movements. Moreover, flow dynamics can vary, with water sometimes flowing over, under, or through the plant structures. While there have been initial attempts to model vegetation within mobile bed conditions, as seen in the works of Chen, Chan, and Li (2012) and Yagci et al. (2016), these models haven't adequately addressed the challenges associated with fluctuating bed elevations and the implications of firmly fixing vegetation elements.

Experimentally examining flows in vegetated rivers presents several challenges: cultivating natural vegetation for laboratory use is resource-intensive; and currently, there are no established proxies for vegetation that replicate similar mass, momentum, and energy exchanges. In response, a technique previously used in aerodynamic modeling of flow around trees in scaled-down wind tunnel research, as seen in Gromke (2011, 2018), was adapted for hydromorphological applications. In Gromke (2011, 2018), a method was devised for modeling vegetation, especially trees, in atmospheric flows. This approach represents a plant as an open porous medium. Unlike typical engineered structures, vegetation, such as bushes and tree canopies, allows fluid to pass through because of its porosity, which consists of a complex structures of trunks, branches, stems, and leaves. In general, solid structures experience form drag, which is the pressure difference from upstream to downstream. However, in the flow through porous media, skin friction becomes a significant factor due to the large volume specific surface area and cannot be neglected as in non-porous media flow. Still, porosity isn't the only determinant for the flow resistance of a porous material. As noted, permeability, a key fluid dynamic attribute of the porous vegetation model, relies on the roughness, form, quantity, configuration, and size distribution of the pores, in addition to the volume proportion of the pores. To account for the previous mentioned aspects, the plant's resistance is represented by examining the flow through a porous medium. The porous media flow is hereby characterized by a pressure loss coefficient λ as shown in figure 4.9 and is calculated as:

$$\lambda = \frac{\Delta p_{stat}}{p_{dyn}d} = \frac{p_{luv} - p_{lee}}{1/2\rho u^2 d}. \tag{4.12}$$
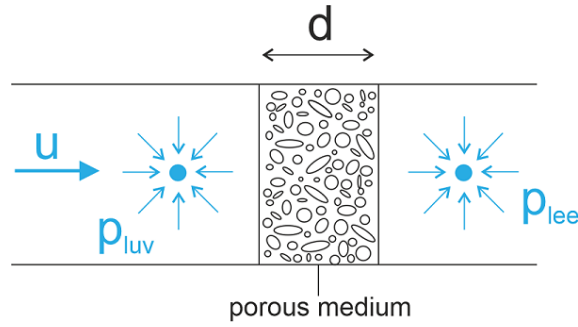
Figure 4.9: Aerodynamic description of the flow through a porous medium under forced-flow conditions (image courtesy of Christof Gromke).

To ensure the transferability of scaled physical model results to full-scale prototype, dynamic similarity is required. This similarity exists when the momentum absorbed by the vegetation F_D is proportional to the momentum of the undisturbed approach flow F_M across both scales (as per eq. 4.13, Gromke (2009)).

$$\left[\frac{F_D}{F_M}\right]_{rs} = \left[\frac{F_D}{F_M}\right]_{fs} <=> \left[\frac{\Delta p A_{cs}}{p_{dyn} A_{cs}}\right]_{rs} = \left[\frac{\Delta p A_{cs}}{p_{dyn} A_{cs}}\right]_{fs} <=> \left[\frac{\Delta p}{p_{dyn}}\right]_{rs} = \left[\frac{\Delta p}{p_{dyn}}\right]_{fs}$$
(4.13)

The plant's criterion incorporates the pressure loss coefficient, which depicts the momentum absorption attributed to both viscous and form drag in porous media. By integrating equation 4.12 into equation 4.13, it is deduced that the proportion of pressure loss coefficients between the full scale ($_{fs}$) and the reduced scale ($_{rs}$) is equivalent to the model scale M as expressed in equation 4.14 (Gromke, 2009).

$$\frac{\lambda_{fs}}{\lambda_{rs}} = \frac{d_{rs}}{d_{fs}} = M$$
(4.14)

In Gromke (2011, 2018), trees were simulated using a lattice cage structure filled with filamentous synthetic wadding material, as shown in figure 4.11. Trunks were omitted from this modeling technique, as their influence on momentum absorption was deemed minimal compared to the tree crown. The objective was to represent tree crowns with varying foliage densities, aligning with different porosities P_{Vol}, and thereby create permeabilities spanning the spectrum found in natural tree crowns. Grunert, Benndorf, and Klingbeil (1984) showcased pressure loss coefficients for multiple vegetation forms under forced-flow circumstances, as illustrated in figure 4.10.

Given the model scale, it is possible to determine pressure loss coefficients for the model vegetation. Standard model scales in scaled-down wind tunnel experiments typically range from 1:100 to 1:500. A filamentous wadding material is employed, enabling easy modulation of porosities. Gromke (2012) conducted forced convection flow measurements to ascertain the pressure loss coefficient of the filamentous synthetic wadding material across varying porosities. As indicated in figure 4.13, the pressure loss coefficient λ remains constant across a flow velocity span from U_0 = 2 m/s to 7 m/s, registering at $\lambda = 80\ m^{-1}$ for P_{Vol} = 97.5 % and 200 m^{-1} for P_{Vol} = 96 %.
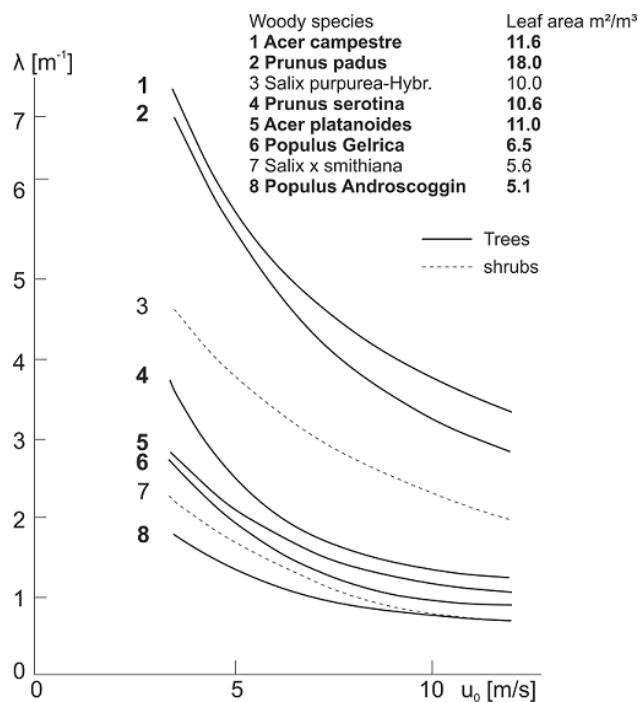
Figure 4.10: Pressure loss coefficients λ for different central european tree and shrub species dependant on the approach flow velocity U_0 under forced-flow conditions. Adapted from Grunert, Benndorf, and Klingbeil (1984).

Two primary distinctions set hydrodynamic models apart from aerodynamic ones. Firstly, (I) the fluid utilized is water, which has a density of three orders of magnitude greater than air. Secondly, (II) the typical model scales range from 1:10 to 1:50, considerably larger than those in aerodynamics. Factor (I) affects the material selection for the wadding material since it can be compressed more easily under the increased absolute static and dynamic pressure of water compared to air. Factor (II) guides the determination of the pressure loss coefficient, and consequently, the porosity of the vegetation patch. Adjusting the pressure loss coefficients from Grunert, Benndorf, and Klingbeil (1984) to fit a model scale of 1:25 (common for hydromorphological flume tests) or 1:200 (standard in wind tunnel experiments) results in the model scale pressure loss coefficient outlined in table 4.5. Porous materials with a pressure loss coefficient λ ranging from 80 to 600 m^{-1} have been employed and discussed in Gromke (2011, 2018) studies. For hydromorphological scaling, porosities with pressure loss coefficients spanning 5 to 75 m^{-1} need to be identified and are derived here.

Table 4.5: Pressure loss coefficients λ for different model scales in hydromorphological and aerodynamic physical model experiments.

	Full scale	Reduced scale hydromorphology (scale 1:25)	Reduced scale aerodynamics (scale 1:200)
with foliage	$1...3\ m^{-1}$	$25...75\ m^{-1}$	$200...600\ m^{-1}$
without foliage	$0.2...0.6\ m^{-1}$	$5...15\ m^{-1}$	$40...120\ m^{-1}$

An aerodynamic testing apparatus was developed, comprising a ventilator, a conical transition section, and a 10 cm diameter pipe (total length of 3 m), as depicted in figure 4.11. To guarantee parallel flow lines, a sequence of honeycombs was placed within the transition section. Verification of the appropriate inflow conditions can be seen in the velocity profiles illustrated in figure 4.12. A few meters from the inlet, a transparent measurement section, made of a perplex tube, was incorporated. The specific vegetation patch was fixed between two grids, as shown in figure 4.11. The vegetation patch was made of a filamentous wadding material called EheimFix, typically utilized as a prefilter in aquatics. This material was evenly distributed by hand within the lattice cage. The exit section extended for 2 m upstream and downstream of the vegetation patch. Pitot-static tubes were positioned to measure the air's static pressure difference. Using these readings, the pressure loss coefficient λ was calculated as per eq. 4.12.
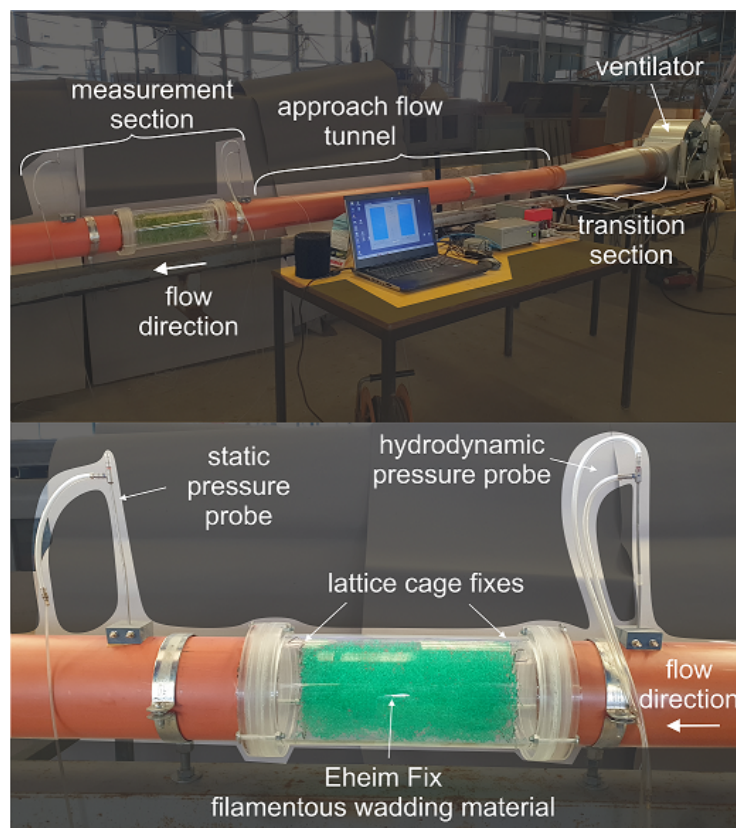
Figure 4.11: Experimental micro wind tunnel for the determination of pressure loss coefficients under forced flow conditions for different porosities.
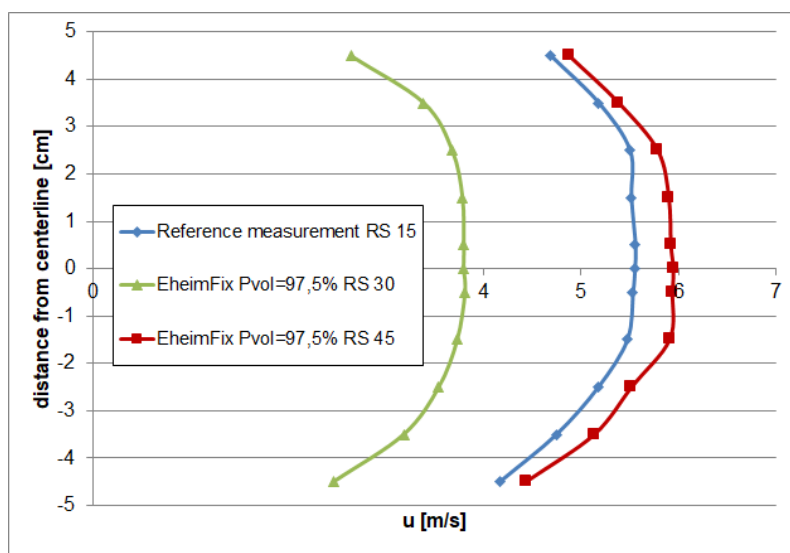
Figure 4.12: Velocity profiles for different rotational speeds (RS) of the ventilator for the measurement without a wadding material in the measurement section and with wadding material EheimFix with a porosity of 97.5 % in the aerodynamic micro wind tunnel. The RS values were chosen randomly, the purpose is to show the appropriate flow conditions in the test rig.

The desired pressure loss coefficient λ for scaled-down hydromorphological experiments can be attained by producing samples with varying porosities and their corresponding pore volume fractions P_{Vol}, using the synthetic wadding material EheimFix. In the testing rig, three distinct pore volume fractions P_{Vol} (97.5 %, 99 %, and 99.25 %) were evaluated to derive the pressure loss coefficients for trees, both with and without foliage, as outlined in table 4.5. Figure 4.13 indicates that the pressure loss coefficient is velocity-dependent, nearing a constant value for higher flow velocities. To maintain dynamic similarity between full-scale and reduced-scale experiments, only velocities within this constant range should be utilized. The pressure loss coefficient derived from Gromke (2011) for a pore volume fraction of 97.5 % was successfully replicated, yielding a value of 80 m^{-1} within this stable zone. This value is at the upper limit of the range for a tree with foliage (refer to table 4.5) and can represent trees with foliage. A pore volume fraction of 99 % has a pressure loss coefficient of 25 m^{-1}, aligning closely with the 5 - 15 m^{-1} range for a tree without foliage. Since both values are at the upper end of the range, these pressure loss coefficients reflect a conservative approach. For small pressure loss coefficients, a deviation by a factor of 2 is acceptable. However, higher pore volume fractions, such as 99.25 %, resulted in compression of the wadding material, as evidenced by the rise in λ with increased inflow velocities, making them unsuitable for application. Table 4.6 summarizes the selected pore volume fractions P_{Vol} and the associated pressure loss coefficients λ that were applied in the experiments. The experimental setup with the application of the filamentous synthetic wadding material as a tree is shown in figure 4.14. The selection of tree sizes is specified in chapter 6.3.1. The lattice cage was fixed at the flume walls with a cord, so that free movement of the cage on the movable bed was possible.
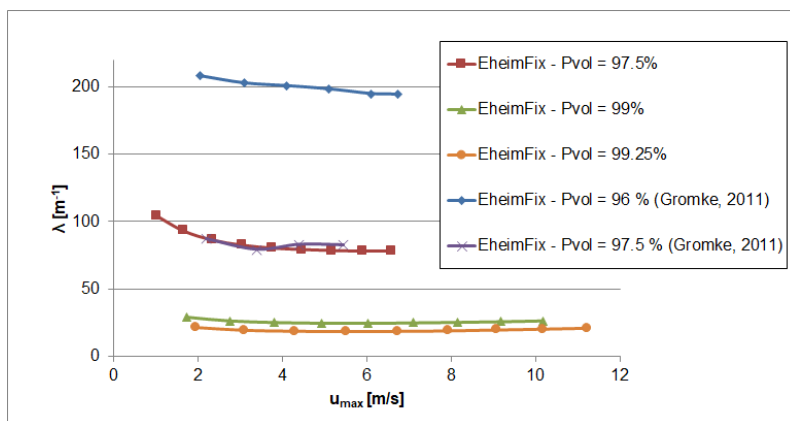
Figure 4.13: Pressure loss coefficients for different porosities of the filamentous wadding material EheimFix determined in the aerodynamic micro wind tunnel.

Table 4.6: Recommendations for pressure loss coefficients in hydromorphological modelling.

	with foliage		without foliage	
	pressure loss coefficient	EheimFix porosity	pressure loss coefficient	EheimFix porosity
full scale (Grunert, Benndorf and Klingbeil (1994))	$\lambda = 1...3\ m^{-1}$		$\lambda = 0.2...0.6\ m^{-1}$	
reduced scale hydromorphology (example 1:25)	$\lambda = 25...75\ m^{-1}$	97.5 %	$\lambda = 5...15\ m^{-1}$	99 %
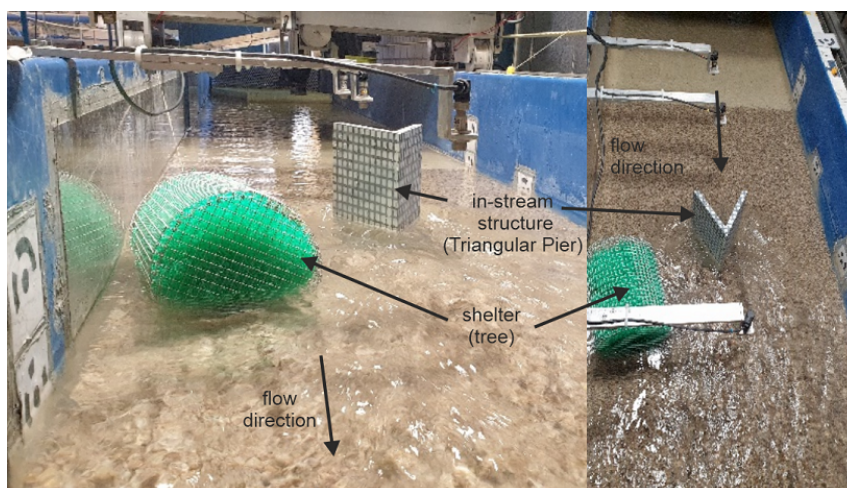
Figure 4.14: Images of the flume experiments with movable bed and implemented in-stream structure as well as the tree-like shelter in form of a lattice cage filled with filamentous wadding material.

4.3 Numerical Model

The physical model experiments which focused mainly on the morphodynamics of the ecological scour were complemented by 3D HN simulations. The simulations were used to analyze the hydrodynamics inside the scour hole in a high spatial resolution. Therefore, the equilibrium bed morphology of the physical model experiments was taken as a geometric boundary condition. Morphodynamic simulations were not performed due to their high complexity and time resources and are proposed to be done in further research. The following chapter is focused on the hydrodynamic simulation part. The simulations were performed with the commercial software package FLOW-3D® HYDRO (Version 2022R2; 2022; https://www.flow3d.com; Flow Science, Inc.). The necessary basics of the software are explained as follows, more details can be found in the manual (Flow Science, 2023).

4.3.1 Basis of 3D hydrodynamic modelling

The mathematical description of fluid flows is based on the continuity equation (eq. 4.15) and the Navier-Stokes-equations (eq. 4.16), which can be derived respectively from the basic principles of continuity of mass and conservation of momentum at a control volume (e.g. Musall (2011), Schlichting and Gersten (2000), and Roberson and Crowe (1993)).

$$\frac{\partial \rho}{\partial t} + \frac{\partial}{\partial x}(\rho u) + \frac{\partial}{\partial y}(\rho v) + \frac{\partial}{\partial z}(\rho w) = 0 \qquad (4.15)$$

The velocity components u, v and w are in the coordinate directions x, y and z.

$$
\begin{aligned}
\underbrace{\frac{\partial u}{\partial t}}_{} &+ \underbrace{u\frac{\partial u}{\partial x} + v\frac{\partial u}{\partial y} + w\frac{\partial u}{\partial z}}_{} = \underbrace{-\frac{1}{\rho}\frac{\partial p}{\partial x}}_{} + \underbrace{G_x}_{} + \underbrace{f_x}_{} \\
\frac{\partial v}{\partial t} &+ u\frac{\partial v}{\partial x} + v\frac{\partial v}{\partial y} + w\frac{\partial v}{\partial z} = -\frac{1}{\rho}\frac{\partial p}{\partial y} + G_y + f_y \\
\underbrace{\frac{\partial w}{\partial t}}_{\text{local acceleration}} &+ \underbrace{u\frac{\partial w}{\partial x} + v\frac{\partial w}{\partial y} + w\frac{\partial w}{\partial z}}_{\text{convective acceleration}} = \underbrace{-\frac{1}{\rho}\frac{\partial p}{\partial z}}_{\text{pressure gradient}} + \underbrace{G_z}_{\text{body force term}} + \underbrace{f_z}_{\text{diffusion term}}
\end{aligned}
\qquad (4.16)
$$

In FLOW-3D® HYDRO, the equations are complemented by terms fulfilling the FAVOR™ method, which describes the fraction of the cell that is filled with fluid as explained in the subsequent subchapter.

4.3.2 The FAVOR™ Method

The discretization of the geometry is based on a structured grid made of rectangular cells. By using a structured grid, geometries can only be displayed by a stepped geometry. To account for this problem the FAVOR™ method is used (Flow Science, 2023). The FAVOR™ (Fractional Area-Volume Obstacle Representation) method computes the area fractions A_x, A_y and A_z on the cell faces and the volume fraction V_F of the open flow. This ensures that boundary cells that intersect with solid surfaces can be calculated partially filled. The additional parameters V_F and A_x, A_y and A_z can block certain parts of the cell. The preprocessor generates an area fraction of each cell by determining the corners of the solid component whether they lay

inside or outside the grid. This implies that each solid component needs to cross at least one grid vertex otherwise it cannot be displayed by the FAVOR™ method as shown in figure 4.15. The area fractions are computed on the basis of the intersection points of the solid component with the face edges and are connected with a straight line.
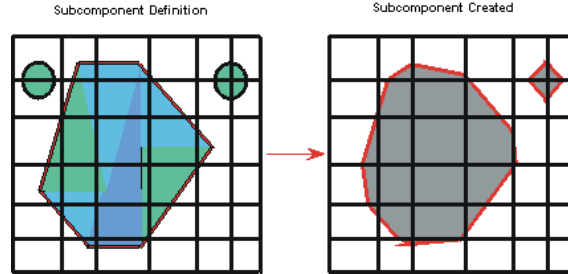
Figure 4.15: Illustration of the application of the FAVOR™ method on a geometric component (image from Flow Science (2023)).

The flattening of the surface in each grid cell neglects edges of the geometry. The severity of falsification of the geometry depends on the discretization. Therefore, different discretization of cell size need to be tested in a sensitivity analysis to ensure the correct description of the flow. Moreover, a shift of half a cell size is advisable to test the discretization of the model geometry (Musall, 2011). The mesh can be made up of different areas with changing cell size. It is to be noted that the boundaries between different mesh sizes need special attention to avoid accuracy problems. To account for this problem, the cell size was doubled/halved at cell size changes (Gabl et al., 2014).

The continuity equation (eq. 4.17) and the Navier-Stokes equations (eq. 4.18) in FLOW-3D® HYDRO (Flow Science, 2023) are then formulated as follows:

$$V_F \frac{\partial \rho}{\partial t} + \frac{\partial}{\partial x}(\rho u A_x) + \frac{\partial}{\partial y}(\rho v A_y) + \frac{\partial}{\partial z}(\rho w A_z) = 0 \tag{4.17}$$

$$
\begin{aligned}
\underbrace{\frac{\partial u}{\partial t}}_{} &+ \underbrace{\frac{1}{V_F}\left\{ uA_x\frac{\partial u}{\partial x} + vA_y\frac{\partial u}{\partial y} + wA_z\frac{\partial u}{\partial z} \right\}}_{} = \underbrace{-\frac{1}{\rho}\frac{\partial p}{\partial x}}_{} + \underbrace{G_x}_{} + \underbrace{f_x}_{} \\
\frac{\partial v}{\partial t} &+ \frac{1}{V_F}\left\{ uA_x\frac{\partial v}{\partial x} + vA_y\frac{\partial v}{\partial y} + wA_z\frac{\partial v}{\partial z} \right\} = -\frac{1}{\rho}\frac{\partial p}{\partial y} + G_y + f_y \\
\underbrace{\frac{\partial w}{\partial t}}_{\text{local acceleration}} &+ \underbrace{\frac{1}{V_F}\left\{ uA_x\frac{\partial w}{\partial x} + vA_y\frac{\partial w}{\partial y} + wA_z\frac{\partial w}{\partial z} \right\}}_{\text{convective acceleration}} = \underbrace{-\frac{1}{\rho}\frac{\partial p}{\partial z}}_{\text{pressure gradient}} + \underbrace{G_z}_{\text{body force term}} + \underbrace{f_z}_{\text{diffusion term}}
\end{aligned}
\tag{4.18}
$$

where:

- V_F is the fractional volume open to flow and

- A_x is the fractional area open to flow in the x-direction, A_y and A_z are similar area fractions for flow in the y and z directions, respectively.

4.3.3 Volume of Fluid (VOF) method

FLOW-3D® HYDRO uses the Volume of Fluid (VOF) method, comprising three key elements: defining the fluid volume, solving the VOF transport equation, and setting free surface boundary conditions. The volume fraction F describes the partial filling of a simulation cell. A value of F=1 equals a completely filled cell and F=0 equals an empty cell. Values 0 < F < 1 show partially filled cells. The transport equation simulating the VOF method is as follows:

$$\frac{\partial F}{\partial t} + \frac{1}{V_F}\left[uA_x\frac{\partial F}{\partial x} + vA_y\frac{\partial F}{\partial y} + wA_z\frac{\partial F}{\partial z}\right] = \frac{\nu_F}{V_F}\left[\frac{\partial}{\partial x}\left(A_x\frac{\partial F}{\partial x}\right) + \frac{\partial}{\partial y}\left(A_y\frac{\partial F}{\partial y}\right) + \frac{\partial}{\partial z}\left(A_z\frac{\partial F}{\partial z}\right)\right] + f_{sF} \quad (4.19)$$

The diffusion coefficient ν_F is defined as

$$\nu_F = C_F \cdot \frac{\nu}{\rho} \quad (4.20)$$

where C_F is the reciprocal of the Schmidt-number S_s and μ is the dynamic fluid viscosity. f_{sF} describes the change in the volume fraction of the fluid by a local fluid source or sink (Musall, 2011).

4.3.4 Initial and boundary conditions and surface roughness

Initial conditions define the solution of different variables at t=0 (Musall, 2011). This can be discharges or water levels at boundaries or inside of the domain. For free-surface flows a water level is a suitable initial condition, so that computational time for filling the model can be saved. The boundary conditions in hydrodynamic models with free water surfaces are often controlled by the discharge entering the domain at the upstream boundary and a water level at the downstream boundary. The surface roughness of the bed and other surfaces inside the fluid domain can be modeled by a designated roughness value k_s. The k_s value is limited to maximum half a cell size to deliver reasonable results.

4.3.5 Turbulence models

Two different models were used to describe the turbulence of the flow. The first model is a Reynolds-averaged model, which statistically averages the turbulence of the flow by using the Reynolds-Averaged-Navier-Stokes-Equations (RANS). The second model Large-Eddy-Simulation (LES), simulates not only the statistical average but also is able to directly solve large eddies and thus can display parts of the turbulent fluctuations of the flow. The turbulence in both approaches is modeled by adding viscous stresses and turbulence quantities to the solution.

Statistical turbulence model: Re-Normalisation Group (RNG/RANS)

As described in equation 2.5, the fluctuations of a velocity field can be divided into an averaged velocity part $\overline{u}$ and a turbulent fluctuating part u', called the Reynolds decomposition. Inserting the Reynolds decomposition of the flow velocities into the Navier-Stokes-equations leads to

the Reynolds-Averaged-Navier-Stokes-equations (RANS). FLOW-3D® HYDRO uses a RNG-k-ε model, which models the Reynolds stresses with two transport equations. The turbulent kinetic energy (TKE) describes the turbulent velocity fluctuations in the flow

$$\kappa_T = \frac{1}{2}\left(\overline{u'^2} + \overline{v'^2} + \overline{w'^2}\right)$$ (4.21)

The turbulent kinetic energy corresponds to a turbulence intensity I of

$$I = \sqrt{\frac{\kappa_T}{\overline{K}}}$$ (4.22)

where $\overline{K}$ is the mass-averaged mean kinetic energy in the domain and $\forall$ is the total volume of the domain.

$$\overline{K} = \frac{\int\limits_{\forall} \frac{1}{2}\rho \cdot \left(u^2 + v^2 + w^2\right) d\forall}{\int\limits_{\forall} \rho \, d\forall}$$ (4.23)

The transport equation of k_T includes the convection and diffusion of turbulent kinetic energy as well as production due to shearing (and buoyancy, which is neglected for this problem) and dissipation due to viscous losses within the eddies.

$$\frac{\partial \kappa_T}{\partial t} + \frac{1}{V_F}\left\{uA_x\frac{\partial \kappa_T}{\partial x} + vA_y\frac{\partial \kappa_T}{\partial y} + wA_z\frac{\partial \kappa_T}{\partial z}\right\} = P_T + \text{Diff}_{\kappa_T} - \varepsilon_T$$ (4.24)

where P_T is the turbulent kinetic energy production, Diff_{κ_T} the diffusion term and ε_T is the rate of turbulent energy dissipation, which is given by the one-equation model.

$$\varepsilon_T = \text{CNU}^{3/4}\frac{\kappa_T^{3/2}}{\text{TLEN}}$$ (4.25)

An additional transport equation is solved for the turbulent dissipation ε_T

$$\frac{\partial \varepsilon_T}{\partial t} + \frac{1}{V_F}\left\{uA_x\frac{\partial \varepsilon_T}{\partial x} + vA_y\frac{\partial \varepsilon_T}{\partial y} + wA_z\frac{\partial \varepsilon_T}{\partial z}\right\} = \frac{\text{CDIS1}\cdot\varepsilon_T}{\kappa_T}P_T + \text{Diff}_\varepsilon - \text{CDIS2}\frac{\varepsilon_T^2}{\kappa_T}$$ (4.26)

where Diff_ε is the diffusion of dissipation. The constants CDS1 and CNU are by default 1.42 and 0.085 in the RNG model. CDS2 is computed from the turbulent kinetic energy (κ_T) and turbulent production (P_T) terms. The kinematic turbulent viscosity ν_T is computed as

$$\nu_T = \text{CNU}\frac{\kappa_T^2}{\varepsilon_T}$$ (4.27)

Large Eddie Simulation model (LES)

Turbulence consists of eddies of different sizes. Kinetic energy is translated between different eddy sizes and dissipates into heat on molecular length scale. The works of Kolmogorov (1941) could show that the size of an eddie is correlated to the energy it contains, called the energy cascade.

$$E(k) \sim k^{-5/3} \tag{4.28}$$

Consequently, this means that large eddies transport the highest energy inside the flow and therefore need to be prioritized in simulations. LES simulations resolve eddies that are larger than the cell size directly and smaller eddies are simulated by subgrid models. The most common subgrid model approach is named after Smagorinsky (Smagorinsky, 1963) and is introduced by increasing the viscosity in the cell. The turbulent kinematic viscosity ν_T is added to the molecular kinematic viscosity ν and together with the density of the fluid ρ leads to the dynamic viscosity μ.

$$\mu = \rho \left(\nu + \nu_T \right) \tag{4.29}$$

The turbulent kinematic viscosity for the LES as used in FLOW-3D® HYDRO is defined as

$$\nu_T = (cL)^2 \cdot \sqrt{2e_{ij}2e_{ij}} \tag{4.30}$$

$$L = (\delta x \delta y \delta z)^{\frac{1}{3}} \tag{4.31}$$

c is the Smagorinsky coefficient, which lays in the range of 0.1 to 0.2 and e_{ij} are the strain rate tensor components. The resolved kinetic energy and hence the quality of the LES simulation is dependent on the cell size, which is why a sensitivity analysis was performed for the cell size.

An important feature of the LES simulation is the time-dependent resolution of the simulation. The preparation of the simulation usually takes more time because fluctuations need to be initialized. The results of the LES simulation is able to not only show the mean velocities but also the standard deviations.

4.3.6 Setup of the numerical model for the investigated in-stream structures

The numerical model that complements the physical model was executed in three steps: the preprocessing, the processing and the post processing. The preprocessing incorporated the preparation of the geometry. Therefore, one set of bed morphology and water level data was selected, that was closest to the average value of the replicate experiments. The average was not selected as the deviations in bed morphology e.g. for the DWD were high enough to also impact the flow velocities and would complicate the comparison of physical and numerical model. Afterwards, outliers of the bed morphology were deleted manually with Cloudcompare (CloudCompare (version 2.12.4) [GPL software]. (2023)). For a smooth transition from the flat

bed to the bed morphology of the physical model experiment ArcGIS® software by Esri was used to interpolate values in between. The bed morphology and the rigid, flat parts upstream and downstream were assembled in one subcomponent in FLOW-3D® HYDRO. The structure itself was added as a separate subcomponent, to be able to extract the force on the structure later. The model was calibrated with the case of the Rectangular Pier, as this experiment showed the smallest sensitivities regarding bed morphology (see chapter 5.2.1). A sensitivity analysis regarding cell size, possibilities of adapted meshing and also a shifting of half a cell size were performed to find the optimal mesh. The final mesh consisted of 3 meshblocks as shown in figure 4.16. The first meshblock compromises the flat, rigid upstream section, the second meshblock the scoured, rigid bed in the measurement section and the third meshblock the rigid, flat part downstream of the measurement section. Square cells with edge lengths of 1.5 cm for meshblock 1 and 3 and 0.75 cm in meshblock 2 were used. In total, the mesh consisted of about 1.5 million cells. All structures and bed morphologies could be displayed in a sufficient accuracy with this method. The grid was used for all simulations including RNG and LES turbulence models.
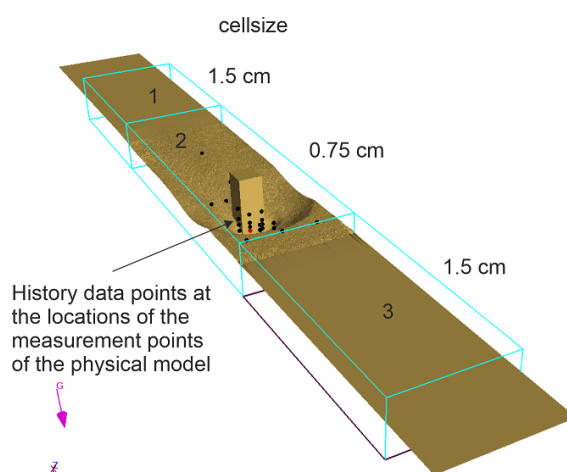
Figure 4.16: Setup of the numerical model including 3 meshblocks and history data points.

The model was rotated to a bottom slope of $I_0 = 0.003$. The initial condition was set to a water level that equals the outlet water level in the physical model. The discharge was increased with a linear time dependent curve from zero to the end value in 5 s. The boundary conditions consisted of a constant discharge and an inlet and outlet water level that was acquired from the equilibrium conditions in the physical model.

As a default, FLOW-3D HYDRO automatically optimizes the time step size within stability thresholds to uphold accuracy and prevent disproportionate increases in the effort required for enforcing continuity conditions, such as controlling the number of pressure iterations. Therefore, the time step size varied for every simulation. An overview is given in table 4.7. The Courant–Friedrichs–Lewy (CFL) condition of < 1 is necessary for convergence. All simulations (see table 4.7) show a maximum CFL of ≤ 0.2 and hence can reach stable conditions.

Table 4.7: Time step for the different structures and turbulence models and respective convergence condition by Courant–Friedrichs–Lewy (CFL).

	Timestep LES [s]	CFL	Timestep RNG [s]	CFL
CP	0.0026	0.19	0.0025	0.18
RP	0.002	0.15	0.002	0.15
TP	0.0019	0.14	0.0019	0.14
DWD	0.0013	0.10	0.0025	0.18
DG	0.0027	0.20	0.0012	0.09
Kdam	0.0013	0.10	0.0018	0.13

The RNG model was run for 60 s and reached equilibrium for all structures except the DG. This simulation was therefore run for 180 s and averaged for the last 90 s. For the LES simulations, a sensitivity analysis regarding the time interval for data extraction was done and a time interval of 1 s was found sufficient discretization. The LES simulations ran for 150 s and the last 90 s were taken for the averaging process. The velocity measurement points of the physical model were implemented as history points in the numerical model to allow a comparison of both models.

The simulations were then processed with FLOW-3D® HYDRO which lasted between 5 h and 26 h. For all structures the following parameters were exported in the post-processing from the different models:

Table 4.8: Parameter exported in the postprocessing from the different turbulence models.

Parameter	model
Mean flow velocity with velocity vector field [m/s]	LES
Standard deviation [m/s]	LES
Streamlines	RNG
Turbulence intensity [%]	RNG
Turbulent kinetic energy [m²/s²]	RNG

The data analysis and visualization was done with FLOW3D POST® and with Python.

Chapter 5

Hydromorphological analysis of local scours around idealized in-stream structures

Parts of this chapter were already published previous to this dissertation. The respective subchapters are indicated.

The following chapter focuses on the six in-stream structures, Circular Pier (CP), Rectangular Pier (RP), Triangular Pier (TP), Double Wing Deflector (DWD), Deflected Groyne (DG), and the Kdam (Kdam) that were introduced in chapter 3.2 and 4.1.1. In the initial step, an idealized form of the structures is examined, characterized by simplified, clearly-defined geometry with sharp edges and smooth surfaces. The time development of the scouring process and the backwater rise is first addressed, considering that all structures are examined in a hydromorphological equilibrium state. Subsequently, in the equilibrium state, the bed morphology, flow field, and backwater rise for all six structures are analyzed and compared. An overview of the methods employed is provided in figure 5.1. The chapters on the flow field and backwater rise start with a methodical comparison to validate the numerical model against the physical model. This is, then for all chapters, followed by an analysis of the data from this study, each concluding with a discussion in the context of existing literature.
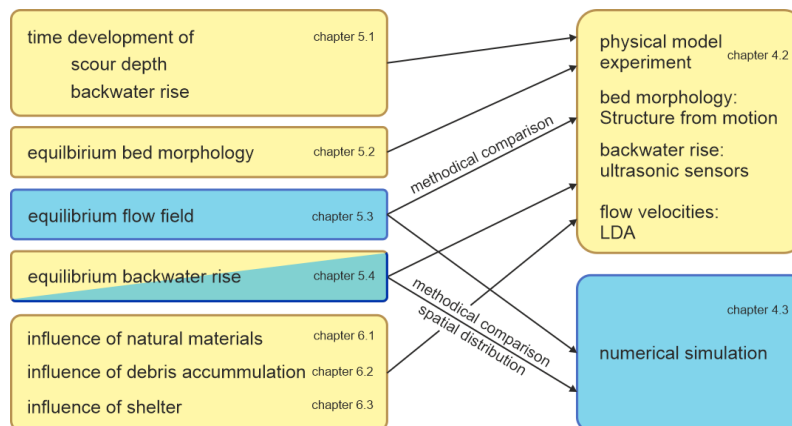
Figure 5.1: Overview of the content of the chapter and the employed model from the hybrid model approach.

5.1 Time development of the scouring process

5.1.1 Time development of the bed morphology

Parts of this subchapter were already published in Kannen, Seidel, and Franca (2022) and Kannen, Seidel, and Franca (submitted in 2023).

Time development of the bed morphology around the Circular Pier

Experiments with 4 different durations were performed for the Circular Pier (CP) to analyze the time development of the scour process. Not only the time development at the deepest point but also the scour pattern around the CP were observed. The point with the deepest scour depth was stable in location and could be observed right upstream of the pier. The time development at this point is shown in figure 5.4. An asymptotic time development of scour depth until reaching an equilibrium value was observed and is addressed later in this chapter.

The scour pattern that evolves around the CP is shown in figure 5.2 for 4 different time steps. Visual observation of the experiments showed that the erosion began due to a downflow in front of the pier. When the downflow reached the bed a small scour hole was excavated and a horseshoe vortex developed. This vortex system is explained in detail in chapter 5.3.3. The horseshoe vortex causes the scour hole to expand circularly both upstream and to the sides of the pier as shown in figure 5.2. Downstream of the structure, two significant lateral scour holes grew in size and depth over time. The eroded sediment either moved downstream or gathered into a central dune downstream of the structure. As time progressed, the distance between the pier and the dune's peak increased. By the end of the first day, the scour hole reached the flume walls, subsequently affecting the flow pattern.
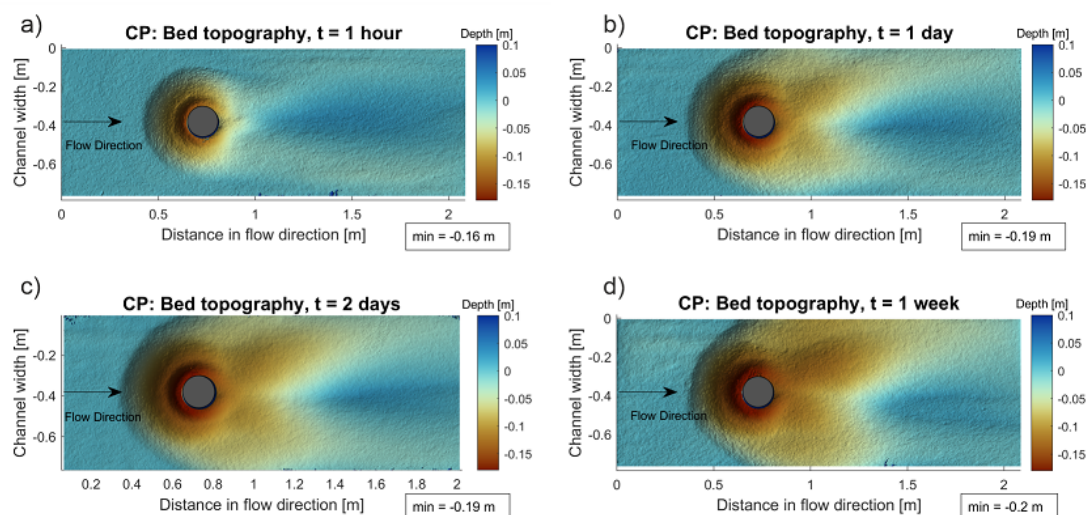
Figure 5.2: Time development of bed morphology around the Circular Pier (CP). a) t = 1 h, b) t =1 day, c) t = 2 days, d) t = 1 week. min = minimum bed elevation which equals maximum scour depth. The results are presented in model scale, this accounts for all following bed morphology illustrations in this chapter if not indicated otherwise.

Figure 5.3 provides a longitudinal profile in the center line of the flume illustrating the evolution of the scour hole and the dune. Between 2 days and 1 week, the rate of erosion notably decreased upstream of the pier, appearing to stabilize during this period. While the size of the scour hole upstream of the pier remained relatively constant from 1 day to 1 week, the downstream dune continued to shift downstream. The analysis reveals that even though the maximum scour depth and hence, by definition, equilibrium conditions are reached upstream of the structure, the central dune downstream of the structure had still not reached equilibrium. This observation is overseen in many publications up to date. For this research the development of the dune is of subordinate importance and hence no further comments are made on this.
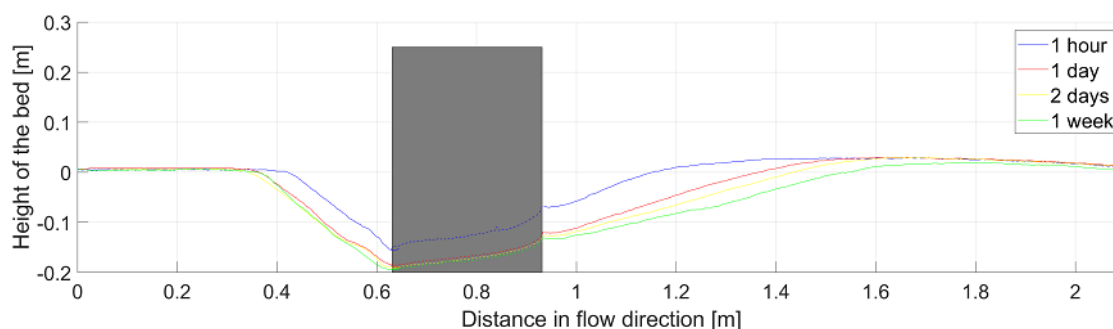
Figure 5.3: Longitudinal profile of time development of bed morphology around the Circular Pier along the flume center line.

Detection of time to equilibrium for the Circular Pier

Prior to the main experiments, a 7-day long-term test was conducted to determine the exact time when equilibrium was reached. For the test case CP, the equilibrium time t_e was estimated before the experiment, using predictor equations and equilibrium equations based on scour rate and visual parameters as outlined in table 3.1 in chapter 3.4.5. The estimation should give a first impression whether the 7 days planned for the long-term test are enough. The results of the pre-estimations are given in table 5.1. According to the predictor equations, the results ranged from 48 hours, as predicted by Franzetti, Larcan, and Mignosa (1982), to 84 hours by Melville and Chiew (1999). Equilibrium times based on scouring rates at the deepest location varied from 24 hours to 160 hours as shown in table 5.1 and figure 5.4 a) (Melville & Chiew, 1999; Coleman, Lauchlan, & Melville, 2003; Grimaldi et al., 2009; Umeda, Yamazaki, & Ishida, 2008). The visual evaluation by Cardoso and Bettess (1999) suggested 24 hours to reach equilibrium, as depicted in table 5.1 and figure 5.4 b). As the equilibrium is no absolute state that is reached after a certain time but rather a time that is per definition defined as equilibrium, the times to equilibrium t_e differ for the different equilibrium concepts. Those concepts were outlined in chapter 3.4.5. As a conclusion, it can be said, that a long-term experiment of 7 days seems a suitable time to safely capture the equilibrium time.

Table 5.1: Time to equilibrium t_e according to different equilibrium criteria. The corresponding formulas can be found in table 3.1.

Criterion from	t_e
EQUILIBRIUM CRITERIA BASED ON SCOUR RATES	
Melville and Chiew (1999)	48 h
Coleman, Lauchlan, and Melville (2003)	48 h
Grimaldi et al. (2009)	160 h
Umeda, Yamazaki, and Ishida (2008)	24 h
EQUILIBRIUM CRITERIA BASED ON VISUAL PARAMETERS	
Cardoso and Bettess (1999)	24 h
PREDICTOR EQUATIONS	
Coleman, Lauchlan, and Melville (2003)	55 h
Melville and Chiew (1999)	84 h
Chang, Lai, and Yen (2004)	84 h
Franzetti (1994)	48 h
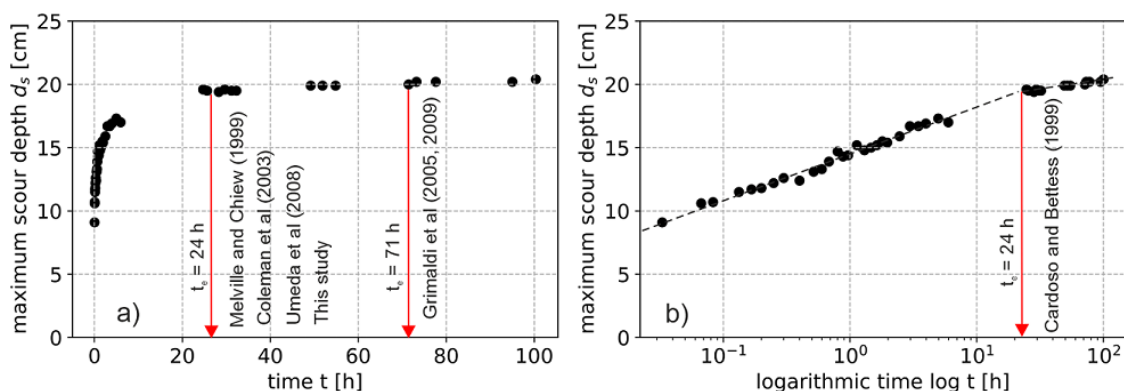
Figure 5.4: Time to equilibrium according to equilibrium criteria based on a) scour rate and b) visual parameter.

The criterion for equilibrium time proposed by Melville and Chiew (1999) is the most-used criterion throughout literature. The criterion defines equilibrium time when the scour rate drops below 5% of the pier width within a period of 24 h. In this work, an adapted criterion to render it applicable to both emergent and submerged structures was developed (see formula 4.11). The adaptation consists of adding the factor of relative submergence h_s/h_0 to the pier width w_s. More details are explained in chapter 4.2.5. The developed equilibrium criterion was applied to the data from the CP experiment, which yielded a time to equilibrium t_e of 24 hours. The time development data was then standardized with the equilibrium time t_e and end scour depth d_{se} (see figure 5.5) and plotted alongside findings from Melville and Chiew (1999). A comparison of the time development in both studies reveals a strong correlation,

as illustrated in figure 5.5. The stages of the scouring process, initial phase, principal phase and equilibrium phase as defined by Ettema (1980), which were outlined in chapter 3.4.5 can clearly be observed here as well.
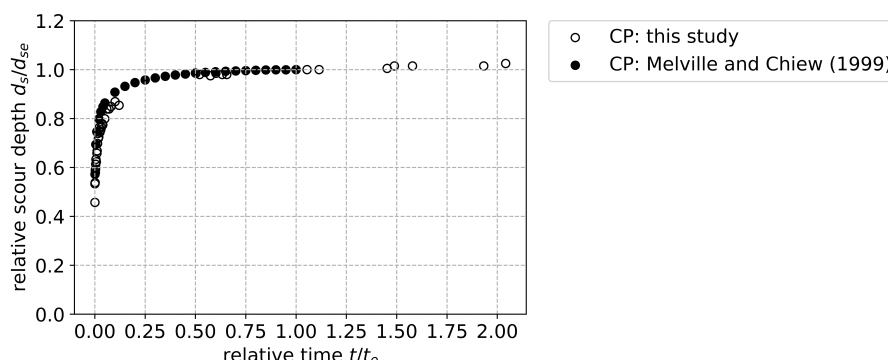
Figure 5.5: Comparison of experimental values (white circles) with literature values of Melville and Chiew (1999) (black circles).

Application of the developed criterion on all structures

The developed equilibrium criterion was applied to all structures with limiting scouring rates given in table 4.4. The equilibrium criterion yielded to times to equilibrium t_e given in table 5.2.

Table 5.2: Times to equilibrium t_e for the different structures.

	t_e [h]
CP	48
RP	24
TP	48
DWD	48
DG	72
Kdam	96

Figure 5.6 illustrates the time development at the deepest point for all structures, with time t normalized by the previously determined time to equilibrium t_e. Both pier-like and stone-like structures exhibited a linear and asymptotic trend. The stone-like structures (DWD and DG) had a more gradual onset in the initial phase of scouring ($t/t_e = 0.25 - 0.5$). In contrast, the dam-like structure displayed a non-linear pattern that wasn't asymptotic. This deviation can be attributed to the high limiting scour rate for the Kdam (see table 4.4), and the placement of the deepest point near the flume walls rather than in the centerline. Furthermore, the mechanisms causing erosion at dam-like structures are distinct from those at pier- and stone-like structures. While the latter form prominent, stable vortex systems with helices, the dam-like structure experiences scouring primarily from constriction effects, which not only involve vortex systems but also increased bed shear stresses (refer to chapter 5.3).
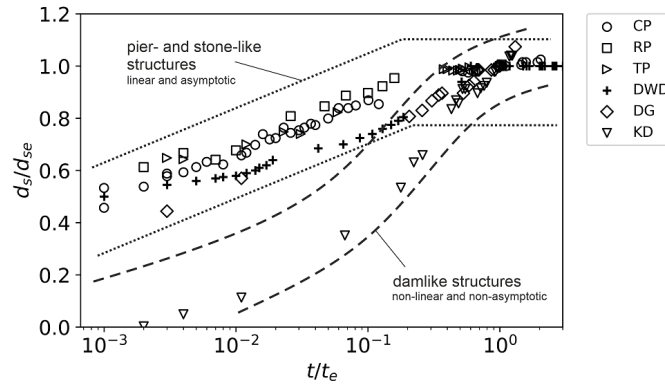
Figure 5.6: Temporal development of relative scour depth d_s/d_{se} for different flow types; time is normalized by the time to equilibrium t_e.

To validate and compare, the time to equilibrium and the associated equilibrium scour depth of the measurement data from several experimental studies, including studies by Melville and Chiew (1999) for CP, Rashak and Khassaf (2020) for DG, Guan et al. (2019) for Kdam, and Coleman, Lauchlan, and Melville (2003) for AB (abutments, as comparison for one-sided, emergent structures) was used. The time development of scour depth is illustrated in figure 5.7 with a logarithmic axis for the relative time t/t_e. The data for pier- and stone-like structures (CP, DG, and AB) consistently fall within the linear and asymptotic behavior boundaries, comparable to the measurements from this work, as evident in figure 5.6. In contrast, the values from dam-like structures (Guan et al., 2019) diverge in a non-linear and non-asymptotic manner. This difference is also evident in the data from this study as shown in figure 5.6. Hence, the formulated criterion might not be suitable for dam-like structures. One potential explanation is that the limiting scour rate for these structures is relatively high, given that the entire river width is factored into the hydraulically significant length scale D. As a result, the determined equilibrium time is rather short, suggesting that the scouring process might not have reached equilibrium yet.
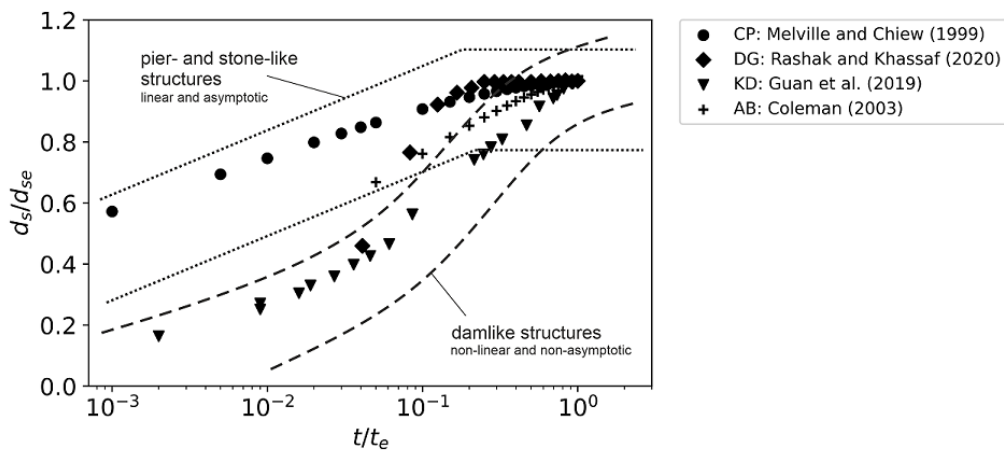
Figure 5.7: Application of the equilibrium criterion on time development data of various literature values of pier- (Melville and Chiew (1999) for CP and Coleman, Lauchlan, and Melville (2003) for abutments), stone- (Rashak & Khassaf, 2020) and dam-like structures (Guan et al., 2019) presented in a semilogarithmic normalized diagram.

In conclusion, the derived criterion seems suitable for pier- and stone-like structures. The criterion shows potential for further research on dam-like structures. In the absence of alternatives, the criterion is still used for this work, even though the boundary conditions resulting from the equilibrium criterion must be taken into account when interpreting the results. Furthermore, the consistency between the data obtained in this work and literature values underlines the robustness of the experimental setup, validating its reliability.

5.1.2 Time development of the backwater rise

As well as the scour depth the backwater rise shows a time dependent development. For the measurement points and instrumentation refer to figure 3.36 and chapter 4.2.3. Figure 5.8 shows the time development of the backwater rise for the different structures. All structures show a decreasing backwater rise from about 1.3 h_{1e} to 1.0 h_{1e} with increasing time t/t_e, where t_e is the equilibrium time that was acquired in the bed morphology development. The initial backwater rise of the pier-like structures is significantly higher than of the other structure types. The Kdam shows the smallest initial backwater rise. This is due to the scour hole developing downstream of the dam and the blocked area does not change for the Kdam during the experiments, which is addressed further in chapter 5.4.2.
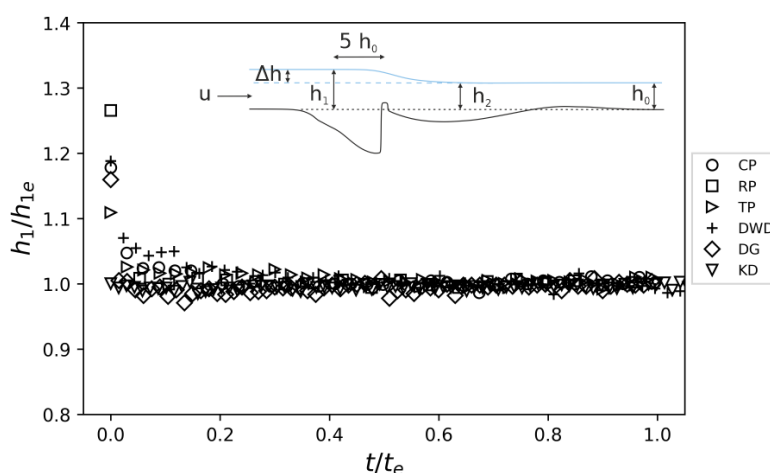
Figure 5.8: Time development of water level h_1 upstream of the structure.

Figure 5.9 shows a comparison of the time development of scour depth and water level. Alongside with the increasing scour depth the water level upstream of the structure decreases. The potential energy upstream of the structure, that manifests in the backwater rise is transferred into a morphological change of the bed, hence the flow tries to find a hydromorphological equilibrium by forming a bed incision. It is notable, that the water level has reached 90 % of its equilibrium value by approximately 10 % of the equilibrium time, whereas the scour depth reached this value only after 60 % of the time. As a conclusion it can be said, that the hydraulic equilibrium time is reached significantly earlier than the morphological equilibrium. Therefore, it is also necessary to base the equilibrium time on the scour rate and not the backwater rise development.
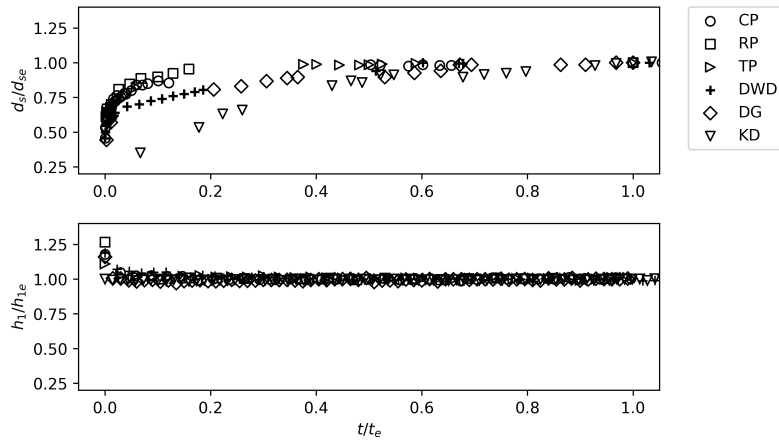
Figure 5.9: Comparison of the time development of scour depth d_s (above) and the water level upstream of the structure h_1 (below).

5.2 Analysis of the bed morphology at equilibrium stage

5.2.1 Reproducibility of the hydromorphological experiments

The results of this subchapter are part of Kannen, Seidel, and Franca (submitted in 2023). Three experimental runs were performed for every structure to characterize the sensitivity and reproducibility of the bed morphology. Figure 5.10 illustrates the standard deviation of the bed morphology at equilibrium stage. Given a d_{50} of 3.1 mm, any deviations ≤ 3 mm are considered as no significant changes.
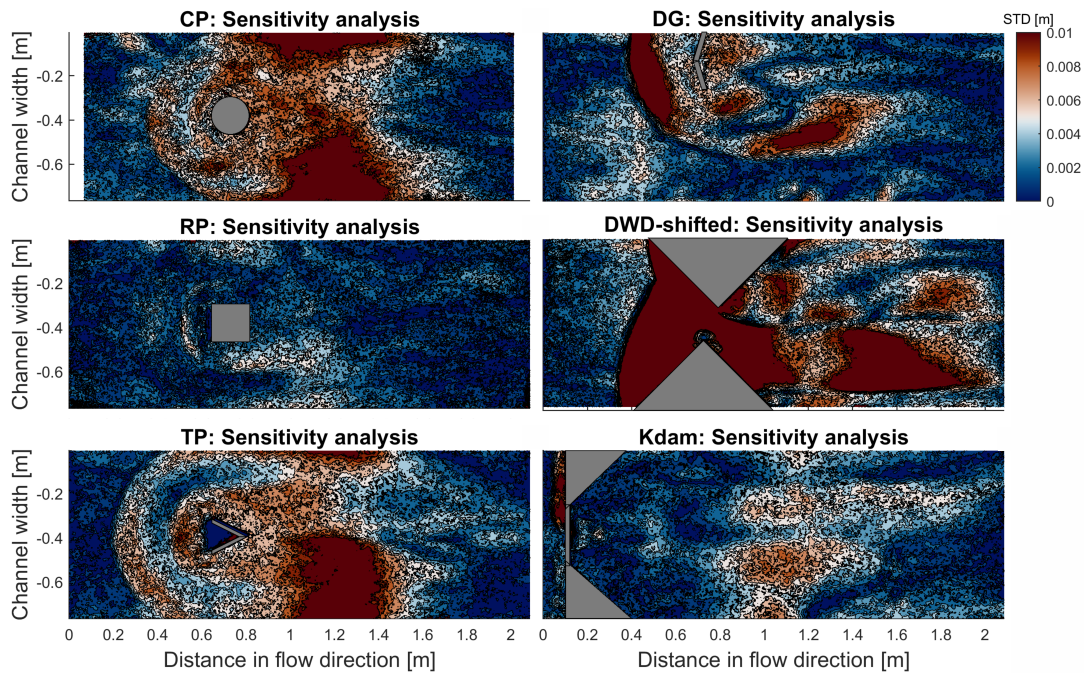
Figure 5.10: Standard deviation of bed morphologies for different structures in equilibrium stage (three replicates).

Analyzing the pier-like structures reveals that the RP exhibits the most consistently repro-
ducible equilibrium bed morphology. The highest standard deviations are observed down-
stream of the CP and TP. The upstream scour hole dimensions of all pier-like structures re-
main similar across all experimental runs, indicated by a distinct line demarcating where no
further changes in bed morphology are detectable. Only minor differences in bed morphology
are evident in the slopes of the scour hole. Stone-like structures present a varied picture of
deviations from the average bed. The DG exhibits higher deviations in sections with steeper
slopes, particularly at the upstream and lateral ends of the scour hole. The DWD displays
the highest sensitivity concerning bed morphology. Initially, the DWD was implemented in a
parallel setup, without the intended shift. For these experiments no reproducible equilibrium
could be achieved. The location of the deepest point varied from the left to the right wing
without any detectable reason. These cases were in an unstable equilibrium. To stabilize
the deepest point at one location the DWD was shifted by 0.1 of the width between the wings.
With this adjustment the deepest point could be stabilized at the upstream wing. Even though,
the DWD showed the highest standard deviations that indicate that the flow field in this case
is of higher variability than the other structures. The Kdam demonstrates good reproducibility,
indicating a stable vortex system.

In general, all structures exhibit a tendency towards higher standard deviations downstream
of the structure. As indicated in chapter 5.1.1 this may be due to the missing equilibrium
downstream of the structure. The experiments are stopped at equilibrium conditions that
are based on the development of the deepest point which is in all cases, except the Kdam,
upstream or at the edge of the structure. In regions with elevated slopes higher standard
deviations are detectable as well. Those regions are associated with sliding mechanisms,
where one sliding event of several particles could lead to differences in the bed morphology.
Despite these variations, the results are deemed sufficiently reproducible for this investigation.
The bed morphology at equilibrium presented subsequently represents the average of the
three replicates.

5.2.2 Bed morphology at equilibrium stage

Parts of this subchapter are part of Kannen, Seidel, and Franca (submitted in 2023).
Figure 5.11 illustrates the average bed morphologies at the equilibrium stage. The deep-
est scour position is consistently found just upstream of all pier-like structures. The scour
hole takes on a circular evolution in the upstream and lateral directions, exhibiting a notable
change in slope within the scour hole, with the TP case showing the most pronounced vari-
ation. This change in slope is often referred to as primary and secondary scour hole (Euler
& Herget, 2012; Kirkil, Constantinescu, & Ettema, 2008), whereof the primary scour hole is
the one closer to the pier. The bed morphology displays symmetry with the center line of
the flume. Downstream of the pier, all pier-like cases feature two deep lateral sections and a
central dune. Notably, all pier-like cases exhibit wall interaction, meaning that the scour hole
extends to the flume walls and is constrained from evolving fully to the sides. Considering that
the engineering structures are intended for implementation in urbanized areas where river-

bank protection is a common practice, there would likely be riverbank interaction in natural conditions. Particularly in the reference rivers where the measures are to be installed and upon which this investigation is based, riverbank protection and levees prevent scouring at the sides. If interaction with the riverbank is undesired, reducing the width of the piers could be considered. This adjustment would result in a smaller scour width but also a smaller scour depth. The optimization of scour width to scour depth is a subject for further research and dependent on local boundary conditions, such as approach flow conditions, cross-sectional area, overflow and discharge variations, and where some aspects are shown in chapter 7.4.
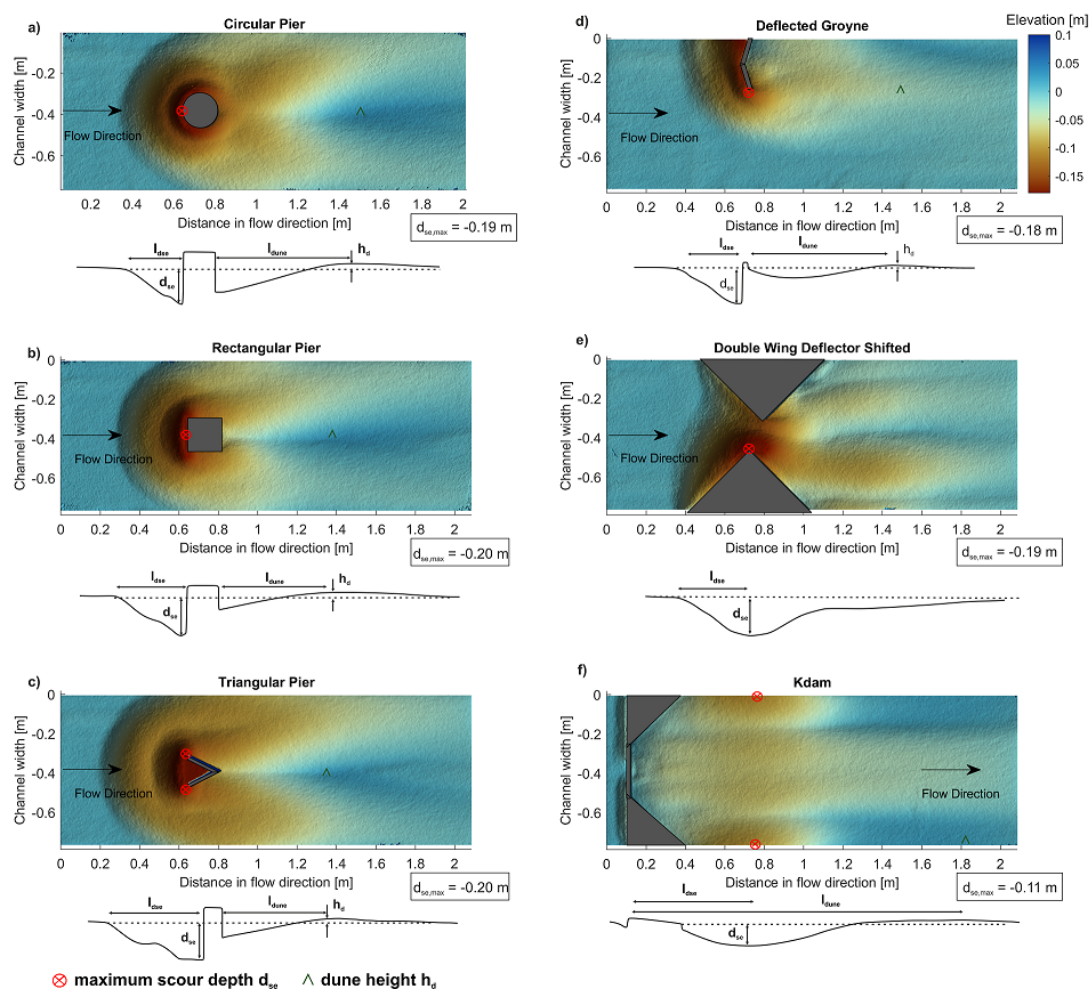
Figure 5.11: In the background: the average of bed morphologies at the equilibrium stage for six distinct structures (three replicates each). The maximum scour depth for each structure is highlighted in red, and its corresponding value is provided in the accompanying box. Beneath each image, the geometric parameters of the scour holes are specified: length of the scour hole (l_{dse}), distance of the dune (l_{dune}), maximum end scour depth (d_{se}), and height of the dune (h_d).

The stone-like structures (DG and DWD) have the deepest scour location at the head of the structure. Visually, it was observed that the scour hole first develops towards upstream and lateral and later also downstream of the structure. Both structures show no symmetry since the geometries are also not symmetrical regarding the center line of the flume. The DG is

a one-sided structure, so the alterations in bed morphology concentrate on one side. At approximately $2\,l_s$ downstream of the DG there is an accumulation of sediment material and a dune is formed. The DWD is a two-sided structure and shows the deepest area around the upstream wing. Downstream of the DWD two deep sections can be identified.

The Kdam shows the smallest scour depth but a long deepening of the bed which reaches the end of the measurement section. At approximately 2/3 of the width of the structure w_s the deepest scour position is located at the flume walls.

Geometric analysis of the scour holes

The geometry of the scour hole can be described with various parameters. The parameters selected for this work are displayed in figure 5.12 and enclose the maximum scour depth d_{se}, the length of the upstream scour hole l_{ds}, the distance of the dune l_{dune} and the height of the dune h_d. Table 5.3 and 5.4 summarize the geometrical parameters of the scour hole for all structures in absolute and normalized values, respectively.
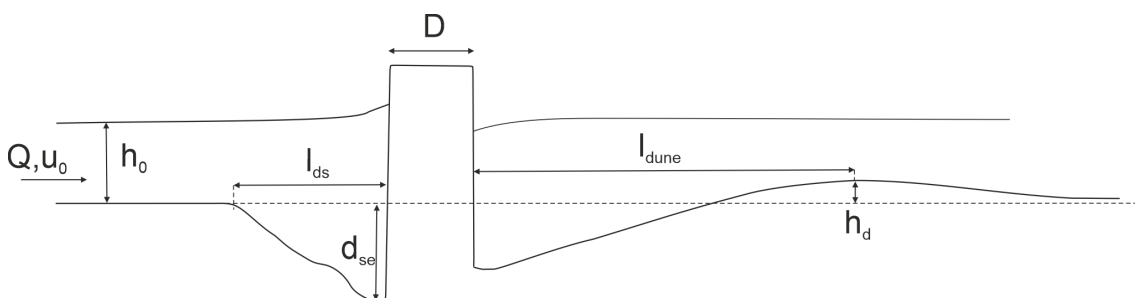
Figure 5.12: Definitions of maximum end scour depth d_{se}, length of the upstream scour hole l_{ds}, distance of the dune l_{dune} and height of the dune h_d.

Table 5.3: Geometrical parameter of the scour hole for the six tested structures.

	CP	RP	TP	DWD	DG	KD
d_{se} [cm]	19.2	20.1	19.9	19.1	18.3	10.9
l_{ds} [cm]	30.2	35.3	44.3	36.6	35.4	(114.1)
l_{dune} [cm]	75.7	62.6	59	-	75	168.5
h_d [cm]	2.93	2.75	2.3	-	1.3	1.8

Table 5.4: Geometrical parameter of the scour hole for the six tested structures normalized with the hydraulically significant length D.

	CP	RP	TP	DWD	DG	KD
d_{se}/D	1.2	1.3	1.3	0.7	1.7	0.3
l_{ds}/D	1.9	2.2	2.8	1.4	3.2	(3.6)
l_{dune}/D	4.8	4.0	3.7		6.9	5.2
h_d/D	0.2	0.2	0.1		0.1	0.1

Except for the Kdam, the maximum scour depth d_{se} lays within a range of 2 cm ($\approx 10\%$ of total depth). The Kdam differs with only half of the scour depth. Looking at the normalized

scour depth d_{se}/D reveals, that the stone- and pier-like structures all lay within a range around $1.2 \pm 0.33\,D$. The only exception is the Kdam where d_{se}/D equals 0.3. The length of the upstream scour hole l_{ds} differs significantly for the three pier-like structures, with TP showing the largest scour hole upstream of the pier. For the DG the length of the scour hole is comparable to the RP. For the Kdam l_{ds} lays downstream of the structure. The length of the scour hole is significantly higher than for all other structures, which can be attributed to the different scouring mechanisms of dam-like structures. The normalized length of the upstream scour hole l_{ds}/D is $2.5 \pm 0.81\,D$ for all structures. The distance of the dune l_{dune}/D has comparable lengths for pier- and stone-like structures and more than double the distance for the Kdam. It lays within a normalized range of $4.9 \pm 1.25\,D$ for all structures. The height of the dune h_d is highest for the CP. For the pier-like structures the height of the dune h_d increases with increasing distance of the dune. The normalized height of the dune lays within a range of $0.1 \pm 0.05\,D$ for all structures. The small ranges that are present for the normalized values show that the developed criterion of the hydraulically significant length is suitable to capture the different geometric parameters of the three different flow types.

The analysis of the scoured area and volume can give further insights into the geometric features of the scour hole. The definitions of the geometric dimensions are displayed in figure 5.13. Table 5.5 summarizes these geometric features of all scour holes.
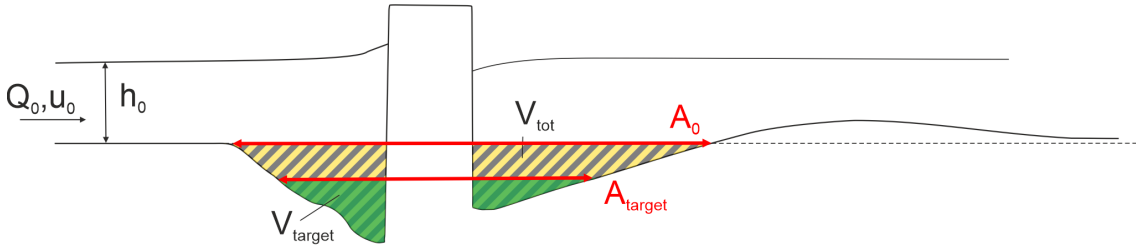
Figure 5.13: Definitions of area in target depth A_{target}, area in initial depth A_0, volume below target depth V_{target} and total volume V_{tot}.

Table 5.5: Area at the target depth of 8 cm A_{target}, area in initial depth A_0, relative area in target depth A_{target}/A_0, volume below target depth V_{target}, and total volume of the scour below an elevation of zero V_{tot}, relative volume in target depth V_{target}/V_0.

	CP	RP	TP	DWD	DG	Kdam
A_{target} [m²]	0.26	0.20	0.47	0.21	0.10	0.07
A_0 [m²]	1.03	1.07	1.19	1.10	1.02	1.17
A_{target}/A_0 [-]	0.25	0.19	0.40	0.19	0.09	0.06
V_{target} [m³]	0.0103	0.0087	0.0158	0.0087	0.0042	0.0012
V_{tot} [m³]	0.0631	0.0563	0.0818	0.0588	0.0386	0.06
V_{target}/V_{tot}	0.16	0.15	0.19	0.15	0.11	0.02

The geometrical parameters of the scour holes reveal that the area at the target depth of 8 cm (A_{target}) is greatest for the TP and smallest for the Kdam. A_0 is the area of the scour in the depth zero, means the size of the scour hole at the level of the initial bed. As the area in target depth is one parameter for the evaluation of the scour as a deep pool habitat, the

ratio A_{target}/A_0 provides a measure of the efficiency how large the scour hole in target depth is related to the scour that can be seen in the initial bed level (refer to Table 5.5). This ratio ranges between 0.06 and 0.40, being small for dam-like structures and high for pier-like structures. This meas that pier-like structures are able to build large areas even in the target depth compared to dam-like structure.

To characterize the scour holes of the different structures, the distribution of area and volume across the scour depth was analyzed, as shown in figure 5.14. As the depth increases, the area of the scour hole decreases asymptotically. For stone-like structures, the decrease is most pronounced, with an area reduction of approximately 0.8 ($A/A_0 = 0.2$) at a scour depth d_s/d_{se} of 0.3 of the total scour depth. For dam-like structures, the reduction in this depth is only 0.40 ($A/A_0 = 0.6$). The geometry of pier-like scour holes falls in between, as depicted in figure 5.14 a) and b). In conclusion, stone-like structures create small scour holes in terms of area, but large scour holes in terms of depth, while dam-like structures create large and flat scour holes.
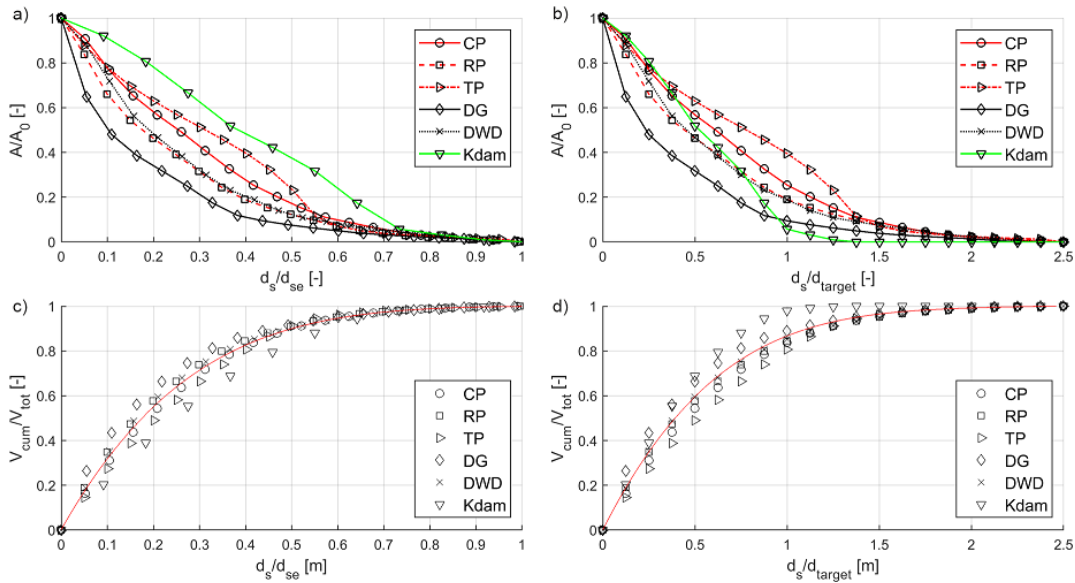
Figure 5.14: a) Relative area A/A_0 over relative scour depth d_s/d_{se}, b) relative area A/A_0 over relative scour depth d_s/d_{target}, c) relative volume V_{cum}/V_{tot} over relative scour depth d_s/d_{se}, d) relative volume V_{cum}/V_{tot} over relative scour depth d_s/d_{target}.

The distribution of cumulative volume over depth is illustrated in figure 5.14 c) and d). As the depth increases, the cumulative volume also increases. It is noticeable that the curves for the cumulative volume lie within a very narrow range, meaning that despite the very different areal distribution and varying absolute depth, the same normalized volume distribution over depth is consistently observed. One reason for this could be the bed slope within the scour hole, which adjusts to a specific depth. At shallower depths, the bed slopes are gentler, while at greater depths, the bed slopes become steeper (refer to figure 5.11). The total volume (V_{tot}) of the scour is highest for TP and lowest for the DG. The target volume (V_{target}) represents the cumulative volume below the target depth. The ratio V_{target}/V_{tot} indicates the proportion of volume below the target depth, thus qualifying as a suitable habitat. The range varies between

0.11 and 0.19 (except for the Kdam with 0.02, as shown in Table 5.5).

Comparison of the bed morphology with existing studies

This subchapter gives a comparison of the bed morphologies acquired within this work and literature values. For an easier comparison the geometric dimensions are normalized with the respective hydraulically significant length D.

Pier-like structures

Figure 5.15 shows the bed morphology of CP and RP in comparison with literature values from Dey and Raikar (2007). In general, the findings from this investigation reveal similar scour pattern in comparison with the literature values from Dey and Raikar (2007). The deepest scour position is located upstream of the pier and two deep lateral sections form further downstream. A central dune emerges downstream of the pier. Both datasets, from this study and Dey and Raikar (2007), indicate that the RP generates a deeper scour hole than the CP. In this study the relative scour depth d_s/D is 1.2 and 1.3 for CP and RP respectively. Dey and Raikar (2007) find a similar scour depth for the CP with 1.3 D, whereas RP shows a slightly larger relative scour depth with 1.7 D. Additionally, there is an observed shift in the initiation of the dune towards the pier, moving from x/D = 3.8 for CP to x/D = 2.2 for RP in this study, mirroring the shift from x/D = 6.7 at CP to x/D = 4.8 at RP in the data from Dey and Raikar (2007). The differences in relative scour depth d_s/D can possibly be attributed to differences in the relative sediment size D/d_{50}, the flow shallowness h_0/D and the blocked width of the flume between the two studies.
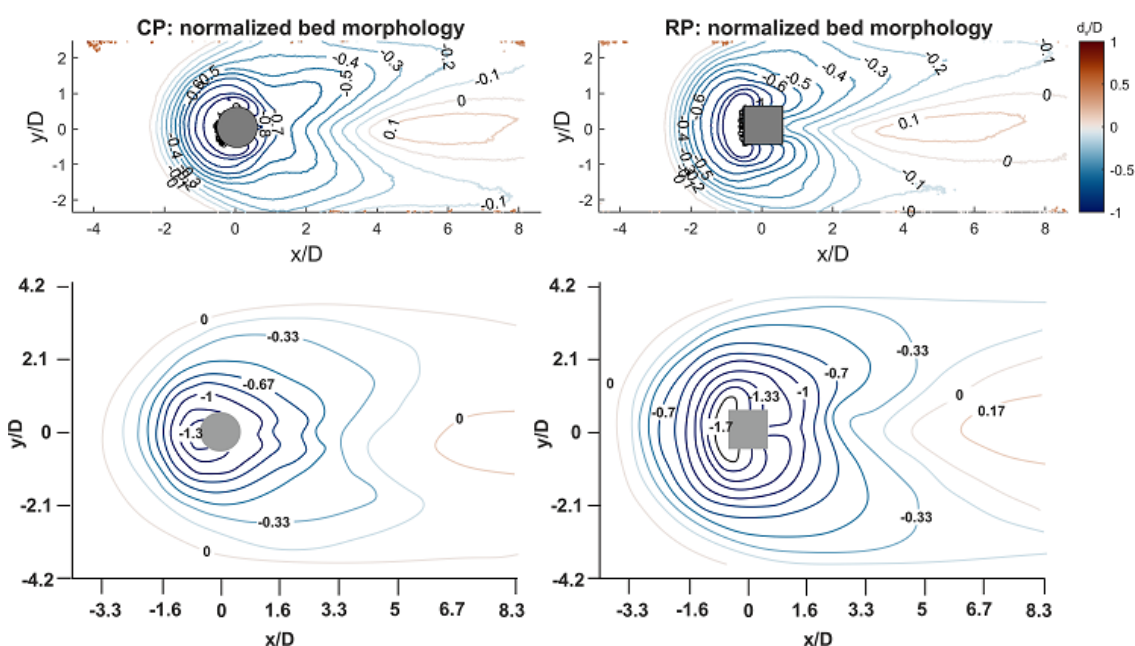
Figure 5.15: Comparison of normalized bed morphologies of this study (above) with values from Dey and Raikar (2007) (below) for CP (left) and RP (right).

Dey and Raikar (2007) used fine sediment with a relative sediment size of D/d_{50} = 148, while this study is positioned at the boundary between fine and coarse sediment with a D/d_{50} of 50. According to Melville (2008), the relationship between relative scour depth and relative sediment size peaks at D/d_{50} of 50 and exhibits decreasing trends for values over and under 50. This relationship would indicate a smaller relative scour depth d_{se}/D for the data of Dey and Raikar (2007). The opposite trend is the case, why d_{50}/D can be excluded as the influencing factor. The blocked width is the second factor differing between this work and the work from Dey and Raikar (2007). The blocked width of the pier-like structures in this work is 0.2 and 0.13 in Dey and Raikar (2007). Larger blocked width lead to higher scour depth as shown in the following chapter 7.4. The opposite trend is the case, why the blocked width can be excluded as the influencing factor. The flow shallowness h_0/D is another factor that can influence the scour depth. The setup of Dey and Raikar (2007), classified as a narrow pier (h_0/D = 2), results in scour depth being independent of water depth (Melville, 2008) as shown in chapter 3.4.2. In the case of this study, the flow shallowness h_0/D is 0.43, falling within the intermediate length category, where relative scour depth d_s/D depends on pier width D and water depth h_0. In the intermediate length category of the flow shallowness smaller relative scour depth are predicted as shown in figure 3.17. Hence a smaller relative scour depth can be expected for this work in comparison with Dey and Raikar (2007), which explains the shallower relative scour depth.

Stone-like structures

The equilibrium bed morphology of the DG experiment can be compared with the experiments from Harada et al. (2013). The comparison is shown in figure 5.16 and in general reveals similar scour pattern.
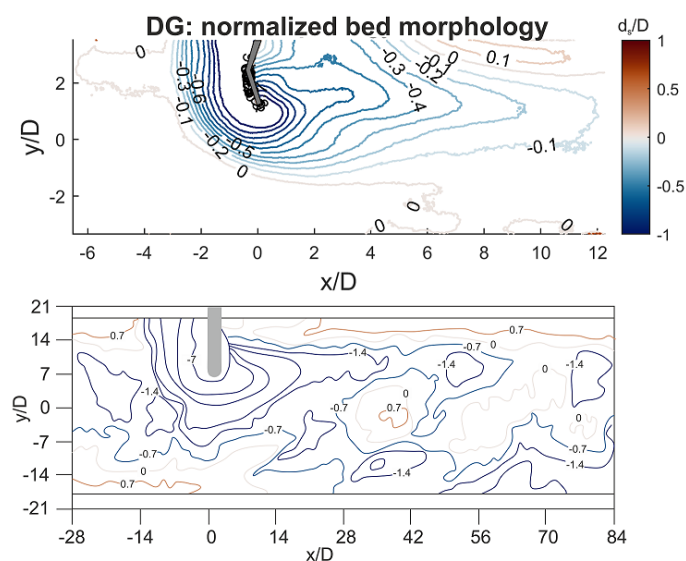
Figure 5.16: Comparison of normalized bed morphologies of this study (above) with values from Harada et al. (2013) (below) for DG.

The deepest point in both cases is situated at the head of the groyne. The scour hole laterally expands in upstream direction up to x/D = 3 in the present case and x/D = 14 in Harada et al. (2013). In downstream direction, the scour hole extends up to x/D = 12 in the present case and x/D = 70 in Harada et al. (2013). The dune initiates at x/D = 5.5 in the present case and immediately downstream of the groyne in Harada et al. (2013). The maximum relative scour depth is 1.2 in this work and 7 in Harada et al. (2013). The differences in relative scour depth and extensions of the scour can be attributed to the differences in the experimental setups: The different relative sediment size, submergence, flow shallowness and blockage ratio. Note, that the relative parameters such as D/d_{50} and h_0/D differ from the pier-like structures as the hydraulically significant length D changes. The relative sediment size, with D/d_{50} = 11.9 in Harada et al. (2013) and D/d_{50} = 35.8 in this study, classify both setups as coarse sediment. The relative sediment size would indicate a smaller relative scour depth for Harada et al. (2013) and is opposing to the trend observed. Therefore, it can be excluded as the main factor. The relative submergence h_s/h_0 is 0.41 in the present case and 0.07 in Harada et al. (2013). Ishigaki and Baba (2004) already showed, that with decreasing submergence the scour depth at groynes increases and reaches its peak value for emergent groynes. As the submergence in Harada et al. (2013) is smaller than in this work, a larger scour depth would be expected for this work. As this is an opposing trend it can be excluded as a main factor as well. The same trend accounts for the blockage ratio which is much smaller for Harada et al. (2013) with 0.02 than in this work with 0.13. Applying the flow shallowness relationship for pier-like structures (refer to chapter 3.4.2), the DG in this study is anticipated to result in a relatively shallow scour depth. This expectation arises from its classification as a "wide pier" with h_0/D equal to 0.63, where the scour depth is primarily determined by the approach flow depth h_0. In contrast, the groyne in the study by Harada et al. (2013) exhibits a significantly higher flow shallowness (h_0/D of 9.8) and is categorized as a "narrow" pier, leading to a much greater relative scour depth d_s/d_{se}. Consequently, the difference in flow shallowness results as the primary influencing factor contributing to the different relative scour depths observed between these two cases. It is to be reminded, that this theoretical consideration is based on the relationship derived for pier-like structures and not stone-like structures and the overflow component is not considered, which limits the significance.

Dam-like structures

Figure 5.17 shows the comparison of the bed morphologies of the Kdam in this work and a sill in the study of Guan, Melville, and Friedrich (2014). The general comparison shows a good qualitative agreement. Both studies show the deepest points at both sides of the flume and at a certain distance downstream of the structure. Both studies show slight erosion upstream of the dam.
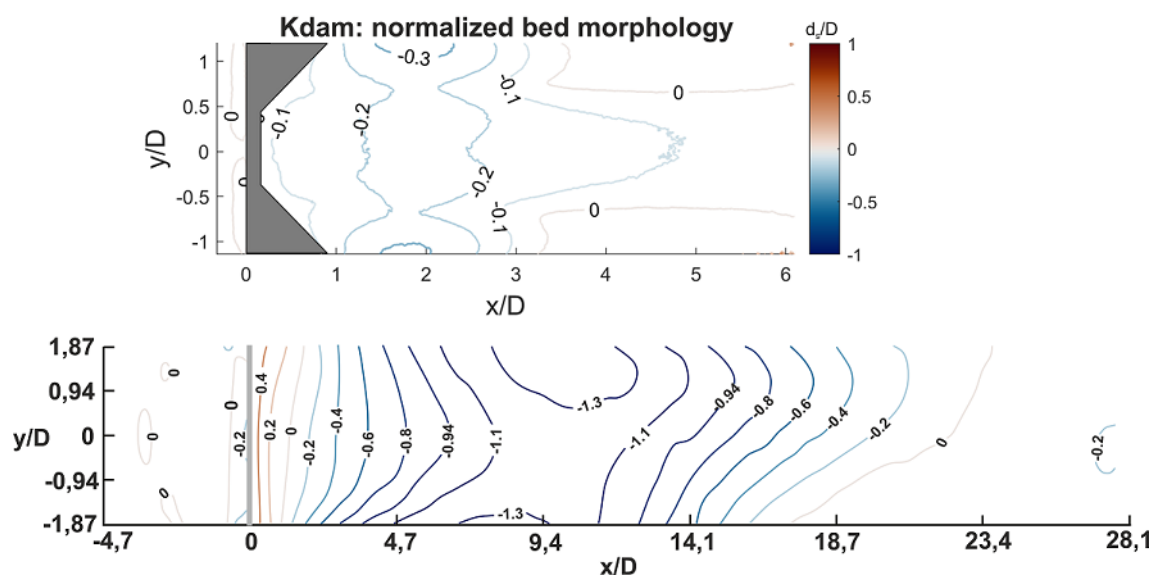
Figure 5.17: Comparison of normalized bed morphologies of this study (above) with literature values from Guan, Melville, and Friedrich (2014) (below) for Kdam.

Immediately downstream of the dam, a slight dune is observable in Guan, Melville, and Friedrich (2014), which is not detected in the present study, possibly due to differing downstream geometries of the structures. The relative scour depth is d_s/D = 1.3 in Guan, Melville, and Friedrich (2014) and 0.3 in the present case. Despite indications such as the difference in flow intensity (U_0/U_c = 0.87 in Guan, Melville, and Friedrich (2014) and 0.9 in the present case), the overtopping ratio (h_s/h_0 = 0.33 for Guan, Melville, and Friedrich (2014) and 0.4 for this study), and the relative sediment size (D/d_{50} = 105 for the present case and D/d_{50} = 137 for Guan, Melville, and Friedrich (2014), categorizing it as fine sediment), suggesting a higher relative scour depth for the present case, the observed trend is opposite. The variations in relative scour depth are attributed to the distinct observed flow fields. Guan, Melville, and Friedrich (2014) note a recirculation zone downstream of the submerged weir and two transversal circulating cells (w/h_0 = 2.9). In this study, another type of flow field was detected and is explained in chapter 5.3.

Concluding remarks

The physical model experiments with movable bed revealed that all tested structures are able to create scour holes that surpass the target scour depth. The TP generates the deepest and the largest (in terms of area and volume) scour and is the favourable variant for further development. Comparison with literature values showed a good qualitative agreement of the scour generated and hence the developed experimental setup can be evaluated at suitable for answering the research question.

5.3   Analysis of the hydrodynamics at equilibrium stage

The preceding chapter presented findings from the physical model experiment, concentrating on bed morphology in the vicinity of the structures. This chapter aims to complement those experiments by providing insights into the hydrodynamics and flow field evolving around the structures and within the scour hole through numerical simulations (see chapter 4.3). The boundary conditions are set to an HQ2 (considered as morphologically active discharge as explained in chapter 4.1.2), intending to contribute to the understanding of scour hole formation and conservation processes. The Landesstudie Gewässerökologie (Becker & Ortlepp, 2022) recommends a discharge range of $Q_{30} - Q_{330}$ (a discharge that is present for 30 to 330 days per year) for assessing habitat functionality. Therefore, additional simulations are necessary for an in-depth biological evaluation as a deep pool habitat. While further scenarios are necessary for comprehensive fish biological evaluations, the simulations at HQ2 offer valuable insights into the scour formation phase and additionally into potential usage as flood refuge habitats. Particularly in modified river landscapes, especially within channelized riverbeds, where traditional flood refuges for fish may no longer exist, a biological evaluation as flood refuge may be interesting. In conclusion, the results presented in this chapter need to be interpreted in the context of revealing hydrodynamics during the scour formation and conservation phase and do not attempt to serve as a basis for the biological evaluation as a deep pool habitat.

The chapter first starts with a methodical validation of the flow velocities of the numerical model with the flow velocities measured in the physical model. Subsequently, sensitivities of the different turbulence models are shown and the chapter concludes with the analysis of the hydrodynamics for all structures.

5.3.1   Comparison of hydrodynamic parameters in the numerical and physical model

The validation of the numerical model involved a comparison of mean flow velocities and standard deviations for the u- and v-components at selected measurement points in the physical model. Figure 5.18 provides an illustration of measurement points, taking the RP as an exemplary case. It's important to note that the simulation time for the Large Eddy Simulation (LES) was 90 seconds, and the Laser Doppler Anemometry (LDA) ceased once 2000 measurements were reached. Consequently, there's a difference in measurement time between the numerical and physical model.
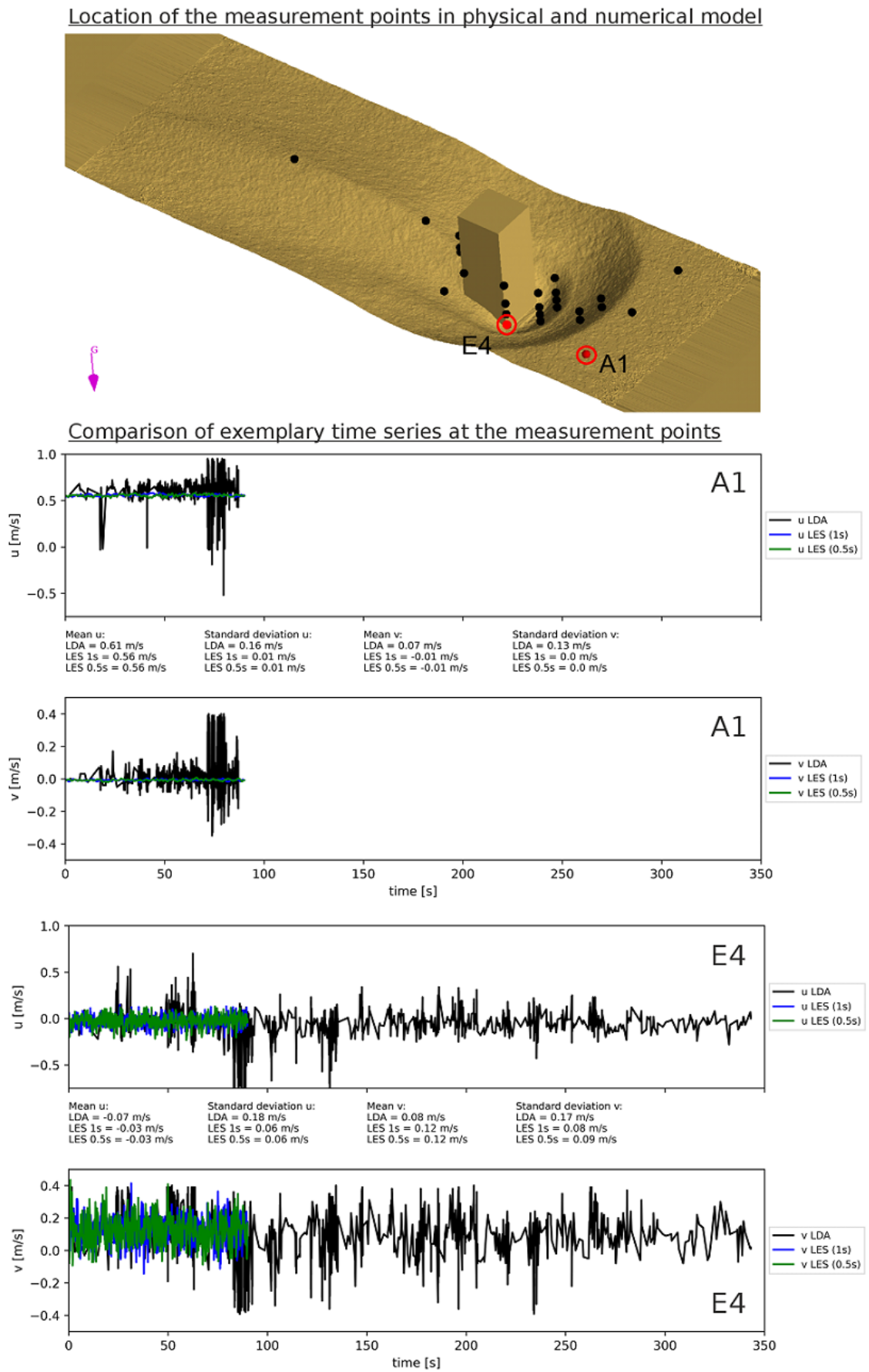
Figure 5.18: Comparison of exemplary measurement points in physical and numerical model.

The two highlighted points in figure 5.18, represent a location in the approach flow (A1) and a point inside the scour hole (E4). A comparison reveals that the approach flow in the numerical model exhibits a slightly smaller mean flow velocity and significantly lower standard deviations. This discrepancy is likely attributed to different inlet conditions in the two models. The physical model is fed by an inlet tank, with flow harmonized by a honeycomb structure and a wave board. Given the relatively short length of the flume in the physical model, it is assumed that perfect approach flow conditions are not achieved until reaching the measurement section. However, since this study primarily focuses on comparing different structures the conditions in the physical model were deemed sufficiently accurate for the research. In contrast, the numerical model assumes "perfect" approach flow, lacking an inlet tank. Consequently, the physical model exhibits higher standard deviations than the numerical model. Examining point E4 inside the scour, it becomes apparent that the approach flow conditions do not significantly influence the flow field inside the scour. Mean flow velocities and standard deviations in both flow components closely align with the physical model.

Additionally, the time intervall for data extraction of the simulation was varied to see eventual sensitivities regarding capturing turbulence for a smaller time intervall. The results demonstrate that the 1-second time intervall is sufficiently short to capture turbulence accurately as it does not differ from the 0.5-second time intervall. The mean flow velocities are therefore based on the simulations with a 1-second time intervall to save simulation time. To facilitate the comparison of all measurement points, the points are organized into four different groups to identify potential differences within each group. These groups correspond to specific flow regions: approach flow (blue), above the scour (orange), inside the scour (green), and downstream of the structure (red). The displayed error for each group represents the differences in mean flow velocities between the corresponding points in the physical and numerical model. Figure 5.19 illustrates the correlation of mean flow velocities in the x-direction. Remarkably, for all structures (except the Circular Pier), the correlation falls within the range of +/- 0.2 U_0. This alignment can be considered a favorable outcome given the complexity of the flow under investigation. Notably, there are no discernible trends indicating that any particular group exhibits consistently higher differences between the physical and numerical model. Figure 5.20 shows a similar trend for the correlation of mean flow velocities in the y-direction.

The above explained differences in physical and numerical model are also known from literature studies, e.g. Khosronejad et al. (2013). In this study they could show that differences between ADV measurements in a physical model and LES simulations are up to 1.0 U/U_0. The main differences for a groyne (rock vane, comparable to DG) were identified in the streamwise velocity profiles near the water surface downstream of the structure and also close to the bed. A J-Hook vane showed differences especially in the vicinity of the recirculating region in the wake of the structure and in the profiles in the middle of the water depth. The cross vane (comparable to Kdam), showed the greatest differences for the streamwise velocities near the bed.
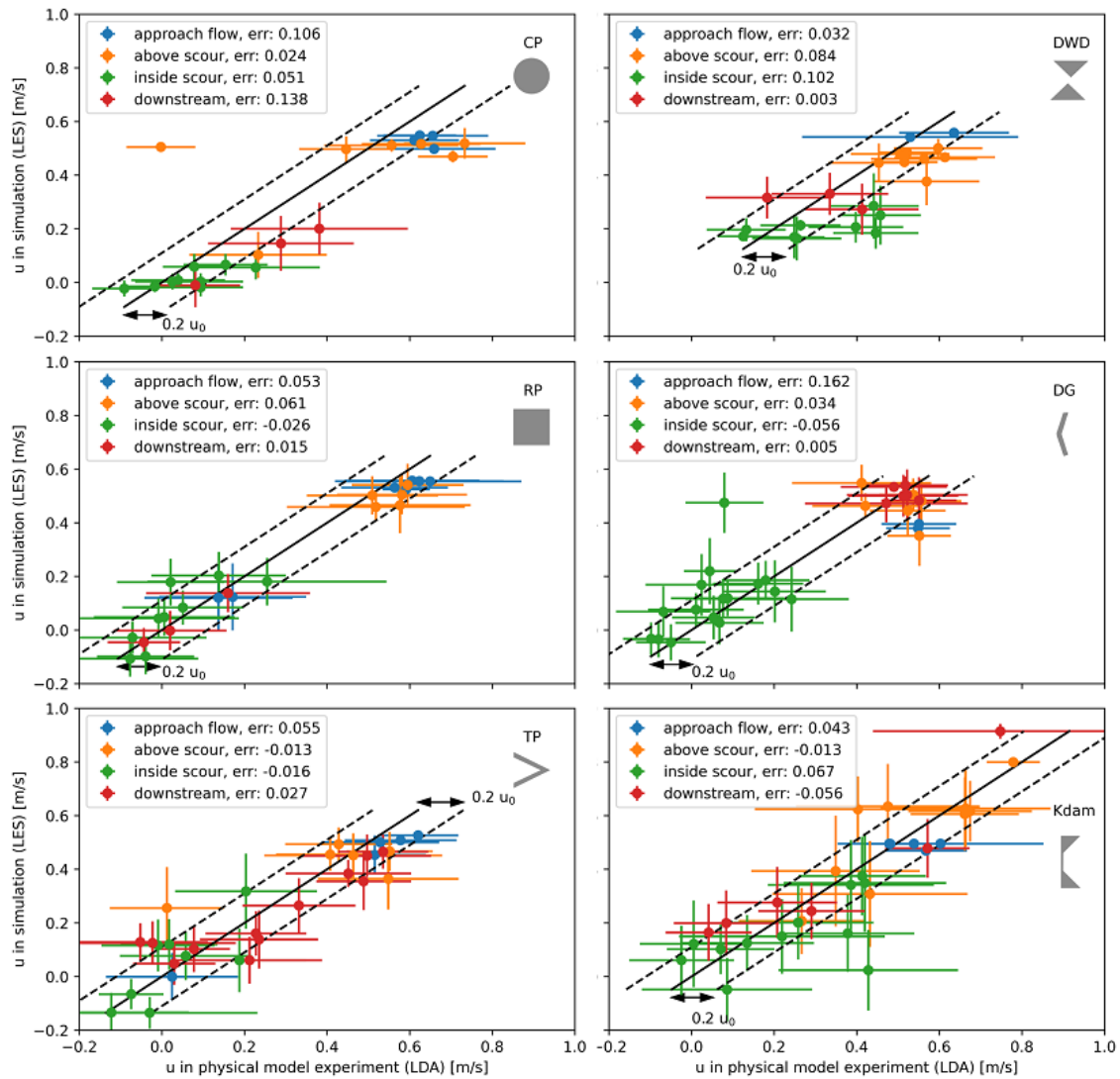
Figure 5.19: Comparison of the mean flow velocities $\overline{u}$ (marked with a dot) and the standard deviations of u (marked with horizontal and vertical lines) at the measurement points in the physical and numerical model.
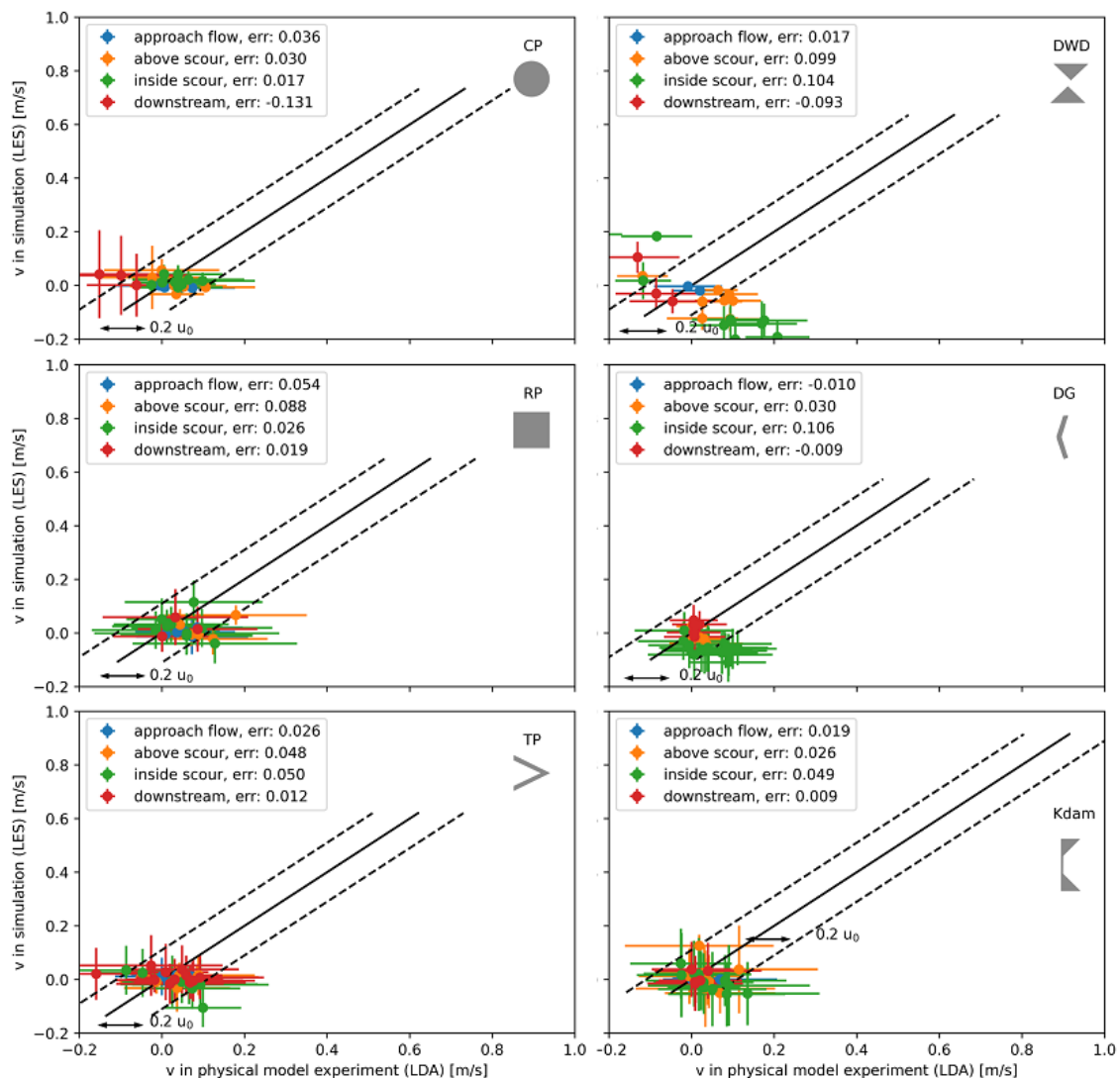
Figure 5.20: Comparison of the mean flow velocities $\overline{v}$ (marked with a dot) and the standard deviations of v (marked with horizontal and vertical lines) at the measurement points in the physical and numerical model.

In conclusion, it can be asserted that the flow velocities predicted by the numerical model align with sufficient accuracy with those observed in the physical model. This validation supports the use of numerical simulations as a valuable complement to physical model experiments, alleviating the need for time-intensive Laser Doppler Anemometry (LDA) measurements. Moreover, this validation extends the capability to model various discharges and predict the flow velocity field with confidence.

5.3.2 Comparison of turbulence models

Within the numerical study, two distinct turbulence model approaches were employed (see chapter 4.3): the Large Eddy Simulation (LES) and the Renormalization Group (RNG) model. Figure 5.21 illustrates the variations that result from applying them to model mean flow velocities.
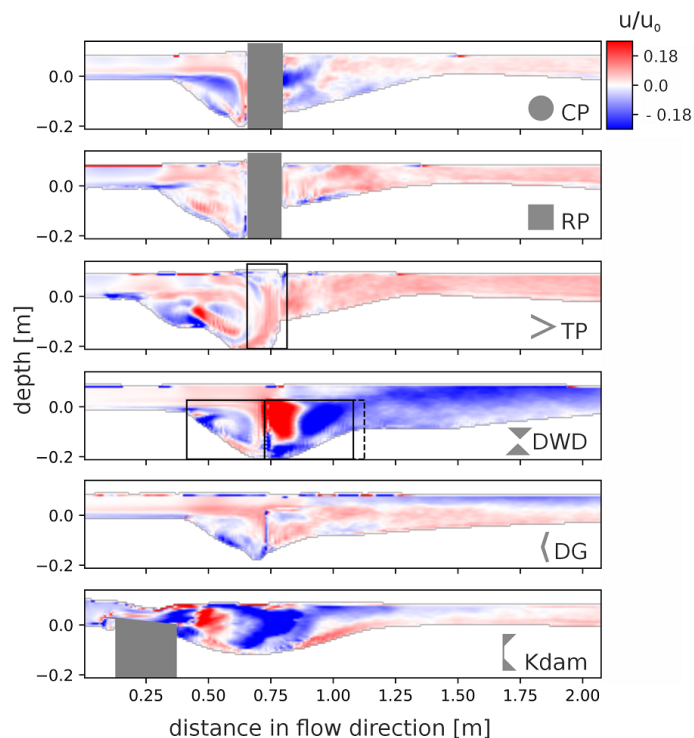
Figure 5.21: Differences of mean flow velocities as simulated with RNG and LES turbulence models ($U_{LES} - U_{RNG}$).

Notably, the pier-like structures exhibit differences in the downflow component upstream of the pier, with the LES predicting higher velocities compared to the RNG. Additionally, the LES model predicts lower mean flow velocities above the bed than the RNG model. Overall, for the pier-like structures these differences are within a range of 0.2 U/U_0, a magnitude consistent with findings from other studies (Khosronejad et al., 2013).

The DG, a stone-like structure exhibits variations comparable in magnitude to those observed in pier-like structures, along with lower mean flow velocity estimates at the bed for the LES model. In contrast, the DWD displays more substantial differences downstream of the structures for both turbulence model approaches. These differences surpass 0.25 U/U_0 in large areas. Comparable studies employing LES and RNG approaches for simulating scours around stone-like structures draw similar conclusions regarding the differences between both model types. In Khosronejad et al. (2013) the differences between the turbulence model approaches were, as for the pier-like structures above, within the range of 0.2 U/U_0 as observed in this investigation. Differences while modeling an inclined groyne with an URANS and LES models were identified primarily in the shear layer zone, in the backwater zone downstream of the

groyne, and near the bed.

The Kdam displays high differences downstream of the structures that surpass 0.25 U/U_0 in large areas. Khosronejad et al. (2013) also investigated a cross-vane structure, which is dam-like and thus comparable to the Kdam. Differences in turbulence models for the cross-vane were noted in shear layer regions and near the bed. Particularly, URANS struggled to predict regions of low streamwise momentum near the side walls. Overall differences between the two turbulence model approaches were around 1.0 U_0 for the cross-vane. The LES model exhibited significantly better performance for the cross-vane, which is attributed to different flow mechanisms. At the cross-vane, the flow accelerates over the structure and plunges on the bed downstream, resembling a jet-like flow with highly unsteady flow patterns. As a result of more accurate flow velocity modeling, the LES also demonstrated better accuracy in recreating the bed morphology from the physical model experiment.

It is crucial to note that the flow field surrounding the investigated structures is of complex, three-dimensional nature. Small alterations, such as changes in the direction or angle of a vortex, can result in significant discrepancies in a single cross-section. Khosronejad et al. (2013) also note the challenge of illustrating the three-dimensional velocity field in velocity profiles and recommends using streamline plots instead. The streamline plots unveil that the LES is capable of simulating more complex vortex structures compared to the RNG model approach. Figure 5.22 depicts a discrepancy downstream of the groyne, where the URANS/RNG shows one vortex cell, whereas the LES shows two cells — similar observations to those made in our simulations.
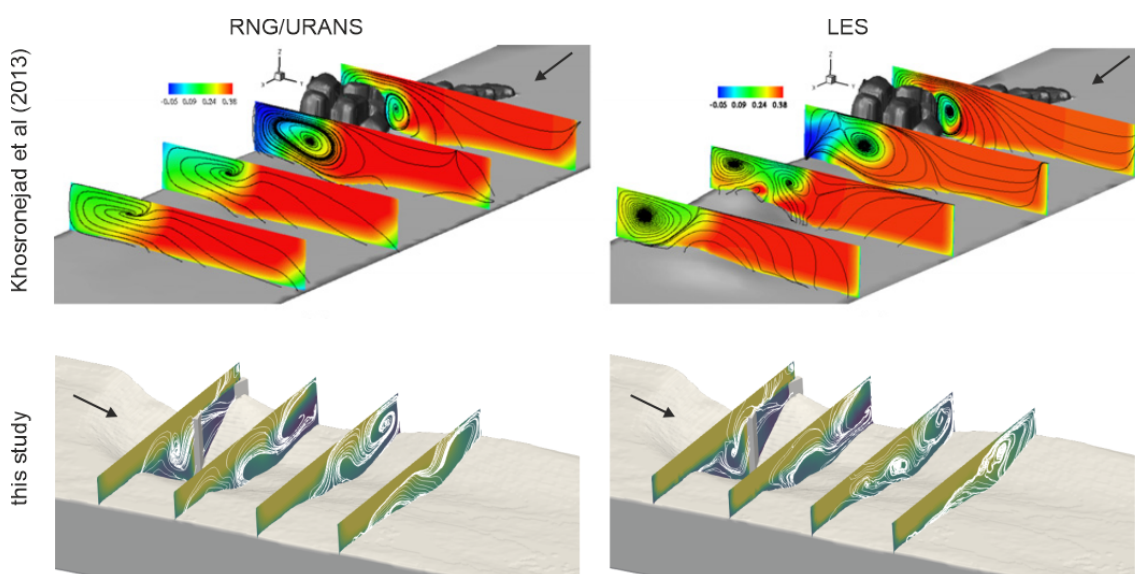
Figure 5.22: Comparison of streamlines in several cross-sections downstream of a groyne for RNG and LES turbulence models.

In conclusion, the differences in mean flow velocities that result from the different turbulence model approaches lay within the known ranges from literature and are suitable for further analysis. The mean flow velocities and standard deviations presented in the following chapters

are based on the LES approach, as this approach enables the characterization of velocity fluctuations and is known to give better results for complex three-dimensional flow fields as RNG models (Kirkil, Constantinescu, & Ettema, 2008; Khosronejad et al., 2013).

5.3.3 Hydrodynamics at equilibrium stage

The following chapter shows the hydrodynamic details of each structure as well as a comparison of the different structures and with literature values.

Hydrodynamics of pier-like structures

Figures 5.23 and 5.24 illustrate the well-known velocity field surrounding a circular pier, featuring a downflow upstream of the pier, a backwards rotating surface roller, a horseshoe vortex and wake vortices downstream of the pier. The flow reaches a stagnation point upstream of the pier where the flow parts into a backwards circulating surface roller at the upper part of the pier and a downflow at the lower part of the pier that initiates the scour hole. The surface roller comes along with a water level increase (see chapter 5.4.2). The downflow exhibits a strength of 0.87 U_0, slightly surpassing the predictions of 0.6-0.8 U_0 as referenced in Raudkivi (1986) and Dey and Raikar (2007) in chapter 3.3. When reaching the bed inside of the scour the flow is deviated into a forward rotating vortex. The flow is then starting a helical motion around the sides of the pier as shown in figure 5.23. This helix is called the horseshoe vortex and is known to be the main driver of sediment transport out of the scour hole (Breusers & Raudkivi, 1991). The reader is reminded that the horseshoe vortex system forms as a result of the scour hole and is not the cause of the scour hole (Kirkil, Constantinescu, & Ettema, 2008). Within the vortex and above the berm low mean flow velocities can be detected as well as downstream of the pier (see figure 5.24). The presence of the customary primary and secondary horseshoe vortex, as shown in studies by Euler and Herget (2012) and Kirkil, Constantinescu, and Ettema (2008), remains elusive in the current simulations. This is more likely attributable to discretization artifacts in the simulation rather than their actual absence. The distinctly observed berm within the scour hole of all pier-like structures strongly suggests the existence of a dual horseshoe vortex system. The cross section in the z-plane in target depth shows a zone of high mean flow velocities at a small layer around the pier which is due to the acceleration of the flow around the pier.

The standard deviations serve as an indicator of velocity fluctuations within the flow, as illustrated in figure 5.24. Elevated standard deviations are observable in the downflow, the primary horseshoe vortex, and notably downstream of the pier. The increased standard deviations downstream of the pier result from vortices alternately detaching from both sides of the structure. As the wake vortices form as a consequence of alternating vortices, they do not considerably contribute to sediment removal (Breusers, Nicollet, & Shen, 1977; Akhlaghi et al., 2020) and a dune forms in this area. Further analysis of turbulence, including turbulence intensity and turbulent kinetic energy, is available in annex B.1. Increased turbulence (turbulence intensity and TKE) can be observed at the sides and downstream of the pier, which is

in accordance with MacVicar and Roy (2007), MacVicar and Roy (2011), and Dashtpeyma (2019) who observed increased turbulence inside of natural and forced pools as shown in chapter 2.2.1. A deeper analysis did not yield additional insights in this instance and is therefore omitted from this analysis.
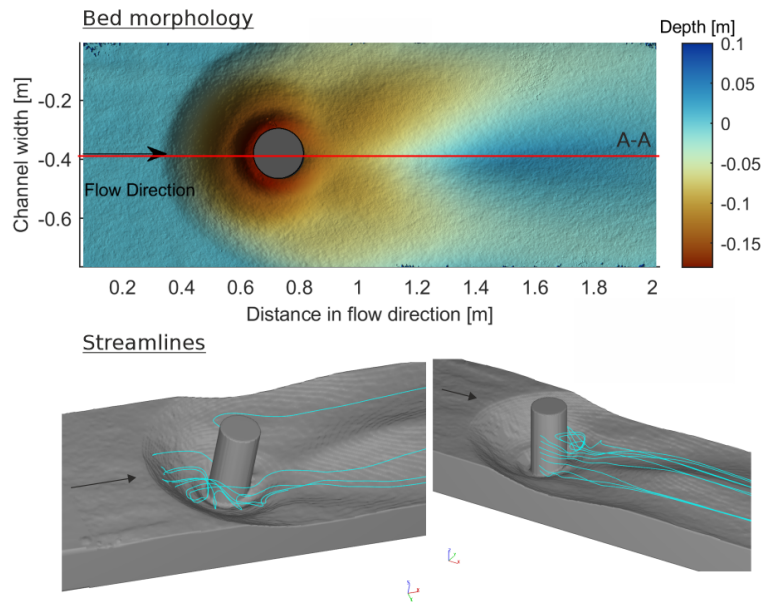
Figure 5.23: Average bed morphology and selected streamlines around the CP. Boundary conditions: $Q = 30.9\,l/s$ and $h_{outlet} = 6.91\,cm$.
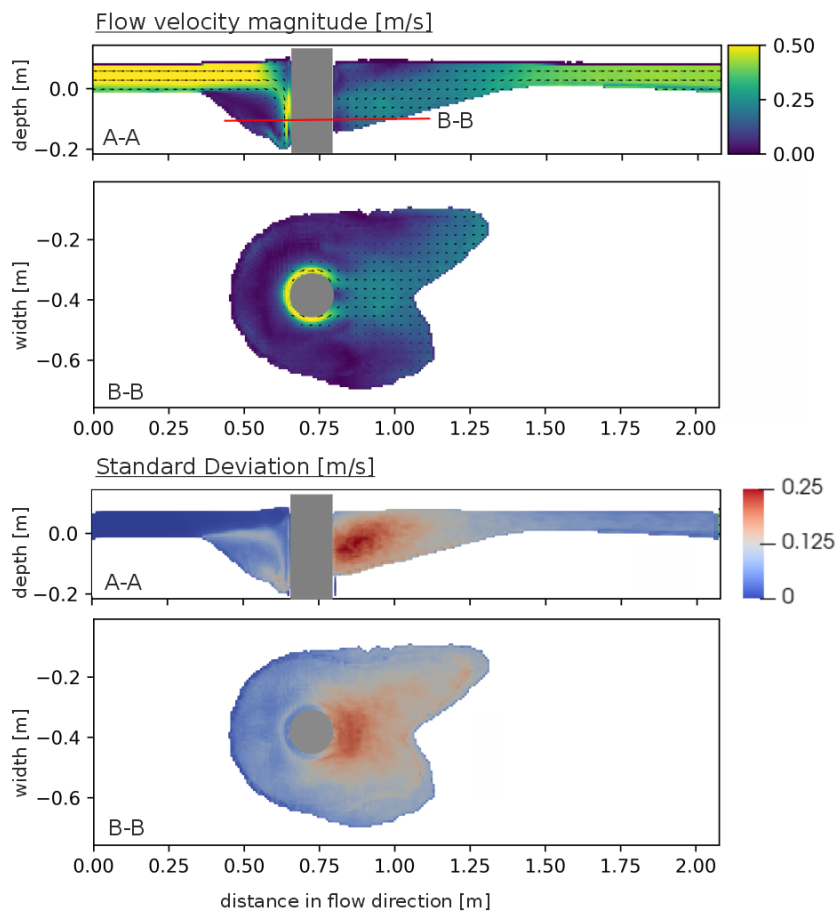
Figure 5.24: Mean flow velocities and standard deviations for y = - 0.39 m (A-A) and z = - 0.08 m (B-B) around the CP. Boundary conditions: $Q = 30.9 \, l/s$ and $h_{outlet} = 6.91 \, cm$.
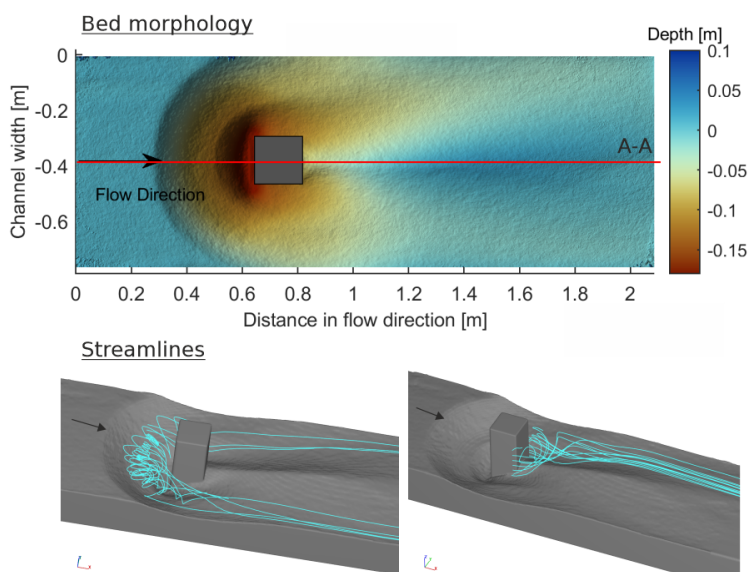
Figure 5.25: Average bed morphology and selected streamlines around the RP. Boundary conditions: $Q = 30.9 \, l/s$ and $h_{outlet} = 6.84 \, cm$.

The flow dynamics around the rectangular pier closely mirror those observed around the circular pier, featuring a primary horseshoe vortex, a surface roller, and a helical motion around the pier, as illustrated in figures 5.25 and 5.26. Consequently, both pier-like structures exhibit similar fundamental flow patterns. However, distinctions emerge, particularly in the rectangular pier (RP), where higher flow velocities are evident directly above the bed, accompanied by elevated standard deviations within the scour hole and downstream of the pier. The downflow component is of a strength of 0.87 U_0, which is in good accordance with the predicted value of 0.8 U_0 (= 40% higher than the circular pier with 0.6 U_0 as referenced in Dey and Raikar (2007)). The edges of the RP induce a well-defined detachment point, characterized by increased velocity fluctuations, notably showcased in the cross-sectional view along the z-axis (B-B) in figure 5.26. The fluctuations are significantly higher at the edges of the RP than at the sides of the circular pier. In the physical experiments a stable vortex could be observed at the edges of the RP, exhibiting sufficient strength to maintain sediment in suspension and which coincides with the location of the increased velocity fluctuations. The stable vortex and the associated velocity fluctuations contribute to an increased scour depth, area, and volume around the RP in comparison with the circular pier (CP).
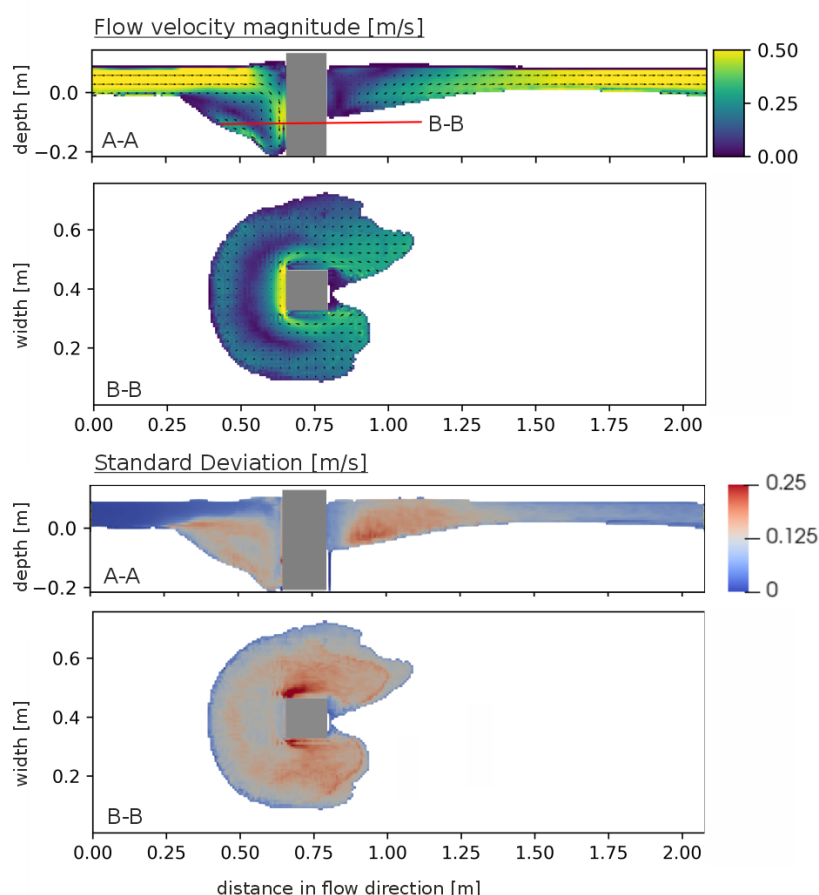
Figure 5.26: Mean flow velocities and standard deviations for y = 0.39 m (A-A) and z = - 0.08 m (B-B) around the RP. Boundary conditions: $Q = 30.9\,l/s$ and $h_{outlet} = 6.84\,cm$.

The Triangular Pier (TP) exhibits a flow pattern similar to the previous pier-like structures, featuring a horseshoe vortex and wake vortices downstream as shown in figures 5.28 and 5.29. However, distinctive characteristics set the TP apart, contributing to a significantly larger scour area and volume for this pier shape. Notably, the TP has an open upstream face, allowing the flow to penetrate the structure—a key difference from the CP and RP, which have closed upstream faces. The closed upstream face causes an immediate redirection of the flow towards the bed at an approximately 90° angle (see figure 5.27) and a deviation of the flow to both sides of the pier. The downflow in these cases reaches velocities of up to 0.87 U_0 before losing strength upon reaching the bed. The open front face of the TP enables the flow to penetrate the structure and concentrates the incoming flow here, in contrast to diverting parts to both sides. The downflow upstream of the TP culminates in a nearly circular vortex, rather than being diverted at a right angle as in the cases CP and RP. Unlike the CP and RP, the highest flow velocities in the TP are not observed in the downflow but at the vortex's end, where it touches the bed and entrains sediment. The undisturbed and full development of the vortex, leading to increased flow velocities at the bed of the scour hole, together with the concentration of the flow inside of the structure is the primary cause of greater scour hole formation for the TP. The primary horseshoe vortex of the TP exhibits high velocity fluctuations, as do the wake vortices downstream. Although the standard deviations at the detachment points of the TP do not reach values as high as those of the RP, it is noteworthy that the edges and the openness of the upstream face both play crucial roles in scour formation. This insight suggests that a similar increase in scour depth could be anticipated if the CP and RP had open faces in the upstream direction.

Considering the drag coefficients (C_D) for a circular cylinder and an open half-cylinder (1.17 and 2.3, respectively, in the Reynolds-invariant range from Hoerner (1965)), it becomes evident that the open half-cylinder imposes much higher resistance to the flow than the closed cylinder. Similar observations were done for a closed and an open triangular shaped pier (C_D values of 2.00 and 2.2 respectively, for more details refer to chapter 5.4.2). This implies the formulation of the hypothesis that the increased flow resistance in open structures, in contrast to closed structures, arises from the different deviation angles and concentration of the incoming flow and hence different vortex shapes and sizes. The full formation of the vortex imposes an additional resistance to the flow and also leads to a deeper scour.
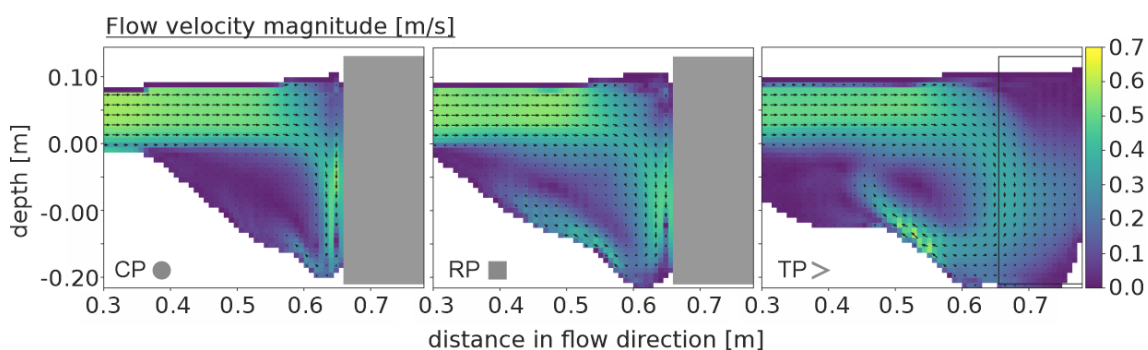
Figure 5.27: Detail of the primary horseshoe vortex for the three pier-like structures. Note the different color bar for this figure.
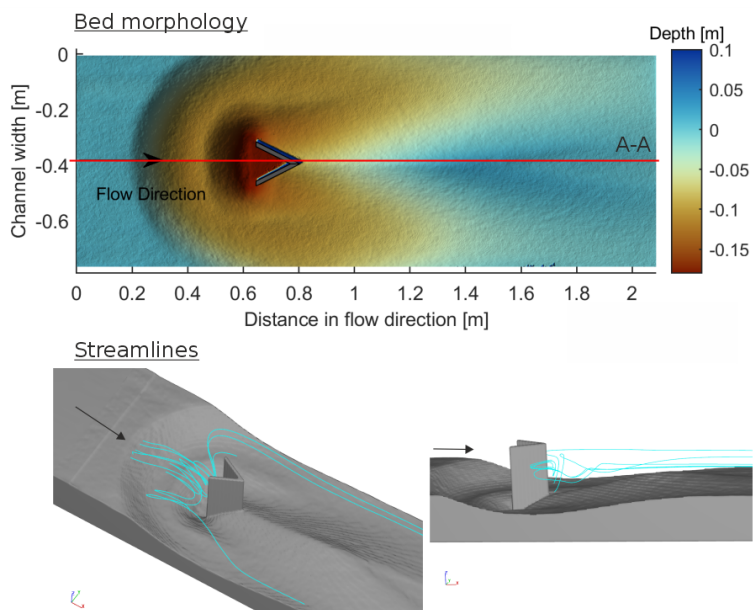
Figure 5.28: Average bed morphology and selected streamlines around the TP. Boundary conditions: $Q = 30.9\,l/s$ and $h_{outlet} = 7.42\,cm$.
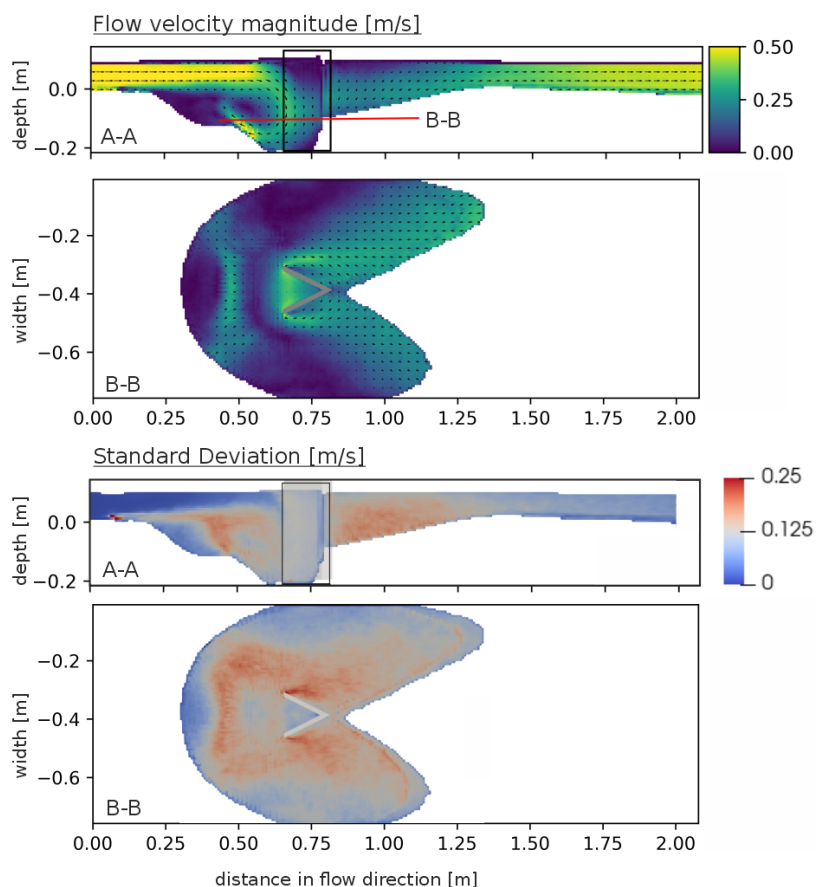
Figure 5.29: Mean flow velocities and standard deviations for y = 0.39 m (A-A) and z = - 0.08 m (B-B) around the TP. Boundary conditions: $Q = 30.9\,l/s$ and $h_{outlet} = 7.42\,cm$.

Hydrodynamics of stone-like structures

Analysis of the mean flow velocities around the DWD (refer to figure 5.31) reveals that the flow is diverted into the scour hole only directly above it. Along the side and at the edge of the right wing, the flow is marked by higher mean flow velocities. Figure 5.30 illustrates a complex helical motion of the fluid both up- and downstream of the right wing, postulated as the primary mechanism driving sediment entrainment and transport. The upstream helix entrains sediment, leading to a transport in downstream direction and concurrent growth of the scour hole in upstream direction. The helix downstream of the right wing plays a crucial role in further sediment transport downstream of the DWD, contributing to the elongated deeper zone downstream of this wing. The edge of the right wing is the initial detachment point for the flow, characterized by a zone of high standard deviations extending downstream from the wing and visible throughout the whole height of the wing (refer to figure 5.31). At the left wing, a stable vortex detaches, observed in both numerical simulations and physical model experiments, where sediment remained in suspension even during equilibrium conditions.
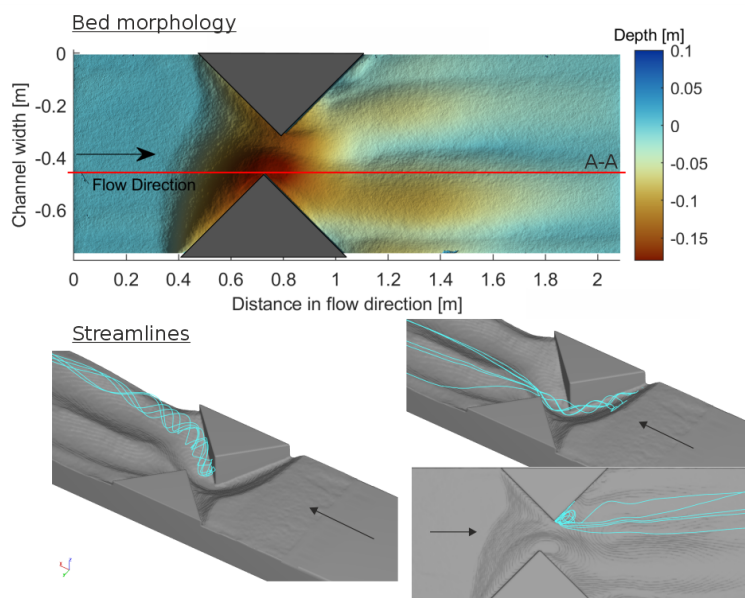
Figure 5.30: Average bed morphology and selected streamlines around the DWD. Boundary conditions: $Q = 30.9 \, l/s$ and $h_{outlet} = 6.90 \, cm$.
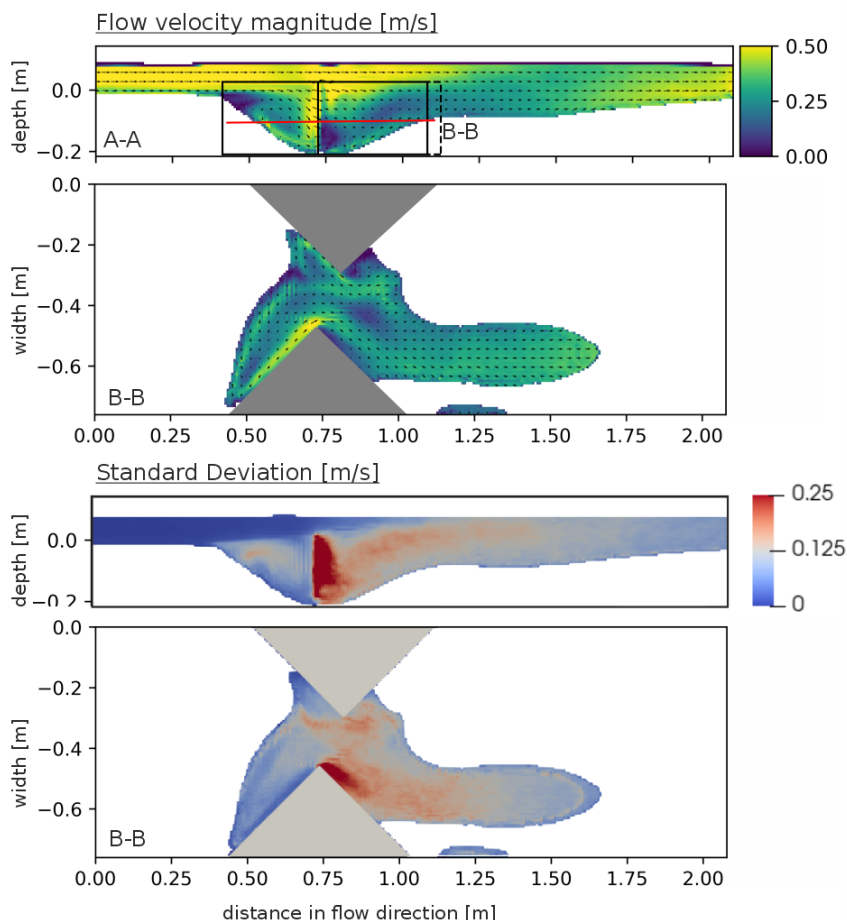
Figure 5.31: Mean flow velocities and standard deviations for y = 0.46 m (A-A) and z = - 0.08 m (B-B) around the DWD. Boundary conditions: $Q = 30.9\,l/s$ and $h_{outlet} = 6.90\,cm$.

An observation, particularly evident in the flow field around the DWD, is that the mean flow velocity profiles in various cross-sections fail to adequately depict the presence of the two helices. The intricate nature of this flow feature is effectively captured only by the streamlines, as already outlined by Khosronejad et al. (2013). Recognizing this is crucial, especially in the context of fish biological evaluation procedures. The helical motion zone may pose challenges for fish, as they could struggle to establish a rheotactic direction. Relying solely on mean flow velocity profiles in biological assessments might lead to overlooking the helical motion, potentially misclassifying the scour as a suitable deep pool habitat. In reality, the fish might prefer the upper part of the scour hole where the helical motion is absent.

At the Deflected Groyne (DG), the incoming flow separates, with one part being redirected into the scour hole and another part flowing above the DG unaffected, as depicted in figure 5.33. Immediately upstream of the DG, the flow is diverted downwards, initiating a helical motion of the fluid in the form of a forward-rotating vortex, as illustrated in figure 5.32. This helix constitutes a primary driver for sediment entrainment and transport. The scour hole commences at the groyne's head, advancing upstream before expanding in the downstream direction. The helix itself is characterized by slower flow velocities than the approaching flow; it regains strength only above the bed, where sediment entrainment occurs. Flow separation oc-

curs at the groyne's head, creating a shear layer between the free flow and the backflow zone. The backflow zone features a stable vortex with vertical axis (similar to what was observed for the DWD), capable of maintaining sediment in suspension. Although standard deviations are elevated within the scour hole and downstream of the groyne, there isn't a distinct zone at the groyne's head with significantly increased standard deviations, unlike the DWD case. This distinction is likely due to the geometric configuration; the DG is a one-sided structure, while the DWD is two-sided. The DWD's dual constriction effect contributes to higher flow accelerations compared to the DG's single-sided influence, which leads to a larger scour hole for the DWD.
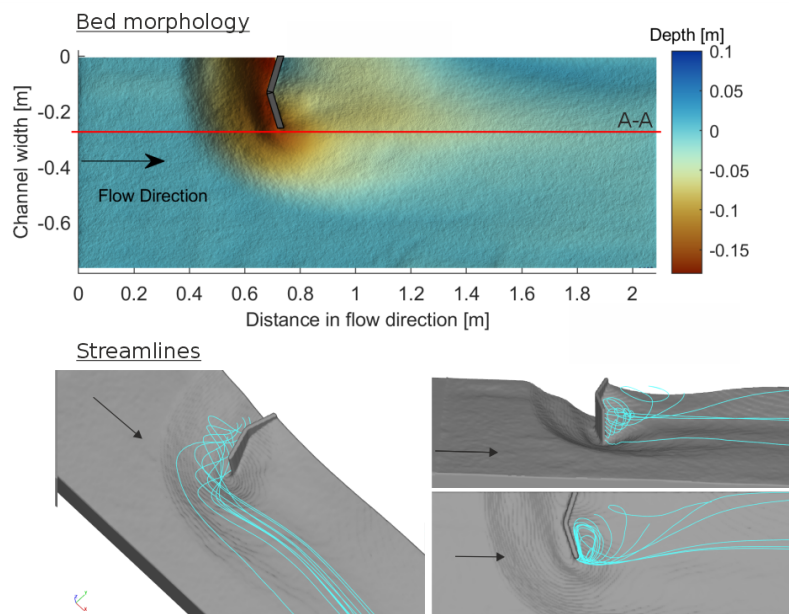
Figure 5.32: Average bed morphology and selected streamlines around the DG. Boundary conditions: $Q = 30.9\,l/s$ and $h_{outlet} = 6.87\,cm$.
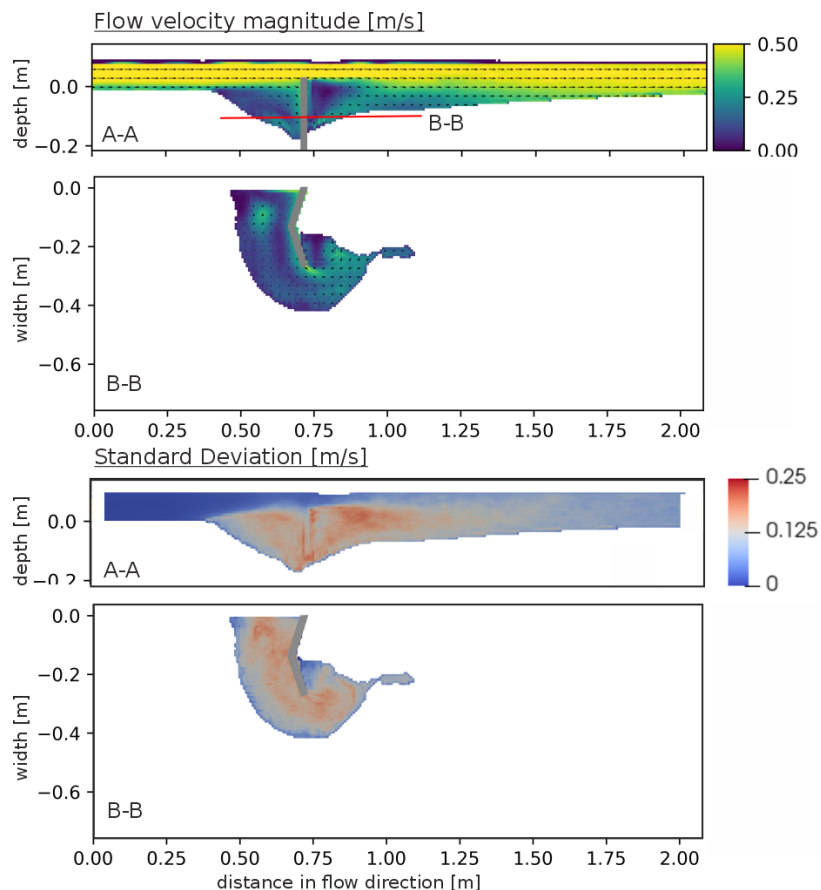
Figure 5.33: Mean flow velocities and standard deviations for y = 0.26 m (A-A) and z = - 0.08 m (B-B) around the DG. Boundary conditions: $Q = 30.9 \, l/s$ and $h_{outlet} = 6.87 \, cm$.

Hydrodynamics of dam-like structures
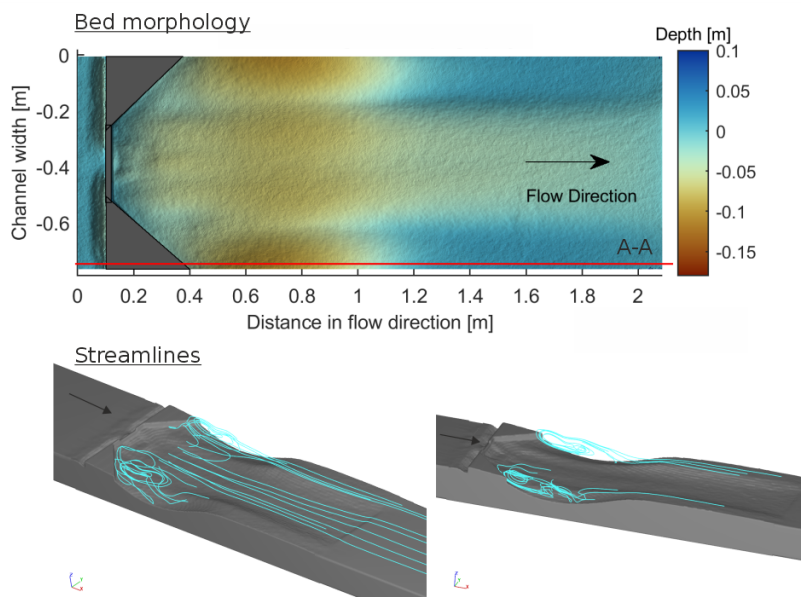
Figure 5.34: Average bed morphology and selected streamlines around the Kdam. Boundary conditions: $Q = 30.9 \, l/s$ and $h_{outlet} = 6.62 \, cm$.
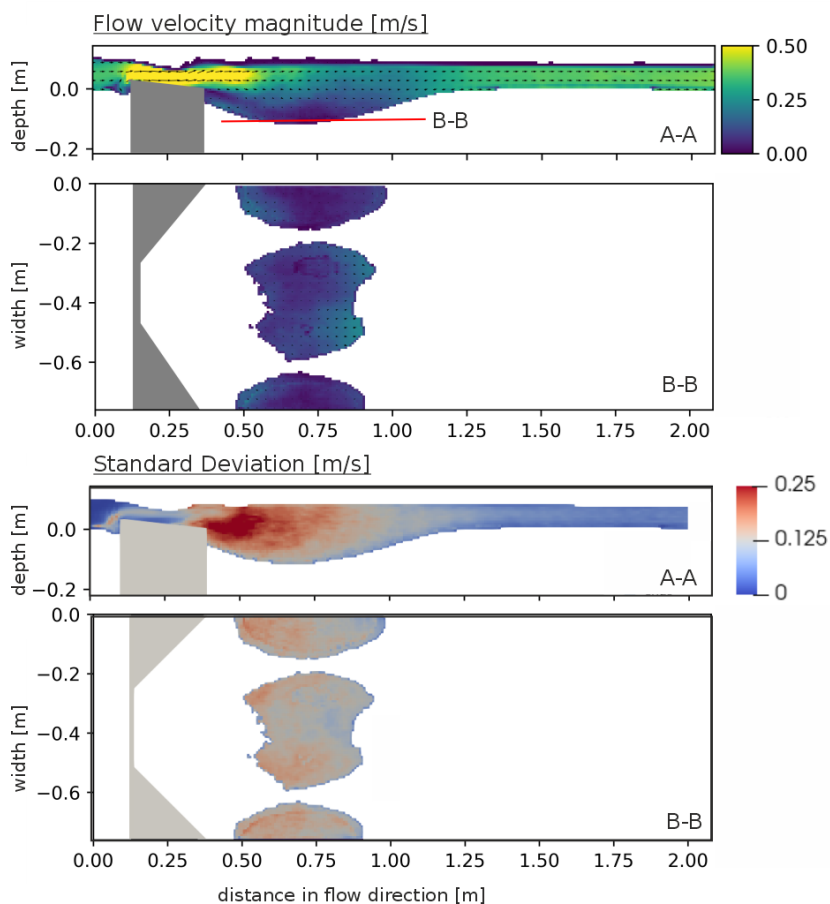
Figure 5.35: Mean flow velocities and standard deviations for y = 0.75 m (A-A) and z = - 0.08 m (B-B) around the Kdam. Boundary conditions: $Q = 30.9\,l/s$ and $h_{outlet} = 6.62\,cm$.

The presence of the Kdam induces a constriction across the entire width of the flume and corresponding simulation, resulting in an upstream water level increase. The flow experiences acceleration above the Kdam, extending downstream of it, as illustrated in figure 5.35. Downstream of the Kdam, the presence of strong waves, also observed in the physical model, is evident, resulting in a significant increase in standard deviations of flow velocities. Within the scour hole, mean flow velocities are notably lower than in the free flow. On either side of the Kdam, a vortex with a horizontal axis in y direction forms, stretching along the entire scour hole and serving as the primary driver for sediment entrainment and transport as shown in figure 5.34. Unlike the preceding structures, no helical motions were detected for the Kdam. In the centerline of the flume the flow plunges jet-like into the tailwater. In contrast to the observations of Guan, Melville, and Friedrich (2014) no circulating cells in longitudinal direction with horizontal axis in x-direction form. This is attributed to the different geometric shape of the dam, Guan, Melville, and Friedrich (2014) investigate a simple rectangular dam and in this study the more complex Kdam with triangular shaped sides and a notch in the middle was under investigation.

Concluding remarks

For pier- and stone-like structures helices seem to be the main driver for sediment entrainment and transport. In the case of the Kdam, vortices with a horizontal axis are present, yet no distinct helical motion can be observed. Analyzing water level differences between the Kdam and the other structures, it becomes apparent that the Kdam converts the kinetic energy of the approaching flow into potential energy. One might expect this potential energy to play a crucial role in creating a deep scour hole. However, the results reveal that potential energy is neither the exclusive nor the most significant factor in the scouring process. On the contrary, the helical motions identified in pier- and stone-like structures prove to be considerably more effective in creating and deepening scour holes.

5.4   Analysis of the backwater rise at equilibrium stage

Besides the bed morphology and the flow field inside of the scour, which are crucial for a functional deep pool habitat, especially the backwater rise is of high interest in urbanized and restricted areas. The subsequent subchapter initiates with a comparison between water level data from numerical simulations and measurements obtained from the physical model, serving as a validation step. Initial results are presented within this chapter. Subsequently, section 5.4.2, focusing on equilibrium backwater rise, primarily relies on data derived from the physical model experiment. Instances where numerical model data is utilized, such as in spatial water level distribution and certain aspects of drag coefficient analysis, are explicitly noted. Then, a simple analysis on the backwater rise based on $\Delta h_1/h_0$ and $\Delta h/h_2$ is done. Later a more complex analysis is done considering the drag coefficient.

5.4.1   Comparison of the backwater rise in the numerical and physical model

For the validation of the numerical model the correlation of backwater rise with the physical model is displayed in figure 5.36. The TP and the Kdam show the highest differences between numerical and physical model. In total the numerical model tends to estimate higher water levels than the physical model. As the differences are higher than expected subsequently a more detailed analysis is done.
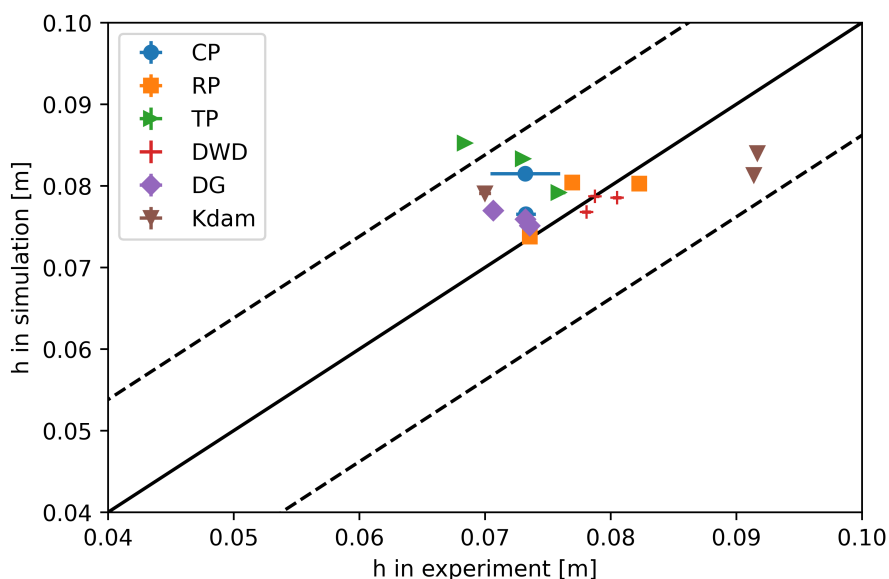
Figure 5.36: Correlation of water levels in the numerical and physical model. The dotted lines show a deviation of 0.2 h_0.

Figures 5.37 and 5.38 show the backwater rise in the longitudinal sections in the centerline of the flume. For the RP and the CP the upstream water level for numerical and physical model coincide very well. The TP shows rather high differences between numerical and physical model. Downstream of the structure the differences for all pier-like structures are high and it seems like that the numerical model is not able to model the water level drop downstream of the structure, when using the default settings of the turbulence models. Moreover the numerical model shows, that the location of the water level measurement devices in the physical model was not able to capture the maximum water level. This was indeed intended, as the maximum water level in the centerline is provoked by the surface roller which has only limited lateral extension as shown in figure 5.45 and therefore subordinate relevance for flood protection questions.
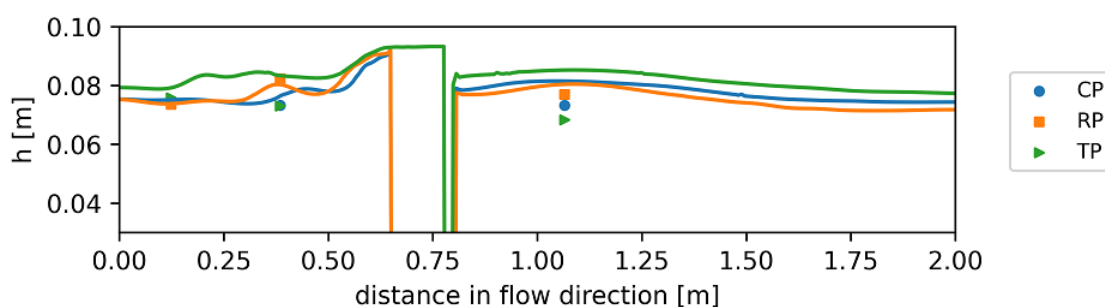
Figure 5.37: Comparison of water levels in numerical model (lines) and physical model (point data) for pier-like structures.

The water levels of the stone-like structures for numerical and physical model coincide very well. For the dam-like structure the numerical model is able to model nearly the height and length of the wave that forms downstream of the Kdam.
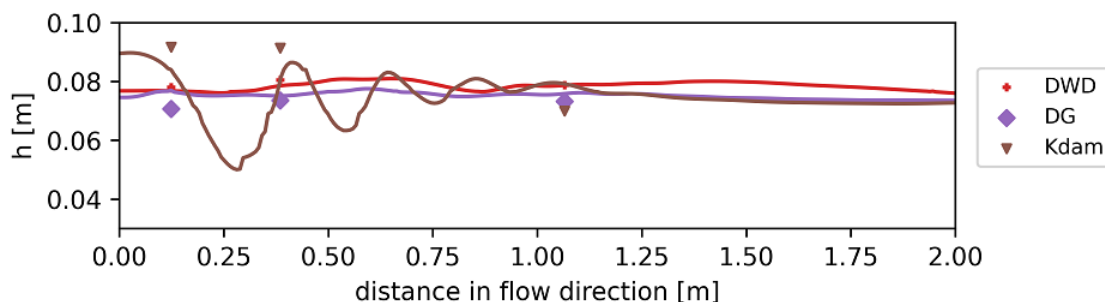
Figure 5.38: Comparison of water levels in numerical model (lines) and physical model (point data) for stone- and dam-like structures.

5.4.2 Backwater rise at equilibrium stage

Parts of this subchapter are part of Kannen, Seidel, and Franca (submitted in 2023).

Backwater rise in comparison with uniform flow conditions $\Delta h_1/h_0$ and $\Delta h/h_2$

The mean values and standard deviations of the water levels around the six different structures are displayed in figure 5.39. The pier-like structures show a significant water level increase upstream and a decrease downstream of the structure. The standard deviations tend to be higher downstream of the structure, which coincides with the region of larger standard deviations in flow velocities (see chapter 5.3). The DWD shows a tendency to higher water levels in comparison with the pier-like structures that extend also downstream of the structure. The Kdam shows significantly higher water levels upstream of the structure that also extend until the beginning of the flume. Consequently, the locations where the Kdam could be implemented in practice is very limited, as restricted and urbanized regions mostly have limited free board capacities. Surprisingly, the water level drop downstream of the structure does not drop below the uniform water level for any of the structures. This may be attributed to the experimental setup, as the regulation of the lamellas of the outlet were not able to keep the correct water level and were up to 5 % higher than previously planned. Obviously, this also influences the water level drop downstream of the structure as well.
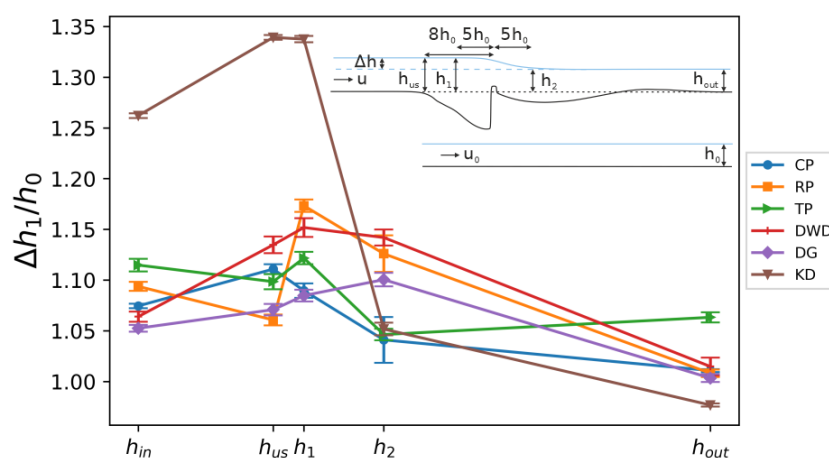
Figure 5.39: Mean values and standard deviations of the water levels in the center line of the physical model experiment. The structure is located between h_1 and h_2.

Especially for practitioners it is important to have a direct estimate on the backwater rise due to the implementation of an in-stream structure in comparison with the uniform water level. Therefore, changes relative to the uniform water level h_0 were assessed using the ratio $\Delta h_1/h_0 = (h_1 - h_0) \ h_0$. This ratio ranged from 7 to 16 % for pier- and stone-like structures, while dam-like structures exhibited a higher value of 31.8 % as shown in table 5.6.

Table 5.6: Normalized backwater rise provoked by different hydraulic structures in a movable bed at equilibrium conditions (data retrieved from physical model experiments).

Structure	$\Delta h/h_2$ [%]	$\Delta h_1/h_0$ [%]
CP	4.7	7.4
RP	4.2	15.7
TP	7.2	10.5
DWD	0.9	13.4
DG	-	6.9
KD	27.1	31.8

Figure 5.40 illustrates the backwater rise as a function of the blockage ratio of the in-stream structures. With increasing blockage ratio the backwater rise increases and a roughly linear correlation can be derived. Even though, it has to be admitted that the deviations from the trendline are quite high, especially evident for the pier-like structures, where the mean backwater rise is nearly doubled between th CP and the RP. For the final validation of a linear correlation more data on backwater rise needs to be included. An extrapolation of the trendline would indicate that structures with a blockage < 5 % could be neglected for backwater rise calculations, validating a common rule of thumb often applied for in-stream measures in river restoration; but with further validation in chapter 7.4.6, this hypothesis can be disproved.
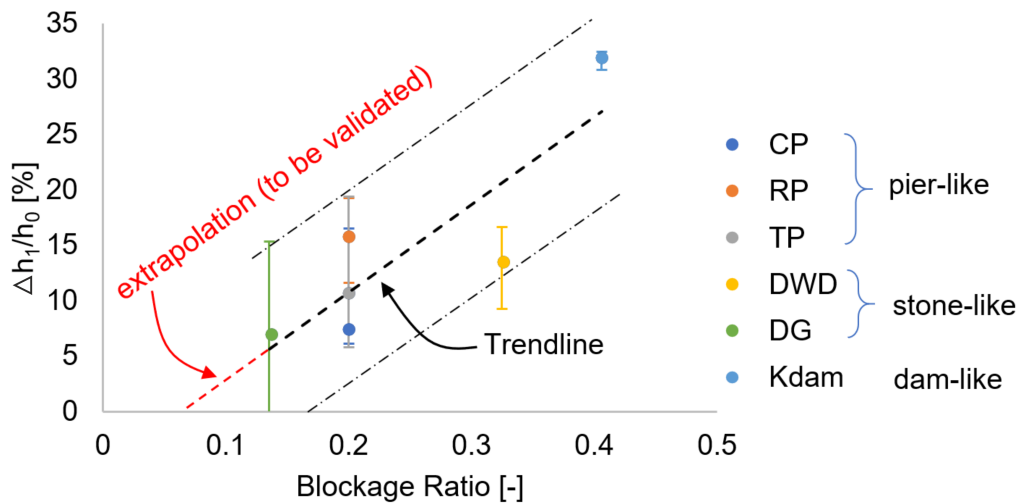
Figure 5.40: Mean values and and standard deviations of backwater rise for pier-, stone- and dam-like structures as a function of the blockage ratio, including a trendline.

To further evaluate the flood risk, the normalized backwater rise, $\Delta h/h_2$, at equilibrium stage is examined (refer to figure 3.36 for the definition of $\Delta h/h_2$). This value is often used in literature to characterize backwater rise (e.g. in Suribabu et al. (2011), Yarnell (1934), and El-Alfy (2006)). This value differs from the previous analysis, as the water level difference from up-to downstream is related to the downstream water level. This needs to be kept in mind for the further analysis. Literature data indicates a correlation between the backwater rise $\Delta h/h_2$ and the downstream Froude Number Fr_2, as demonstrated in different studies such as El-Alfy (2006) and Suribabu et al. (2011). Hence, the initial graphs present the downstream Froude Number Fr_2 on the x-axis. Although the discharge remained constant during the experiments

conducted in this work, resulting in minimal variation in downstream flow velocity and hence the downstream Froude Number Fr_2, this analytical approach may seem unconventional at first. Nevertheless, it ultimately serves the purpose of facilitating comparisons with values reported in literature. The second mainly influencing factor analysed in literature is the blockage ratio (Suribabu et al., 2011; Azinfar & Kells, 2009), which is analysed in detail within the drag coefficient considerations.The pier-like structures exhibited a normalized backwater rise, $\Delta h/h_2$, ranging from 4 to 8 % as shown in table 5.6. The DWD showed a minimal normalized backwater rise of 0.9 %. In the case of the DG, a water level drop was observed, which is not physically plausible. The author attributes this to the interference of a standing wave with the mean water level and thus exclude it from further analysis. The dam-like structure (Kdam) displayed a substantial normalized backwater rise of 27.1 %.

Figure 5.41 illustrates the mean value of three experiments for the backwater rise as a function of the downstream Froude number Fr_2 for various structure types. Among these, stone-like structures exhibit the lowest backwater rise, pier-like structures show an intermediate level, and the dam-like structure demonstrates the largest backwater rise. The variance in backwater rise can be attributed to the different flow patterns. Consequently, structures solely overflown induce a higher backwater rise compared to those diverting the flow on both sides. Structures that are overflown and do not span the entire river width result in the smallest backwater rise.
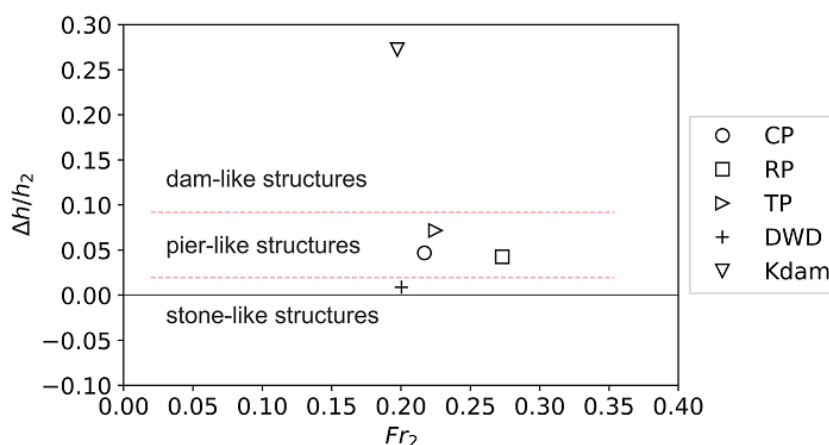
Figure 5.41: Mean values of backwater rise $\Delta h/h_2$ for different flow types (three replicates, data retrieved from physical model experiments).

Literature values for pier-like structures, as indicated in El-Alfy (2006), Suribabu et al. (2011), and Yarnell (1934), reveal an inconsistency in characterizing the backwater rise $\Delta h/h_2$, displaying an one-order-of-magnitude difference (refer to figure 5.42). The equations proposed by Suribabu et al. (2011) and Yarnell (1934) predict significantly lower backwater rise compared to the equation provided by El-Alfy (2006). The values obtained in this study fall between the predictions of these two literature sources. Conversely, the values for dam-like structures notably differ from the literature values of Gebhardt et al. (2012), likely attributed to the optimized Jambor weir sill geometry that significantly reduces backwater rise. In summary, it can be stated that the water level predictions around in-stream structures are still subject to sig-

nificant uncertainties, as evidenced by variations observed across various literature sources and in this work.
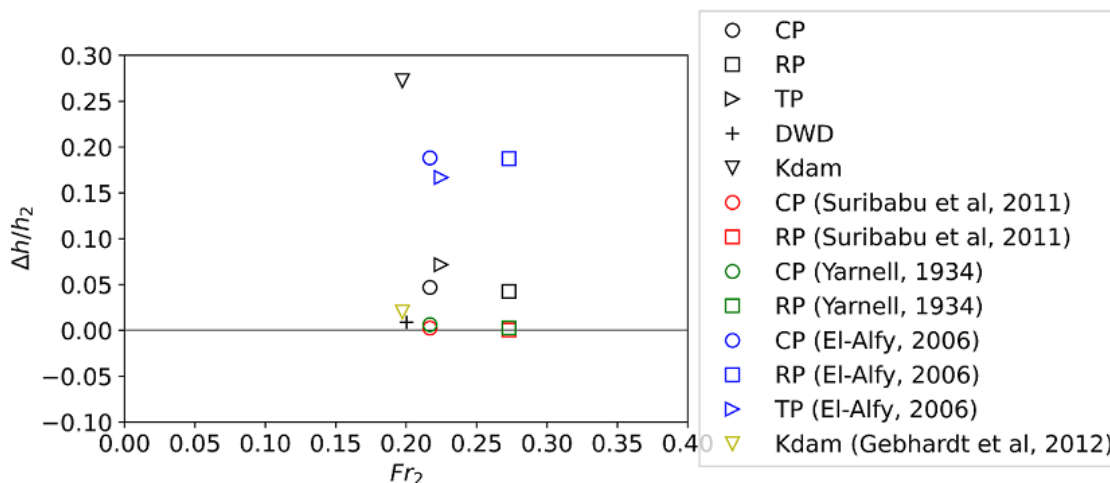
Figure 5.42: Comparison of the backwater rise of different flow types with literature values (data retrieved from physical model experiments).

Considerations on drag coefficients

The flow induced forces on a body are dependent on the drag coefficient C_D, the projection area A_p and the approach flow velocity U_0 as indicated in equation 3.4. The normalized projection area, called to blockage ratio is the most influencing parameter on backwater rise according to Addy and Wilkinson (2016), Suribabu et al. (2011), Azinfar and Kells (2008), and Azinfar and Kells (2009) as outlined in chapter 3.5. According to Azinfar and Kells (2009) the blockage ratio A_r for a fixed, flat bed is defined as:

$$A_r = \frac{\text{solid area of the in-stream structure}}{\text{total flown through area}} = \frac{A_s}{A_f} = \frac{A_s}{h_1 \cdot w} \tag{5.1}$$

Until now most studies were performed under fixed and flat bed conditions and the drag coefficients were acquired for those cases. Under movable bed conditions, alterations in bed morphology lead to changes in the cross-sectional area and, consequently, the blockage ratio evolves over time. This is why the comparison of above mentioned backwater rise for fixed and flat bed with the movable, scoured bed in this work, needs to be seen critical and is further analysed in the following paragraph.

Figure 5.43 illustrates the definition of various areas during the scouring process. At the beginning of the experiment at time t_0, A_{s0} represents the frontal projection of the solid area (red), and A_{f0} is the flown-through area without considering the structure (yellow). As the scouring progresses, the bed undergoes erosion, causing an increase in the flown-through area until reaching equilibrium time t_e. A_{fe} denotes the flown-through area in equilibrium stage (green). Simultaneously, the structure becomes more exposed to the flow, corresponding to an area A_{se} (blue). For subsequent analysis, the blockage ratio during equilibrium conditions A_{re} is defined as illustrated in figure 5.43 and equation 5.2.
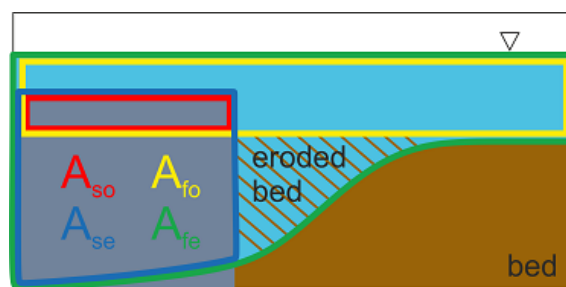
$$A_{re} = \frac{A_{se}}{A_{fe}} \tag{5.2}$$

Figure 5.43: Definition of solid and flown through areas in initial stage (A_{so} and A_{fo}) and in equilibrium stage (A_{se} and A_{fe}) and definition of the blockage ratio in equilibrium stage (A_{re}).

The drag coefficient obtained from the physical model C_{Dphys} is determined using equation 3.5 according to (Azinfar & Kells, 2009) with the aforementioned blockage ratio A_{re}. For the calculation of the drag coefficient of the numerical model the flow induced force on the structural component F_D was determined directly from the numerical model. The drag coefficient was then calculated with formula 3.4. Both C_D values and literature values are displayed in table 5.7. Among the structure types, the stone-like structures exhibit the lowest C_D values, the pier-like structures fall in the intermediate range, and the dam-like structures demonstrate the highest drag coefficient at equilibrium, which is in alignment with the previous analysis of the backwater rise $\Delta h / h_2$.

The drag coefficient of the CP with a value of 1.3 aligns well with literature values reported by Roberson and Crowe (1993), Hoerner (1965), and Naudascher (1992) all within a range of 1-1.3. Aksel et al. (2021) report slightly higher C_D values with 1.65. The drag coefficient for the RP with 1.4 is lower than values predicted in literature with 2-2.05 (Roberson & Crowe, 1993; Hoerner, 1965). The TP shows a higher C_D value of 2.9 than the literature value of 2.2 (the open face needs to be considered here) by Hoerner (1965). The variations of C_D and in the recorded backwater rise compared to literature values may be attributed to several factors. One potential explanation is that many studies were conducted under fixed bed conditions, where the mechanism of changing cross-sectional area and hence a change of the blockage ratio does not take place. Schalko et al. (2018) estimated 25 % less backwater rise for movable bed conditions in comparison with fixed, flat bed for a large wood accumulation. Aksel et al. (2021) observed a more pronounced reduction in the C_D value, approximately 50 %, around a Circular Pier with a flat or scoured bed. They attribute this to the streamlining effect of the scour hole around the pier. The effect of the reduction of backwater rise and hence C_D value due to scouring could be replicated in the current experiments as shown in the time development analysis in chapter 5.1.2. The initial backwater rise, with flat bed conditions, was about 25 % higher than the equilibrium value. Nevertheless, this does not explain the differences of the measured C_D values at equilibrium stage in this study compared to literature values, as this would suggest smaller C_D values. Another possible explanation could be the influence of free surface flow on the C_D value. Most experiments to measure the flow

Table 5.7: Summary of drag coefficients obtained from this study and literature values around different types of structures

	this study				literature values					
					flat bed					scoured bed
					in between walls		free surface flow			
	Re	Fr	$C_{D\,phys}$	$C_{D\,num}$	Roberson and Crowe (1993) Re $>10^4$	Summary of Hoerner (1965) $10^4<$Re$<10^6$	Naudauscher (1992) $2\cdot10^3<$Re$<7\cdot10^3$ Fr $=0.1$-1	Azinfar and Kells (2009) Fr$=0.15$-0.58	Aksel et al (2021) Re$=52800$ Fr$=0.19$	Aksel et al (2021) Re$=52800$ Fr$=0.19$
CP	$8.7\cdot10^4$	0.67	1.3	3.6	1.1	1.17[1] 2.3[2]	1-1.3		1.65	0.78
RP	$8.7\cdot10^4$	0.67	1.4	1.4	2	2.05[1]				
TP	$8.7\cdot10^4$	0.67	2.9	2.4		2.00[1] 2.2[2]				
DWD	$1.4\cdot10^5$	0.67	0.9	1.0						
DG	$6\cdot10^4$	0.67	-	1.5				6.73		
Kdam	$2.7\cdot10^4$	0.67	9.6	1.0						

[1] full body with closed upstream front face

[2] body with open upstream front face

induced force F_D on a body were done in air flows. A typical experimental setup for force measurements on a circular cylinder in air flows consists of two parallel walls where the body is constrained horizontally between the two walls (Roberson & Crowe, 1993; Hoerner, 1965). For water flows there are two distinct differences: a) the circular cylinder is installed vertically and b) free surface flow conditions are present in river engineering due to the higher density of water. Therefore the gravity component, considered in the Froude number, needs to be considered additionally (Naudascher, 1992). Comparing the C_D values of experiments in a classical setup (Roberson & Crowe, 1993; Hoerner, 1965) and in a free surface flow setup in river engineering (Naudascher, 1992), reveals that the values lay in the same range as shown in table 5.7. Consequently, no final explanation could be found for the differences of C_D values. Therefore, a hypothesis was developed that could explain the differences, which is explained subsequently.
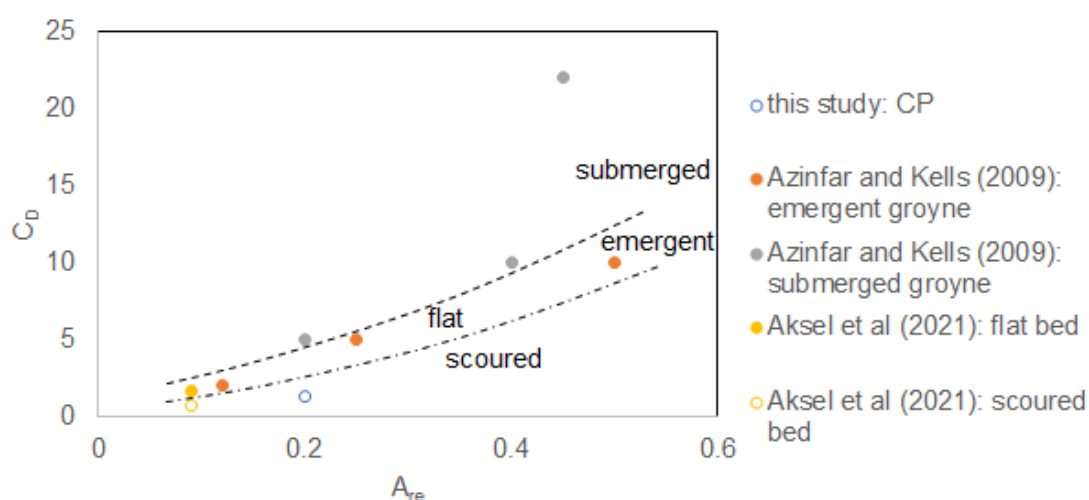
Figure 5.44: Hypothesis of influence of submergence and scour on the C_D value (to be verified with further experiments).

Figure 5.44 shows C_D values of several studies and dependent on the blockage ratio A_{re}. Here included is the study of Azinfar and Kells (2009), who investigated submerged and emergent groynes under fixed and flat bed conditions and which belong to the group of stone-like structures according to the definition in this work. Furthermore, the study of Aksel et al. (2021) is displayed, that investigated the influence of a scour hole on the C_D value of a circular pier. This structure is categorized as pier-like structures in this work. The data set is complemented by the data of the CP acquired in this work. A trend to higher C_D values for higher blockage ratios is visible for all types of structures. Moreover a distinction between submerged and emergent structures can be hypothesized. The comparison of flat and scoured bed reveals that the measured C_D values without scour would fit in the context of the literature values. It clearly needs to be said, that this hypothesis needs to be verified with more experiments.

Spatial distribution of water levels

The spatial distribution of water levels is shown in figure 5.45. The pier-like structures all show the well known surface roller just upstream of the pier which is associated with an increase in water level. This increase is a locally confined phenomenon and does not extend longer than one pier width in upstream and lateral direction. It is as well visible, that the numerical model is not able to model the water level drop downstream of the pier-like structures as indicated above. The stone-like structures show a slightly asymmetrical water level distribution which can be attributed rather to the asymmetric geometry than to the flow type. This means, the highest water level is not to be expected in the centerline but at the sides of the flume. Especially for flood risk assessment this has to be taken into account for planning the height of the levees. The Kdam leads to a significant increase of water level upstream of the dam, which extends further upstream than the upstream end of the flume and respectively the simulation length.

Figure 5.45: Top view of the spatial distribution of water levels (data retrieved from the numerical model).

Concluding remarks

The quantification of absolute and relative backwater rise for all structures enhances the predictability of water level curves around in-stream structures, thereby facilitating flood risk assessment. However, upon analyzing literature values and comparing them with the findings of this study, it becomes evident that significant uncertainties persist in determining backwater rise. The examination of drag coefficients indicates a pronounced dependency on the blockage ratio, with bed morphology state (flat or scoured) and submergence playing crucial roles in determining C_D values and, consequently, backwater rise. A hypothesis has been proposed, requiring validation through further experiments.

Chapter 6

Additional considerations for the implementation in practice: Influence of natural materials, debris accumulations and shelters

The previous chapter looked at deep pool habitat structures as idealized structures in form of rather technical hydraulic engineering structures. This chapter highlights three aspects that need to be considered additionally to implement the investigated in-stream structures. The results presented within this chapter were acquired in the physical model experiment and show the differences that each parameter imposes on the equilibrium bed morphology and the backwater rise. The Circular Pier and the Rectangular Pier are excluded from the analysis as they were benchmark experiments. The Kdam is excluded from further investigation due to its limited applicability due to the high backwater rise. The additional ecological considerations are:

I. Usage of Natural Materials
Developments in the field of river revitalization in recent years have shown that the trend is moving towards nature-based solutions, in which purely technical structures are no longer implemented, but instead biological-engineering construction methods are used. The implementation should therefore primarily use natural materials that occur in the immediate vicinity of the river. Natural materials such as stones, dead wood and soil materials have several basic hydromorphological differences in comparison with technical engineering structures. Chapter 6.1.1 investigates the influence of the edge design, chapter 6.1.2 the influence of surface roughness and chapter 6.1.3 the influence of porosity on the bed morphology pattern and the backwater rise.

II. Debris Accumulation
Natural materials are more likely to dissolve or when they are not fixed in the river bank or bed can be transported downstream during flood events. Especially emergent structures like pier-like structures are therefore exposed to a higher risk of debris accumu-

lations that can increase the backwater rise and therefore increase flood risk. Chapter 6.2 investigates the influence of debris accumulation in different sizes on the backwater rise and bed morphology pattern.

III. Coverage and Shelter

Fish biologists were able to demonstrate that a combination of a deep pool habitat and a shelter or cover structure can increase the biological potential of deep pool habitats. This is due to a joint effect of overhead cover as a protection from predators, shadowing for lower water temperatures and low flow velocities during flood events. The influence of coverage and shelter on the bed morphology pattern and the backwater rise is summarized in chapter 6.3.

6.1   Influence of natural materials

Formerly, hydraulic structures in rivers had to fulfill mainly an engineering function such as foundation for bridges (bridge piers), maintaining a sufficient water level in navigation channels (e.g. groyne fields), fish passages at weirs and sluices. Those structures are typically made of engineering materials such as concrete, steel and big stones. With the shift of philosophy of river engineering towards ecosystem engineering the urge to use natural materials for instream structures arose in the last decades. Natural materials in this context are defined as materials that can be found in the natural surrounding of a river such as stones, wood, soil, grass, living plants etc. Engineering structures made of natural materials have fundamentally different hydraulic properties in comparison with those made of classical engineering materials such as a concrete pier. The characteristics can be summarized in three groups and are explained briefly here:

I. Edge Design

The edge design addresses the effect that piers and other hydraulic structures can be produced with defined and sharp edges in a high accuracy. Natural materials are restricted in accuracy due to natural constrictions such as growth of trees or type of soil. To illustrate the problem with an example: A submerged groyne can be made out of concrete where the dimensions and shape can be defined by the planning engineer. If the groyne is implemented with a series of tree trunks, the shape of the groyne is rather irregular and the head of the groyne has a round rather than a sharp shape. The theoretical considerations and the influence of the edge design on bed morphology is discussed in chapter 6.1.1.

II. Surface Roughness

Another property that influences the hydraulics and morphodynamics around structures is the surface roughness of the in-stream structures. Concrete structures can be categorized as hydraulically smooth in most hydraulic conditions, whereas tree trunks with bark or irregular stones lay within the hydraulically rough regime. Details on the qualitative and quantitative influence on the bed morphology is given in chapter 6.1.2.

III. Porosity/Permeability

The installation of in-stream structures with natural materials often requires the disso-
lution of the structure into smaller parts such as the construction of a groyne with big
stones or an arrangement of tree trunks driven into the river bed. Additionally, river sur-
roundings pose a challenge for the technicians and the implementation accuracy of in-
stream structures is limited. The inaccuracy of implementation comes along with small
passages through the structure. From hydraulic point of view these structures can be
characterized as porous and/or permeable. The influence of porosity and permeability
on the bed morphology and backwater rise is discussed in chapter 6.1.3.

6.1.1 Influence of edges

As explained above an implementation with natural material is favorable for practice. Figure
6.1 shows a possible implementation technique for the TP and the DG. The formerly solid
structure is dissolved into various tree trunks. With this dissolution the front edges of the pier
and the Deflected Groyne are not sharp anymore but show a round rather irregular shape due
to the natural variations of tree stems.
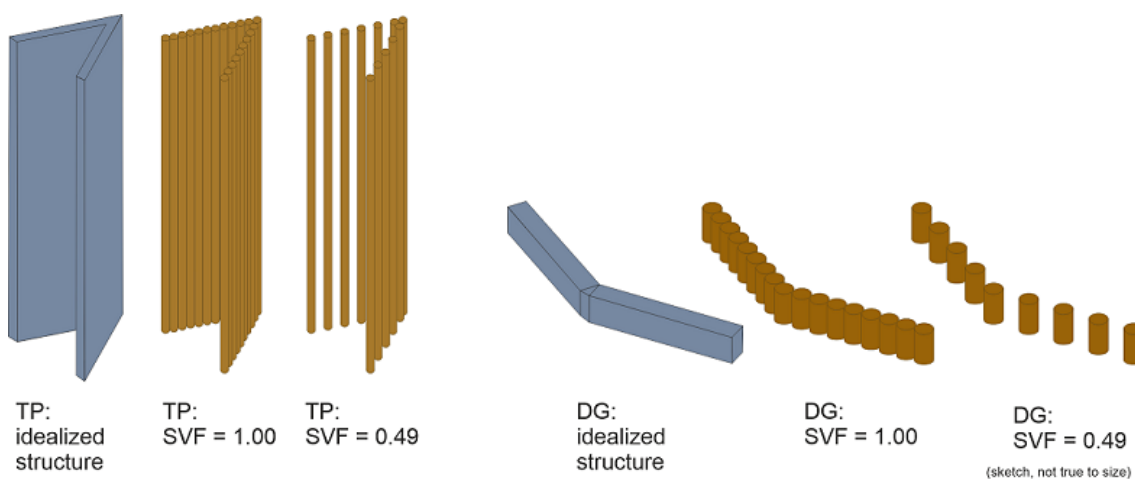
Figure 6.1: Dissolution of a rigid structure into a structure made of tree trunks for TP and DG
with defined solid volume fractions (SVF).

It is well known that the separation point and the development of the wake zone is fundamen-
tally different for bodies with round edges such as a cylinder and bodies with sharp edges
such as a rectangular pier. For the rectangular pier the separation point and the wake zone
are independent of the approach flow conditions, which can be seen in a constant C_D value
over a large range of Reynolds numbers as shown in figure 6.2. The flow separates at the
sharp edge and the wake zone is characterized by a vortex zone of constantly increasing
width. In contrary, for a cylinder the separation point and wake zone is highly dependent
on the Reynolds number. The different positions of the separation point and changing wake
zones in dependence of the Reynolds number are sketched in figure 6.2. The Reynolds de-
pendency of the cylinder shows that the flow field can be influenced by the edge design of the
structures.
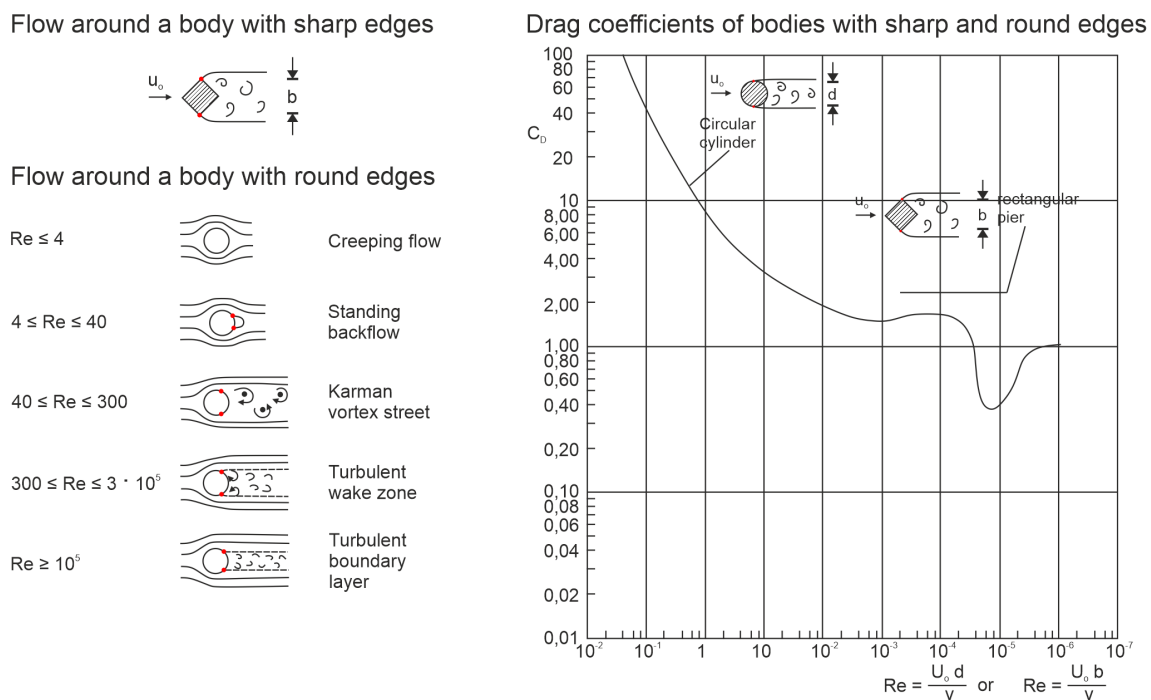
Figure 6.2: Reynolds number dependency of the edge design of different hydraulic structures. Adapted from Roberson and Crowe (1993).

As the hydrodynamic flow field has a high impact on the development of the bed morphology the influence of the edges of the TP and the DG as representatives for emergent and submerged structures were investigated. The results of the experiments are summarized in the following chapter.

Influence of the edge design on the bed morphology in equilibrium state

It was supposed that equilibrium was reached within the same time as for the idealized structures which was 48 h for TP and 72 h for DG. Figure 6.3 shows the bed morphologies of the TP with a) sharp edges and b) round edges. The characteristics of the scour hole upstream of the structure are similar. In both cases a primary and a secondary scour hole can be identified. Downstream of the structure in both cases a central dune and two deep lateral sections form. Looking at the qualitative changes of the two cases major differences can be observed as shown in figure 6.4. The round edges lead to a shallower and shorter scour hole (see table 6.1 and figure 6.4). The differences inside the scour hole are significant for the primary and secondary scour hole with above $0.2 \, d_{se}$. The changes are smaller in the part of the plateau which divides the primary and secondary scour hole. The length of the scour hole l_{ds} is reduced from 44.2 cm to 37.9 cm. The cross-sectional view shows that the characteristic pattern with the primary and secondary scour hole is shifted towards the pier. The dune downstream of the pier undergoes smaller changes than the upstream scour hole in a range of smaller than 10 % of the maximum scour depth. The cross-sectional view in figure 6.4 shows that the dune is shifted towards the pier from l_{dune} = 70.8 cm to l_{dune} = 59.8 cm. The depth of the scour d_{se} cannot be evaluated as the scour hole touches the flume bottom. Extrapolation may give a hint that the scour depth of the round edge variant would be smaller than the scour

depth of the sharp edge variant.
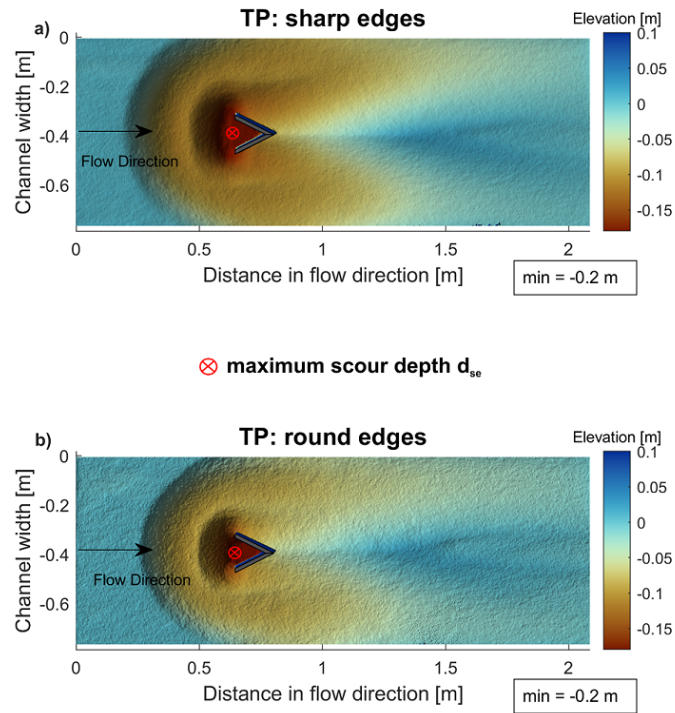
Figure 6.3: Comparison of bed morphologies in equilibrium state for the TP with a) sharp and b) round edges.
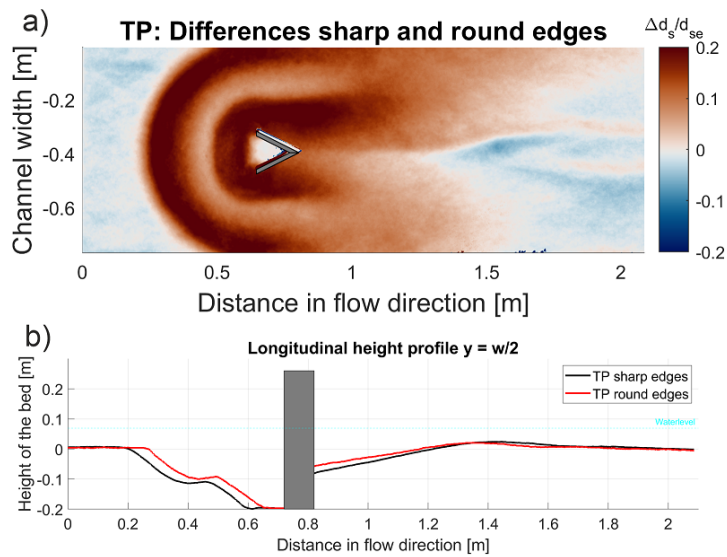
Figure 6.4: a) Differences in bed elevation between TP with sharp and round edges. b) Longitudinal cross-profile in the center line of the flume.

141

Table 6.1: Geometrical parameters of the scour hole for TP with sharp and round edges.

Version	TP Sharp edges	TP Round edges	DG Sharp edges	DG Round edges
d_{se} [cm]	19.9	19.7	18.3	18.4
l_{ds} [cm]	44.3	37.9	35.8	31.3
l_{dune} [cm]	59	52.5	(70.8)	(59.8)
h_d [cm]	2.4	2.1	1.3	1.5

The comparison of bed morphologies of the Deflected Groyne with sharp and round edges shows no significant differences in the characteristic patterns as shown in figure 6.5. Both develop the scour hole upstream of the structure and a long deep stretch downstream of the DG. The qualitative analysis in figure 6.6 and table 6.1 also reveals that the changes in bed morphology are not significant.
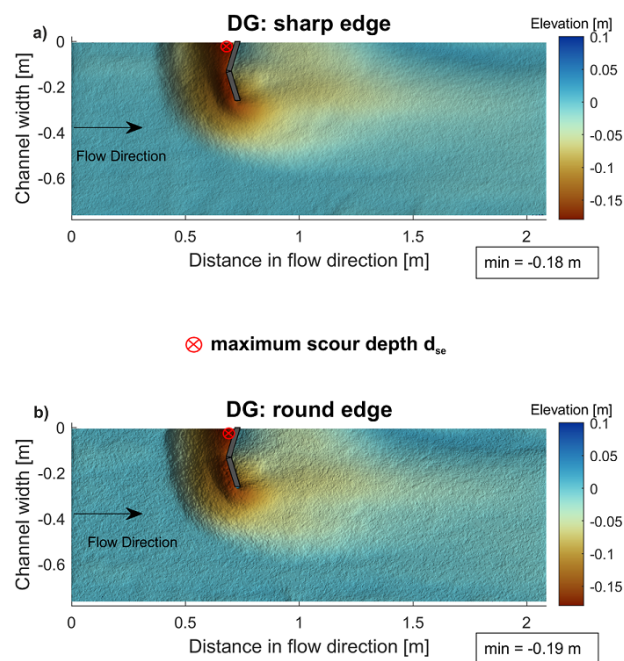
Figure 6.5: Comparison of bed morphologies in equilibrium state for the DG with a) sharp and b) round edges.
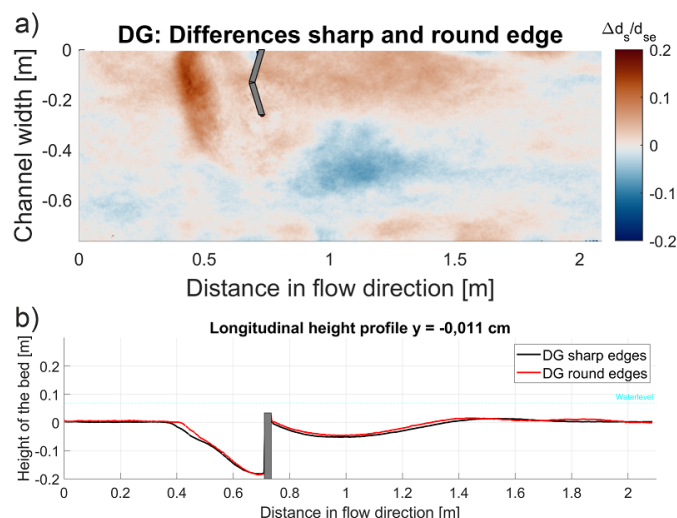
Figure 6.6: a) Differences in bed elevation between DG with sharp and round edges. b) Longitudinal cross-profile in the center line of the flume.

Influence of the edge design on the backwater rise

The relative backwater rise $\Delta h_1/h_0$ was quantified accordingly to chapter 3.5. The edge design has no significant effect on the relative backwater rise $\Delta h_1/h_0$ for both structures TP and DG as shown in table 6.2.

Table 6.2: Backwater rise for different edge designs of TP and DG.

Edge Design	$\Delta h_1/h_0$ [%]
TP – sharp edges	10.5
TP – round edges	10.0
DG – sharp edges	6.9
DG – round edges	6.2

Conclusion on the influence of edge design

The experiments on the influence of edge design showed, that the form of the edges have major impact for emergent structures like pier-like structures and lead to a reduction of scour depth of larger than 20 %. In contrary, submerged structures like the stone-like structures are not significantly affected by the edge design. For practical implementation this means, that the installation of sharp edges is worth the additional effort for pier-like structures and is not necessary for submerged structures. The backwater rise showed no significant changes between the design with sharp and round edges and therefore plays no role in the evaluation which variant is preferred for implementation. Comparable investigations could not be found in literature and are therefore not discussed at this point.

6.1.2 Influence of surface roughness

Natural materials such as tree trunks with bark have larger surface roughness values than typical engineering materials such as concrete or sheet pile constructions. A change in surface

roughness leads to a change in hydraulic behaviour and hence could influence the scouring process. To the authors knowledge the influence of surface roughness on scouring processes has not been investigated systematically yet. Shamloo (1997) investigates the hydraulics and scour pattern of simple habitat structures such as a cube, a half sphere and a natural stone. The scour pattern around a cube and a natural stone are shown in figure 3.33. The scour hole upstream and the dune height downstream of the natural stone are significantly smaller than those of the half spheres and the cube. The significance of the investigation for this work is limited as not only the surface roughness but also the shape of the structure (half sphere, cube and ellipsoid) was different. The author assumes that the influence of the shape of the structure is of higher order of magnitude for the scour process than the surface roughness for this study. Therefore, a general meaning cannot be drawn from this investigation.

Design of the physical model experiments on surface roughness

The material that was used for the previous experiments was PVC with a smooth surface. In contrast, in-stream structures in revitalization projects are often realized with a composition of wood and stone structures that have a rougher surface. Figure 6.7 shows a typical triangular groyne as implemented in river restoration projects. The groyne consists of a supporting wood structure of tree trunks in horizontal and vertical direction and is filled with stones. All materials that can be found in the surrounding of the river.

Figure 6.7: Implementation of a triangular groyne with natural materials in a river restoration project in the Neckar near Börstingen, Source: Regierungspräsidium Tübingen, 2023. URL: `https://rp.baden-wuerttemberg.de/rpt/abt5/ref532/neckar-natur-weg/seiten/buhnen/` (accessed on 31.12.23).

The following aspects need to be considered for characterizing the roughness hydraulically:

    I. Which of the investigated structures is the most influenced one by surface roughness?

    II. Which is the hydraulically significant length scale to look at for surface roughness considerations?

III. How is the roughness characterized? Which roughness regime is relevant for the selected roughness (micro or macro roughness)? Depending on that which different phenomena need to be considered?

IV. Does the roughness elevate above the boundary layer and protrude the free flow?

Surface roughness significantly influences hydrodynamics when the surface is facing or parallel to the main flow direction, defining such a configuration as a "flow-facing surface". In the scope of this study, particular emphasis is placed on the hydraulically relevant scenario, which involves the structure displaying the largest flow-facing surface. It is assumed that structures with a smaller flow facing surface show less sensitivity with regard to surface roughness. As illustrated in table 6.3, the DWD stands out as the structure with the largest flow-facing surface of the structures investigated in this work and is consequently selected for the experiments.

Table 6.3: Flow facing surfaces for different types of structures.

Structure	Flow facing surface [cm²]
CP	338
RP	322
TP	210
DWD	3068
DG	137
Kdam	1731

The DWD shall be modeled in the physical model experiment in a similar way as indicated in the example shown in figure 6.7. The construction consists of a composition of tree trunks, which would be driven into the river bed in a real case scenario. The volume enclosed by the trunk construction can be filled with stones and locally existing soil material. The top of the wing needs to be covered with large stones or as well with tree trunks. The implementation of the envisioned construction for investigating surface roughness is depicted in figure 6.8. For the experiments realistic trunk diameters of typical local trees were chosen as 20 cm, 40 cm and 62.5 cm. The roughness elements (tree trunks) were geometrically scaled to the model scale of 1:25.
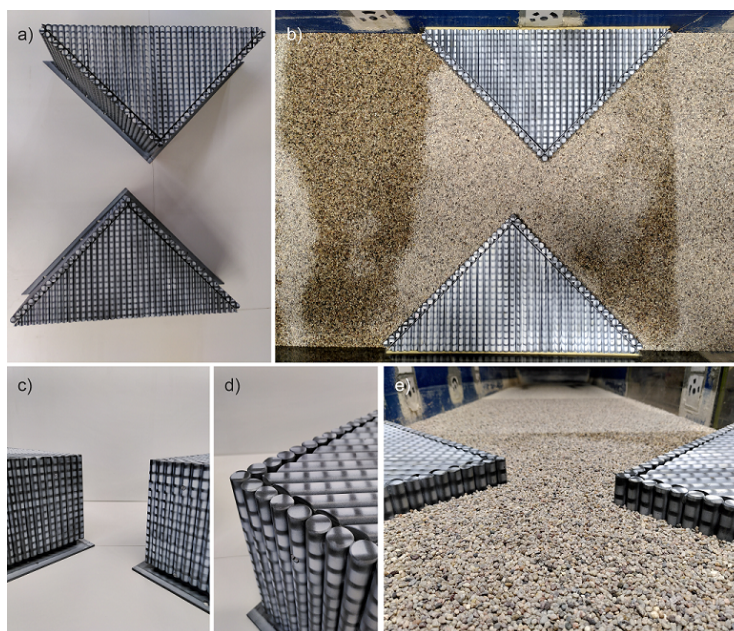
Figure 6.8: Experimental installation of roughness elements on the DWD with cylinders with $k_s = 16 \; mm$.

Several scales of surface roughness are detectable for this construction. Firstly, there is the surface roughness of each single tree trunk which consists of the bark of the wood. It is in an order of magnitude between $0 - 5$ cm. Through the arrangement of the different tree trunks there is a roughness of the diameter of the tree trunks which is of an order of magnitude higher from 10 cm to 50 cm. The latter is therefore the most important. A filling with big stones would represent a roughness in the same order of magnitude.

The influence of surface roughness on the flow field is dependent on several parameters, the height and the distance of the roughness elements and on the Reynolds number. To estimate the potential influence of the above selected surface roughness values on the flow field and hence the scouring process, a characterization of the roughness regime is necessary. There are several ways how to characterize surface roughness which are explained in the following paragraphs.

Influence of surface roughness on the flow around structures

The influence of surface roughness on the flow around structures is known for e.g. spheres (Flachsbart, 1927; Blevins, 1984) and cylinders (Fage & Warsap, 1929; Roberson & Crowe, 1993) as mentioned in Bezzola (2002). The shift from a laminar to a turbulent boundary layer manifests in a sharp reduction of the C_D value at the critical Reynolds number as shown in figure 6.9. Irrespective of whether it as a 2D structure (cylinder) or a 3D structure (sphere), a higher surface roughness leads to a reduction of the critical Reynolds number. For very rough cylinders the C_D value stays almost constant over a wide Re range. For the planned in-stream structure this indicates, that a hydraulically rough surface is favorable as it shows lower sensitivity to Reynolds number changes due to differing approach flow velocities.
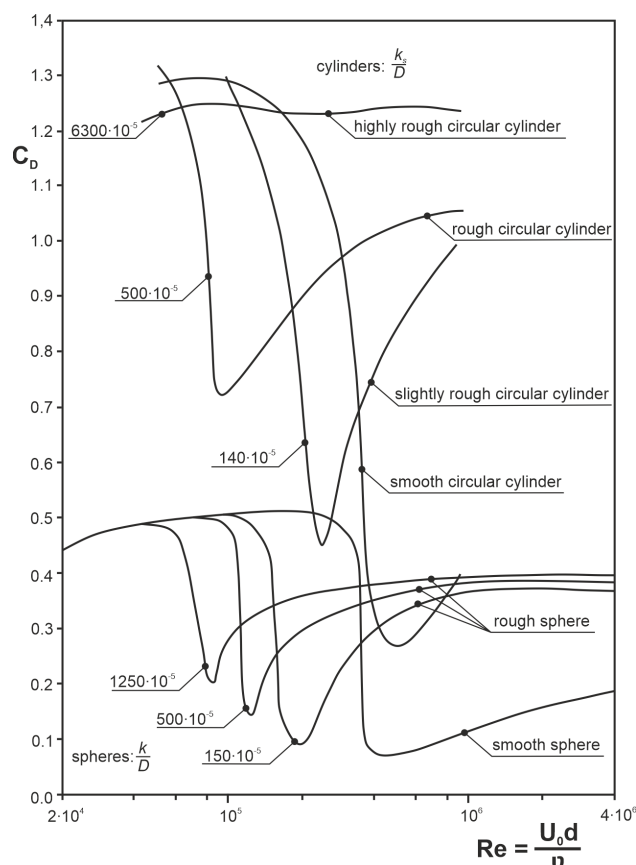
Figure 6.9: Influence of surface roughness of spheres (data from Blevins (1984)) and cylinders (data from Roberson and Crowe (1993)) on the critical Reynolds Number. k is the geometrical height of the surface roughness (not to be confound with the equivalent sand roughness k_s as defined by Nikuradse (1932)).

Classification of surface roughness according to Flammer, Tullis, and Mason (1970)

The classification according to Flammer, Tullis, and Mason (1970) can be used as a first estimation of the influence of the roughness:

- Large Scale Roughness/Macro roughness: $h/k_s < 2$

- Intermediate roughness: $2 < h/k_s < 7.5$

- Small scale roughness: $h/k_s > 7.5$

k_s is the equivalent sand roughness height of one sand particle as described by Nikuradse (1932). The height h equals the water depth above the Wing y_{DWD} as shown in figure 6.10. Applying the characterization of Flammer, Tullis, and Mason (1970) to the present case this leads to the classification in table 6.4.

Table 6.4: Classification of surface roughness according to Flammer, Tullis, and Mason (1970) applied to the surface roughness values in this study.

natural tree diameter	20 cm	40 cm	62.5 cm
model tree diameter	8 mm	16 mm	25 mm
$h/k_s = y_{DWD}/k_s$	10	5	3.2
classification of roughness	small scale roughness	intermediate roughness	intermediate roughness
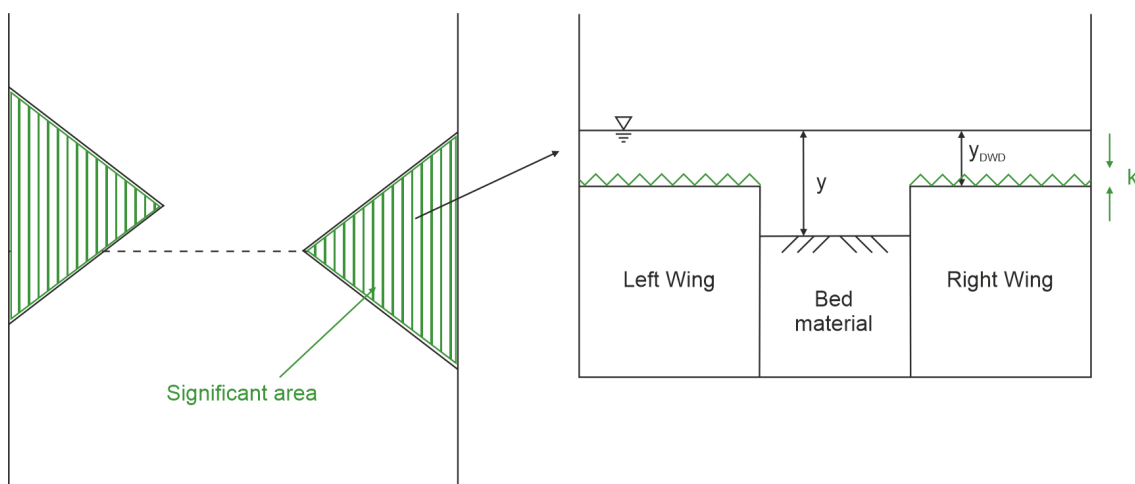
Figure 6.10: Left: Significant flow facing area on top of the submerged Double Wing Deflector (DWD). Right: the significant length scale D = y_{DWD} and the equivalent sand roughness k_s for the characterization of the relative surface roughness k_s/D.

Small scale roughness according to Moody Diagram

The roughness variant $k_s = 8\ mm$ can be characterized as a small scale roughness according to Flammer, Tullis, and Mason (1970). The roughness regime of a small scale roughness can be identified by the relation of the relative roughness k_s/D to the Reynolds number of the flow. D is the significant length scale of the roughness. In the case of the DWD it is the water depth above the wing y_{DWD} as shown in figure 6.10. The top of the DWD is parallel to the flow and therefore has the highest impact on the flow field and hence the bed morphology. According to the Moody diagram the roughness variant $k_s = 8\ mm$ can be characterized as a hydraulic rough regime ($k_s/D = 0.1$ and Re = 22000).

Large scale roughness (Form roughness) according to Morris (1955)

Large scale roughness consists of individual roughness elements. Dependant on the distance w and the height k of the elements, different flow regimes can be distinguished according to Morris (1955) as shown in figure 6.11. For w/k > 10 an isolated flow evolves where each roughness element triggers a wake that is protruding into the cavities. The wakes do not interfere with each other. In the wake interference flow the wakes interfere and the flow is still protruding into the cavities (3 < w/k < 7). For w/k < 3 there is quasi smooth flow and no strong interference of the cavities and the flow field can be observed.

a) Isolated-Roughness Flow

b) Wake-Interference Flow

c) Quasi-Smooth Flow
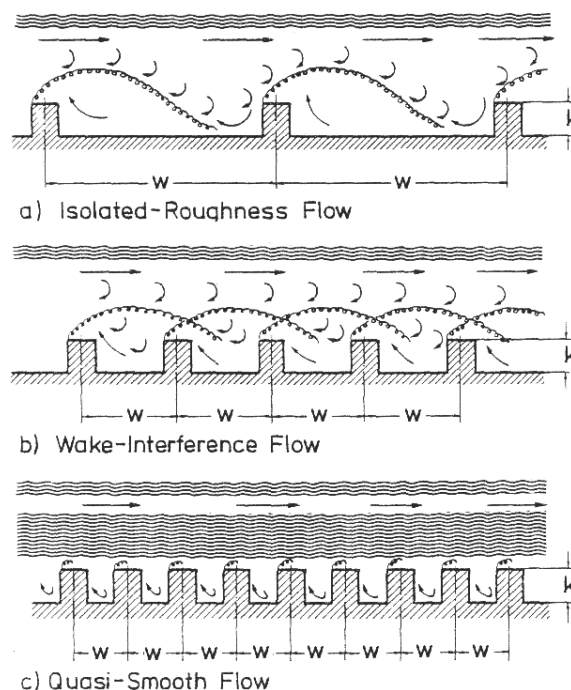
Figure 6.11: Roughness types in rough wall channel flow according to Morris (1955) as seen in Stoesser, Rodi, and Jirka (2004).

For the application of the regimes of Morris (1955) the additional variant of w needs to be known (see figure 6.11). The planned design is to install the logs directly next to each other. Calculating the w/k leads to a hydraulically smooth regime for all three trunk diameters. Morris (1955) investigated rectangular roughness elements and in this study round roughness elements are present. Nevertheless, Stoesser, Rodi, and Jirka (2004) could proof that the form of the roughness elements (e.g. bars and rods) has much less impact on the flow field than the distance of the roughness elements. They could show that there is no significant difference in the mean velocity profile between bars and rods.

Protrusion of roughness elements into the free flow - Boundary layer theory according to Schlichting and Gersten (2000)

When the flow approaches the DWD, the flow detaches from the structure and a boundary layer with increasing thickness forms along the wing. A theoretical sketch is shown in figure 6.12 showing first a laminar, then a turbulent boundary layer as it would happen at a flat plate. In this experimental setup only the turbulent boundary layer is initiated at the beginning of the wing which is superimposed by vortices that detach from the upstream edge of the wing.

149
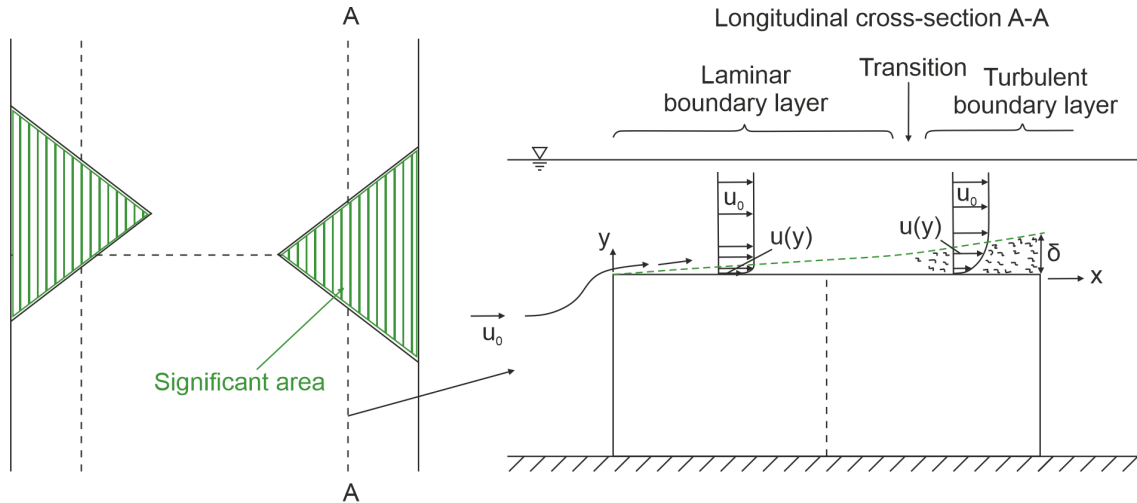
Figure 6.12: Boundary layer evolving at the upper edge of the Double Wing Deflector.

According to the boundary layer theory of Schlichting and Gersten (2000) a turbulent boundary layer has a thickness δ. δ equals the height above the boundary where 99% of the free stream velocity U_o is reached. The turbulent boundary layer is composed of several zones. Right above the boundary there is the viscous sublayer that is dominated by viscous effects. Above is the inner turbulent zone that is also influenced by viscous effects and reaches up to 0.15 δ. The turbulent outer zone without a viscous effect is from 0.15 δ to δ. The boundary layer zones, the velocity laws and its respective validity range are shown in appendix B.2.1. Depending whether the roughness elements protrude from the turbulent boundary layer or not, a surface is characterized as smooth or fully rough. Fully rough conditions can be assumed for (Pope, 2011):

$$\frac{k_s}{l_v} > 70 \tag{6.1}$$

wherein l_v is the viscous length scale (sometimes also written as δ_v):

$$l_v = \frac{\nu}{u*} \tag{6.2}$$

Under the consideration that the viscous sublayer is neglected, the boundary layer thickness of a turbulent boundary layer can be described as

$$\delta = \frac{0.37 \cdot x^{4/5} \cdot \nu^{1/5}}{U_o^{1/5}} \tag{6.3}$$

where x is the distance from the detachment point, ν is the kinematic viscosity and U_o is the velocity in the free stream. The condition for fully rough regime is satisfied for all variants. $k_s = 8\ mm$ lies within the turbulent inner zone and $k_s = 16\ mm$ and $k_s = 25\ mm$ lay within the turbulent outer zone as shown in table 6.5.

Table 6.5: Characterization of protrusion level of the roughness elements in the turbulent boundary layer and the free stream according to Schlichting and Gersten (2000).

k_s	8 mm	16 mm	25 mm
k_s/l_v	$274 > 70$	$549 > 70$	$858 > 70$
roughness	fully rough	fully rough	fully rough
zone	turbulent inner	turbulent outer	turbulent outer

The boundary layer thickness that evolves at the DWD is plotted in figure 6.13 as well as the height of the different roughness elements. It can be seen, that $k_s = 8\,mm$ stays mostly within the turbulent boundary layer and that $k_s = 16\,mm$ and $k_s = 25\,mm$ are mostly and completely outside of the turbulent boundary layer along the length of the wing. So the hypothesis is that $k_s = 8\,mm$ has no influence on the flow field and hence on the bed morphology and $k_s = 16\,mm$ and $k_s = 25\,mm$ have an influence on the flow field and hence on the bed morphology.
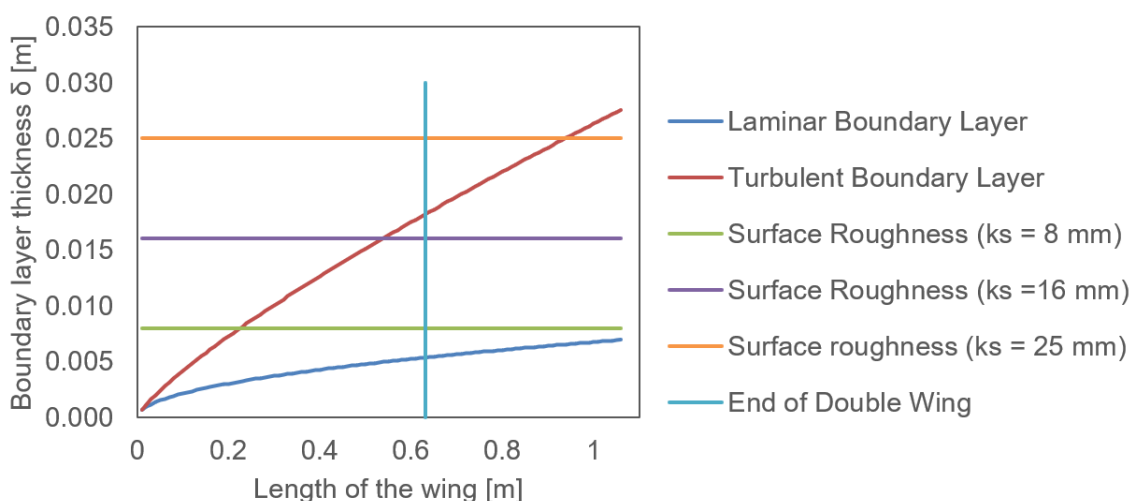
Figure 6.13: Boundary layer thickness at the Double Wing Deflector for surface roughness of $k_s = 8\,mm$, $k_s = 16\,mm$ and $k_s = 25\,mm$.

Another crucial factor to consider during the experiments is the impact of added roughness elements on the effective cross-sectional area, in addition to the surface roughness. This introduces a combined effect involving a reduction in area and increased surface roughness.

Influence of the surface roughness on the bed morphology in equilibrium state

The bed morphology in equilibrium state for the different surface roughness values is shown in figure 6.14. The general characteristics with the deepest scour hole at the upstream wing and two deep longitudinal sections and a central dune downstream of the structure are present for all variants. The relative differences $\Delta d_s/d_{se}$ lay mostly within a range of +/- 20 % and do not differ significantly between the variants as shown in figure 6.15. The differences lay within the deviations of the DWD replication experiments (compare to figure 5.10). The geometrical parameters of the scour hole as the maximum scour depth d_{se} and the length of the scour hole l_{ds} do not differ significantly for the different surface roughness values (see table 6.6).
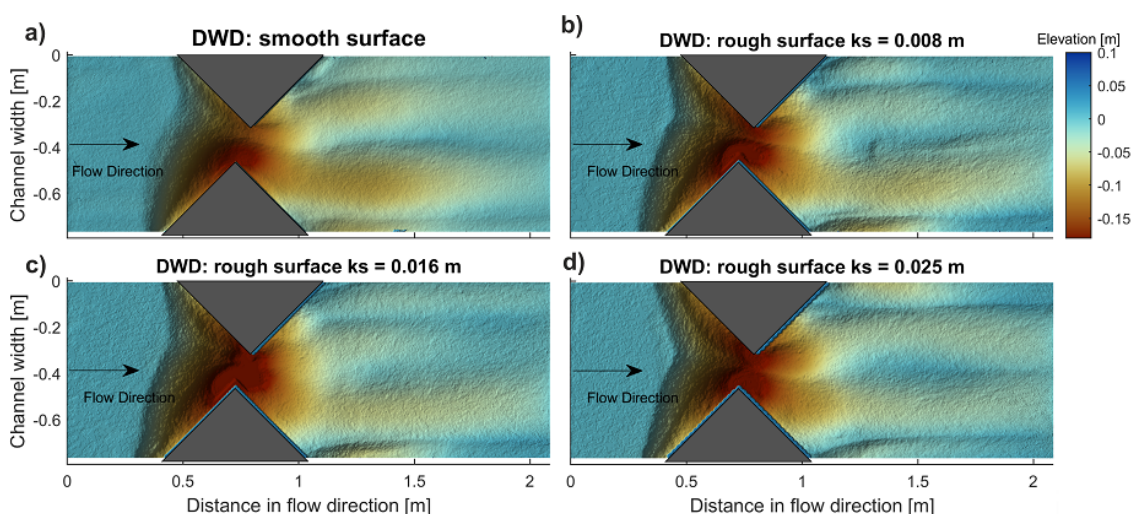
Figure 6.14: Comparison of bed morphologies in equilibrium state for different surface roughness values. a) smooth surface, b) $k_s = 8\ mm$, c) $k_s = 16\ mm$, d) $k_s = 25\ mm$.
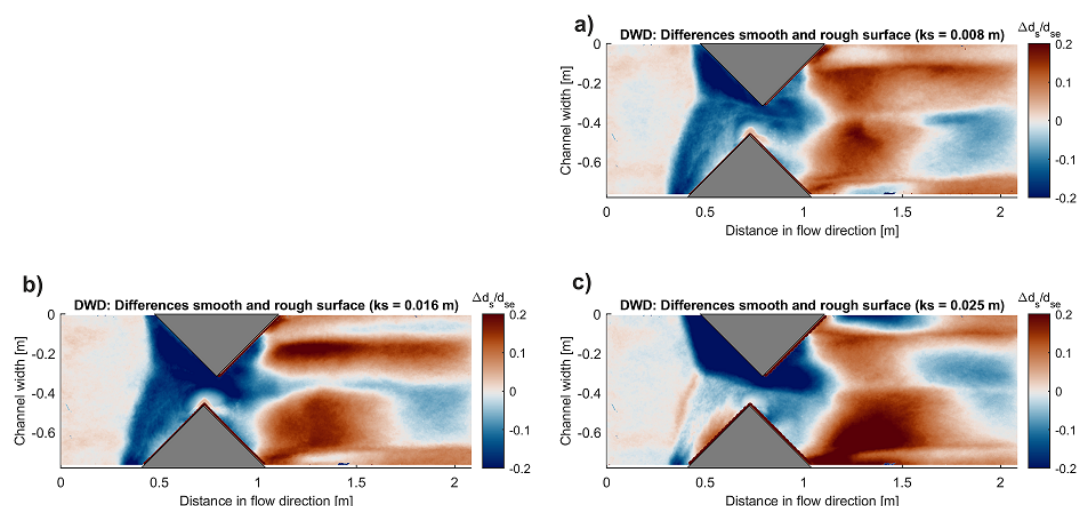
Figure 6.15: Differences in bed elevation between smooth surface and variants with surface roughness of a) $k_s = 8\ mm$ b) $k_s = 16\ mm$ c) $k_s = 25\ mm$.

Table 6.6: Geometrical parameters of the scour hole with different variants of roughness.

	DWD smooth	DWD $k_s = 8\ mm$	DWD $k_s = 16\ mm$	DWD $k_s = 25\ mm$
d_{se} [cm]	19.1	19.3	19.3	19.2
l_{ds} [cm]	36.6	36.2	36.8	33.8

In conclusion, the surface roughness has a negligible influence on the bed morphology in contrast to the hypothesis proposed above.

Influence of the surface roughness on the backwater rise

Table 6.7 summarizes the influence of surface roughness on the backwater rise. The rough surface leads to a slight increase in relative backwater rise $\Delta h_1/h_0$ for $k_s = 8\ mm$ and $k_s = 16\ mm$. $k_s = 25\ mm$ shows an sharp increase of backwater rise of 22.3 % which is nearly doubled in comparison with the smooth surface. One reason is the increased roughness on top of the wings as it poses a higher resistance to the flow and increase backwater rise. As mentioned above, additionally the roughness elements reduce the flown through area which can also lead to an increase in backwater rise. As a result, the constriction effect was mitigated by subtracting it from the measured value. The mean water depth h_m of the DWD is determined following the guidelines outlined in DWA M-509 for fish passes, as depicted in figure 6.49. To account for the impact of roughness elements, the volume of the half cylinder was computed, and equivalent cuboids were derived to establish an equivalent height. This mean water depth is subsequently factored into the calculation of the upstream water level h_1. As a result, the backwater rise with considered constriction effect shows no influence for the case $k_s = 8\ mm$. The cases $k_s = 16\ mm$ and $k_s = 25\ mm$ even show a lower backwater rise. This may be due to the fact, that the roughness lays mostly in the turbulent outer zone and outside of the boundary layer as shown in table 6.5 and figure 6.13. Also the classification of Flammer, Tullis, and Mason (1970) supports this explanation as $k_s = 8\ mm$ is classified as small scale roughness and the other variants as intermediate roughness as shown in table 6.4. According to Bezzola (2002), Blevins (1984), and Roberson and Crowe (1993) rough surfaces lead to a reduction of the critical Reynolds number alongside a smaller drop of the C_D value. Consequently, a more stable velocity field can be expected for the rougher variants. It may be hypothesized that this results in the different backwater rise of the surface roughness variants. Even though it must be admitted that this conclusion is contradictory to the initial thought, that a higher surface roughness leads to a higher resistance and hence higher backwater rise. As a consequence no clear conclusion can be drawn here.

Table 6.7: Backwater rise for different surface roughness of DWD.

	without constriction effect	with constriction effect
Surface Roughness	$\Delta h_1/h_0$ [%]	$\Delta h_1/h_0$ [%]
DWD – smooth surface	13.4	13.4
DWD – $k_s = 8\ mm$	16.8	12.3
DWD – $k_s = 16\ mm$	15.2	6.1
DWD – $k_s = 25\ mm$	22.3	8.1

In conclusion the surface roughness has no significant influence on the bed morphology. The backwater rise shows an increase of up to 50 % in comparison with the smooth case as far as the constriction effect is not considered. When the constriction effect of the roughness elements is considered the backwater rise is equal or lower than the smooth case.

6.1.3   Influence of porosity and permeability

Structures implemented in nature are often realized with natural materials as described in the previous chapters and shown in figures 6.1 and 6.7. Additionally, to the edge design and surface roughness there is another factor that needs to be considered. The structures are not completely impermeable but have small gaps and passages where water can flow through. In-stream structures can be built with an intended permeability such as engineered log jams in form of a triangular pier in figure 1.1 or when implementing dead wood trees or root wads. In contrast, structures can also be permeable due to implementation accuracy, where water flows through small gaps and passages. In hydraulics, the fluid flow through media that is not solid is described as porous media flow. In literature several different terms and concepts are used to describe this type of flow such as porosity, permeability, void fraction, solid volume fraction and packing density. Table 6.8 explains several concepts.

The concepts void fraction, porosity and solid volume fraction all relate in a way to a solid and a pore volume of the porous media. There is not mentioned how the pores look like in size, number, arrangement, connection etc. These factors also influence the flow through porous media and this characteristic is described by the permeability of the porous medium. The difference of porosity and permeability is explained in figure 6.16.
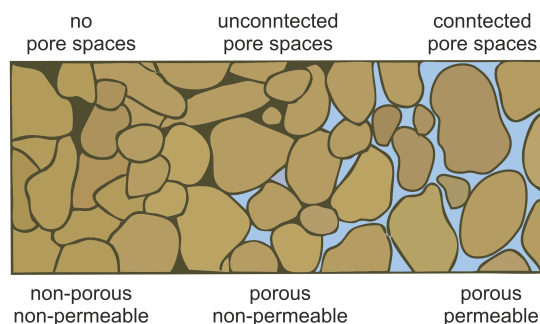
Figure 6.16: Differentiation of porosity and permeability of a medium.

The following paragraphs describe the characteristics of porous media flow in the context of first solely hydrodynamic and later also hydromorphological boundary conditions. Each study uses a different definition of porous media and permeability, which easily can lead to confusion of the parameters. As far as there are geometrical details given all porosities are recalculated as a solid volume fraction (SVF).

Table 6.8: Concepts of defining porous and permeable media flow.

Concept	Definition	Example and formula
Volumetric concepts		
Void fraction	In the context of porous media flow the void fraction describes the void space in a material, such as pores, that can be filled or flown through by a fluid e.g. water. In this context also the term packing density is used, especially when some space is filled with bodies of the same shape e.g. an array of cylinders in a cylindrical array.	Nicolle and Eames (2011) define a void fraction for an array of cylinders with an array diameter D_G, a cylinder diameter D and the number of cylinders N_C. $$\Phi = N_C \left(\frac{D}{D_G} \right)^2 \quad (6.4)$$
Porosity	The porosity Φ is defined as the relation of the volume of the void (pores) to the total volume, including the solid and the void component of the flown through medium.	$$\Phi = \frac{V_{total} - V_{solid}}{V_{total}}$$ $$= \frac{V_{void}}{V_{total}} = 1 - \frac{V_{solid}}{V_{total}} \quad (6.5)$$
Solid volume fraction (SVF)	The solid volume fraction is the opposite of the porosity and describes the fraction of solid volume in a porous medium. $$SVF = 1 - \Phi$$ $$= 1 - (1 - \frac{V_{solid}}{V_{total}})$$ $$= \frac{V_{solid}}{V_{total}} \quad (6.6)$$	A definition used by Zong and Nepf (2012) for the solid volume fraction of a cylinder patch is $$SVF\,(cylinder) = n\pi\frac{d^2}{4} \quad (6.7)$$
Permeability	The permeability K is defined as: $$K = k_f \frac{\nu}{g} \quad (6.8)$$ wherein K is a permeability coefficient $[m^2]$, k_f is the hydraulic conductivity $[m/s]$, and ν is the kinematic viscosity $[m^2/s]$.	
Area based concepts		
element based	number of elements per bed unit n $[cm^{-2}]$	applied in Zong and Nepf (2012)
frontal area per unit volume	$a = n \cdot d \; [cm^{-1}]$	applied in Zong and Nepf (2012)

Influence of porosity and permeability of structures on the hydraulics

Three different regimes of flow can be observed around porous structures (Nicolle & Eames, 2011). Regime (I) (SVF > 0.15), the *global wake regime*, shows a comparable flow pattern to that around a solid body with a slight offset of the vortex street in downstream direction as displayed in figure 6.17 c) and d). In regime (II) (0.05 < SVF < 0.15) the flow increasingly starts to flow through the structures, which is called the *bleed flow regime*. A locally stable, steady-state flow field is formed downstream of the array. In the wake, a shear layer is formed, which collapses further downstream and leads to a vortex street (see figure 6.17 b)). In Regime

(III) (SVF < 0.05), the *isolated elements regime*, the flow interaction between the cylinders is very small and the vortex system on an individual element is comparable to those of isolated cylinders as shown in figure 6.17 a).
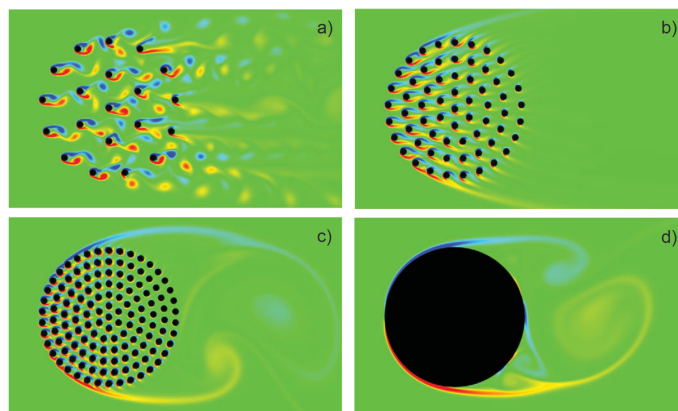
Figure 6.17: Flow around an array of cylinders for different solid volume fractions. a) SVF = 0.0454, b) SVF = 0.1451, c) SVF = 0.3016, d) SVF = 1. Adapted from Nicolle and Eames (2011).

Especially, the wake zone is changing with increasing porosity. Porous cylinder arrays showed two distinct zones, first a steady wake up to $x/D = 9$, followed by a Karman's vortex street which is formed due to the interaction between the shear layers (Zong & Nepf, 2012). With decreasing array porosity, the length of the steady wake decreases, the lateral extent of the wake oscillation becomes larger and the vortex street weakens and is not present anymore for SVF ≤ 0.04 (Zong & Nepf, 2012). In contrast, for a solid cylinder no steady wake region forms and the Karman vortex street initiates immediately downstream of the cylinder (Zong & Nepf, 2012). The length of the wake is significantly shorter than the wake of the porous patch (Zong & Nepf, 2012). Studies on groynes showed, that impermeable groynes form a pronounced rotating whirl downstream of the groyne (Mostafa et al., 2013; Haider et al., 2022). Permeable groynes showed reduced flow velocities downstream of the groyne but did not show a rotating whirl (Mostafa et al., 2013; Haider et al., 2022). The velocity field downstream of the impermeable groyne showed negative velocities in x-direction that stay until 12 L (L equals the length of the groyne) distance of the end of the groyne (Yeo et al., 2006). The permeable case showed no negative velocities in x-direction and after 9 L distance of the groyne already regained 50% of the mean velocity (Yeo et al., 2006). In total, flow velocities downstream of groynes increase with increasing porosity (Mostafa et al., 2013; Haider et al., 2022) and also with increasing permeability (Haider et al., 2022). The reattachment length downstream of the groyne increases with decreasing porosity and with decreasing permeability (Haider et al., 2022).

It can be concluded that porosity and permeability primarily affect the wake zone behind a porous structure. The higher the porosity the more the elements of the array gain importance and act like isolated elements. The wake is then characterized by a shift of the Kárman vortex street downstream and a wake zone right after the structure. For the solid structure this wake zone is absent and the Kárman vortex street initiates immediately downstream of the

structures. Higher porosity and permeability leads to a longer reattachment length and higher average flow velocities. The described effects also influence the resulting bed morphology, which is explained in the following paragraphs.

Influence of porosity and permeability on the morphodynamics

The flow dynamics around non-porous structures are altered by the presence of these structures, leading to a notable diversion of the flow and a flow shadow characterized by reduced velocities and circulating whirls behind them (Zhang & Nakagawa, 2009; Yagci et al., 2016, 2017). The author's observations in figures 3.10 and 3.5 in chapter 3.3.2 additionally indicate a highly three-dimensional flow with a downward component upstream of a solid emergent structure. In contrast, porous structures show no significant diversion of flow, recirculation or the formation of a dead water zone downstream of the structure as shown in figure 6.18. This is attributed to a distinct bleed flow through the structure, as detailed by Euler et al. (2014), Zhang and Nakagawa (2009), and Ismail, Xu, and Liu (2021). With an increase in porosity, the downflow strength diminishes due to increased bleed flow through the structure. As the downflow strength plays a crucial role in the scouring process, porous structures result in shallower and narrower scour holes (Kitsikoudis et al., 2016; Yagci et al., 2016, 2017; Euler et al., 2014). The bleed flow also induces internal erosion within the structure (Ismail, Xu, & Liu, 2021). For porous structures with very low SVF, the local scour around the individual elements of the porous array becomes more pronounced than the scour around the entire structure (Yagci et al., 2017). Porosity significantly influences various dimensions of the scour, including depth, width, area, volume, and the downstream dune (Zhang & Nakagawa, 2009; Yagci et al., 2016, 2017; Ismail, Xu, & Liu, 2021). Ismail, Xu, and Liu (2021) demonstrated a reduction in scour depth from ½ to ¼ of the structure width for a porous rectangular pier, while Yagci et al. (2017) observed a 22 % reduction in scour depth and a 27 % reduction in scour volume for a circular cylinder array as shown in figure 6.19. Submerged structures, such as solitary woody riparian plants, exhibited a substantial reduction in scour volume ranging from 44 % to 84 % (Euler et al., 2014). Yeo et al. (2006) identified a nearly linear relationship between decreasing dimensionless scour depth and increasing permeability of structures such as groynes. Furthermore, the time development of the scouring process undergoes significant changes, with a noticeable delay observed (Euler et al., 2014; Ismail, Xu, & Liu, 2021).
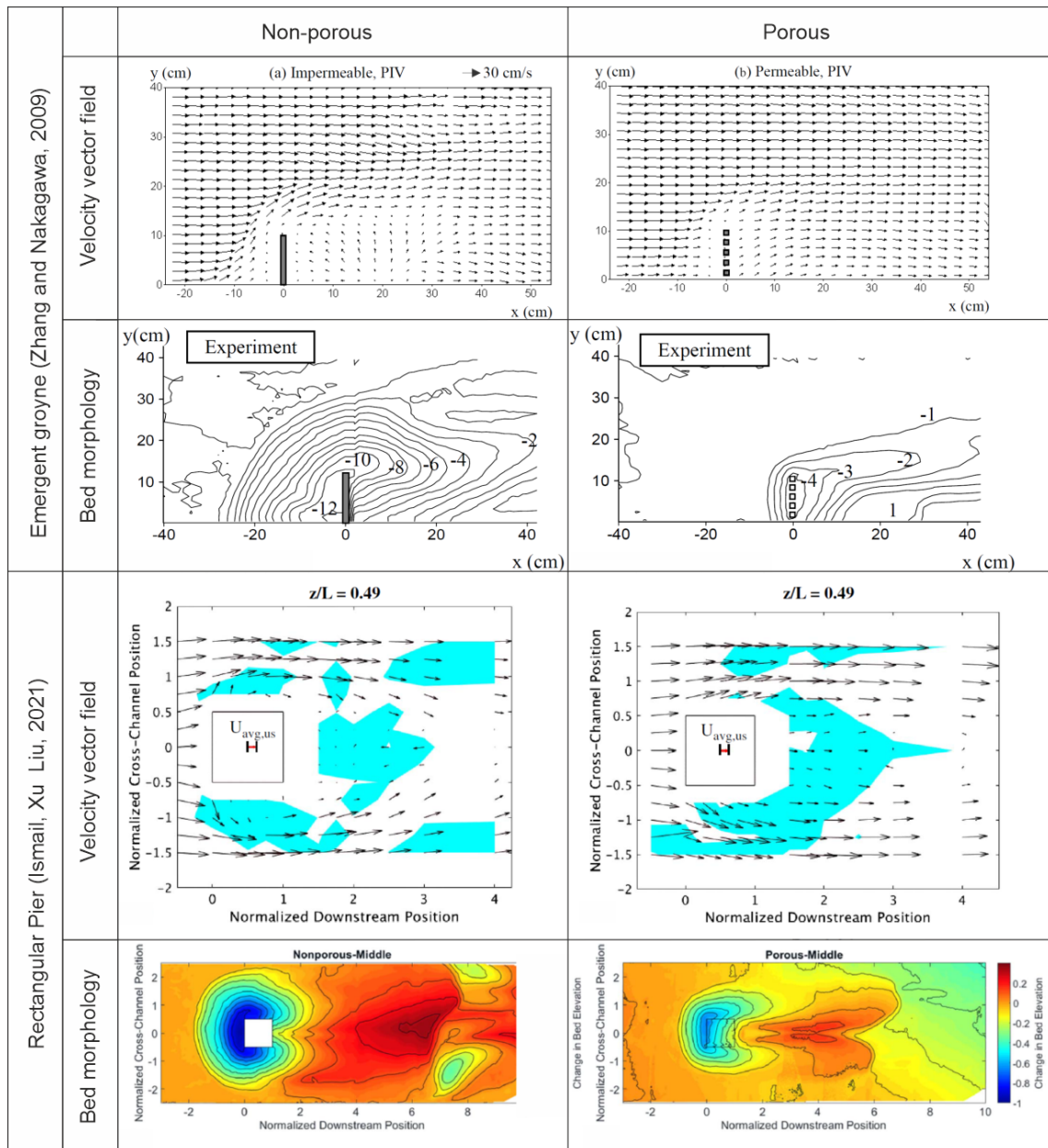
Figure 6.18: Velocity vector field and bed morphology around non-porous and porous structures.
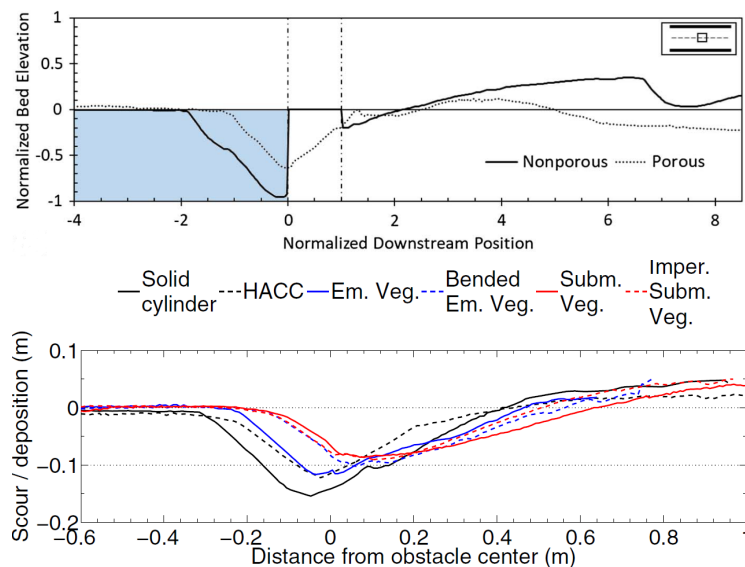
Figure 6.19: Scour profiles through solid and porous structures: Rectangular Pier according to Ismail, Xu, and Liu (2021) (above) and circular cylinder array according to Yagci et al. (2016) (below).

Design of the physical model experiments on influence of porosity

The experimental program was designed upon the results of the literature review. There are several points that need to be considered when working with porous and non-porous in-stream structures:

- Identification of the flow structure

  - Characterization of the flow structure such as the wake structure

  - Which regimes do we expect based on the literature review?

- Changes in morphodynamics

  - Based on the identified flow structures which bed morphology is created?

  - Is the scour dependent on the SVF or on the blocked area?

- Changes in backwater rise

  - Are there regimes where a water level change can be detected?

  - Is the water level change dependent on the SVF, on the blockage ratio or both?

According to the literature study it was supposed that three different regimes can be expected as shown in table 6.9. A turbulent wake flow, a porous media flow and a flow around a group of isolated of cylinders. The hydraulically significant length scale is selected as the width of the pier w_s. For the porous variants this length scale serves as a reference length scale. Table 6.10 summarizes the geometric specifications of the investigated porous variants. As the table shows, the intermediate and the isolated cylinder regimes were not investigated. The variants with higher SVF were tested first and already showed a nearly complete reduction of the scour

159

hole, therefore the SVF was not decreased more than 0.3, as the habitat requirements could not be fulfilled in this setting. As the previous experiments the measurement time was set to 48 h in accordance with the idealized structure.

Table 6.9: Classification of flow types around a porous Triangular Pier.

	Type 0	Type 1	Type 2	Type 3
	Flow around TP	Flow around dissolved TP	Intermediate	Flow around an array of cylinders
Hydraulic phenomena	Turbulent wake flow	Turbulent wake flow	Porous media flow	Flow around a group of cylinders
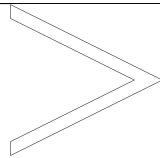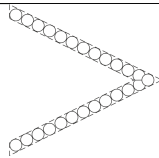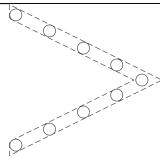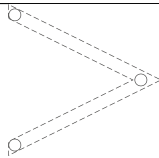
Table 6.10: Geometric specifications of porous variants of the Triangular Pier.

SVF	0.30	0.49	0.77	1.00
number of cylinders	13	21	33	43
Blockage (frontal view) [%]	73.4	100	100	100

Influence of porosity on the time development of the scouring process

The time development of the porous triangular piers is shown in figure 6.20. The lower the SVF the faster the time development of the scour. The porous pier with a SVF of 0.3 reaches equilibrium within 0.2 t_e whereas the variant with SVF = 1.00 reaches the end scour depth d_{se} after approximately 0.6 t_e. The trend is given for all porous variants. The idealized non-porous variant does not confirm with this trend and shows a medium time to equilibrium. This result shows the high dependency of the scouring processes upon the definition of the equilibrium condition.
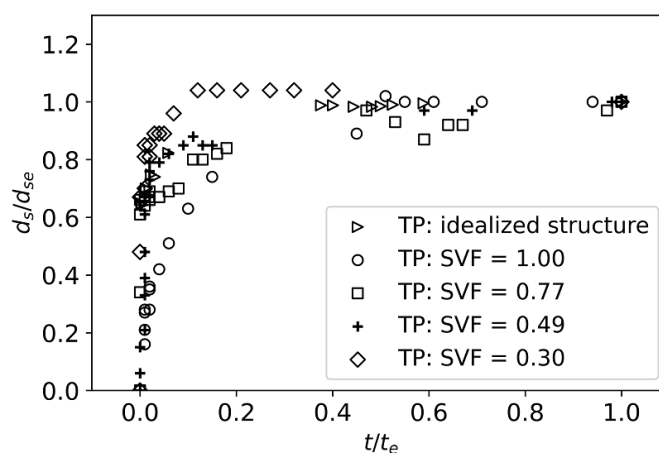
Figure 6.20: Time development of the scouring process for different SVF.

Ismail, Xu, and Liu (2021) identified four stages of time development of the scour process around porous structures. In the first stage erosion is initiated at the upstream corners of the rectangular pier and the scour hole expands upstream and lateral of the structure. The sediment is deposited immediately downstream of the structure. The second stage of the non-porous structure is dominated by the horseshoe vortex system whereas the porous variant shows erosion at the corners and inside of the structure. The third stage is dominated by changes in the downstream dune. Equilibrium stage is reached when the sediment does not move anymore. Similar stages were observed in the experiments performed in this work. Especially the incision inside the structure in stage three and the ongoing changes in the downstream dune although the scour hole already reached an equilibrium were detected in the present experiments as well.
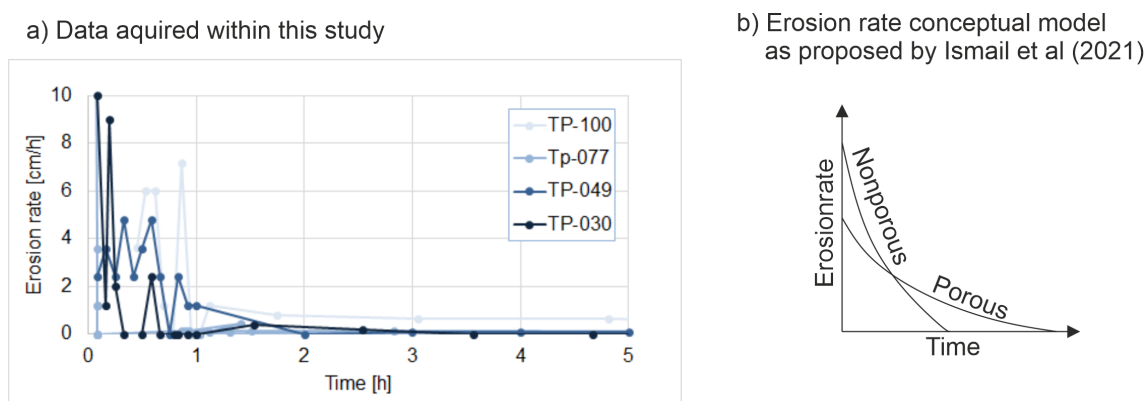
Figure 6.21: Comparison of a) Erosionrate measured in the experiments in this study with b) the erosionrate conceptual model for porous and non-porous structures as proposed by Ismail, Xu, and Liu (2021).

Ismail, Xu, and Liu (2021) propose a model for the erosion rates of non-porous and porous structures, which is displayed in figure 6.21 b), together with data which was acquired in the present experiments a). Ismail, Xu, and Liu (2021) state that the non-porous case showed higher erosion rates at the beginning of the experiment due to a higher blockage ratio and acceleration around the structure. The non-porous variant also reached equilibrium faster. The erosion rate was calculated for the experiments in this work. As figure 6.21 a) shows, the erosion rate varies highly in the first hour of the experiment which is probably due to the different time steps that were taken. The overall trend are decreasing erosion rates for all variants. Distinct differences between the porous and the non-porous variants cannot be detected. The experimental data are not in agreement with the proposed model of Ismail, Xu, and Liu (2021). This may be due to the fact, that the equilibrium condition and the erosion rate in Ismail, Xu, and Liu (2021) were estimated based on visual observation and not on measurement as it was done in this study.
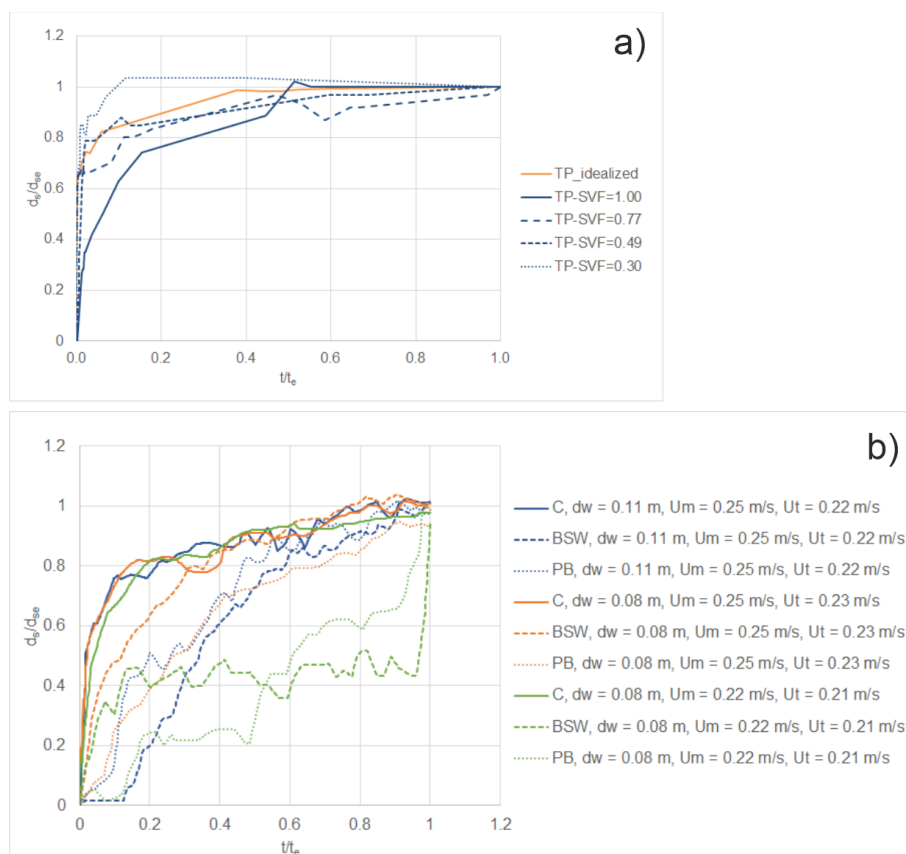
Figure 6.22: Comparison of a) Time development of porous structures measured in the experiments in this study with b) the time development of a solid cylinder (C, SVF = 1.00), a brush with steel wood (BWS, SVF = 0.09) and a plain brush (PB, SVF = 0.07) adapted from Euler et al. (2014).

Euler et al. (2014) shows that the scour depth upstream of a circular pier (C, SVF = 1.00), a brush with steel wood (BWS, SVF = 0.09) and a plain brush (PB, SVF = 0.07) with decreasing porosity is delayed for porous obstacles as shown in figure 6.22 b). Despite the absence of a discernible general trend, such as increased porosity resulting in a greater delay in the time-dependent process, the comparison with present experiments does not support this observation. Instead, the measurement data in this study suggests an opposing trend: the lower the SVF, the faster the time development. The differences between Euler et al. (2014) and this study can be explained by the different applied equilibrium conditions. Euler et al. (2014) has a defined experimental time of 28 h and it is assumed that near steady state conditions are reached within this time span. According to the criterion applied throughout this work, some of the cases would not have reached equilibrium within this time. Consequently, the normalization leads to a bias in the results.

Influence of porosity on the bed morphology in equilibrium state

The bed morphology in equilibrium state for the different SVF is shown in figure 6.23. For the variant SVF = 1.00 the general bed morphology pattern with a primary and a secondary scour hole as well as a central downstream dune are similar to the idealized case. Already for the SVF = 0.77 the scour hole significantly reduces in area and depth. The downstream dune is splitted into two dunes on the sides. The variant SVF = 0.49 shows no significant scour hole upstream and a small dune downstream of the structure. For SVF = 0.30 the same bed morphology pattern can be observed, also in quantitative extent.
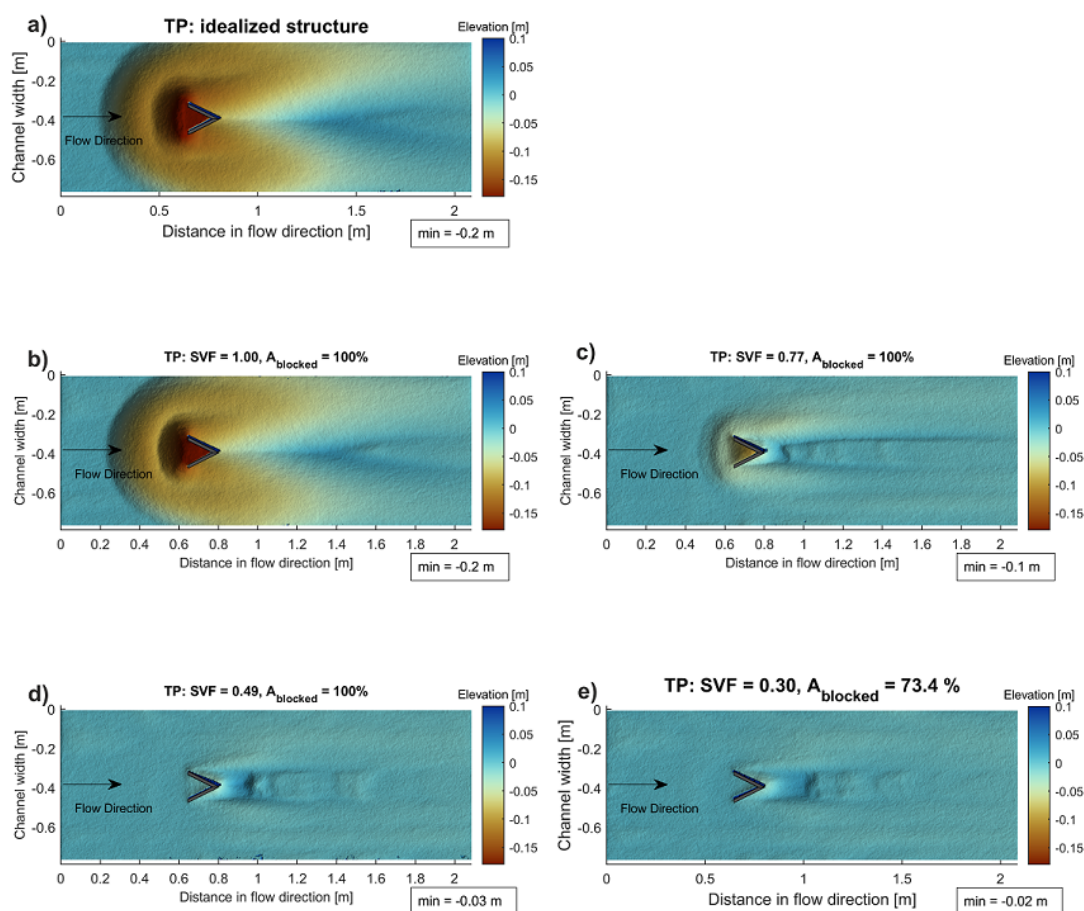
Figure 6.23: Comparison of bed morphologies in equilibrium state for different SVF. a) idealized structure, b) SVF = 1.00, c) SVF = 0.77, d) SVF = 0.49, e) SVF = 0.30.

The scour profiles along the center line of the flume are shown in figure 6.24. The decrease of SVF leads to a significant reduction of scour depth upstream of the pier. The dune downstream of the structure gets shifted towards the structure up to SVF = 0.49 and then shifts back away from the structure. A shifting behaviour of the distance of the dune was also observed by Yagci et al. (2017).
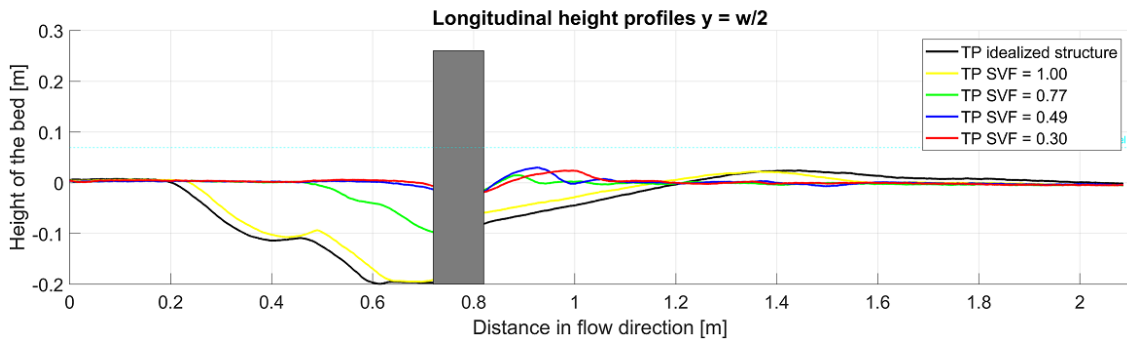
Figure 6.24: Longitudinal heightprofiles along the center line of the flume for different SVF for the Triangular Pier.

The experiments were repeated three times to quantify the sensitivity of the bed morphology. The results show that the sensitivity of the porous variants do not differ significantly from the non-porous variant and the experiments can be classified as not sensitive as shown in figure 6.25.
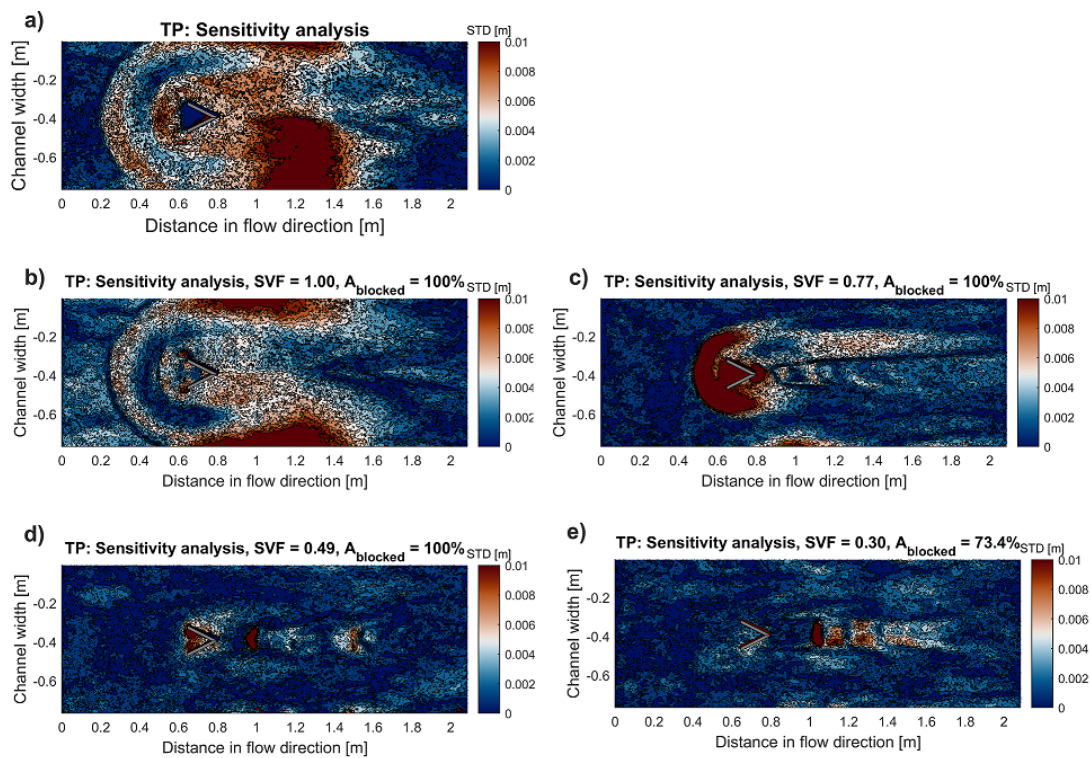
Figure 6.25: Comparison of standard deviations for different SVF. a) idealized structure, b) SVF = 1.00, c) SVF = 0.77, d) SVF = 0.49, e) SVF = 0.30.

The relative differences between the non-porous and the porous variant are displayed in figure 6.26. The dissolved structure with SVF = 1.00 shows the largest differences in the regions with highest slopes inside the primary and secondary scour hole which are up to 20 % in comparison with the end scour depth d_{se}. This is in good agreement with the results obtained in the investigation of the edge design (see figure 6.6). This leads to the conclusion that

the changes in bed morphology are majorly provoked by the round edges and not by the dissolution of the structure into several smaller cylinders. All other variants show significant differences which are much larger than 20 % in comparison with the end scour depth d_{se}.
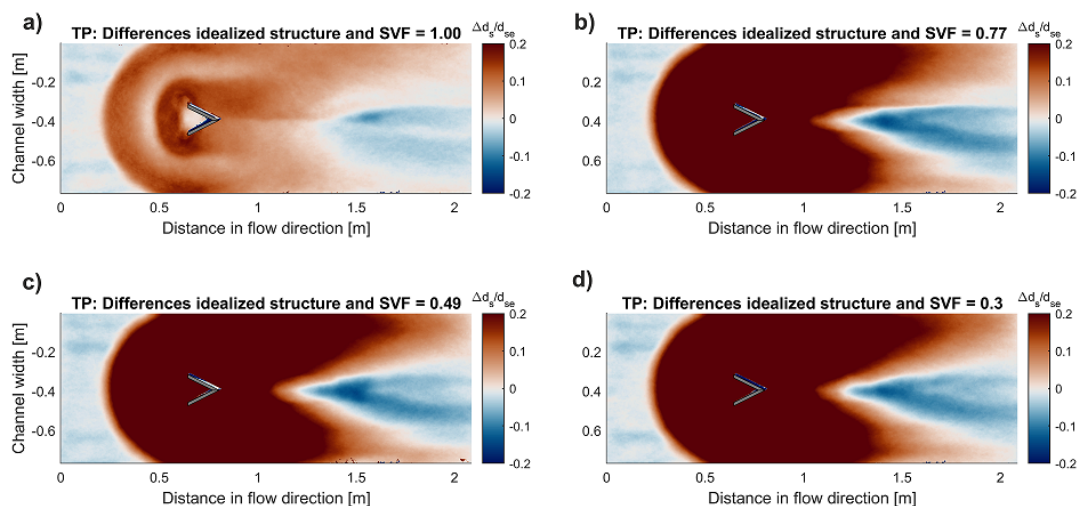
Figure 6.26: Relative differences in bed elevation between idealized structure and dissolved structure with SVF of a) 1.00 b) 0.77 c) 0.49 d) 0.30.

Table 6.11 summarizes the geometrical parameters of the scour hole and the downstream dune around the porous Triangular Pier. The scour depth is reduced up to 87 %, the upstream scour hole length up to 100 % and the distance of the dune up to 90 %. The height of the dune seems to be not influenced by the porosity. Although it needs to be considered that changes in the bed morphology downstream of the structure were still observed even though the scour hole already had reached the end scour depth (compare to results from Ismail, Xu, and Liu (2021)). Therefore, it is possible that the distance and height of the dune have not reached equilibrium conditions yet. Furthermore, the results show that the SVF tends to have a higher impact on the bed morphology than the blocked area since the differences of the variants 0.49 with $A_{blocked}$ = 100 % and 0.30 with $A_{blocked}$ = 73.4 % are not significantly different but the blocked area varies in the two cases.

Table 6.11: Geometrical parameters of the scour hole for TP with different SVF.

	TP	TP	TP	TP	TP
SVF	0.30	0.49	0.77	1.00	idealized
$A_{blocked}$ [%]	73.4	100	100	100	100
d_{se} [cm]	2.5	3.0	10.0	19.5	19.9
l_{ds} [cm]	-	-	17.7	40.7	44.3
l_{dune} [cm]	15.3	10.3	6.3	52.9	62.0
h_d [cm]	2.4	3.0	1.5	2.2	2.4

Changing the porosity and here within the SVF of the structure leads to significant changes in scour depth, scour area and scour volume. The phenomena have been observed in previous studies as well and are discussed in the context of this work in the following paragraphs.
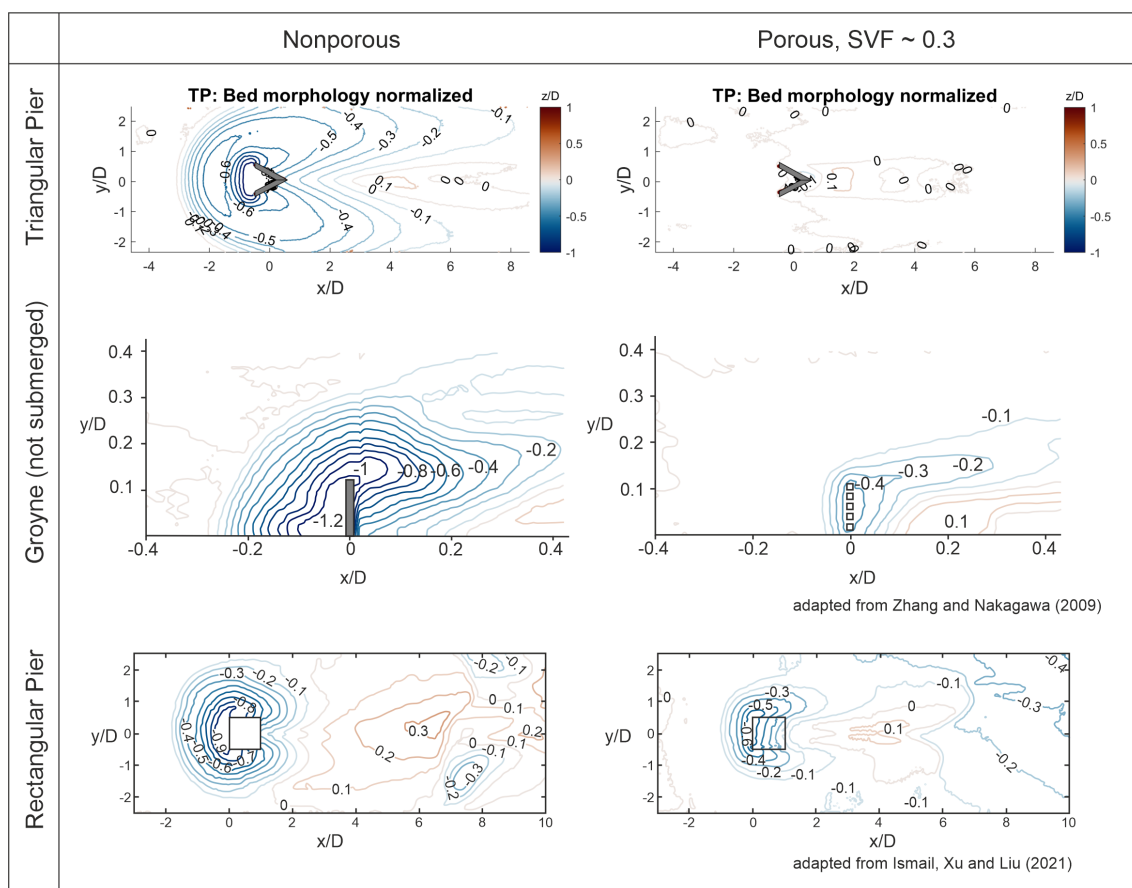
Figure 6.27: Comparison of normalized bed morphologies for a non-porous and a porous (SVF~0.3) variant of a Triangular pier (this study), a groyne (adapted from Zhang and Nakagawa (2009)) and a rectangular pier (adapted from Ismail, Xu, and Liu (2021)).

Figure 6.27 shows the normalized bed morphologies of the TP (this work), an emergent groyne (adapted from Zhang and Nakagawa (2009)) and a rectangular pier (adapted from Ismail, Xu, and Liu (2021)). The same trends are observed for all studies: with decreasing SVF the maximum scour depth, area and volume is reduced. Furthermore the length of the scour hole in upstream direction and the distance of the dune change with decreasing SVF. The scour dimensions are summarized in table B.1 in appendix B.2.1.

Zhang and Nakagawa (2009) measure a scour depth reduction of $0.8\ d_s/D$ from an impermeable to a permeable groyne (SVF = 0.5). Ismail, Xu, and Liu (2021) come to similar results for a rectangular pier (SVF = 0.29), where the scour depth reduces $0.5\ d_s/D$. Yagci et al. (2017) observed similar trends for a circular pier with a scour depth reduction of 22 %. Comparable values in this study at the Triangular Pier show a scour depth reduction of $1.0\ d_s/D$. All authors state that the bleed flow through the structure leads to internal erosion inside the structure and is the reason for the reduction of scour depth (Zhang & Nakagawa, 2009; Ismail, Xu, & Liu, 2021; Yagci et al., 2017; Kitsikoudis et al., 2016). Moreover, the downflow component upstream of the structure was significantly reduced for the porous variants. Bleed flow through the structure and a reduced downflow component could also be observed in the present experiments and is supposed to be the reason for the significant reduction of scour

depth.

The scour area decreases with decreasing SVF as shown in table B.2.1, which can be evaluated by looking at the length of the scour hole l_{ds} since the scour holes show a round shape. The length of the scour hole l_{ds} reduced by 2.4 x/D for the groyne (Zhang and Nakagawa (2009)) and by 1.0 x/D for the rectangular pier (Ismail, Xu, and Liu (2021)). Kitsikoudis et al. (2016) and Yagci et al. (2016) come to similar conclusions for a circular pier where a solid circular pier created much longer and wider scour holes. The TP in this study showed the largest reduction of 3 x/D for the length of the scour hole.

The distance of the dune h_d reduced by 1.0 x/D for the groyne (Zhang & Nakagawa, 2009), 1.0 x/D for the rectangular pier (Ismail, Xu, & Liu, 2021) and 2.0 x/D for the TP (this study). Yagci et al. (2017) found that the distance of the dune increases with increasing SVF until SVF = 0.32 and decreases again afterwards. This trend cannot be verified due to missing data below SVF = 0.30.

Ismail, Xu, and Liu (2021) observed that the total scour volume was larger for the non-porous case. Yagci et al. (2017) determined a scour volume reduction of 27 % for SVF = 0.14 around a circular cylinder array in comparison with a non-porous case. Euler et al. (2014) detected a scour volume reduction between 44 and 84 % (SVF = 0.07 and 0.09 respectively) for submerged cylinders. The Triangular Pier showed a reduction of up to 88 % for SVF = 0.30. The differences in the presented cases are probably due to the different SVF.

Figure 6.28 gives an overview of the dependency of normalized scour depth, distance of the dune and scour volume on the SVF for several literature studies in comparison with the values acquired in this study. The dimensionless scour depth increases with increasing SVF for all structures. Taking all values into account an approximately linear relationship could be derived. Even though, for distinct structures no linear relationship can be identified, such as the Triangular Pier. For the distance of the dune no general relationship can be derived. The circular pier according to Yagci et al. (2017) shows a linear relationship, but the other structures differ from this trend. The scour volume also shows a linear trend for the circular pier according to Yagci et al. (2017), but a rather exponential relationship for the Triangular Pier tested in this study.
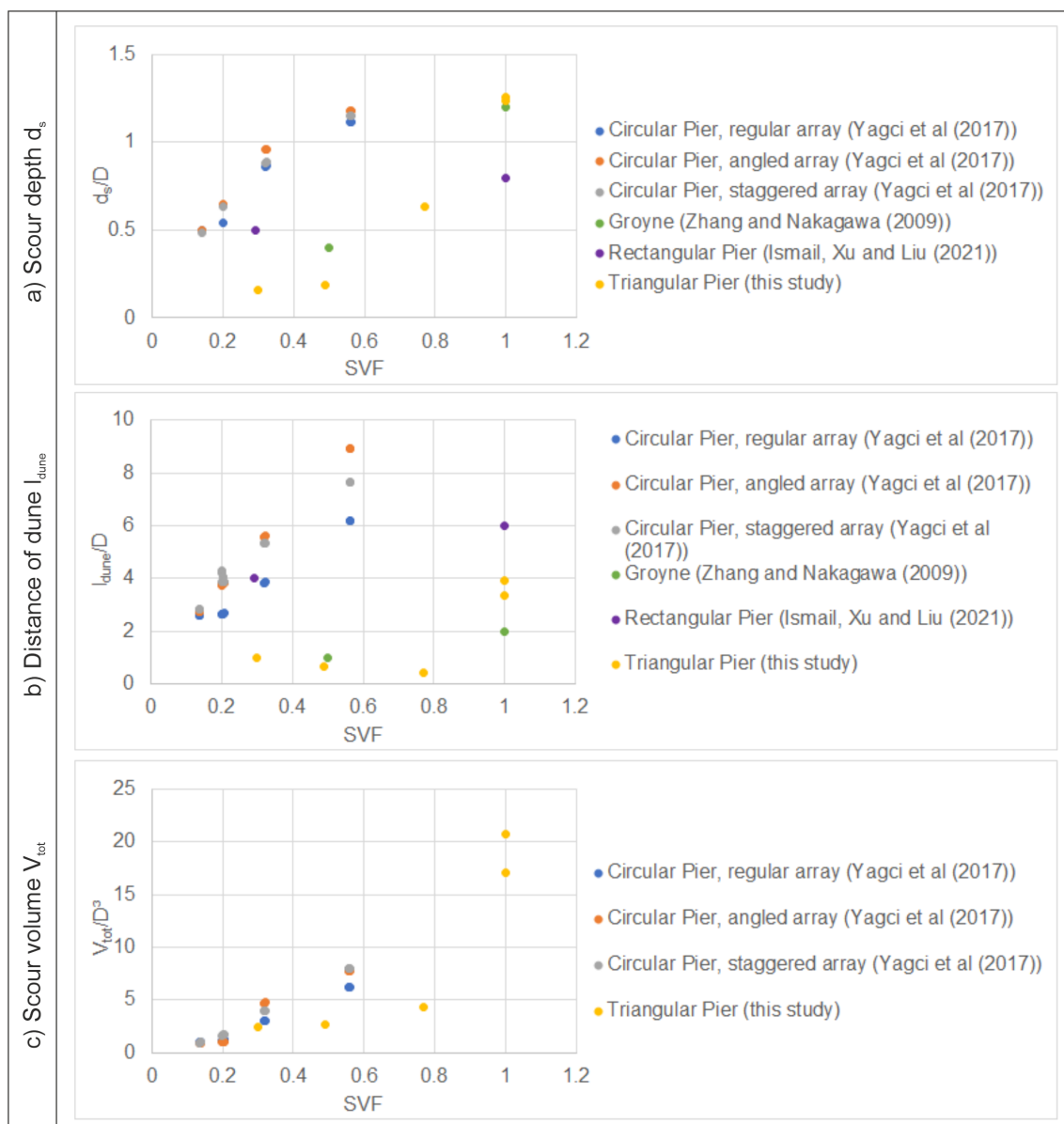
Figure 6.28: Dependency of normalized a) scour depth, b) distance of dune and c) scour volume on the solid volume fraction (SVF) for different structures with data adapted from Zhang and Nakagawa (2009), Ismail, Xu, and Liu (2021), and Yagci et al. (2017).
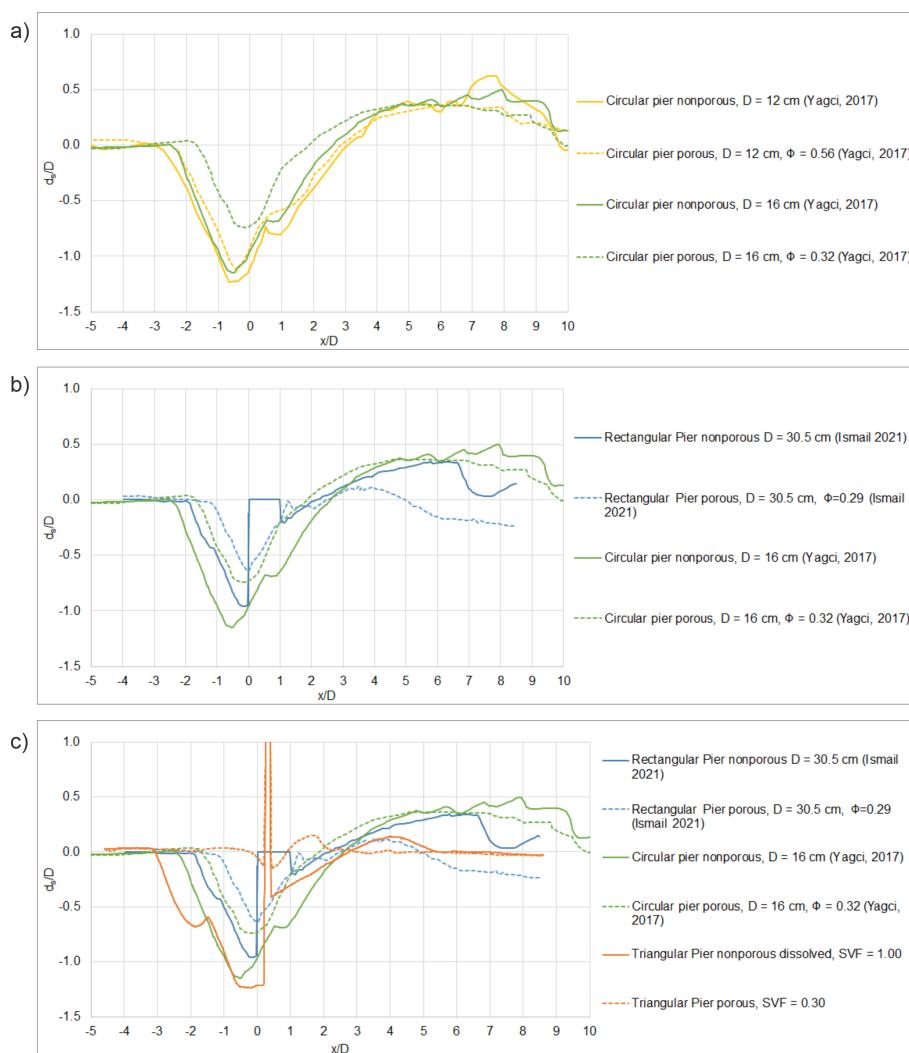
Figure 6.29: Comparison of a) different porosities for a circular pier (data from Yagci et al. (2017), b) comparison of different structure types with the same porosity SVF $\approx$ 0.3. The circular pier data are adapted from Yagci et al. (2017) and the rectangular pier data are adapted from Ismail, Xu, and Liu (2021).

The quantitative changes in bed morphology are shown in the cross profiles along the center line of the flume in figure 6.29. Figure 6.29 a) shows the changes in scour depth for a solid circular pier and for two different porosities (SVF = 0.56 and 0.32) based on data from Yagci et al. (2017). A porosity of SVF = 0.56 leads to a reduction of maximum scour depth from -1.23 d_s/D to -1.13 d_s/D, whereas a porosity SVF = 0.32 leads to a reduction from -1.15 d_s/D to -0.74 d_s/D. The height and distance of the dune does not seem to be majorly affected. Looking at two different pier-like structures (CP and RP) with a similar porosity, the circular pier leads to a reduction of 0.41 d_s/D (Yagci et al., 2017) and the rectangular pier of 0.33 d_s/D (from -0.96 to -0.63 d_s/D) (Ismail, Xu, & Liu, 2021) as shown in figure 6.29 b). The Triangular Pier leads to a reduction of 1.08 d_s/D (from -1.23 to -0.15 d_s/D). As shown in figure 6.29 c) the Triangular Pier leads to a significantly higher reduction of scour depth due to porosity as the other two pier-like structures. It is hypothesized that this difference can be traced back to the different geometries of the structures.

Upon the results, a conceptual model is derived that can theoretically explain the differences. A groyne and a triangular pier are considered as so called *linear structures* as the streamlines only pass one element of the dissolved structure and are therefore diverted only one time. These type of structures are defined as **mono-pass structures**. A rectangular and a circular pier have a *volumetric extent* in flow direction and the streamline passes various elements of the dissolved structure and are therefore diverted several times. This type of structure is defined as **multi-pass structures**. The difference of the two types is illustrated in figure 6.30. Multi-pass structures induce higher internal losses than mono-pass structures. Consequently, changing the SVF has a higher impact on mono-pass structures than on multi-pass structures.

Multi-pass structure
(circular pier)

Mono-pass structure
(triangular pier)
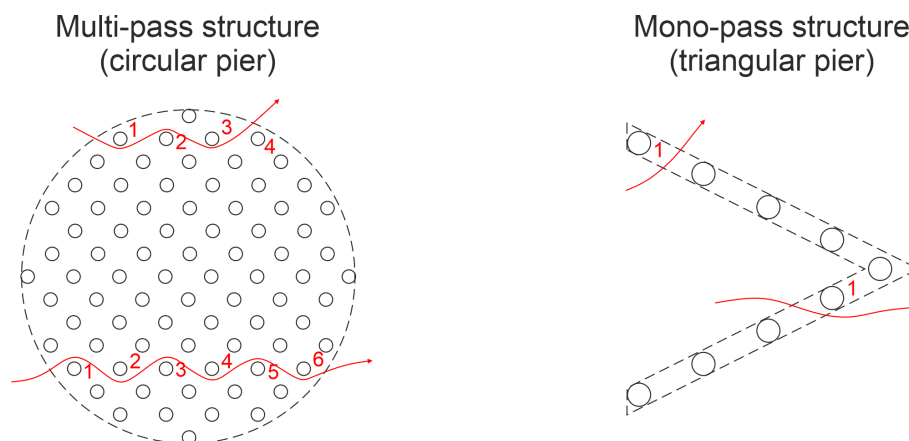
Figure 6.30: Conceptual drawing of a mono-pass structure and a multi-pass structure. The number of "passes" around elements of the porous array is indicated with numbers.

Influence of porosity on the backwater rise

The influence of porosity on the backwater rise is shown through the relative value $\Delta h_1/h_0$ in table 6.12. The results show that the backwater rise does not differ significantly for the porous variants in comparison with the non-porous variant. It is hypothesized that the system of backwater rise and scour depth reaches an energetic optimum which lays around 10.5 % for the Triangular Pier. No comparable studies could be found that investigate the influence of porosity on the backwater rise in the context of movable bed and is therefore not discussed here.

Table 6.12: Backwater rise for different SVF of TP.

Porosity	$\Delta h_1/h_0$ [%]
TP – non-porous, idealized structure	10.5
TP - $SVF = 1.00$, $A_{blocked} = 100\%$	10.9
TP - $SVF = 0.77$, $A_{blocked} = 100\%$	11.3
TP - $SVF = 0.49$, $A_{blocked} = 100\%$	11.1
TP - $SVF = 0.30$, $A_{blocked} = 73.4\%$	10.0

In conclusion, porosity proves to be the predominant factor among natural materials in influencing bed morphology. Scour depth can be reduced by up to 87 %, scour hole length by 100 %, and the distance of the dune by 90 %. A qualitative comparison with literature val-

ues demonstrates good agreement. Discrepancies between the Triangular Pier and other pier shapes (such as circular and rectangular) can be attributed to differences in their geometric extent in the flow direction, distinguishing linear structures (mono-pass, e.g., groynes and the TP) from volumetric structures (multi-pass, e.g., circular and rectangular piers). Mono-pass structures exhibit a higher sensitivity to porosity than multi-pass structures. The influence of porosity on the backwater rise remains relatively negligible compared to the idealized case, with the absolute backwater rise reaching a maximum of 11.3 %.

6.2 Influence of debris accumulations

River floods often bring debris such as wood, leaves but also human trash. Especially emergent in-stream structures are at a high risk of trapping floating debris. The accumulated materials cause an additional obstruction to the flow and the flow field gets altered as shown in figure 6.31. The flow is deviated and plunges beneath the debris (Melville and Dongol (1992), Lagasse, Zevenbergen, and Clopper (2010), Pagliara and Carnacina (2011a), Pagliara and Carnacina (2011b), and Pagliara and Carnacina (2013)). The flow gets constricted below the debris accumulation due to the generation of a boundary layer beneath the debris bottom (Pagliara & Carnacina, 2013). Hence, higher kinetic energy is present below the debris. As a consequence of the altered flow field also the scour hole that forms around a pier with debris accumulation is different. Higher kinetic energy and sediment burst lifts lead to deeper and larger scour holes (Pagliara & Carnacina, 2013). An additional upstream scour hole could be observed in some cases (Lagasse, Zevenbergen, & Clopper, 2010).
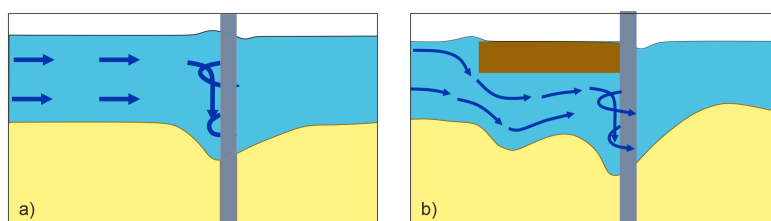
Figure 6.31: Flow pattern around a pier a) without debris and b) with debris. Adapted from Lagasse, Zevenbergen, and Clopper (2010).

6.2.1 Influence of debris accumulations on the morphology

The influence of debris accumulations or ice cover on the bed morphology has been widely investigated for several types of bridge piers, such as circular (Pagliara & Carnacina, 2011a; Melville & Dongol, 1992; Rahimi et al., 2018; Dias, Fael, & Núñez-González, 2019), square (Lagasse, Zevenbergen, & Clopper, 2010; Zevenbergen et al., 2006) and typical long bridge piers (Ebrahimi et al., 2018). The alteration in flow and local scour around a pier due to a debris accumulation is dependent on various factors:

- Form of the debris (round, rectangular, triangular)

- Thickness of the debris (T_d)

- Submergence of the debris (h_d/h_0)

- Length of the debris (L_d) (upstream length L_{du} and downstream length L_{dd})

- Roughness and Porosity

- Width of the debris (w_d)

The parameters that influence the bed morphology are displayed in figure 6.32.
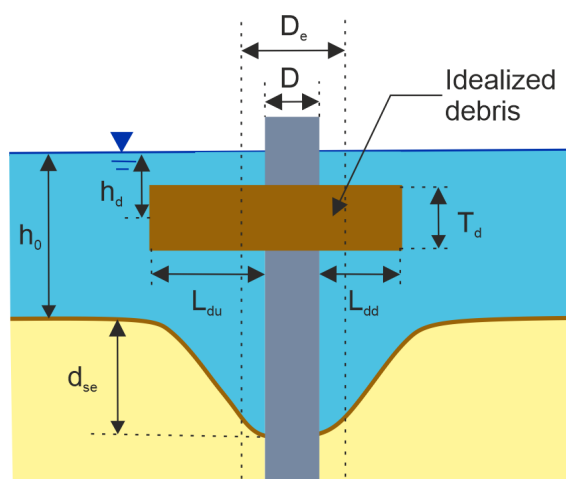
Figure 6.32: Definition of debris parameters.

Form of the debris

The form of the debris can be varied in the planview and the sideview. The sideview is typically varied in rectangular and triangular form as in Lagasse, Zevenbergen, and Clopper (2010) and Dias, Fael, and Núñez-González (2019). Lagasse, Zevenbergen, and Clopper (2010) report that the triangular shaped debris leads to higher scour depth and scour width than the rectangular variant. Moreover, the rectangular debris showed a second scour hole upstream of the scour around the pier, which could not be detected for the triangular debris. The planview of the debris was changed in several works (Melville & Dongol, 1992; Rahimi et al., 2018). Melville and Dongol (1992) identified the deepest scour for a cylindrical shape. In contrast, Rahimi et al. (2018) found the rectangular shape to create the deepest scour in comparison with a cylindrical and a triangular shaped debris. The increase of scour depth was 22 %, 18 % and 15 %, respectively.

Thickness of the debris

Two factors that are often not considered separately, but are investigated in a combined way, are the thickness D_d and the submergence h_d/h_0 of the debris. Even though the effects need to be seen separately. Melville and Dongol (1992), Ebrahimi et al. (2018), Rahimi et al. (2018), and Lagasse, Zevenbergen, and Clopper (2010) could show for different shapes of debris that the thicker the debris, the deeper is the scour hole. Moreover, they identified, that the effect of the thickness is also dependent on the flow shallowness h_0/D. The thickness

has the highest effect for a flow shallowness of $h_0/D = 4$ and gets small for $h_0/D > 9$ as shown in figure 6.33. Increasing the relative thickness T_d/D from 0.5 to 2.66 the relative scour depth $d_s/d_{s-nodebris}$ increased by 49%, 56 %, 60 % for triangular, cylindrical and rectangular shaped debris, respectively (Rahimi et al., 2018).
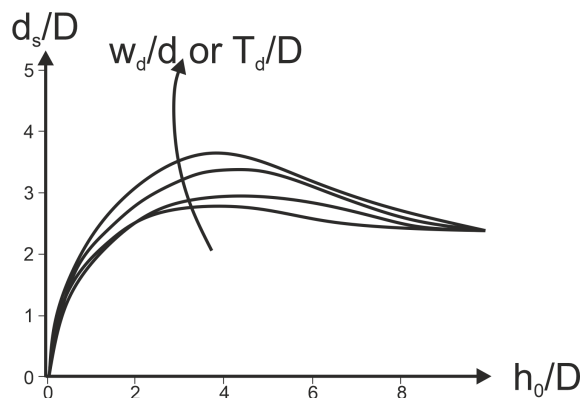
Figure 6.33: Influence of the thickness of the debris T_d on the maximum scour depth d_s as a function of flow shallowness h_0/D. Adapted from Melville and Dongol (1992).

Submergence of the debris

The submergence of the debris h_d/h_0 leads to a division of the flow into a part that diverts above the debris and a part that diverts below the debris (Ebrahimi et al., 2018). First, the submergence leads to an increase of scour depth and reaches a maximum value. Is the debris close to the bed a protecting effect can be observed and the scour depth decreases again (Ebrahimi et al., 2018; Rahimi et al., 2018; Dias, Fael, & Núñez-González, 2019). It is to be noted that the definition of h_d varies in the different publications. Ebrahimi et al. (2018) define h_d from the initial bed to the lower end of the debris accumulation whereas Dias, Fael, and Núñez-González (2019) and Rahimi et al. (2018) define h_d from the water surface to the center of the debris accumulation. The definition used throughout this work is according to the latter. The relative submergence where the peak of scour depth is reached differs in literature. Ebrahimi et al. (2018) identifies a ratio of h_d/h_0 = 0.6-0.8, Rahimi et al. (2018) concludes 0.46 and Dias, Fael, and Núñez-González (2019) identifies 0.5 as the maximum.

Length of the debris

According to Ebrahimi et al. (2018) the scour depth increases with increasing upstream length until a value of $L_{du}/h_0 = 1.8$. For values above 1.8 no significant changes were detected. Lagasse, Zevenbergen, and Clopper (2010) found that the maximum scour occurs when the length of the debris is equal to the flow depth h_0. Pagliara and Carnacina (2011a) identified $L_{du} = 2.5$ to $3.7\,D$ as the maximum scour depth. The effective length of the debris was also investigated by Rahimi et al. (2018). They found that increasing the effective length of a rectangular debris from 1.66 to 10 L_{du}/D could increase the scour hole by 47 % in comparison with the case of no debris. The effect decreases for ratios greater than $L_{du}/D > 8.33$.

Roughness and porosity

The roughness and porosity of a debris were classified as second order variables compared to size, shape and location of the debris (Lagasse, Zevenbergen, & Clopper, 2010).

Width of the debris

The width of the debris correlates directly with the width of the scour hole irrespective of the shape of the debris (Lagasse, Zevenbergen, & Clopper, 2010). To consider debris in numerical models Melville and Dongol (1992) proposed to use an "equivalent width D_e" of the pier that takes the additional obstruction into account. The equation uses the width D_d and the thickness T_d of the debris. The shape of the debris and the upstream length are not considered.

$$D_e = \frac{T_d\,w_d + (h_0 - T_d)D}{h_0} \tag{6.9}$$

Lagasse, Zevenbergen, and Clopper (2010) optimized this equation including the shape, by adding the coefficient K_{d1} and the length of the debris with coefficient K_{d2}:

$$
\begin{aligned}
D_e &= \frac{(K_{d1}T_d w_d)(L_D/h_0)^{K_{d2}} + (h_0 - K_{d1}T_d)D}{h_0} \quad &for\ L_D/h_0 > 1.0 \\
D_e &= \frac{(K_{d1}T_d w_d) + (h_0 - K_{d1}T_d)D}{h_0} \quad &for\ L_D/h_0 \leq 1.0
\end{aligned}
\tag{6.10}
$$

K_{d1} equals 0.79 for rectangular debris and K_{d2} equals -0.79 for rectangular debris. Rahimi et al. (2018) further developed the equation to:

$$D_e = \frac{0.52\,T_d\,w_d + (h_0 - 0.52\,T_d)\,D}{h_0} \tag{6.11}$$

6.2.2 Design of the physical model experiments on influence of debris accumulations

The research question imposed in this section is to verify whether the identified governing parameters also apply for Triangular Piers. Additionally, the question whether the downstream length has an influence on the scour pattern, as proposed by Pagliara and Carnacina (2011a) is explored. The variation of parameters in this study is limited to the submergence and the planview size of the debris (upstream and downstream length). To the author's knowledge the backwater rise of debris accumulations has not been addressed systematically in literature yet. The debris accumulation was modeled with PVC plates of a rectangular shape with different sizes that could be adjusted in height with a threaded rod as shown in figure 6.34. The thickness of the debris was selected to 1.2 cm. According to Melville and Dongol (1992) the influence of the thickness $T_d/D = 0.076$ is small. The submergence of the debris was varied in 3 steps $h_d/h_0 = 0.46$, 1.00 and 1.05. The upstream length was varied in the range of L_{du}/D of 0, 0.25 and 0.5. The downstream length was varied in the range of L_{du}/D of 0.25, 0.5 and 0.75. The dimensions were selected upon best knowledge, but it has to be mentioned that the

dimensions of the debris accumulation are of high variability and to define the dimensions is highly complex, as already stated by Melville and Dongol (1992). The experiments were run the equal time as the idealized structure which was 48 h for the TP.
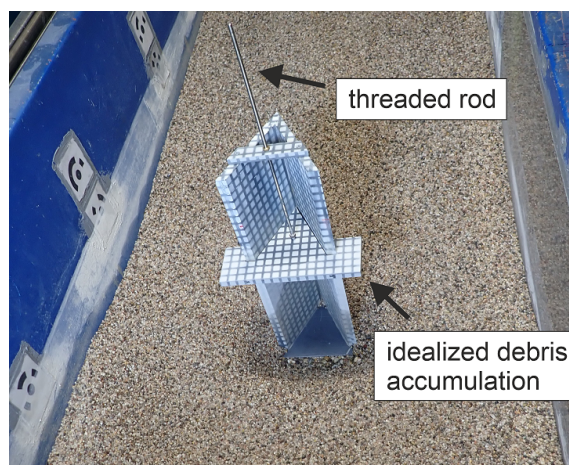
Figure 6.34: Experimental setup of the debris accumulation experiments.

6.2.3 Influence of debris accumulations on the bed morphology in equilibrium state

The general scour pattern does not change significantly in comparison with the case without debris as shown in figure B.8 in appendix B.2.2. Therefore, the differences for the variation of submergence, upstream and downstream length are highlighted as follows.

Influence of submergence h_d/h_0

Figure 6.35 shows the differences in bed morphologies for two different submergence levels h_d/h_0 = 0.46 and 1.00 for three different sizes of debris accumulation. All cases show that a submergence level of h_d/h_0 = 0.46 leads to an increase of scour depth inside of the primary scour hole. The secondary scour hole shows a decrease in scour depth. In total, the pronounced step of the primary and secondary scour hole reduces and tends to a constant slope, especially for bigger dimensions of the debris as shown in figure B.9 in appendix B.2.2. The submergence level of h_d/h_0 = 1.00 shows much smaller changes in comparison with the idealized TP. The influence of submergence shows a peak value for scour depth at h_d/h_0 = 0.46 according to Rahimi et al. (2018), Ebrahimi et al. (2018), and Dias, Fael, and Núñez-González (2019) as shown in figure 6.36. The scour depth cannot be compared directly with the current set of experiments, as the scour reached the flume bottom and is limited in depth development. Even though, the primary scour hole shows significantly higher scour depth for h_d/h_0 = 0.46 in comparison with h_d/h_0 = 1.00 and the case without debris, which is in accordance with the literature values shown in figure 6.36.
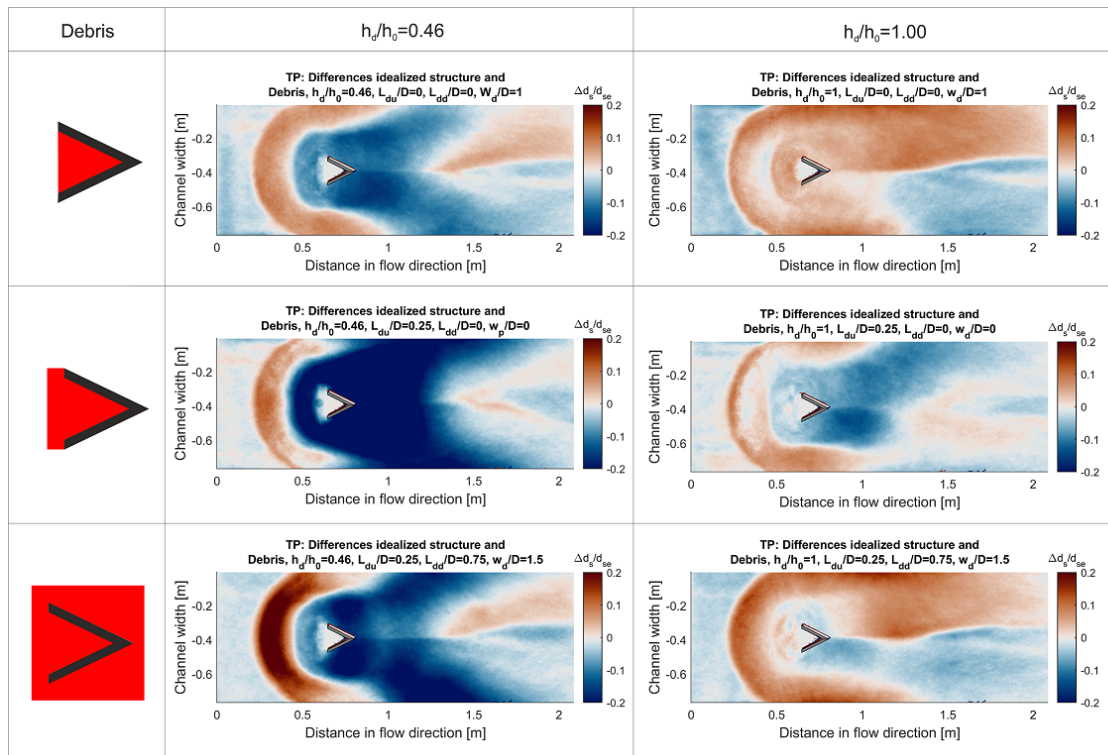
Figure 6.35: Differences in bed elevation between an idealized TP with and without debris accumulation for submergence levels of $h_d/h_0 = 0.46$ and 1.00 for different debris dimensions.
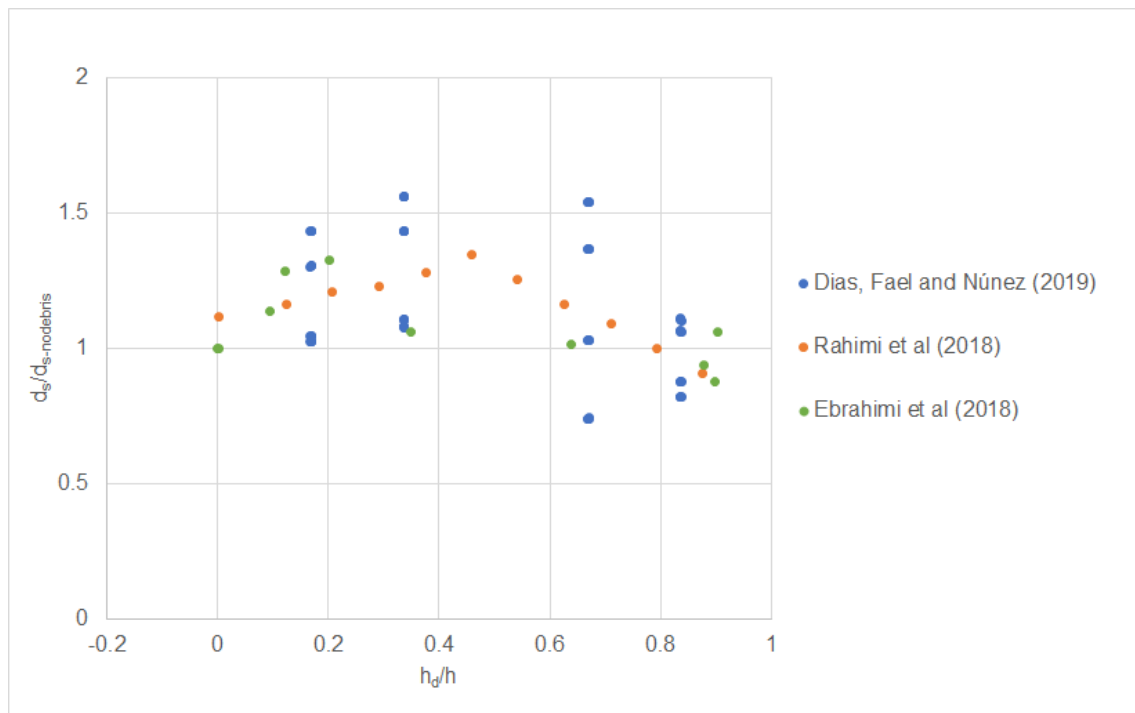
Figure 6.36: Influence of submergence of a debris accumulation on the relative scour depth according to Dias, Fael, and Núñez-González (2019), Rahimi et al. (2018), and Ebrahimi et al. (2018).

176

Influence of upstream length L_{du}

The influence of upstream length L_{du} is shown in figure 6.37. The larger the relative upstream length L_{du}, the larger the scour depth in the primary scour hole and the smaller the scour depth in the secondary scour hole. Irrespective of the submergence level, a larger relative upstream length leads to a reduction of the pronounced step between the two scour holes but to a constant slope as shown in figure B.10 in appendix B.2.2.
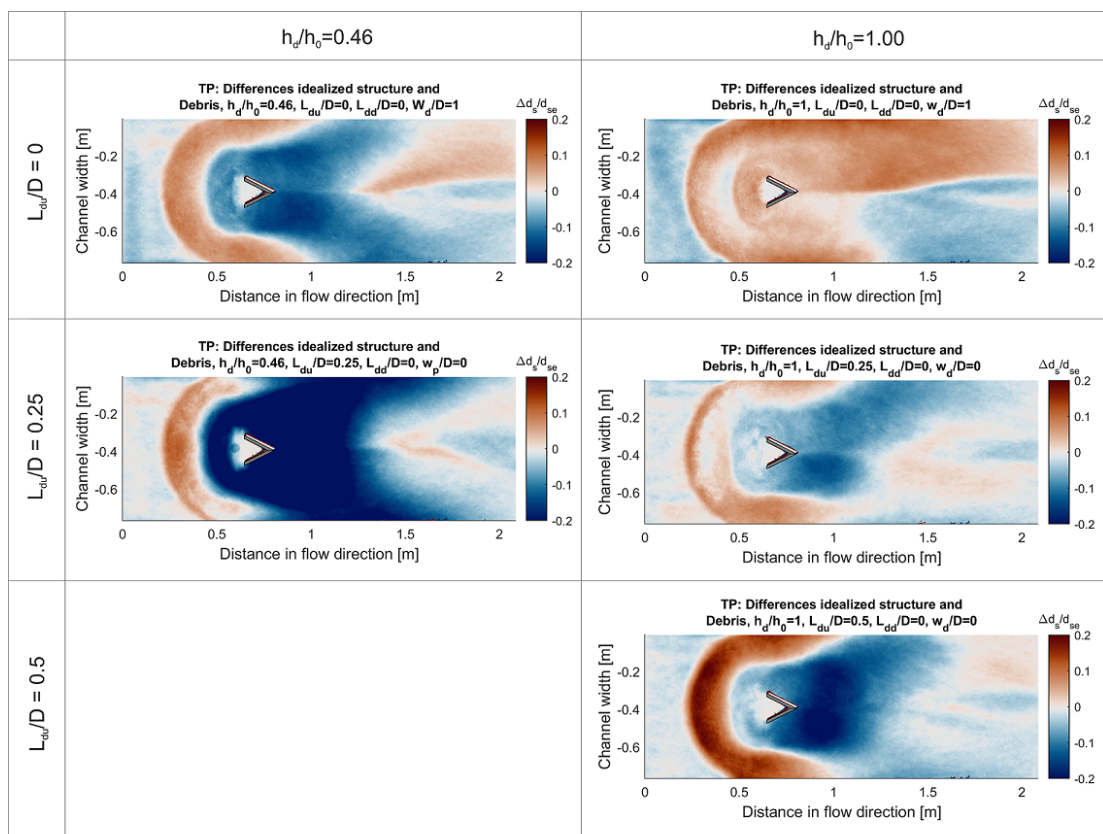
Figure 6.37: Differences in bed elevation between an idealized TP without and with debris accumulations of different upstream lengths L_{du}.

Ebrahimi et al. (2018) and Lagasse, Zevenbergen, and Clopper (2010) reported the largest scour depth for upstream length of the debris of 1.8 L_{du}/h_0 and 1.0 L_{du}/h_0, respectively. Pagliara and Carnacina (2011a) related the upstream length to the significant length of the pier L_{du}/D and found a maximum in scour depth for 2.5 - 3.7. In this study the upstream length was varied in a range of 0 - 1.1 L_{du}/h_0 or 0.25 - 0.5 L_{du}/D. Larger scour depth was detected for larger L_{du}/h_0 or L_{du}/D in the primary and secondary scour hole. The end scour depth cannot be evaluated for the reasons stated above. Moreover, the investigated dimensions differ significantly which complicates the comparison.

Influence of downstream length L_{dd}

The variation of downstream length L_{dd} shows a small influence on the scour hole characteristics and can therefore be classified as secondary order influence as shown in figures 6.38 and B.11 in appendix B.2.2.

177
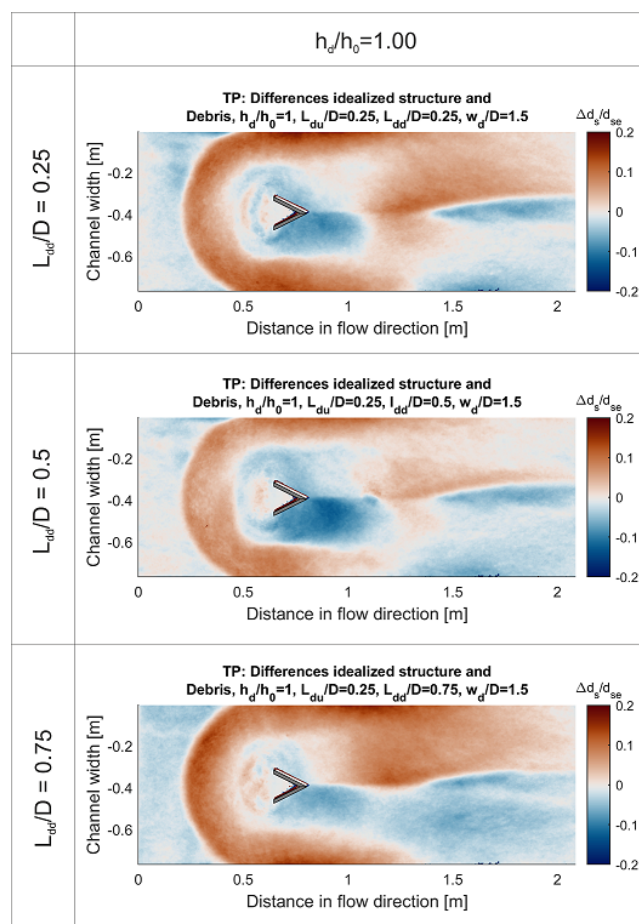
Figure 6.38: Differences in bed elevation between an idealized TP without and with debris accumulations of different downstream lengths L_{dd}.

6.2.4 Influence of debris accumulations on backwater rise

The influence of submergence, upstream and downstream length on backwater rise $\Delta h_1/h_0$ is given in tables 6.13, 6.14 and 6.15. All cases where debris is present, a higher backwater rise could be detected. Systematic influences of the investigated parameters cannot be drawn from the results and need further experiments, that were not completed within the scope of this work. To further understand the influence of the parameters, the author recommends to widen the range of the geometrical dimensions of the debris to larger dimensions.

Table 6.13: Backwater rise $\Delta h_1/h_0$ [%] due to different submergence h_d/h_0 and different dimensions of debris.

	Submergence h_d/h_0	
Debris dimensions	0.46	1
no debris	10.5	
small	11.2	23.6
middle	16.9	17.4
big	19.9	10.8

Table 6.14: Backwater rise $\Delta h_1/h_0$ [%] due to different relative upstream lengths L_{du}/D and different submergence h_d/h_0.

	Submergence h_d/h_0	
L_{du}/D	0.46	1
0	11.2	23.6
0.25	16.9	10.8
0.5		17.0

Table 6.15: Backwater rise $\Delta h_1/h_0$ [%] due to different relative downstream lengths L_{dd}/D.

L_{dd}/D	$\Delta h_1/h_0$
0.25	18.2
0.5	12.1
0.75	17.4

The submergence of debris emerged as the decisive factor influencing bed morphology in the conducted experiments on debris accumulation, contributing to an approximate 20 % increase in scour depth. While the lengths both upstream and downstream exhibited an impact, their influence primarily manifested in the slopes within the scour hole upstream of the pier, resulting in a reduction of the plateau within the scour hole. Moreover, the presence of debris led to a significantly higher backwater rise, exceeding the comparable case without debris by approximately 110 %. The absolute backwater rise peaked at 23.6 %, underscoring the substantial impact of debris accumulations.

6.3   Influence of coverage and shelter

6.3.1   Structural functions of a shelter inside of a deep pool habitat

Investigations of fish biologists showed that deadwood structures inside of deep pool habitats can increase fish abundance and species diversity (Wright & Flecker, 2004) additionally to the depth and connection to other habitats (Kalogianni et al., 2020). Observations of local authorities confirm that the functional combination of a deep pool and a shelter is decisive for fish (personal communication, Frank Hartmann, 11.11.2022). A shelter can consist of large wood, root wads and trees (Solazzi et al., 2000; Nickelson et al., 1992), as well as submerged branches and leaves trapped in branches (Zika & Peter, 2002). The shelter fulfills several biological functions that are listed below:

- Obstruction of the inter- and intraspecific interference of fish (Valdimarsson & Metcalfe, 1998)

- Refuge from predators through shadow (refuge and escape structure) (Bond & Lake, 2005; Helfman, 1981; Harvey & Stewart, 1991) (Zika and Peter (2002) and McCrimmon and Kwain (1966) found the photo-negative response to be the reason for this behaviour)

- Visual isolation between individuals (Fausch, 1993), allowing more fish per unit of available space. Dolloff (1986) called this the "condominium effect".

- Competition among fish (McMahon & Hartman, 1989; Sundbaum & Näslund, 1998)

- Protection from high water temperatures (Bond & Lake, 2005)

- Overwintering habitat (Matthews (1998) in Dolloff and Warren (2003) and Solazzi et al. (2000) and Nickelson et al. (1992) in Nagayama and Nakamura (2010))

- Greater depths during low-flow periods (Matthews (1998) in Dolloff and Warren (2003))

- Capture of food items in the drift (Matthews (1998) in Dolloff and Warren (2003))

- Velocity refuge (low flow velocity) (Bond & Lake, 2005; Dolloff & Warren, 2003; Harvey & Stewart, 1991; Fausch, 1993)

- Wood accumulations have a joint effect of cavity space, stem diameter, suspended and benthic leaves, depth, inside and outside flow, undercut bank, and lateral position (Monzyk, Kelso, & Rutherford, 2003).

It is important to consider that these functions are important on a seasonal, species-specific and size-selective basis. If structures are missing it can lead to a disappearance of individual populations or parts of populations (McIntosh et al., 2000). The resulting research question from fisheries was whether it is possible to combine a deep pool habitat with a shelter habitat in form of a tree without significant decrease in the depth of the pool. By combining the deep pool habitat with a shelter a multi-functional habitat can be created.

6.3.2   Design of the physical model experiments on coverage and shelter

Two types of shelters were tested, a tree-like shelter where the fish can hide inside the system of stem, branches and leaves, and a platform-like shelter that serves as an overhead cover structure. First the tree-like shelter is explained. The size and species of the tree was selected according to Bundeswaldinventur 2012 (Schmitz et al., 2016). The most prominent tree species in Baden-Württemberg is the beech tree in an age class of 41-60 years old (Schmitz et al., 2016). Fichtner et al. (2013) analyzed beech trees of the upper layer and a typical size of a beech tree was derived (see table B.2 in appendix B.2.3). The orientation of single trees and wood structures to the flow was analyzed by Kail et al. (2007) and the most frequent angle of 0-30° to the flow was selected for this study. Experience of local authorities also confirmed this angle for river reaches in Baden-Württemberg (personal communication, Dr. Frank Hartmann, 11.11.2022). The tree imposes an obstruction to the flow so it is important to know how the tree influences the bed morphology around the in-stream structures and whether the target values of scour depth and area can still be met. Moreover, the impact on backwater rise needs to be quantified. The basic concept of modelling the obstruction is to scale the pressure loss coefficient λ that the tree imposes on the flow. The concept was described in further detail in chapter 4.2.6. The aspect of foliage stages is considered additionally, as temperate deciduous vegetation is present in the project region. Different foliage stages can also be observed when a tree with foliage falls into a river. The leaves and small branches dissolve over time and get washed off during floods. Two different foliage stages were modelled: a

stage with typical summer foliage and a stage without foliage. The two foliage stages impose a different resistance to the flow and were modelled with different porosities of the filamentous material, which correspond to different pressure loss coefficients. The physical background and selection of the porosity values for the different foliage stages is described in chapter 4.2.6. For the stone-like structures the tree was fixed with a rope at the head of the structure with a rope (see figure 6.39 a) and b)) and for the pier-like structure (TP) the trees was fixed with ropes in the river banks (see figure 6.39 c) and d)).
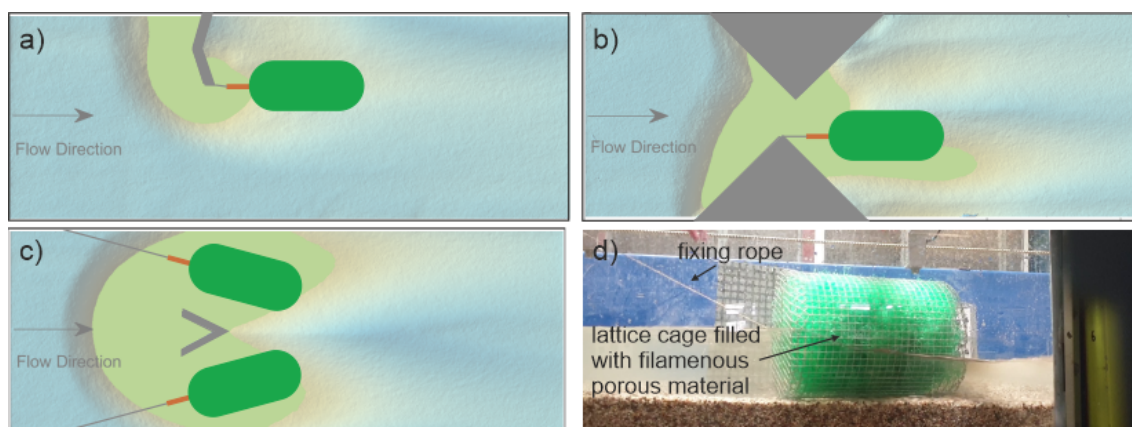
Figure 6.39: Positioning of the tree-like shelter in the physical model experiment for a) and b) the stone-like structure DG and DWD, c) the pier-like structure TP and d) with a filamentous porous material inside a lattice cage fixed with a rope.

For the pier-like structure additionally two arrangements were tested. One arrangement consisted of one tree installed on one side and a second arrangement with two trees symmetrically installed on both sides (see figure 6.40).
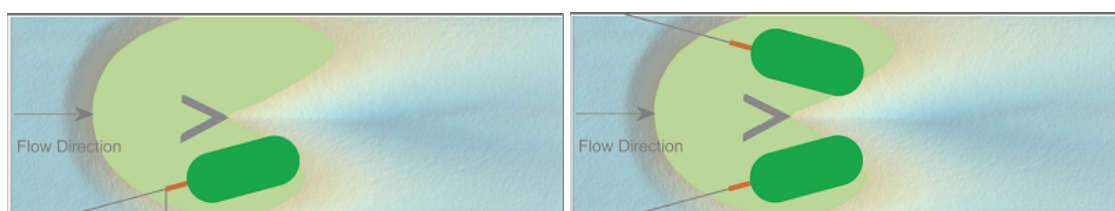
Figure 6.40: Arrangement of trees at the pier-like structure with one tree (left) and two trees (right).

The second type of shelter was inspired by so called "fishhotels" as designed by Bernd Walser in a river restoration project at the river Elz (see figure 6.41, Vitale Gewässer (2021)). The structure consists of a hole that is digged into the river bank and which is covered by a steel platform that is driven into the river bank. The purpose of this structure is to provide a shelter comparable to undercut banks. This structure seemed feasible to apply together with the DG. The size was selected to 1/3 of the length of the groyne and installed on the same height. The only difference is that the platform was installed downstream of the groyne and inserted a notch for a constant flow through the undercut bank to protect the shelter from being filled up with sediment. In our case the platform is installed upstream of the structure and is kept free from sediments due to the present vortex system.
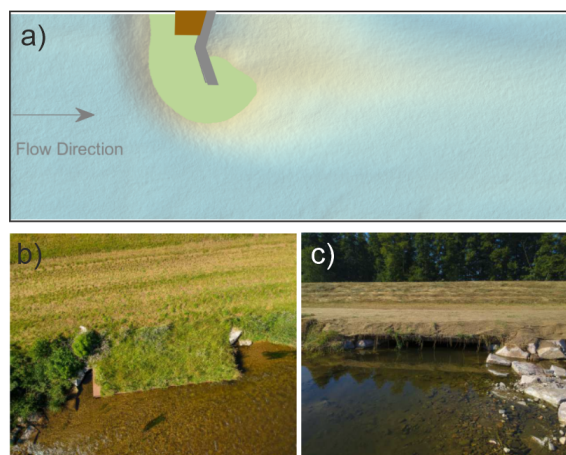
Figure 6.41: a) Positioning of the platform-like shelter upstream of the DG. b) and c) Implementation of a shelter in a revitalization project at river Elz close to Riegel (image courtesy of Bernd Walser).

6.3.3   Time development of the position of the tree-like shelter

As the tree-like shelter is only fixed with ropes, the tree can move freely in the flow as shown in figure 6.42. In the experimental procedure the protection plates are removed from the bed and an initial scouring starts. Immediately after removing the plates the trees are inserted manually into the flume. An increase in water level upstream of the tree can be detected and the water level decreases as it passes the tree. A local scour below the tree forms shortly after inserting the tree. With increasing local scour the water level difference between upstream and downstream of the tree decreases. When the scour hole reaches the upstream end of the tree it tilts and slides slowly into the scour hole (figure 6.42 t-6). By not fixing the tree in the bed, the tree is able to follow the changes of the bed and stays inside the scour hole, which is a movement that would also happen in nature.
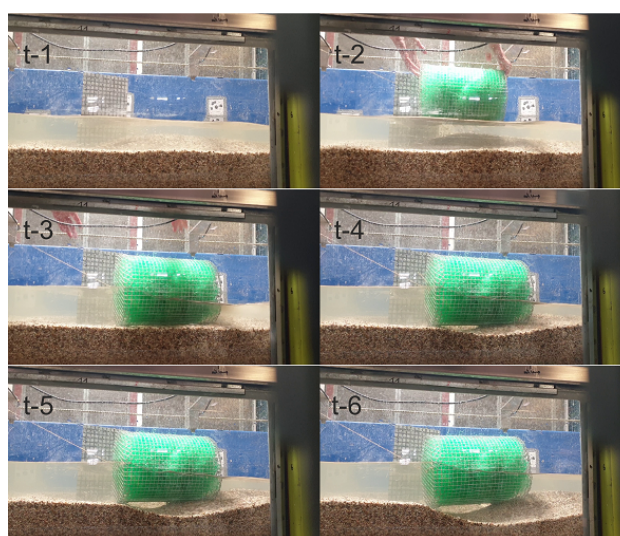
Figure 6.42: Positioning of the tree-like shelter in the physical model experiment (t-1 to t-3) and temporal development of the scour hole (t-4 and t-5) and tilting of the tree-like shelter (t-6).

6.3.4 Influence of the shelter on bed morphology

The bed morphology in equilibrium state is shown in figure 6.43 for all shelter cases of the pier-like structure (TP). It was supposed that the equilibrium was reached within the same time as for the idealized structures which was 48 h for TP and DWD and 72 h for DG. The general scour pattern with a primary and a secondary scour hole is still persistent for all variants. The upstream scour hole is shallower and shorter as it can be seen in the cross-sectional view in figure B.12 in appendix B.2.3. Major changes can be identified at the locations of the tree-like shelters and downstream of the structure. The dune is shifted from a central dune to a side dune or split into two lateral dunes depending on the arrangement as shown in figure 6.43. The distance of the dune l_{dune} is higher for all cases whereas the height of the dune stays in the same order of magnitude as shown in table 6.16a. A local scour hole can be detected at the location of the tree-like shelter, on one side or on both sides dependent on the arrangement.
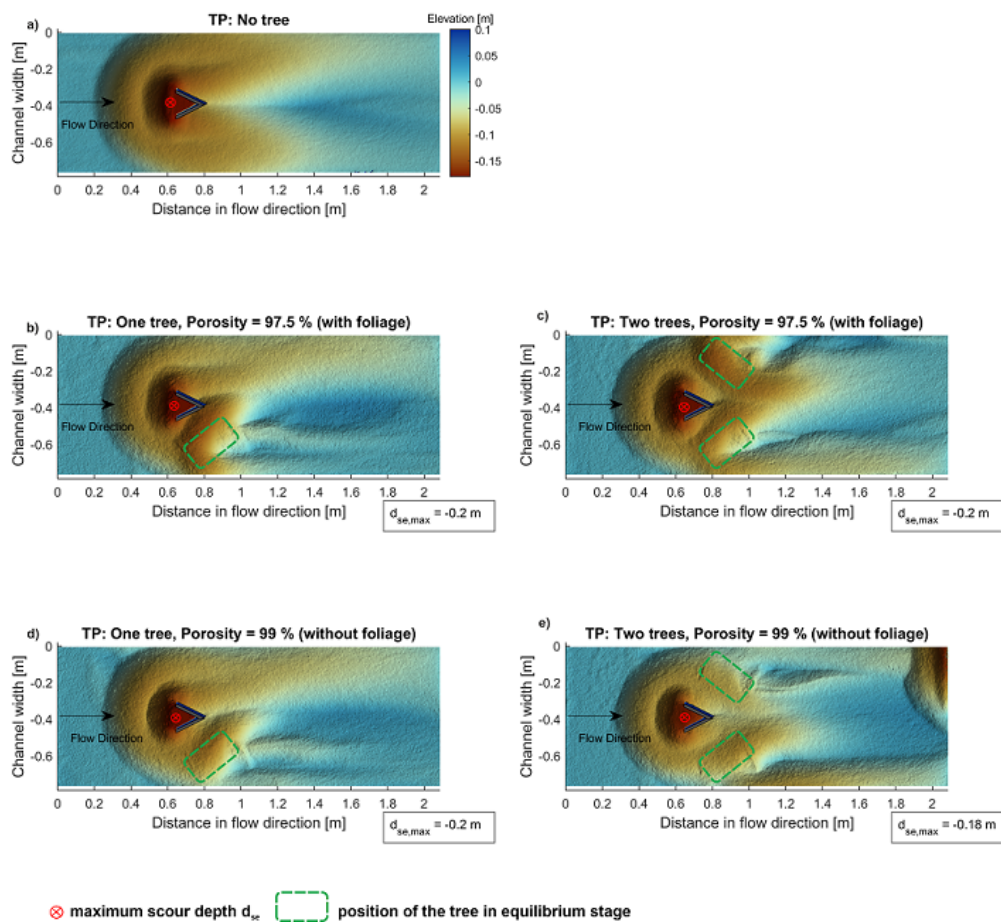
Figure 6.43: Bed morphology patterns around a pier-like structure (TP) with different variations of tree-like shelters in comparison with the case without a shelter.

183

For the DG, the upstream scour hole characteristics of the shelter cases are similar to the case without shelter as shown in figure 6.44. Downstream of the DG the longitudinal deep section that departs from the head of the groyne is elongated for the tree-like shelter cases. Additionally, the dune downstream of the groyne is shifted closer to the groyne and is higher in elevation. The other geometrical values stay in the same order of magnitude. The platform-like shelter showed very little changes in comparison with the shelter-less case.
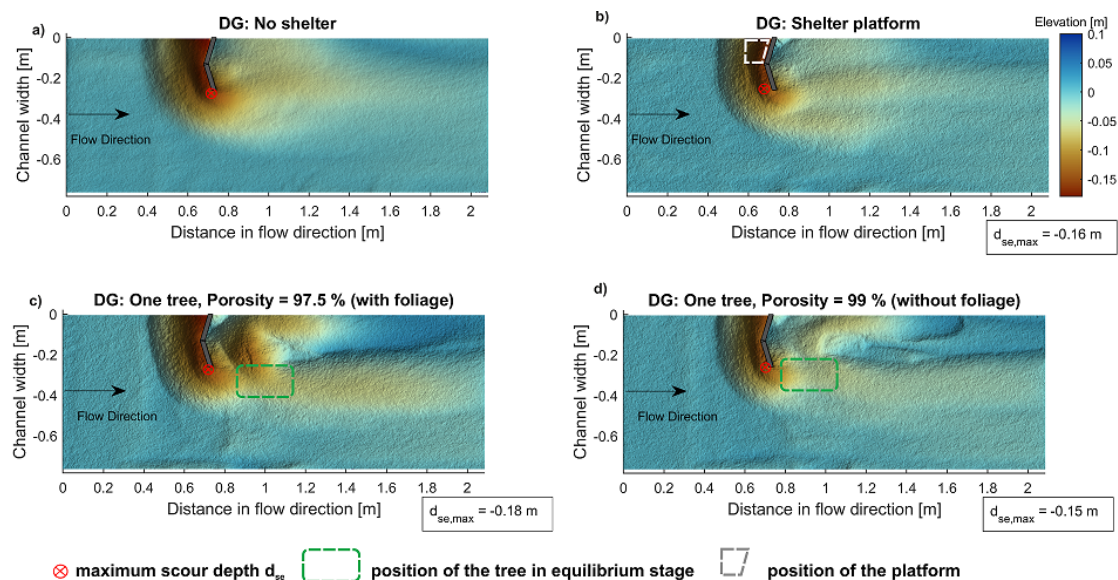
Figure 6.44: Bed morphology patterns around a stone-like structure (DG) with different variations of shelters in comparison with the case without a shelter.

If a tree is inserted in the scour hole of the DWD, the deepest point of the scour hole shifts from the upstream to the downstream wing and therefore also the scour hole shifts as shown in figure 6.45. The two deep sections departing from the DWD are intensified and additional scour holes form at the flume walls. The case "DWD tree-like shelter without foliage" showed an additional scour hole at the end of the measurement section, which also could have influenced the upstream development of the bed morphology. This case has to be interpreted with particular caution. In total, the DWD showed the highest sensitivity regarding bed morphology, when inserting a tree-like shelter, as not only the downstream bed morphology changed but also the upstream scour hole showed major changes. Due to the high sensitivity the combination of a DWD and a tree-like shelter is not recommended for practical implementation.
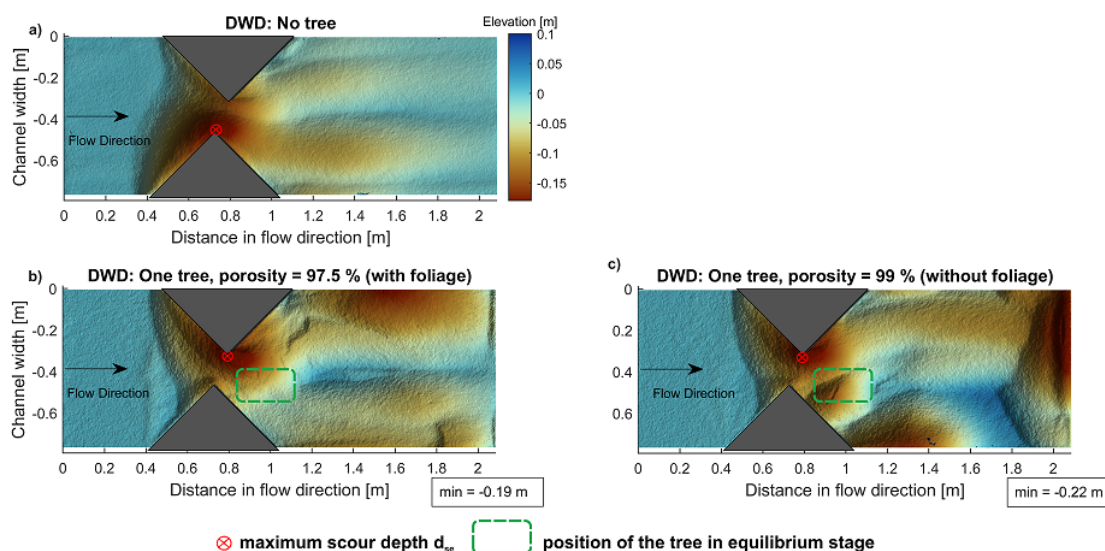
Figure 6.45: Bed morphology patterns around a stone-like structure (DWD) with different variations of tree-like shelters in comparison with the case without a shelter.

A literature review revealed that the combination of movable bed experiments with tree-like structures has not been investigated in a similar manner to the present experiments. A comparable study by Schnauder, Anlanger, and Koll (2022) implemented trees with stems and root wads in a river within the Wilde Mulde project. They found local scouring around the root wad and traced this back to a jet-like flow underneath the root wad through the scour hole. The same phenomenon could be observed in our experiments, where a distinct local scour around the tree-like shelter evolved as shown in figure 6.42.

Influence of foliage

As explained above, different foliage stages pose a different resistance to the flow and therefore also influence the bed morphology. The changes in bed morphology in comparison with the case without shelter are investigated in this chapter. The upstream scour hole does not change significantly with changing foliage stage for the pier-like structure TP as shown in figure 6.46. Major differences can be detected downstream of the structure, as the tree with foliage leads to larger changes in the dune extensions (height, width and length, as shown in table 6.16a) and a deeper and larger local scour around and beneath the tree. The longitudinal deep section is deepened and elongated.
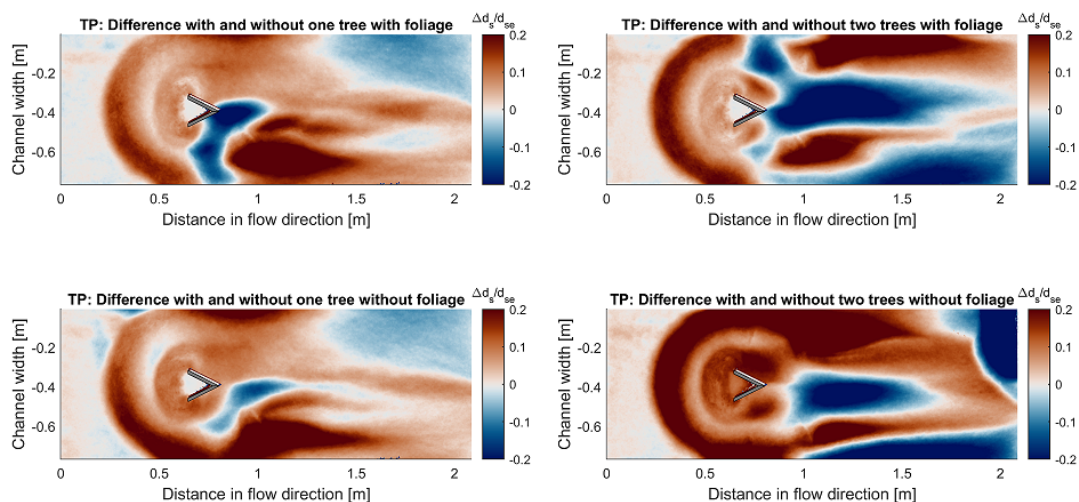
Figure 6.46: Difference of bed level elevation around a pier-like structure (TP) between different foliage stages of tree-like shelters and the case without a shelter.

The changes of bed morphology due to different foliage stages around the DG are shown in figure 6.47. The erosion downstream of the groyne is more pronounced for a tree with foliage than without foliage. For the case with foliage, the deep section departing from the head of the groyne is deeper and longer and the dune is higher as shown in figure 6.44. The local scour around the tree with foliage is more pronounced.
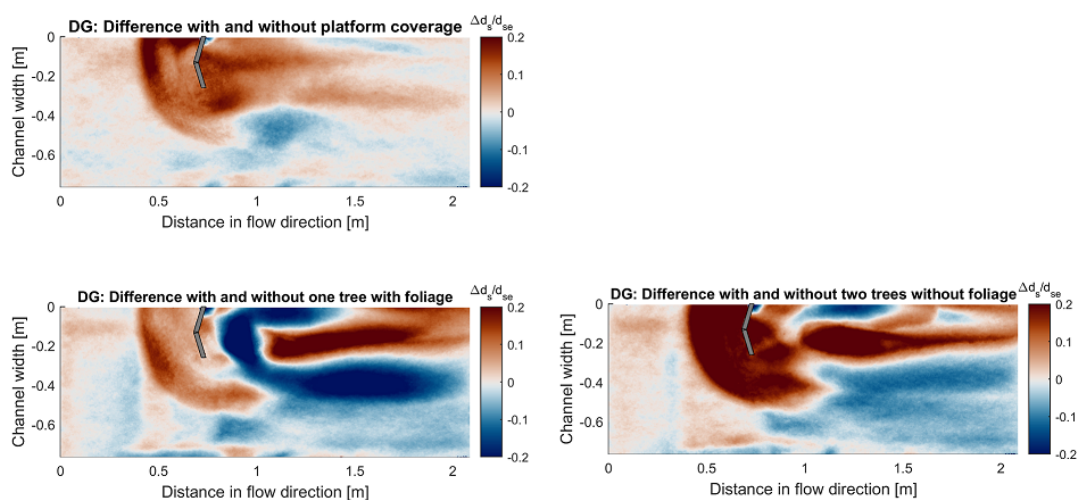
Figure 6.47: Difference of bed level elevation around a stone-like structure (DG) between different foliage stages of tree-like shelters, a platform-like shelter and the case without a shelter.

The changes of the bed morphology around the DWD due to the tree-like shelter are in general so large that the changes due to foliage stages are of subordinate role as shown in figure 6.48.
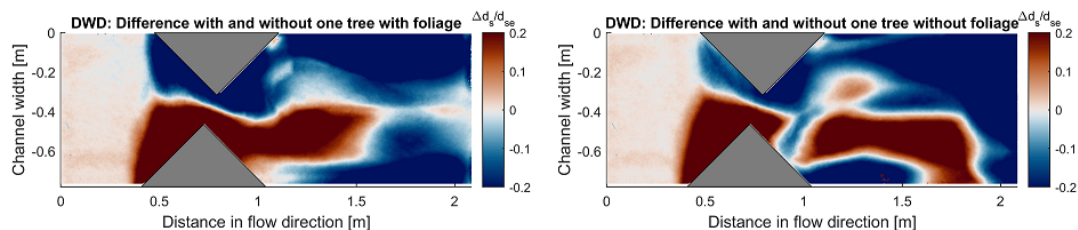
Figure 6.48: Difference of bed level elevation around a stone-like structure (DWD) between different foliage stages of tree-like shelters and the case without a shelter.

Table 6.16: Geometrical parameters of the scour holes for different cases of tree- and platform-like shelters

(a) Pier-like structure TP

Version	TP				
	No tree	One tree	Two trees	One tree	Two trees
Foliage stage	none	With	With	Without	Without
d_{se} [cm]	19.9	19.8	19.8	19.8	17.9
l_{ds} [cm]	44.3	39.8	39.3	40.17	37.5
l_{dune} [cm]	59	71.1	109.7	70.8	103.8
h_d [cm]	2.3	3.6	0.7	2.6	2.8

(b) Stone-like structure DG

Version	DG			
	No shelter	platform	One tree	One tree
Foliage stage	none	none	With	Without
d_{se} [cm]	18.3	14.4	15.3	13.4
l_{ds} [cm]	35.4	28.13	39.2	38.45
l_{dune} [cm]	75	-	-	-
h_d [cm]	1.3	-	-	-

(c) Stone-like structure DWD

Version	DWD		
	No tree	One tree	One tree
Foliage stage	none	With	Without
d_{se} [cm]	19.1	12.3	15.7
l_{ds} [cm]	36.6	22.03	16.5
l_{dune} [cm]	-	49.9	97.1
h_d [cm]	-	1.33	1.12

Influence of arrangement

The influence of the arrangement of tree-like shelter was solely tested for the TP. The general characteristics of the upstream scour hole are the same for both arrangements of trees and do not differ significantly from the case without a shelter as shown in figures 6.43 and 6.46. The arrangement with two trees leads to a shallower scour hole than the arrangement with

one tree. Major changes can be detected downstream of the TP. One tree leads to a shift of the dune from the center to the right side downstream of the tree whereas the arrangement with two trees splits the dune into two lateral dunes. The arrangement with one tree shows an elongated deep section on the opposite side of the pier. It has to be mentioned that the variant "two trees with foliage" has been influenced by the downstream end of the measurement section. A scour hole is visible at the end of the measurement section that would not be present in nature and can be interpreted as an error due to the experimental setup.

6.3.5   Influence of the shelter on backwater rise

The influence of the tree on the backwater rise was characterized by the measurement of water level upstream and downstream of the structure in the center line of the flume. Asymmetric setups, as the arrangement of the one-sided tree-like shelter, can show variations in backwater rise along the cross section and hence the highest water level upstream of the structure might not have been captured as shown in chapter 5.4.2. Therefore, the interpretation of the results needs to be drawn carefully in the cases of tree-like shelters.

All structures show a significant increase in backwater rise $\Delta h_1/h_0$ for the tree-like shelter cases in comparison with the case without tree as shown in table 6.17. The backwater rise is roughly doubled for the cases with one tree installed and tripled for the cases with two trees installed. Also the stone-like structures show a doubling and even tripling of the backwater rise for certain cases. Hence, the installation of a tree-like shelter is only recommended, when enough free board capacity is available in the surrounding area. Optimizations could be reached with decreasing the size of the tree-like shelter, which need to be investigated in further experiments. The influence of foliage on the backwater rise $\Delta h_1/h_0$ shows no clear trend for all structures. This is probably due to the changes in bed morphology that significantly can influence the spatial distribution of the water level as well. The arrangement with one tree leads roughly to a doubling of the backwater rise $\Delta h_1/h_0$ whereas the arrangement with two trees leads to a tripling of the backwater rise. The doubling and the tripling seems a feasible result as the resistance of the trees is the same.

The platform-like shelter in the DG case shows no significant influence on the backwater rise and can therefore be implemented without further planning.

Table 6.17: Normalized backwater rise $\Delta h_1/h_0$ due to a combination of a deep pool habitat structure and a shelter habitat structure for pier-like (TP) and stone-like (DG, DWD) structures.

Shelterversion	$\Delta h_1/h_0$ [%]
TP – no tree	10.5
TP – one tree, with foliage (porosity = 97.5 %)	19.5
TP – two trees, with foliage (porosity = 97.5 %)	30
TP – one tree, without foliage (porosity = 99 %)	24.2
TP – two trees, without foliage (porosity = 99 %)	29.4
DWD – no tree	13.4
DWD – one tree, with foliage (porosity = 97.5 %)	20.7
DWD – one tree, without foliage (porosity = 99 %)	27.1
DG – no tree	6.9
DG – one tree, with foliage (porosity = 97.5 %)	23.6
DG – one tree, without foliage (porosity = 99 %)	21.6
DG – platform	6.2

In conclusion, this experimental set examined tree-like and platform-like shelters in combination with a deep pool habitat. For the TP and DG, the upstream scour hole remained relatively unchanged, while the downstream bed morphology experienced significant alterations. Conversely, for the DWD, both upstream and downstream bed morphology exhibited notable changes. Looking only at bed morphology changes, it is recommended to implement tree-like shelters only for TP and DG. The DWD showed too high sensitivity to bed morphology changes for the tree-like shelter. The platform-like shelter at the DG resulted in negligible alterations of bed morphology and can be installed without further planning. The critical issue identified across all shelter cases is the significant backwater rise. The backwater rise doubled or even tripled for all tree-like shelter cases, making installations feasible only when sufficient freeboard is available. Optimization of the tree's dimensions is hypothesized to be a key factor in addressing backwater rise, suggesting that smaller tree dimensions could significantly reduce this issue. However, implementing tree-like shelters in practice requires careful planning, as improvisation during the implementation phase may lead to uncontrollable bed morphology changes and increased backwater rise. It is emphasized that river restoration projects involving the installation of root wads or trees necessitate thorough planning to avoid unforeseen consequences.

6.4 Discussion and conclusions on additional considerations for the implementation in practice

This chapter presented investigations on additional considerations for the implementation in practice. The influence of natural materials (edge design, surface roughness and porosity), debris accumulations and shelters on bed morphology and backwater rise has been characterized and quantified. A comprehensive summary of the findings is provided in table 6.18, and further practical recommendations are given in chapter 6.4.1. The influence of edge design on bed morphology is pronounced in the case of emergent structures, resulting in a noteworthy reduction of scour depth by more than 20 % compared to the idealized scenario. In contrast,

submerged structures exhibit no significant impact from the edge design. Notably, the back-water rise remains unaffected by the edge design, regardless of whether the structures are emergent or submerged. Surface roughness has a modest effect on bed morphology, yet it can lead to a considerable increase in backwater rise, reaching up to 110 % compared to the idealized case (with an absolute backwater rise of $\Delta h_1/h_0$ peaking at 22 %). Porosity emerges as the factor with the most substantial impact on bed morphology. It has the poten-tial to reduce scour depth by up to 87 %, scour hole length by 100 %, and the distance of the dune by 90 %. Although a trend of lower backwater rise with decreasing solid volume fraction (SVF) is discernible, the overall change compared to the idealized case remains negligible, with the absolute backwater rise reaching a maximum of 11.3 %. The submergence of the debris emerged as the most influential factor affecting bed morphology in the conducted de-bris accumulation experiments, contributing to an approximate 20 % increase in scour depth. While the upstream and downstream lengths of the debris exhibited an impact, their influence was primarily observed in the slopes within the scour hole upstream of the pier, resulting in a reduction of the plateau inside the scour hole. Furthermore, the presence of debris led to a substantially higher backwater rise, surpassing the comparable case without debris by about 110 %. The absolute backwater rise reached a maximum of 23.6 %, underscoring the significant impact of submergence. The impact of tree-like shelters on the bed morphology of TP, DG, and DWD structures is particularly significant, especially in downstream regions of the structure. The upstream scour hole experienced minimal alterations in the presence of the tree-like shelter, and, notably, could be largely preserved for both TP and DG structures. However, substantial changes manifested at the location of the tree, introducing a local scour hole, and downstream of the structure, where the central dune was replaced by a dune on one side or a division into two parallel dunes. In the case of the DWD, changes were not confined to downstream areas but extended upstream of the structure as well, rendering them less favorable for practical implementation. The tree-like shelter induced a doubling, and in some instances, even a tripling of the backwater rise. This increase in backwater rise becomes a limiting factor when considering the implementation of a shelter alongside a deep pool habitat structure in this context. Therefore, careful consideration is advised when combining these elements in a practical setting. In conclusion, when considering bed morphology, porosity and tree-like shelters emerge as first-order influences. Edge design and debris accumulation fol-low as second-order influences, while surface roughness exhibits negligible influence. When examining backwater rise, tree-like shelters, debris accumulations, and surface roughness are identified as first-order influences. On the other hand, edge design and porosity result in negligible additional backwater rise, aligning closely with the backwater rise observed in the idealized case.

Table 6.18: Summary on additional considerations for implementation in practice and their influence on the bed morphology and the backwater rise

	Changes in comparison with the idealized case		Changes in comparison with uniform flow conditions
	Bed morphology changes $\Delta d_s/d_{se}$	Backwater rise change $\Delta\left(\Delta h_1/h_0\right)$	Absolute backwater rise $\Delta h_1/h_0[\%]$
Idealized (TP, DG)			TP: + 10.5 % DG: + 6.9 % DWD: 13.4 %
Edge Design (TP, DG)	emergent structures (TP): >-20% submerged structures (DG): negligible	negligible	TP: + 10.0 % DG: + 6.2 %
Surface Roughness (DWD)	negligible	+ 110 %	+ 6.1 - 22 %
Porosity (TP)	- 87 %	negligible	SVF = 0.3-1.0: + 10.0 - 11.3 %
Debris Accumulations (TP)	+ 20 %	max. + 119 %	+ 10.8 - 23.6 %
Shelter (TP, DG, DWD)	upstream scour hole: negligible for TP and DG, high for DWD downstream: very high for all structures	max. + 186 %	TP: + 19.5 - 30% DG: + 21.6 - 23.6% DWD: + 20.7 - 27.1%

6.4.1 Practical implications for engineers

The practical implications for engineers regarding the use of natural materials, the considerations needed for quantifying the impact of debris accumulations and tree-like shelters are summarized as follows. These conclusions were made upon hydraulic boundary conditions which equal an HQ2 and can differ for other hydraulic boundary conditions:

1. The edge design is relevant for emergent structures, where sharp edges are preferable since they increase scour depth by up to 20 %. Achieving this involves adding sharp-edged attachment parts. Submerged structures are minimally affected by edge design and require no additional attention. There was no significant effect on the backwater rise detected due to the edge design.

2. Surface roughness has an insignificant effect on bed morphology and can be neglected in morphological planning. However, determining the structure's height is crucial for hydraulic boundary considerations (see figure 6.49). The mean water depth h_m above the surface roughness needs to be determined since an additional surface roughness can cause a constriction of the effective cross-sectional area and lead to significant additional backwater rise of up to 50 % in comparison with a smooth surface. The calculation of the mean water depth h_m can be done according to DWA M-509 for fish passes.
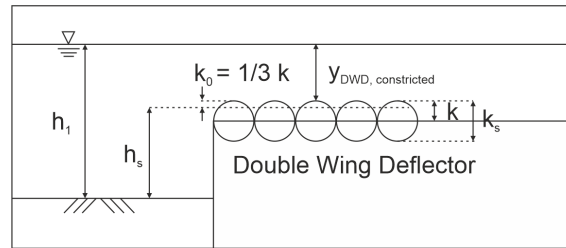
Figure 6.49: Determination of the height of the structure h_s for submerged structures.

3. When implementing dissolved structures it is of highest importance that the dissolved structure is not permeable or porous. Small passages (in the range of centimeters!) through a structure lead to significant loss of scour depth. This means a high implementation accuracy needs to be ensured by appropriate qualification of the technicians and a supervision team with expertise in hydromorphology.

4. Debris accumulations increase the backwater rise of emergent in-stream structures, hence it is recommended to keep the structure free from debris. Regarding bed morphology, the debris is able to even increase the scour depth and therefore can be neglected in morphological planning.

5. A combination of a deep pool habitat and a tree-like shelter is possible for the TP and the DG where the upstream scour hole of the structure can be conserved. The DWD could not preserve the upstream scour hole why an implementation is not recommended. The crucial factor is the backwater rise that peaks at $\Delta h_1 / h_0 = 30\,\%$. Consequently, an implementation is only recommended when the project site has enough free board capacities. Further optimization would be possible by reducing the dimensions of the shelter.

Chapter 7

Hydromorphological evaluation, recommendations for practice and outlook

This chapter initiates by giving an overview of the findings presented in the preceding two chapters. Subsequently, a hydromorphological evaluation is conducted on bed morphology and the mean flow velocity field. This evaluation is performed with respect to the suitability as potential deep pool habitats, aligning with the specified target values outlined in the Landesstudie Gewässerökologie (LSGÖ) (Becker & Ortlepp, 2022). The exploration extends to other methodologies for evaluating scours in the context of deep pool habitats. The chapter concludes with recommendations and an outlook, addressing critical considerations and outlining necessary steps for the potential establishment of a pilot site. Finally, the potential of application of the developed approach on other habitat types and research possibilities for a modular concept are outlined.

7.1 Overview of the scour hole geometry of all investigated variants

For a quantitative comparison of the geometry of the scour holes, figures 7.1, 7.2, and 7.3 depict the maximum scour depth d_{se}, the area in target depth A_{target}, and the target volume V_{target} across pier-, stone-, and dam-like structures. The definition of the different geometric values is given in figures 5.12 and 5.13. All values within this chapter are given in natural scale, to enable a direct comparison to the target values given in LSGÖ. Notably, the target depth of 2 m is achieved for all structures. However, a distinct observation emerges, indicating that the dam-like structure exhibits a significantly smaller maximum scour depth compared to the other structures. Figure 7.1 illustrates that both the TP and the RP achieved a scour depth of approximately 5 m. Upon examining figure 5.11, it becomes apparent that both structures reached the flume bed, situated at 5 m. A hypothesis can be formulated that the RP and TP might have the capacity to create even deeper scour holes than what was observed in the experiments. Moreover, a low sensitivity of the scour depth across the rehearsal experiments

can be observed, which validates the experimental setup.
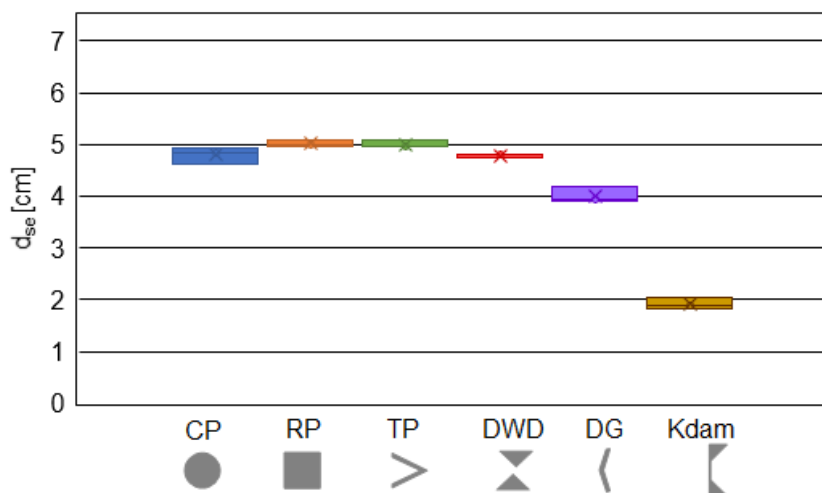
Figure 7.1: Comparison of maximum scour depth of pier-, stone- and dam-like structures.

As previously mentioned, the scour depth of the TP was constrained by the experimental setup, and this limitation is particularly evident in the area and volume at the target depth. Notably, the TP yields a significantly larger scour area and volume in comparison with the other pier-like structures. This difference arises from the distinct evolution of the downflow and vortex system at the TP, as illustrated in figure 5.27. The significantly larger scour area and volume in target depth as well give a hint, that the maximum scour depth in this experiment was not reached due to the flume bed. The Kdam exhibits a comparable area at the target depth to that of the DG; however, the target volume is significantly smaller. This suggests that the Kdam generates a larger scour hole in terms of area but with a shallower depth, whereas the DG creates a smaller scour hole in terms of area but with a greater depth. In total, the scour area as well as the scour volume show higher standard deviations as the scour depth.
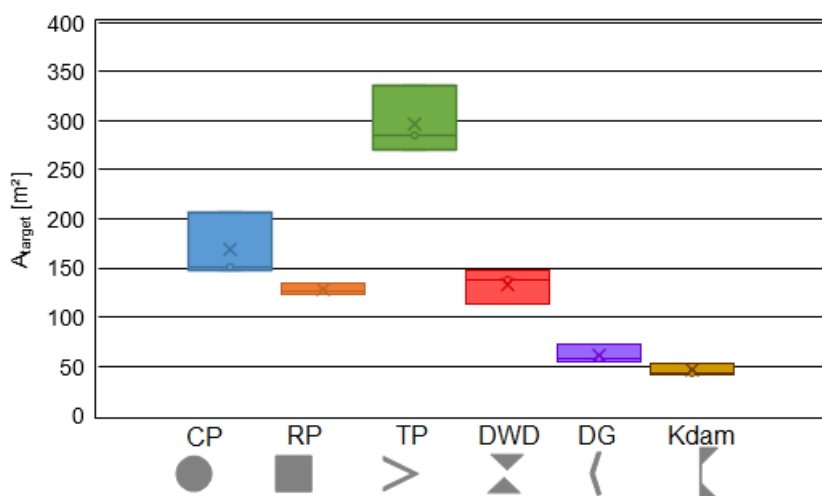
Figure 7.2: Comparison of the area in target depth of pier-, stone- and dam-like structures.
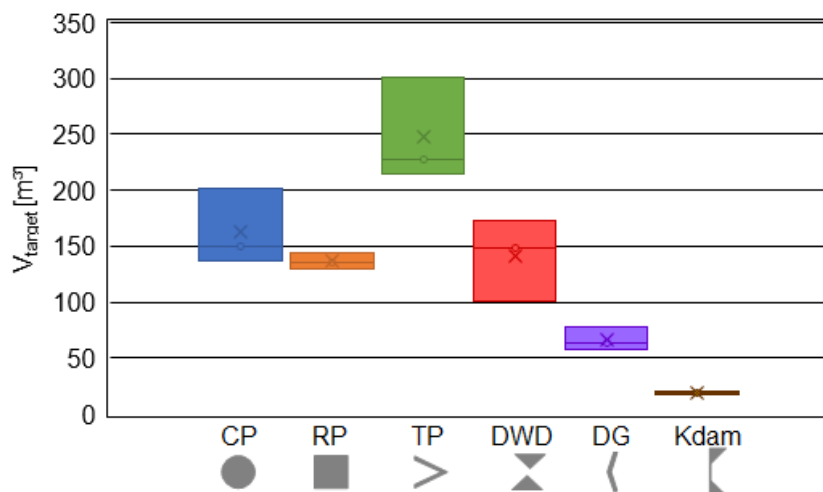
Figure 7.3: Comparison of the volume below target depth of pier-, stone- and dam-like structures.

Comparing the idealized structures with the variations explored in the additional considerations outlined in chapter 6 provides a comprehensive understanding of their impact on bed morphology. Figures 7.4, 7.5, and 7.6 visually depict the variations in scour depth, area and volume for the TP. The maximum scour depth remains consistent across the additional considerations, except for cases involving porosity, where the scour depth is notably reduced, sometimes reaching depths lower than 1 m. Similarly, the area and volume in the target depth are significantly affected, diminishing to zero depending on the SVF. The scour depth exhibits the lowest standard deviation among the variables considered. Variations in mean value and standard deviation are more pronounced for the area and volume in the target depth. Notably, the debris considerations result in the highest area and volume in target depth, surpassing even the idealized version. Conversely, the introduction of rounded edges leads to a substantial reduction, approximately 50 %, in both area and volume in target depth. While the presence of shelter also causes a reduction in area and volume in target depth, this effect is less pronounced compared to the impact of the edge design.
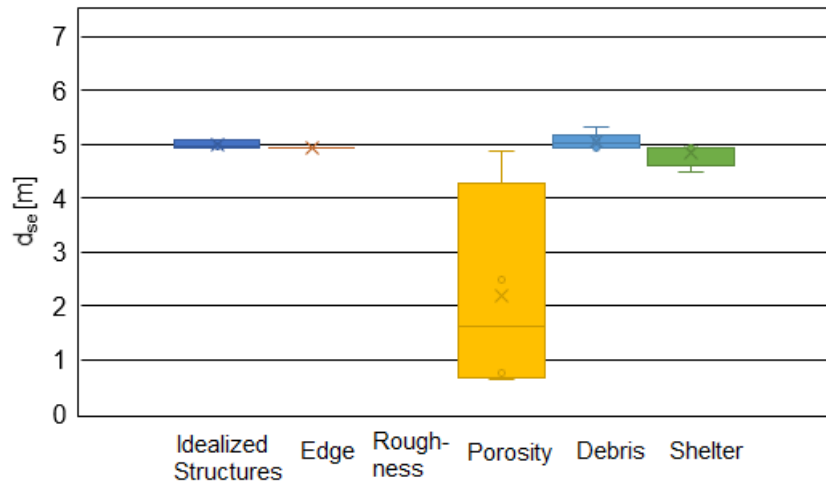
Figure 7.4: Comparison of maximum scour depth for additional considerations for the Triangular Pier.
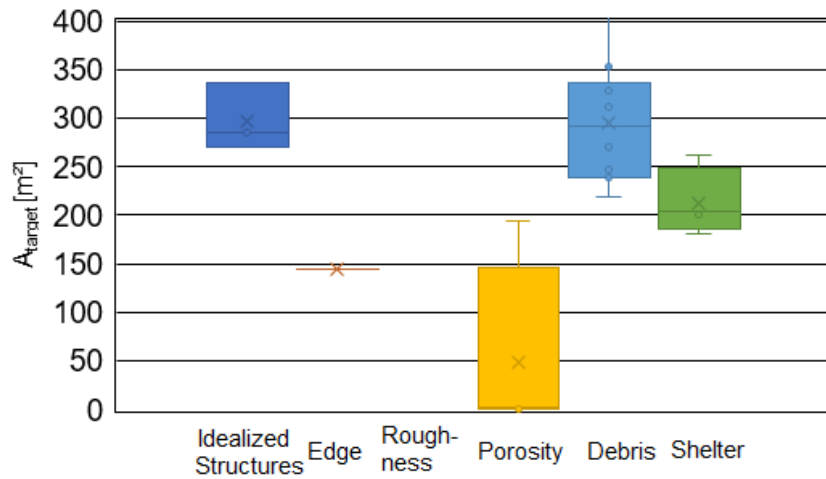
Figure 7.5: Comparison of the area in target depth for additional considerations for the Triangular Pier.
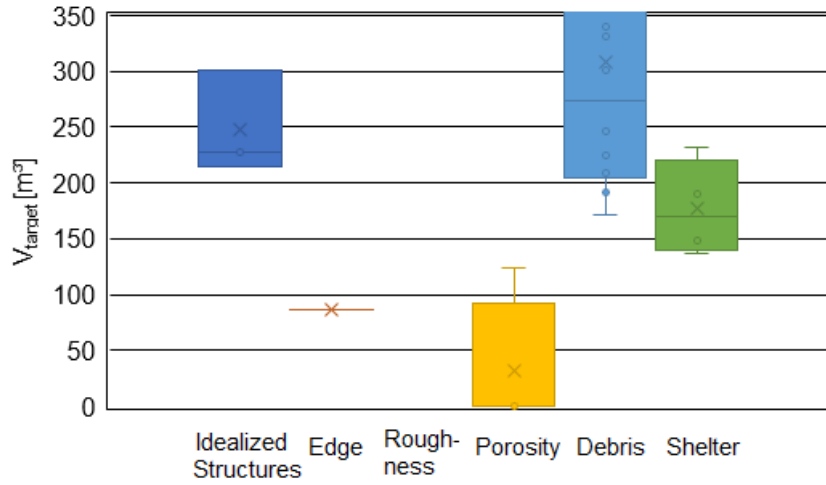
Figure 7.6: Comparison of the volume below target depth for additional considerations for the Triangular Pier.

In contrast to the TP, the additional considerations applied to the DG reveal less pronounced differences as shown in figures 7.7, 7.8 and 7.9. The average values for scour depth and area and volume in target depth do not exhibit significant variations between the edge design and the inclusion of an additional shelter. The only discernible difference lies in the slightly elevated standard deviation observed in the variants involving shelters.
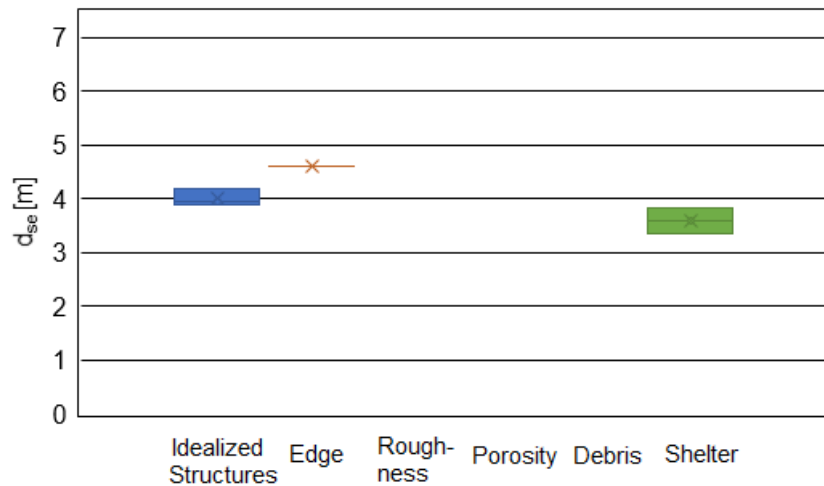
Figure 7.7: Comparison of maximum scour depth for additional considerations for the Deflected Groyne.
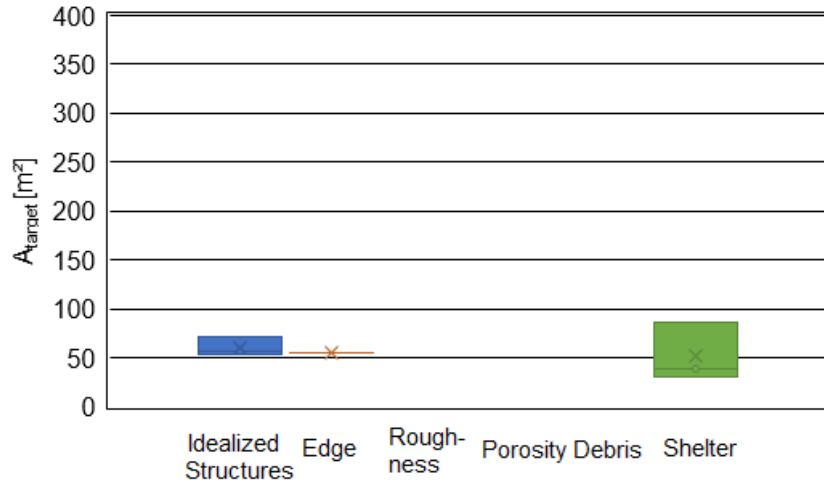
Figure 7.8: Comparison of the area in target depth for additional considerations for the Deflected Groyne.
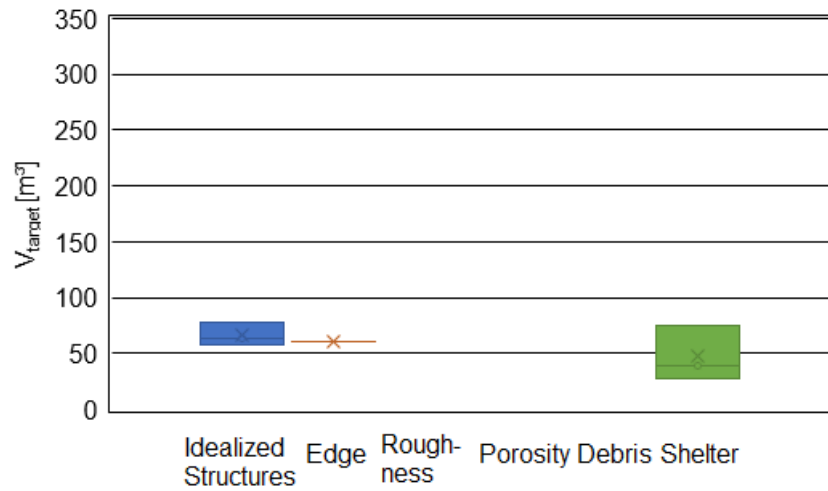
Figure 7.9: Comparison of the volume below target depth for additional considerations for the Deflected Groyne.

The DWD exhibits minimal variations in scour depth across different variants. However, the area and volume in the target depth are notably higher in the variant with an added shelter. The impact of surface roughness appears to be relatively modest.
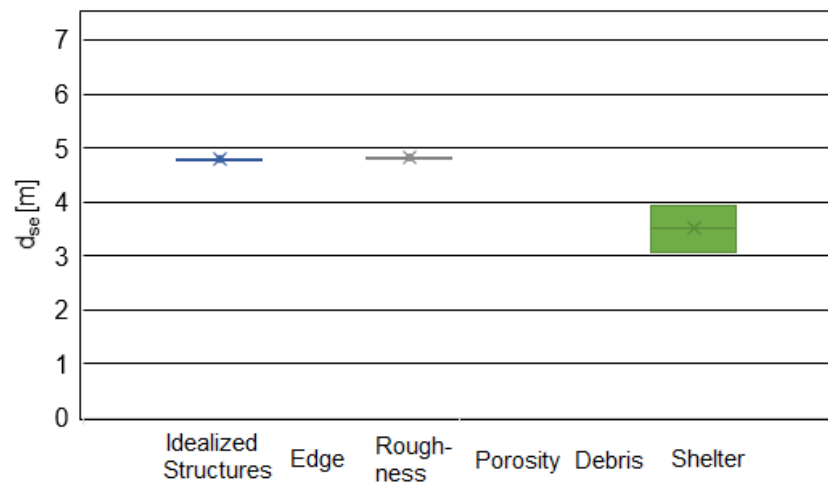
Figure 7.10: Comparison of maximum scour depth for additional considerations for the Double Wing Deflector.
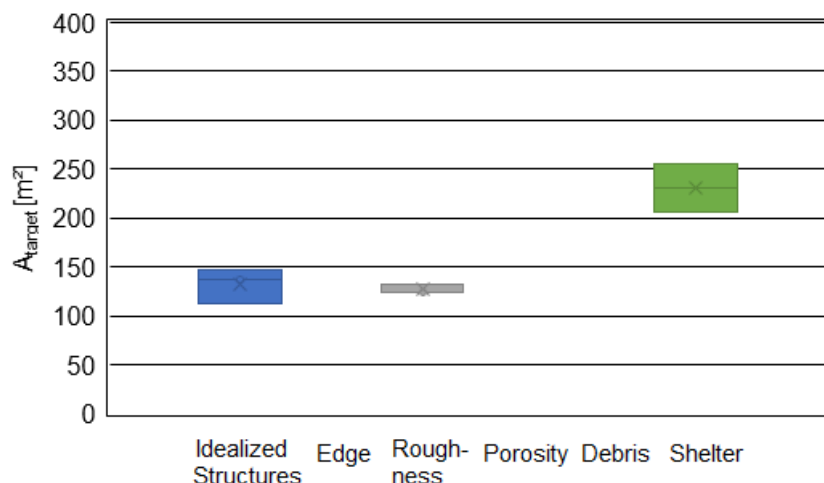
Figure 7.11: Comparison of the area in target depth for additional considerations for the Double Wing Deflector.
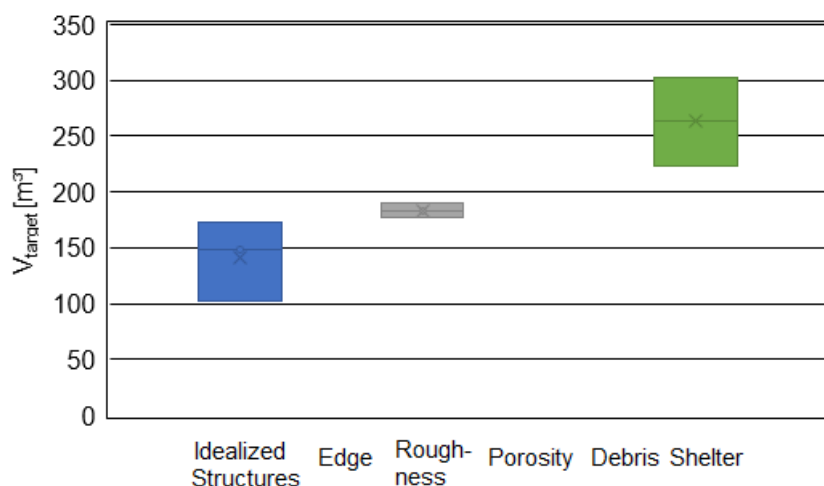
Figure 7.12: Comparison of the volume below target depth for additional considerations for the Double Wing Deflector.

In summary, porosity emerged as the factor with the most significant impact on bed morphology. While it was specifically tested on the pier-like structure, similar effects can be anticipated for stone- and dam-like structures. Notably, the edge design exerted a more pronounced influence on the area and volume in target depth for emergent structures, while its impact on submerged structures remained relatively minimal. Surface roughness, although examined only for a stone-like structure, demonstrated a relatively minor effect on bed morphology. The inclusion of a shelter resulted in increased standard deviations in scour depth, as well as increased area and volume in the target depth.

7.2   Overview of the backwater rise of all investigated variants

The comparison of backwater rise $\Delta h_1/h_0$ among pier-, stone-, and dam-like structures is illustrated in figure 7.13. Pier- and stone-like structures exhibit a similar behavior, displaying mean backwater rises ranging from 7 % to 15 %. In contrast, dam-like structures result in a doubling of the backwater rise (> 30 %). Notably, standard deviations are higher for pier- and stone-like structures, while dam-like structures show considerably smaller standard deviations.
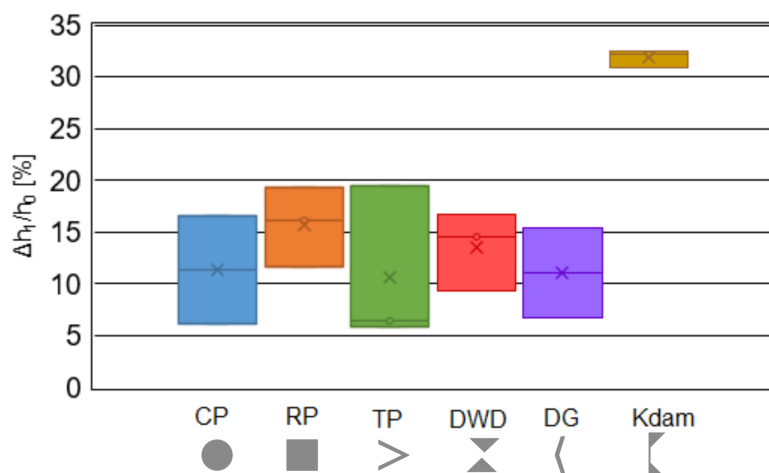
Figure 7.13: Comparison of the backwater rise of pier-, stone- and dam-like structures.

The additional considerations for the TP reveal that natural materials and debris exhibit mean values and standard deviations in a similar range as observed in the idealized case as shown in figure 7.14. However, the inclusion of a shelter results in an elevated backwater rise. Similarly, for the DG, the impact of the edge design is relatively minimal (see figure 7.15). Nevertheless, the introduction of a shelter yields higher mean backwater rise and increased standard deviations. At the DWD, backwater rise is influenced by both surface roughness and shelter, contributing to an overall increase in mean backwater rise as shown in figure 7.16.
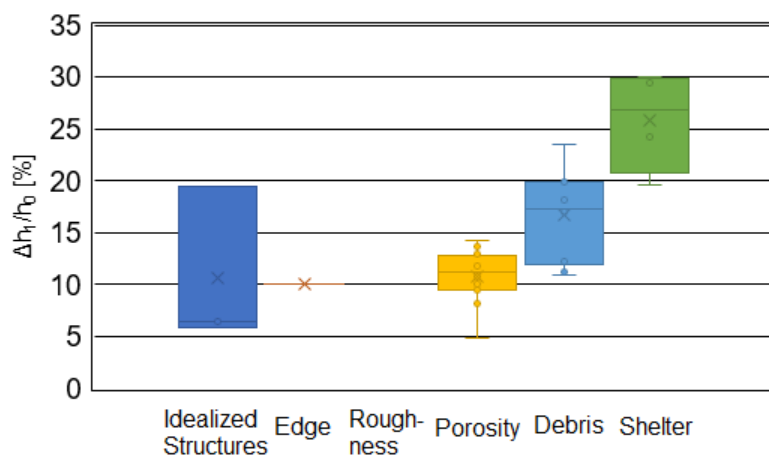
Figure 7.14: Comparison of the backwater rise for additional considerations for the Triangular Pier.
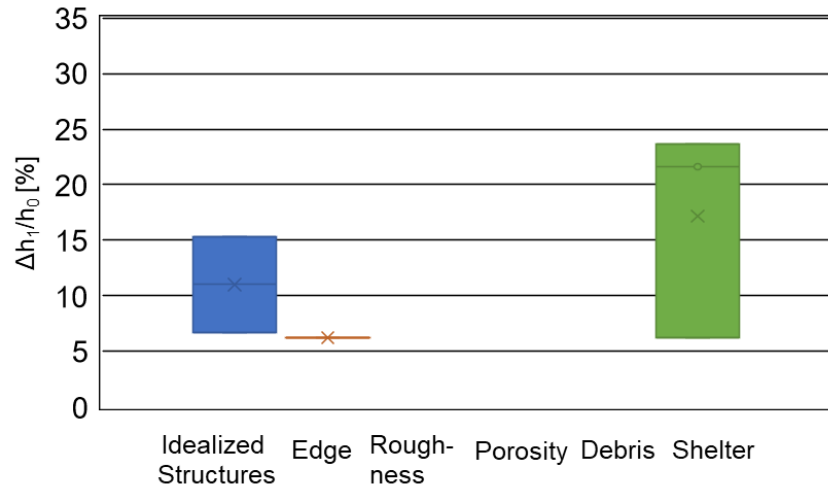
Figure 7.15: Comparison of the backwater rise for additional considerations for the Deflected Groyne.
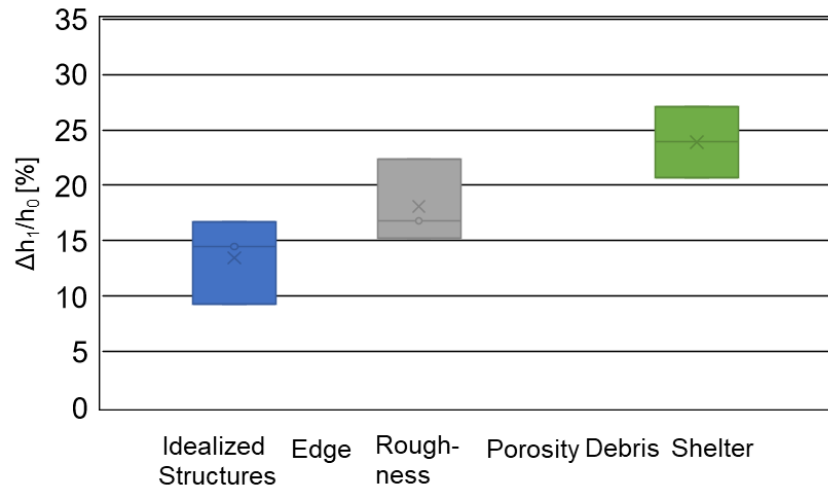
Figure 7.16: Comparison of the backwater rise for additional considerations for the Double Wing Deflector.

7.3   Hydromorphological evaluation of the structures

In chapter 2, hydromorphological parameters were derived to assess the scour holes in terms of their suitability as deep pool habitats. These parameters are consolidated and presented in table 7.1.

Table 7.1: Parameters for the hydromorphological evaluation of deep pool habitats.

parameter	derived from
scour depth [m]	Landesstudie Gewässerökologie
area in target depth [m²]	Landesstudie Gewässerökologie
volume below target depth [m³]	this work
mean flow velocity with velocity vector field [m/s]	this work (cooperation with Fisheries)
velocity fluctuations [m/s]	this work (cooperation with Fisheries)
strength of the whirl	derived in this chapter

In chapter 7.3.1, the hydromorphological evaluation of bed morphology is presented, utilizing parameters recommended by the LSGÖ. Chapter 7.3.2 explores methods for evaluating hydrodynamics, including the testing of a traffic light rating system and quantifying vortex strength by evaluating mean flow velocities along streamlines within the vortices. Additionally, an integral approach is examined by adapting the specific power density definition, commonly used in fish passes, to assess deep pool habitats.

The hydromorphological evaluation focuses on target values identified for the common barbel, as derived in chapter 2.3.1. It is important to note that while the analysis in this chapter serves as an example for the barbel, the enhancement of the deep pool habitat does not exclusively benefit this species. The overall betadiversity of the river section is improved through increased variability in water depth, flow velocities, turbulence, and potentially substrate composition. It is emphasized that this chapter does not intend to provide a biological analysis but rather establishes the hydromorphological data foundation and suggests the types of additional data required for a comprehensive biological assessment.

7.3.1   Hydromorphological evaluation of the bed morphology

To assess the bed morphology of the deep pool, initially the straightforward criteria of target depth and target area are considered, as recommended by the LSGÖ. The LSGÖ advocates for a flow depth exceeding 2 m and a minimum area of 15 m² for a large pool. In figure 7.17, the maximum scour depth and the area in target depth are depicted for six different structures, with the target values marked by red lines. Notably, all structures meet both the target depth and target area criteria. It is worth highlighting that the TP stands out due to its significantly larger area in target depth, indicating its superior performance in this aspect.
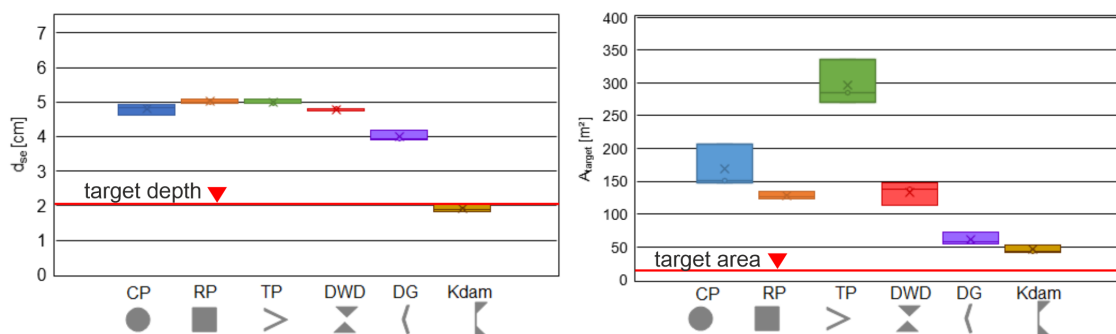
Figure 7.17: Target depth and target area for different pier-, stone- and dam-like structures.

For the combination of hydrodynamics and morphodynamics at a later point, it is necessary to know the distribution of the suitable area around the structure, which is displayed in figure 7.18. For pier-like structures, the area of suitable depth is located in the frontal and lateral zones surrounding the structure. In the case of CP and TP, this area extends downstream into two pronounced deep lateral sections, with the TP exhibiting the longest extension of these deep sections. Around stone-like structures, the suitable areas extend from the head of the structure in up- and downstream direction. In the case of DWD, an elongated suitable zone is observed on the right side. The suitable areas for the Kdam are situated on both riverbanks.
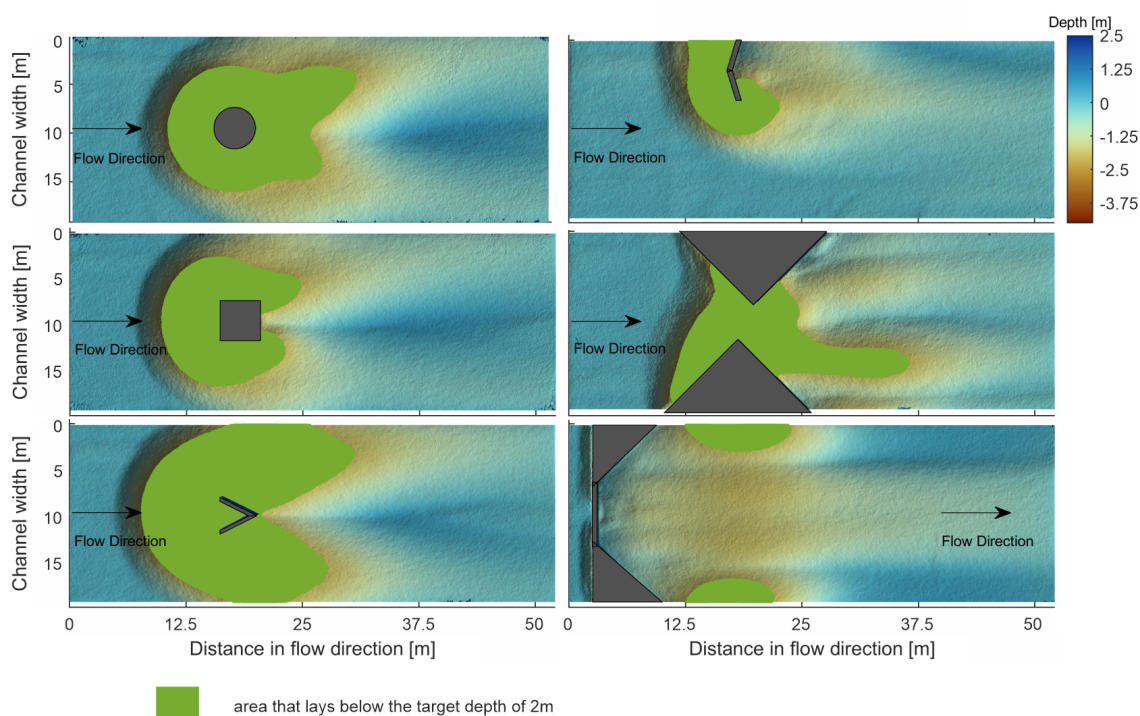
Figure 7.18: Distribution of area in target depth for different pier-, stone- and dam-like structures.

For further insights into the characteristics of scour holes associated with different structures, an analysis was conducted on the distribution of area and volume concerning the scour depth as depicted in figure 7.19. As the depth increases, the relative area of the scour hole A/A_0 experiences an asymptotic decrease as shown in figure 7.19 a). Stone-like structures exhibit the

most pronounced reduction, with an approximate reduction in relative area of 0.8 at a relative scour depth of 0.3. In contrast, dam-like structures show a more moderate reduction of 0.40. This suggests that stone-like structures tend to create smaller yet deeper scour holes, while dam-like structures generate larger and more shallow scour holes. The distribution of area of pier-like structures falls between these extremes, as depicted in figure 7.19 a). Examining the distribution of area concerning the target depth, illustrated in figure 7.19 b), it becomes evident that pier-like structures exhibit the highest relative area at the target depth, comprising approximately 20 % to 40 % of the area at zero depth. The relative cumulative volume of the scour holes V_{cum}/V_{tot} demonstrates a noteworthy consistency across all structures, as indicated by a red trendline.
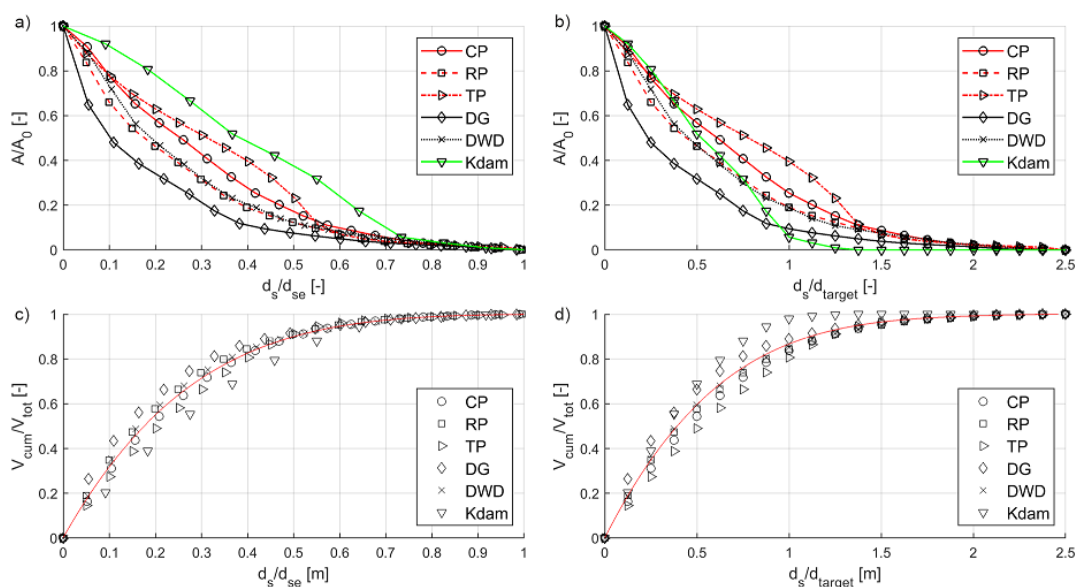
Figure 7.19: a) Relative area A/A_0 over relative scour depth d_s/d_{se}, b) relative area A/A_0 over relative scour depth d_s/d_{target}, c) relative volume V_{cum}/V_{tot} over relative scour depth d_s/d_{se}, d) relative volume V_{cum}/V_{tot} over relative scour depth d_s/d_{target}. In c) and d) a trendline is indicated in red.

The analysis of target depth, target area, and the distribution of target area was conducted for all experiments undertaken within the scope of this dissertation. Key findings are highlighted below, with detailed data available in appendix B.3. The impact of edge design was pronounced primarily on emergent structures, resulting in a significant reduction of the area in target depth. Interestingly, submerged structures exhibited no significant sensitivity to rounded edges as opposed to sharp ones. Surface roughness demonstrated an influence of similar magnitude to emergent structures with round edges. Among the natural materials, porosity exerted the most substantial impact, resulting in the suitable depth no longer being attainable and completely disappearing. The presence of shelter did not significantly affect the area at the target depth, although the distribution of area was altered in some variants due to the local scour hole around the tree-like shelter. In contrast, the platform-like shelter showed no significant differences.

7.3.2 Hydromorphological evaluation of the hydrodynamics

Besides the bed morphology also the hydrodynamics is relevant for the suitability as deep pool habitat. The LSGÖ suggests a mean flow velocity of < 0.3 m/s. The analysis of the flow velocity field in chapter 5.3 revealed a high heterogeneity of flow velocities inside the deep pool. Therefore, possibilities need to be found for evaluating the hydrodynamics. First, a traffic light rating system is applied to the mean flow velocity field and further the vortex structures inside of the deep pool are characterized. Lastly, an integral approach is applied and the concept of specific power density from fish passage analysis for the characterization of turbulence is adapted.

Hydromorphological evaluation on the basis of a traffic light rating system

In evaluating flow velocities, a traffic light rating system is employed on the mean flow velocities shown in chapter 5.3.3, using dark green to denote suitable areas according to LSGÖ criteria and light green for areas reported in other literature with slightly higher mean flow velocities deemed suitable. All other mean flow velocities are color-coded from yellow to red. These velocities, scaled to a full scale (from 1:25 in the physical model experiment), reflect conditions at HQ2 in the exemplary rivers as derived in chapter 4.1.2. Figure 7.20 illustrates a cross section at the deepest point, with mean flow velocities classified according to the traffic light rating system, while figure 7.21 depicts a cross-section in target depth. Pier-like structures exhibit suitable areas, particularly at the berm inside the scour hole and directly downstream of the pier as shown in figure 7.20. However, the DWD shows no suitable areas due to excessively high mean flow velocities. The DG displays a suitable area upstream of the groyne within the scour hole and a small section in the dead water zone downstream of the groyne. Notably, the long deep section departing from the groyne's head reveals velocities that are too high. The Kdam shows suitable mean flow velocities inside the scour holes along both riverbanks. It's important to emphasize that the LSGÖ sets 0.3 m/s as a target mean flow velocity for hydraulic conditions at $Q_{30} - Q_{330}$. The conditions discussed in this chapter represent an HQ2, indicating higher flow velocities. Despite the flood conditions at HQ2, the scour hole may still offer zones as a flood refuge for fish.

The analysis of the cross-sections of the mean flow velocity show a high heterogeneity of the flow velocities inside of the scour hole. Based on the hydromorphological parameter some zones inside the scour can be evaluated suitable for a deep pool, and other zones show too high flow velocities. Consequently, showing only one mean flow velocity for the entire scour hole cannot reflect the hydrodynamic conditions inside of a scour hole and leads to a false evaluation of the deep pool. A distribution of flow velocities needs to be measured to identify suitable and also non-suitable zones.

While a similar analysis could enhance results by considering flow velocity fluctuations, the absence of quantitative target values prevents the compilation of corresponding graphs in this context.
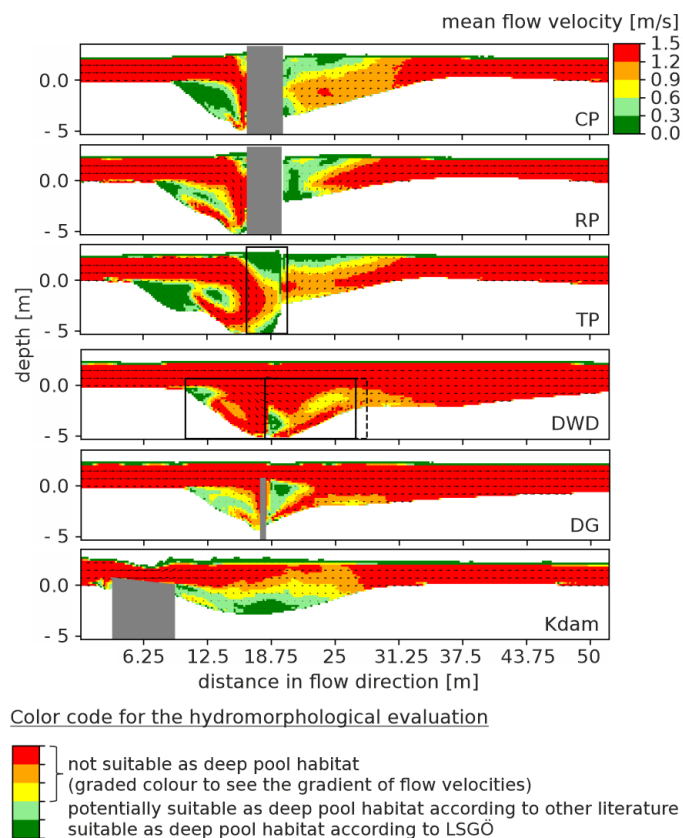
Figure 7.20: Hydromorphological evaluation according to a traffic light rating system based on mean flow velocities at HQ2. Displayed is the x-z-cross-section at the location of the deepest point.
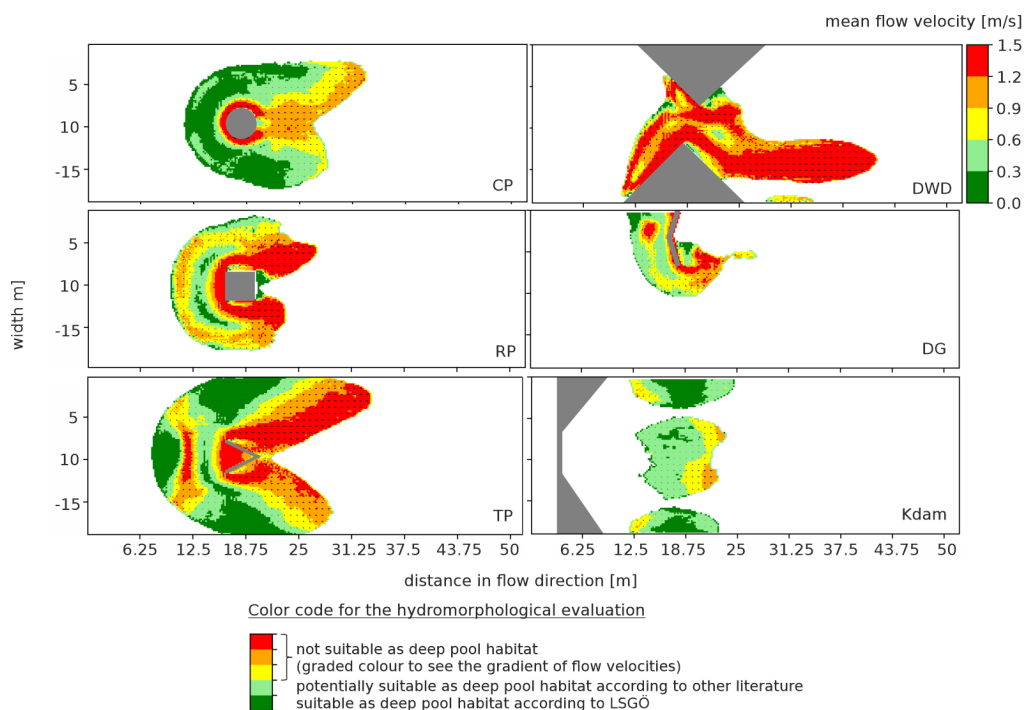
Figure 7.21: Hydromorphological evaluation according to a traffic light rating system based on mean flow velocities at HQ2. Displayed is the x-y-cross-section in target depth.

Hydromorphological evaluation of the structures based on the strength of vortices

To evaluate the strength of the vortices inside of the scour holes the mean flow velocity along the streamline was plotted and is shown in figure 7.22. For pier-like structures the velocities are displayed in the inner (b,d,f) and outer (a,c,e) part of the vortex. The inner part of the vortex shows slow flow velocities not exceeding the target value. The downflow in the outer part of the vortex (a,c,e) that is initiated directly upstream of the piers shows flow velocities that exceed the suitable mean flow velocities. The TP additionally shows an acceleration of the mean flow velocity above the berm, exceeding the target value. The DG shows a rotating vortex in the upstream scour hole where flow velocities stay below the maximum suitable flow velocity. The flow velocities in the long deep stretch exceed the suitable mean flow velocities as shown in figure 7.22 g). The small suitable area downstream of the DG that was identified in the previous subchapter shows a small vertical vortex provoked by a shear layer zone that is clearly visible at this point (see figure 7.22 f)). The velocities inside of this vortex in parts also exceed the mean flow velocities. The helices that are present up- and downstream of the DWD show mean flow velocities along the streamlines that exceed the suitable target value (see figure 7.22 i), j), k)) and therefore, the velocity field of the DWD can be classified as not suitable during flood conditions. The Kdam shows a horizontal vortex inside of the scour hole which shows suitable conditions directly above the bed as show in 7.22 l) and m).

The examination of vortices reveals that assessing cross-sections solely through the traffic light rating system is insufficient for a comprehensive hydrodynamic evaluation of the deep pool. To capture crucial details, particularly concerning vortex strength, streamlines augmented with mean flow velocity data prove more effective. These streamlines highlight zones where local accelerations within the vortex exceed tolerable flow velocities for an ideal deep pool habitat. Overall, the flow velocities in the inner regions of vortices within the scour holes of CP, RP, TP and DG exhibit favorable conditions. In contrast, the DWD displays excessively high flow velocities within its helical vortex system. For the Kdam, favorable conditions are observed close to the riverbed within both scour holes along the riverbanks.
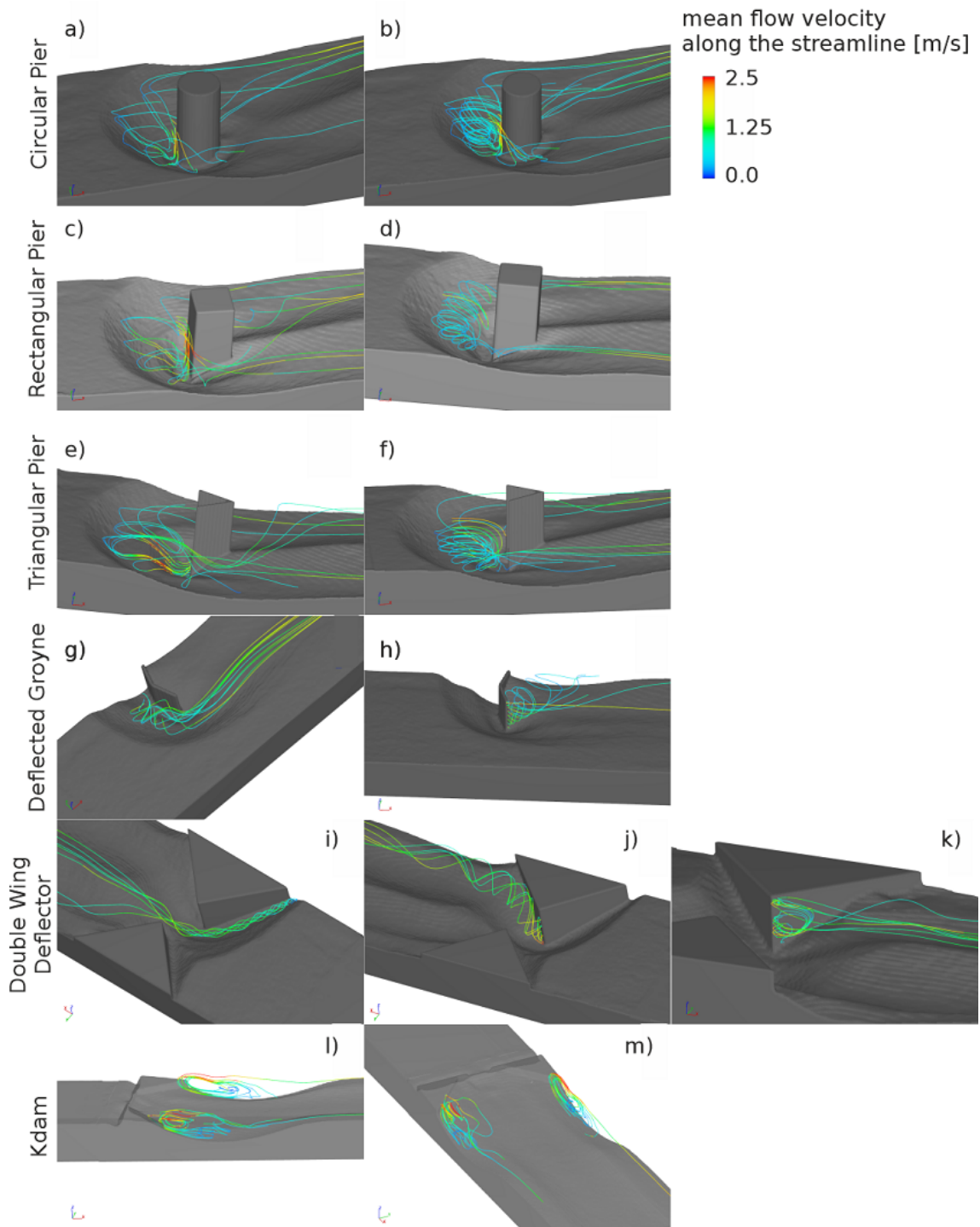
Figure 7.22: Hydromorphological evaluation based on the mean flow velocities along the streamlines illustrating the strength of the vortices inside of the deep pool.

Hydromorphological evaluation of the structures based on the definition of specific power density from fish passage hydraulics

In fish pass hydraulics the "mean turbulence level" is a crucial parameter when designing the dimensions of the pools to enable a safe fish passage (Weichert, 2006). The specific power density [W/m³] according to Larinier et al. (1999) has become established in fish passage hydraulics as a measure of turbulence and energy dissipation (Seifert, 2016). It is to be noted that the specific power density is a 1D consideration as it only considers integral quantities, but it has been proven to be suitable to relate flow and pool size to determine the hydraulic loading (Weichert, 2006). However, Weichert (2006) state that drawing conclusions about the turbulence that a fish actually experiences while swimming through the pools is not possible. The specific power density is defined as:

$$P_D = \rho_w \cdot g \cdot Q \cdot \frac{\Delta h}{V} \tag{7.1}$$

Typical specific power densities as used in Germany and Switzerland for the design of fish passes are shown in table 7.2. The design is based on different ecosystems, water level differences of the pools and the construction technique of the fish pass.

Table 7.2: Specific power densities for fish passes in W/m^3.

		Adam et al. (2014) (Germany)		Seifert (2016) (Bavaria)	Hefti (2012) (Switzerland)			
construction technique		pool-type	boulders	slot pass/ pool-type/ ramps	pool-type	slot pass	pool-type	still pool
hydraulic boundary conditions		$Q_{30} - Q_{330}$		MNQ, Q_{30}				
	$\Delta h[m]$							
Epirhitral	0.2	250	300	140			200	50
Metarhitral	0.18	225	275	120			150-200	50
Hyporhithral	0.15	200	250	120			120-150	50
Epipotamal	0.13-0.10	150	200	100			100-120	50
Metapotamal	0.10-0.08	125	175	80				
Cyprinids					150	150-200		
Salmonids					200	150-201		

The concept of specific power density shall now be adapted to the deep pool habitat. This concept has not been applied to evaluate the hydromorphology of a habitat yet, hence some thoughts and considerations are needed. At first, the driving force compelling fish into a fish pass or a deep pool habitat differs significantly in both cases. A fish traverses a fish pass due to its instinct for migration, e.g., to access a spawning habitat. In contrast, a deep pool is sought as a winter, summer or resting habitat during periods when the fish tends to rest due to external influences. It is challenging to assert whether the migratory drive motivates the fish to endure more challenging hydraulic conditions than it would require for a resting habitat. Therefore, the precise numerical values provided for fish passes are likely not directly transferable to the deep pool habitat. Nonetheless, calculating the specific power density for

the habitat allows for a magnitude estimation and facilitates a comparison between natural conditions in the deep pool habitat and technical conditions in the fish pass.

For the computation of specific power density in the deep pools, certain assumptions were necessary. Firstly, determining the relevant discharge passing through the pool was not as straightforward as in the case of fish passes, which have a predefined discharge. To address this, a conservative approach was adopted, aligning with the width of the scour. For pier-like structures, the DWD, and the Kdam, this entailed considering the entire width of the river, given that the scour extends across the entire width. The discharge of the DG was proportionally reduced based on the relative width of the scour hole to the river width. Due to questionable results from water level data measured at the DG, further calculations were omitted in this instance. The Δh remained consistent with the values obtained for backwater rise, and the total volume had already been calculated for the distribution of volume above the depth of the scour, as illustrated in figure 7.19. The specific power densities obtained are presented in table 7.3.

Table 7.3: Specific power densities for the different in-stream structures as deep pool habitat

Structure	P_D $[W/m^3]$
CP	80
RP	87
TP	94
DG	-
DWD	17
Kdam	492

Typical tributaries of the Rhine, such as the exemplary river Murg, are classified as Epipotamal. The water level differences induced by pier- and stone-like structures fall within a range of 0.02 - 0.13 m, closely aligning with the specified water level differences of the pools of a fish pass of the same region (see table 7.2). Notably, the Kdam stands out with an induced water level difference of 0.48 m. However, for the sake of comparison, the suggested values for the Epipotamal are considered. The various literature sources offer specific power densities ranging from 100 to 200 W/m^3 for pools in the Epipotamal. Additionally, a Swiss guideline provides a value for a still pool, presumed to be a resting place during extended passages, which is 50 W/m^3. The values calculated for the pier-like structures lay slightly below the recommended values for fish passes. The DWD stands out with a much lower specific power density of 17 W/m^3, which is due to the small water level difference between up- and downstream water level. The Kdam shows a significantly increased specific power density of 492 W/m^3, which is due to a high water level difference of up-and downstream water level. It is to be expected that the turbulence level of the pier-like structures and the DWD are suitable for a habitat and that the high turbulence level inside of the scour hole downstream of the Kdam is not suitable as a deep pool habitat.

It is notable that the calculated specific power densities are in the same order of magnitude as for the fish passage pools, which on the one hand could show a good validation of the

measurements in the physical model or could show that the turbulence levels that were derived for fish passes are not far away from the turbulence levels that would occur in natural rivers. Both conclusions are not valid at the same time but show the relevance of comparing the values calculated for the deep pool habitat with the existing values for fish passes.

7.3.3 Conclusion on the hydromorphological evaluation of the structures

When merging the assessments of bed morphology and mean flow velocities based on LSGÖ, as illustrated in figure 7.23, the definitively suitable zones surrounding the in-stream structures become evident. In the case of pier-like structures, these zones are notably concentrated at the berms within the upstream scour hole and along the sides of the structures. Suitable zones for the DG are predominantly found within the upstream scour hole. Contrarily, the DWD is categorically deemed unsuitable. The Kdam, on the other hand, exhibits two distinct suitable zones, each situated along the riverbanks.
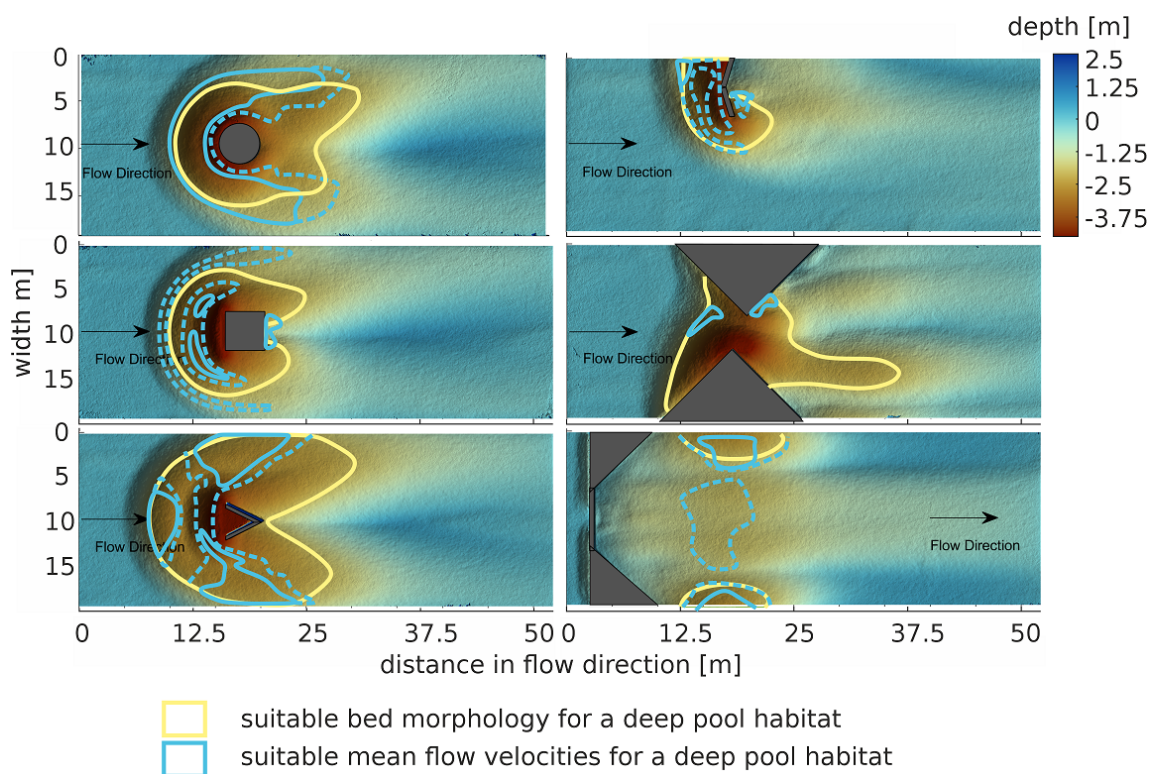
Figure 7.23: Hydromorphological evaluation based on scour depth and mean flow velocities.

In total, an extensive hydromorphological evaluation of in-stream structures has been conducted, with a primary focus on assessing scour holes for their suitability as deep pool habitats, particularly with respect to the common barbel. The evaluation encompassed both bed morphology and hydrodynamics, utilizing recommended parameters from LSGÖ. Criteria such as target depth and area were applied to assess bed morphology, revealing that all examined structures meet these standards. The distribution of suitable areas around the structures displayed varied patterns based on the structure type. Stone-like structures tended to create smaller yet deeper scour holes, while dam-like structures generated larger and shallower scour holes. For the evaluation of hydrodynamics, various methods were employed. A traffic

light rating system, vortex strength assessment, and adaptation of the specific power density from fish passage hydraulics were applied. The traffic light rating system indicated suitable areas for the structures, emphasizing the need for a detailed understanding of flow velocity distribution within the scour holes and not only giving one mean flow velocity for the entire deep pool habitat. The vortex strength analysis offered additional insights, highlighting the importance of considering local flow dynamics additional to the mean flow velocity fields. The adaptation of specific power density from fish passage hydraulics for deep pool habitats provided a magnitude estimation and facilitated comparison, suggesting that turbulence levels in the deep pool habitat are mostly comparable to those in designed fish passes. In conclusion, the combined analysis of bed morphology and hydrodynamics provides valuable insights into the suitability of different structures for creating diverse and dynamic habitats. While the primary focus has been on the common barbel, it is crucial to note that the enhancement of deep pool habitats positively impacts overall river beta diversity. This chapter lays the basis for future biological assessments by presenting a thorough hydromorphological data foundation and outlining additional data needs.

7.4 Outlook and recommendations for a pilot site - location-specific questions

This dissertation gives fundamental basics on the hydromorphological pattern for the implementation of in-stream structures as deep pool habitats. In the context of practical restoration projects, several additional considerations need to be taken into account, and these will be briefly discussed here.

7.4.1 Approach flow conditions

The flume and simulation assume perfectly straight approach flow conditions. However, in natural settings, structures are often approached at an angle, deviating from these ideal conditions. In the case of pier-like structures, the calculation of maximum scour depth can be simplified by incorporating the alignment factor as depicted in figure 3.28. Nevertheless, it is essential to note that the scour distribution around the structure and, consequently, the backwater rise may also undergo changes. For other types of structures, additional experimental work will be required.

7.4.2 Bed material

The bed material was not varied throughout this dissertation; hence, additional considerations are necessary when implementing the structure. Firstly, the mean sediment diameter, d_{50}, and sediment uniformity, σ_g, significantly impact the maximum scour depth. As d_{50} and σ_g increase, the scour depth decreases. The reduction due to varying d_{50} can be estimated using the relationship outlined in chapter 3.4.3. The influence of σ_g can be approximated using figure 3.21. Moreover, as d_{50} and σ_g increase, the spatial distribution of the scour hole undergoes changes. For increasing d_{50}, all dimensions of the scour hole, including depth,

width, and ridge, are reduced. An increase in σ_g results in a modified shape of the scour hole, accompanied by sediment sorting as observed in investigations by Okhravi et al. (2022). An armour layer forms on the approach flow bed and within the scour hole, leading to a shorter scour hole upstream of the pier, as illustrated in figure 7.24. It's noteworthy that, even with a smaller d_{50}, the scour hole is smaller for non-uniform sediment. The width of the scour remains unaffected, as the flow accelerates around both sides of the pier. The downstream dune is shifted upstream towards the pier.
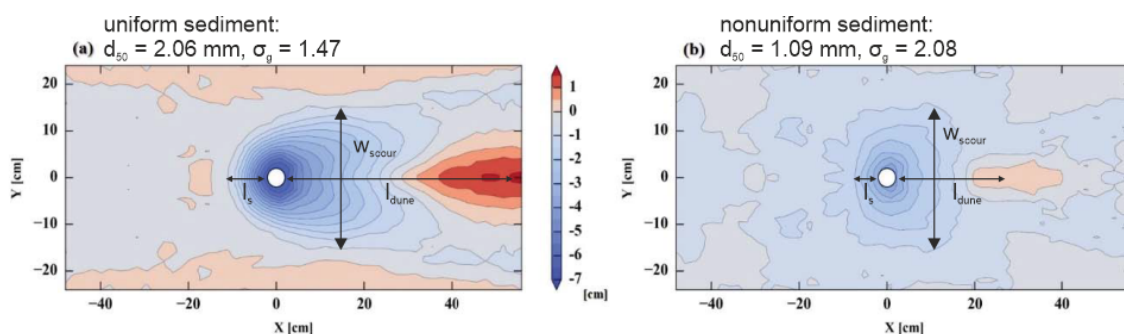
Figure 7.24: Influence of sediment uniformity on the maximum scour depth and shape of the scour hole, adapted from Okhravi et al. (2022).

Additionally, sediment size and uniformity may vary within different sediment layers in the ground. Another critical factor is the presence of cohesive sediment in the bed, which requires careful consideration. The influence of cohesive sediments on the scour process is not well investigated up to date, the reader is referred to DWA-M 529 for further information (Ettmer et al., 2021).

7.4.3 Variation of discharge

The experiments were performed under clear-water scour conditions at an approximate HQ2 and bed shear stresses right below threshold conditions. For different discharges the flow field may exhibit variations. Particularly, stone- and dam-like structures are affected by varying discharges. As the discharge diminishes to Q < MQ, the water depth decreases until the structures emerge above the water surface. The flow characteristics for these discharges can be simulated using the method developed in this study, as the numerical model proved to deliver reliable results. Concerning the DWD, an acceleration of the flow between the wings is anticipated for Q < MQ. Elevated shear stresses downstream of the structure could potentially amplify the scour depth. The flow pattern around the DG transforms from a 3D to a 2D flow field, as elaborated in chapter 3.3. The K-dam will only experience flow through the central notch and might induce an additional central scour hole directly downstream of the Kdam. These hypotheses require further experimental validation. For the TP, as an example for pier-like structures, an additional simulation was performed with a discharge equalling an MQ for the exemplary river Murg. The comparison of the mean flow velocity field and the evaluation of the flow velocities based on the traffic light rating system with target values of the LSGÖ is displayed in figure 7.25. The analysis shows a similar overall flow velocity field with a downflow upstream of the pier and a vortex that accelerates above the bed. The areas that

are hydromorphologically evaluated as suitable as a deep pool habitat are significantly larger for the MQ case than the HQ2 case. The area upstream of the pier shows significantly larger suitable parts and especially downstream of the pier the entire area is evaluated as suitable.
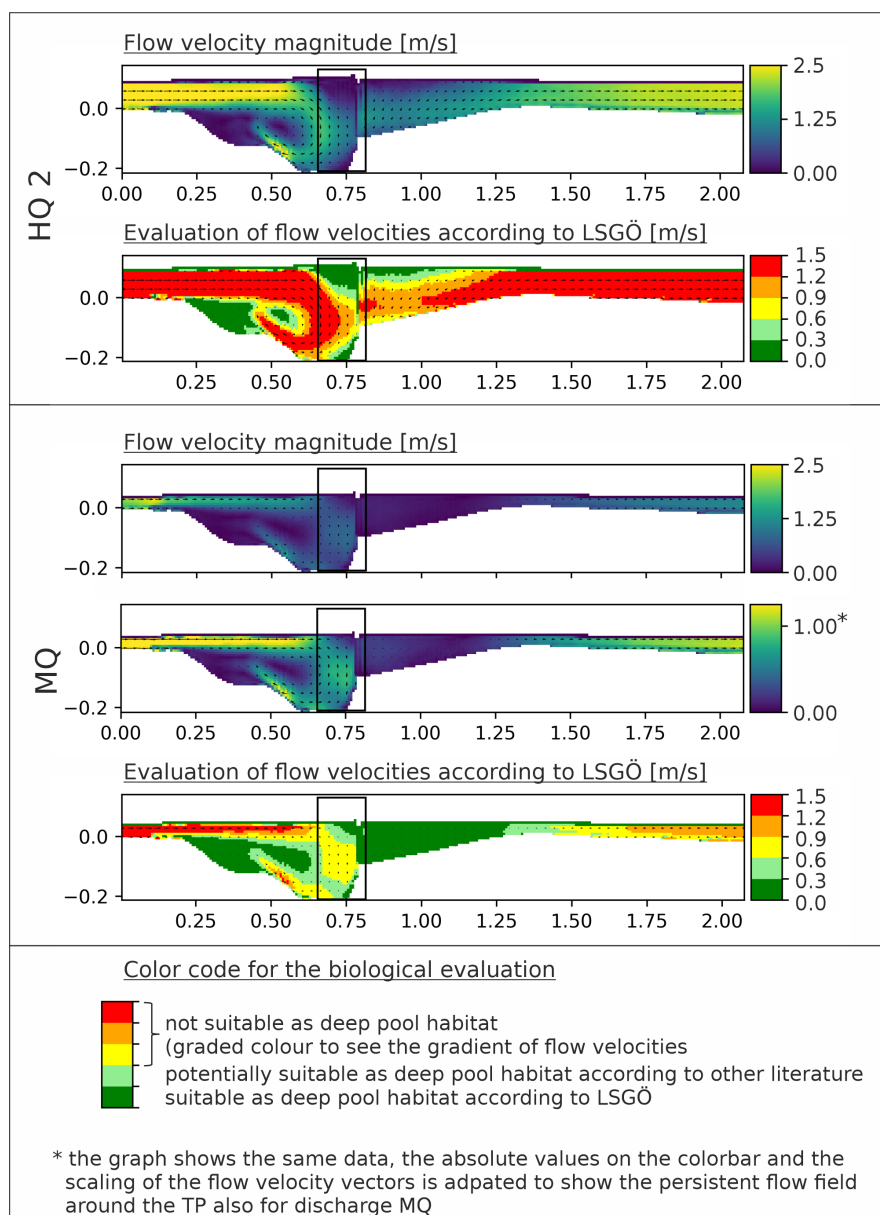
Figure 7.25: Influence of varying discharge on the flow field around the TP and the respective evaluation of the flow velocity field based on the traffic light rating system.

The experiments and simulations conducted in this study were carried out under steady-state conditions, neglecting the dynamic aspects of a flood event. Figure 7.26 summarizes some theoretical considerations on the interaction between the discharge curve and the sediment transport condition during a flood event. A flood event consists of a time-dependent discharge curve. In the initial phase, both the discharge and consequently flow velocities increase until reaching a discharge peak after a defined duration. Subsequently, the discharge diminishes until returning to the mean discharge (MQ). The change in discharge is closely linked to the sediment transport conditions. At a certain point, threshold conditions are attained, triggering

a shift in sediment transport from clear-water to live-bed conditions. On the descending limb of the flood wave, the sediment transport conditions transition from live-bed to clear-water. Consequently, as the flood subsides, a phase characterized by clear-water scour conditions is inevitably encountered, making it realistic to assume the prevalence of clear-water scour conditions (Raudkivi & Ettema, 1983).
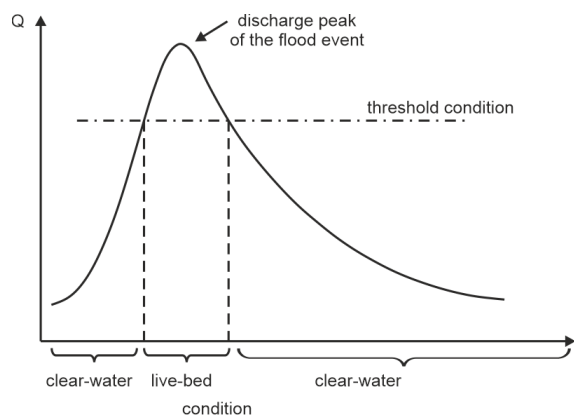
Figure 7.26: Scheme of sediment transport conditions during the passage of a flood wave.

7.4.4 Maintenance due to varying discharges

Discussion may arise as to whether lower discharges result in sediment redeposition within the scour hole. Lower discharges correspond to reduced bed shear stresses, with only smaller sediment fractions in motion. For pier-like structures, the flow field inside the scour hole remains persistent even at lower discharges, up to MQ, and approach flow velocities as shown in the previous subchapter. Consequently, no significant redeposition is expected. In contrast, for stone- and dam-like structures, the flow field at lower discharges has not been thoroughly examined, preventing a definitive conclusion on redeposition processes. Nevertheless, with the next HQ2 event, sediments will likely be flushed out of the scour hole, classifying the structure as "self-maintaining". Furthermore, morphological changes naturally occur across the river reach due to varying discharges and should therefore be accepted also for technically built structures.

7.4.5 Cross-sectional area

The experiments and simulations conducted in this study utilized a rectangular river cross-section. Given that the majority of rivers do not exhibit a rectangular cross-section, this aspect needs to be considered. Whether it features a trapezoidal, double-trapezoidal (following the Tulla configuration), or any other shape, the cross-section is notably enlarged compared to a rectangular main channel bed. Consequently, the blockage ratio of the structure diminishes in comparison to a rectangular channel. This reduction in the resistance, that is imposed by the structure on the flow, leads to a decrease in both scour depth and backwater rise as a natural consequence. The amount of reduction is up to further investigation.

7.4.6 Backwater rise reduction and possible geometric adaptation options

The dimensioning of the structure is dependent upon two external factors: the required scour depth for the establishment of a functional habitat and the potential backwater rise induced by the structure. Especially in urbanized regions, the available freeboard is often limited, thereby constraining the options for in-stream structures. Two approaches can be considered to align the structure with location specifications. Firstly, the width of the structure can be reduced to lower the blockage ratio, consequently decreasing the backwater rise. The impact of varying the width was examined for the TP and is illustrated in figures 7.27 a) to c) and 7.28. Notably, by reducing the width from 0.2 of the main channel width to 0.1 and 0.05, a significant decrease in scour depth was observed. The target scour depth was only achieved at 0.1 w, while it fell short for 0.05 w. Consequently, the maximum advisable reduction in width is 0.1 times the main channel width, as any further reduction may compromise achieving the target scour depth. The backwater rise could be reduced from 13.8 % to 8.3 %. Alternatively, an adaptation possibility involves adjusting the overflow height. For pier-like structures, reducing the height allows for overflow, while for stone- and dam-like structures, the submergence changes. Similar to the width reduction, decreasing the structure's height lowers the blockage ratio. Pier-like structures, in particular, exhibit a modified flow field, as they can be overflown, leading to a reduction in the downflow component in front of the structure and initiating overflow. Additional trailing vortices develop as described in Dey, Raikar, and Roy (2008). The reduction of the TP's height leads to a reduction of scour depth of about 50 % and the target depth can only be reached at the maximum scour depth location, whereas the backwater rise could not be reduced by this geometrical adaptation as shown in figure 7.27 d).
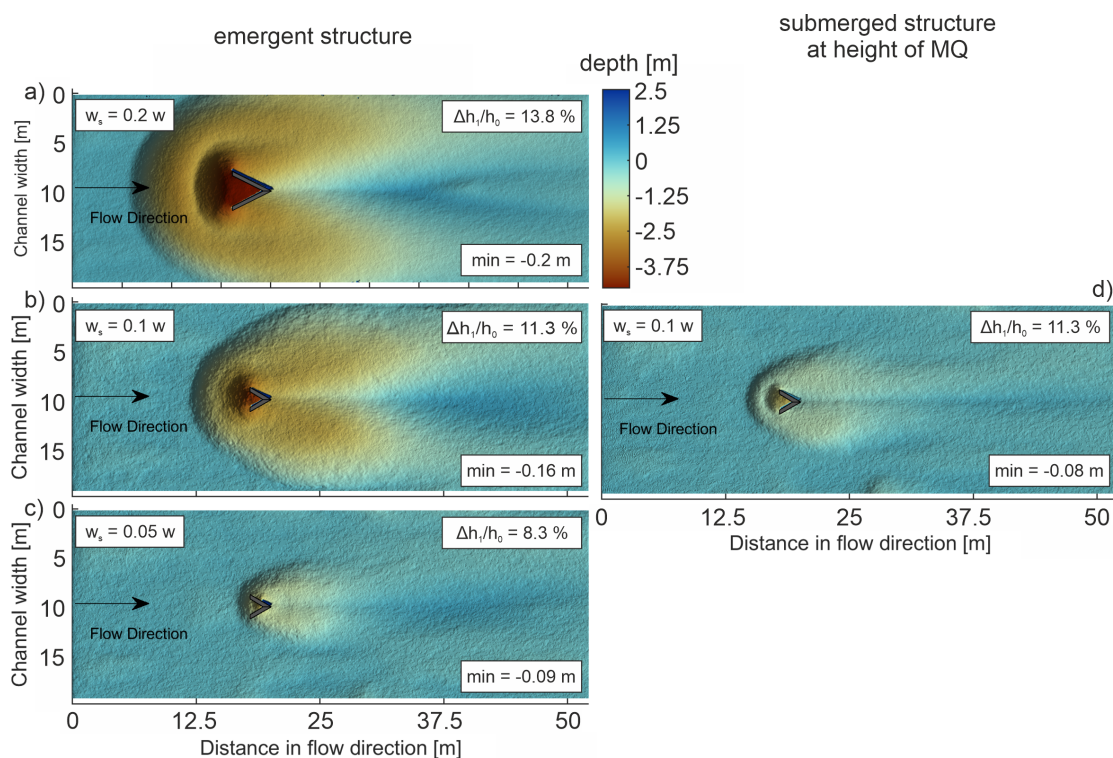
Figure 7.27: Influence of width and height of a TP on the scour depth development and backwater rise.

In summary, narrowing the structure width results in a decrease in backwater rise, whereas reducing the height to allow overtopping does not contribute to backwater rise reduction. Consequently, adjusting the structure's height does not appear to be an effective measure for minimizing backwater rise. Figure 7.28 illustrates the influence of the blockage ratio on both backwater rise and scour depth. A roughly linear relationship is observed for the scour depth, which increases proportionally with the blockage ratio. However, analyzing the trend for backwater rise reveals that a clear linear relationship is not evident. Particularly, in the case of 0.1 w, it is apparent that the submergence of the structure had no influence on backwater rise. It should be noted that the reduction in blockage ratio from 0.1 to 0.08 is very small and that uncertainties in backwater rise detection have a higher impact here. Even though, revitalization measures often involve very small blockage ratios, as such these sensitivities must be taken into account.
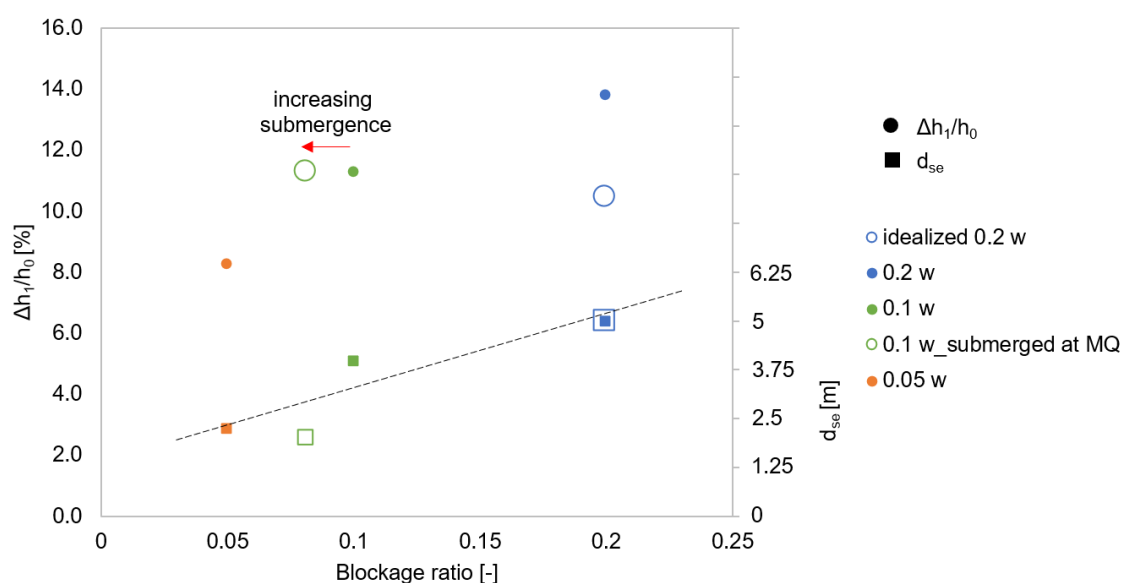
Figure 7.28: Influence of the blockage ratio on the backwater rise $\Delta h_1/h_0$ and on the maximum scour depth d_{se}.

Integrating the data of the geometric variations of the TP into figure 5.40 leads to an adjustment of the linear correlation resulting in higher backwater rise predictions especially for lower blockage ratios as shown in figure 7.29. In conclusion, the rule of thumb, stating that in-stream structures with a blockage ratio of < 5 % can be neglected in the flood neutrality proof, can be disproved and needs to be considered in the current engineering practice. Again it needs to be said, that this correlation is based on very few measurements and needs further datasets to be finally validated.
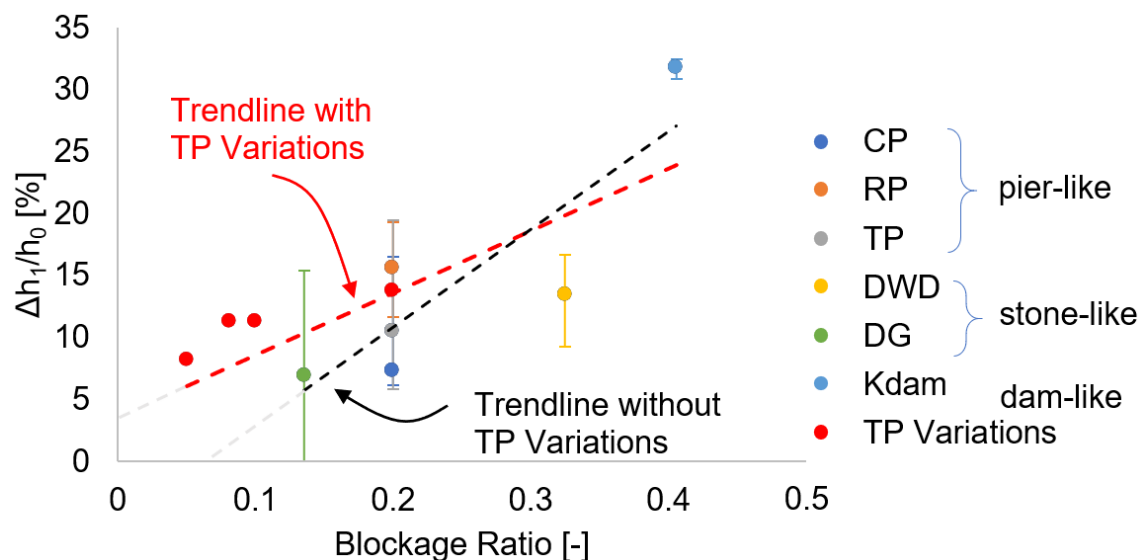
Figure 7.29: Mean values and and standard deviations of backwater rise for pier-, stone- and dam-like structures as a function of the blockage ratio, including a trendline based on the experiments a) with and b) without considering the TP variations.

7.4.7 Consideration of the in-stream structures in a 2D numerical model

In the state of Baden-Württemberg, the proof of flood neutrality currently requires compliance with specifications through the HydroAS software package, which is based on a 2D numerical approach. In this study, a 3D model was employed for the modeling of water level elevations. For the flood neutrality proof in HydroAS a transmission approach needs to be developed that considers backwater effects within a 2D framework. A critical factor in this context is the precise prediction of the scour depth, as it significantly influences the backwater, as evidenced by the temporal development of backwater rise (see chapter 5.1.2). Under local conditions, such as variations in discharge, differences in grain size distribution, varying mean grain diameters, and unexpected layering, the predicted backwater rise may not manifest. In such cases, significantly higher water levels, approximately 25 % higher, can be anticipated. In the context of a conservative assumption, calculations can also be made with a flat instead of a scoured bed, but this will result in significantly higher backwater rise.

7.4.8 Construction method and design concept

It remains an open question how the different structures are to be implemented as a construction. First considerations have been made, that the TP could be implemented as a pile row made of wood piles. A construction in form of a sheet pile wall are possible as well. In any case it is advised to consult a geotechnical expert opinion for the structural design of the foundation of the structure for a specific pilot-site.

Furthermore, it is recommended to excavate a scour hole during construction, corresponding to the equilibrium stage scour hole, to avoid high water levels in the initial phase.

7.4.9 Further environmental factors for the success

To assess the impact of deep pool habitats on the pilot site, a comprehensive monitoring program is proposed for implementation. The monitoring initiative should start prior to the installation of in-stream structures, incorporating both biological and hydromorphological monitorings to capture the baseline conditions before intervention. Subsequent monitoring should occur at strategic intervals, such as post-major floods of HQ2, to document changes resulting from these events. Additionally, monitoring after periods of low water is essential to document potential sedimentation processes.

The complexity associated with temperature considerations was excluded from this dissertation. However, temperature is an additional factor influencing the success of deep pool habitats. Questions regarding potential temperature gradients within the pool and the local mixing processes become relevant and require further investigation. Recent studies have demonstrated the significance of the location within a river reach, with a combination of shading through vegetation proving favorable (Kurylyk et al., 2015). Groundwater upwellings are identified as suitable locations for deep pools, though it is essential to acknowledge that oxygen concentrations might be lower in groundwater, necessitating effective mixing (Kurylyk et al., 2015). A conceptual plan for the ongoing research involves locating in-stream structures downstream of a cold water inlet, as depicted in figure 7.30.
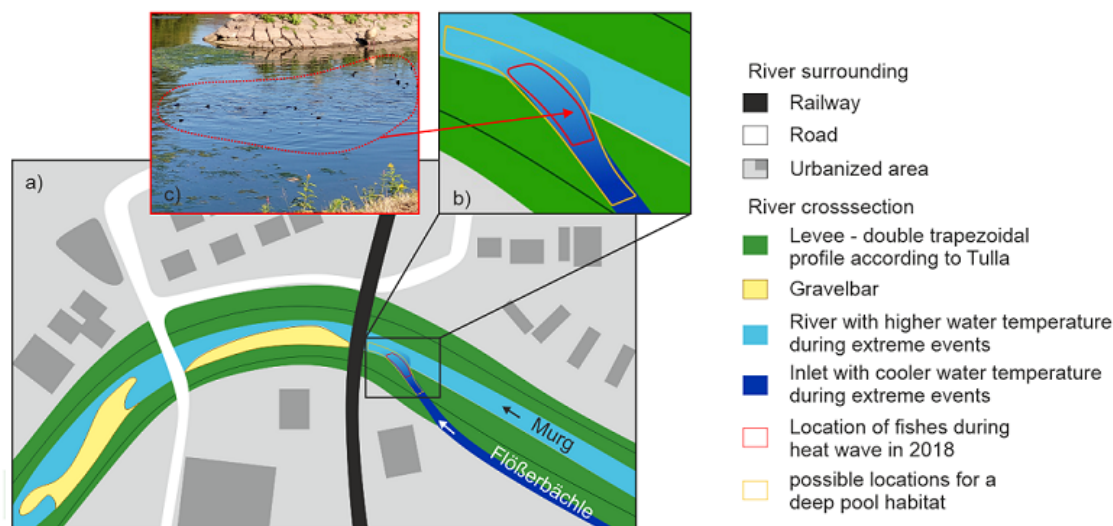
Figure 7.30: Example of a potential deep pool habitat location: a) The site features the convergence of a small creek, Flößerbächle, supplying cool water temperatures, with a larger river, Murg, characterized by higher water temperatures. This site is situated in an urbanized area, and the river is confined within two levees with a double trapezoidal cross profile. Downstream of the creek inlet, two significant gravel bars are present along the inner bank of the river bend. b) The area represents a mixing zone where cooler and warmer water meet. During the heat waves in both 2018 and 2022, fish sought refuge in the cooler waters, with the red frame marking the specific location where fish gathered for a cold-water retreat. The orange frame designates a potential site for a deep pool habitat. c) Accumulation of fishes (visible by their fins) at the cold-water inlet of Flößerbächle during the 2018 heatwave (image courtesy of Dr. Frank Hartmann). Illustration is part of Kannen, Seidel, and Franca (submitted in 2023)

.

7.5 Expanding the concept to other habitat types

The methodological framework developed in this disseration is versatile and can be applied to investigate various habitat types, such as runs (german: Fließrinne), gravel bars as spawning habitats, or low-flow areas for juveniles. The integration of physical model experiments and numerical simulations offers a robust representation of future habitat conditions, significantly enhancing the predictability of implemented measures. Alongside the delineated evaluation methods, the developed approach can constitute a toolbox for the examination of additional in-stream structures. Practical engineers can use this information to determine the specific in-stream structures needed to create a designated habitat. Additionally, the data generated provides essential insights for flood assessments, allowing for an evaluation of the impact of in-stream measures on flood risk.

The conceptual framework can be expanded to not only explore individual habitat types but also to investigate the synergistic interactions between multiple habitat types, delving into the hydromorphological dynamics among these diverse habitats as shown in figure 7.31. Particular attention should be directed towards strategic positioning; for instance, positioning a juvenile habitat downstream of a spawning habitat. This consideration is grounded in the un-

derstanding that fish larvae typically drift downstream after the larval stage, as their swimming capabilities are not yet sufficiently developed to resist the current. Conversely, adult habitats may be strategically placed upstream of spawning habitats, given that adult fish possess the capability to navigate against the flow. This modular approach paves the way for illustrating comprehensive river restoration measures.
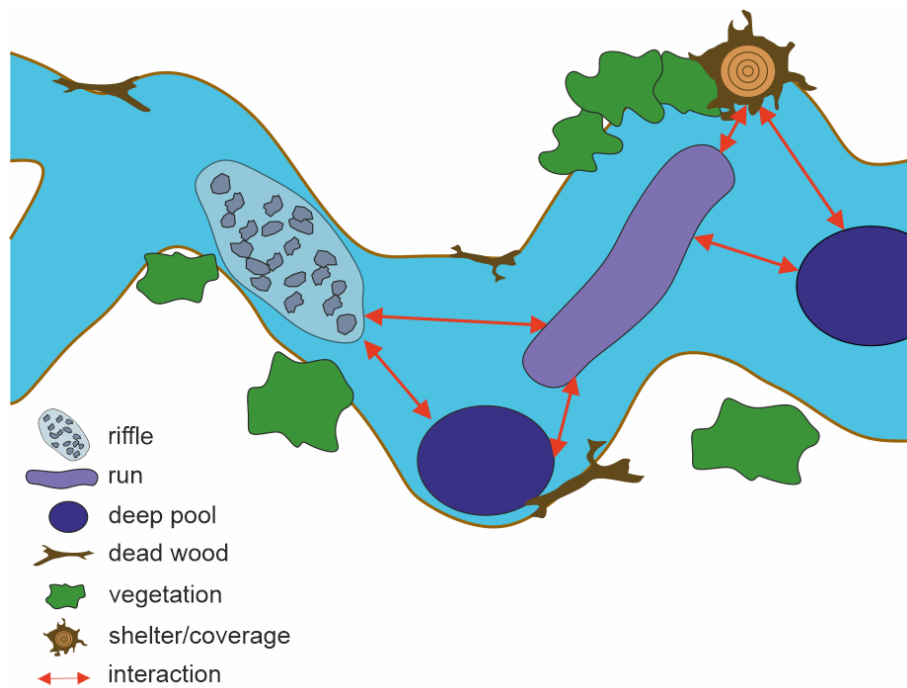
Figure 7.31: Modular concept of habitat types and interaction between the different types (illustration inspired by LSGÖ).

Chapter 8

Concluding remarks

Due to human intervention key habitats such as deep pool habitats have vanished from riverine systems, imposing a threat to fish biocenosis. Especially during droughts with low water depth and high water temperatures fishes face challenges to find adequate habitats. Engineering measures from the in-stream portfolio can be a promising approach in solving this problem, especially in restricted urbanized areas, where predictable hydromorphological conditions are imperative. This dissertation analysed different in-stream structures regarding their suitability to sustainably create deep pool habitats, developed an approach to investigate eco-hydromorphological effects connected to in-stream structures and created a toolkit to efficiently assess the suitability of in-stream measures in revitalization projects.

To identify effective measures, it was necessary to first determine the boundary conditions defining suitable habitats, which were to-date unknown in the community, and second to identify measures suitable for implementation. Consequently, extensive literature reviews were conducted to address both tasks. Defining the hydromorphological boundary conditions for a general deep pool habitat presented a challenge which is why one fish species, the barbel (*Barbus Barbus*), was selected as indicator species due to its high requirements regarding habitat preferences. An in-depth exploration through literature on the fish species barbel resulted in establishing boundary conditions including a minimum water depth (2 m) and a maximum mean flow velocity (< 0.3 m/s), achievable for a discharge of Q_{30-330}. However, suitable literature and experiences proved scarce, and a critical discussion regarding the suitability of mean flow velocities as the sole parameter for defining suitable hydrodynamic boundary conditions in a deep pool habitat was initiated. Consideration was given to incorporating additional parameters related to turbulence characteristics. In order to identify measures that can meet the hydromorphological boundary conditions derived above, especially regarding the water depth, a second comprehensive literature research on local scouring processes was conducted. This involved reviewing 400 international sources from disciplines spanning fish biology, ecology to hydromorphology. The installation of in-stream structures showed to be an effective measure for local scouring in restricted urbanized areas. Three different basic flow types leading to local scouring around in-stream structures were identified and defined as pier-, stone-, and dam-like structures. The definition is based on submergence and the width of the instream structure, characterizing whether a structure is overflown and/or flown

around laterally on one or both sides. The quantification of all known parameters affecting scour depth, including flow intensity, relative sediment size, sediment uniformity, temporal development and structural parameters, was a major goal of this part of the investigation. The literature revealed that while parameters for each flow type are generally well-documented, there is a serious lack of information to correlate flow type and its capability to form deep scours under the same boundary conditions.

Six structures, including at least one representative for each flowtype, were selected for further investigation with a hybrid model approach combining physical model experiments and 3D HN simulations. The experiment included a movable bed to capture the bed morphology and backwater rise at equilibrium. Simulations were based on a scoured, rigid bed to complement the dataset with hydraulic data on flow velocities and turbulence characteristics.

The first set of experiments explored idealized forms of the six in-stream structures, revealing three phases of the scouring process for all flow types: the initial phase, the principal phase and the equilibrium phase. A universal criterion for equilibrium conditions across all flow types was formulated. The bed morphology measured at equilibrium conditions showed a strong reproducibility of the replicate experiments, which affirmed the robustness of the physical model setup. For different types of structures, different generalized behavior was observed: Pier-like structures exhibited a distinct downflow upstream of the pier, initiating the scouring process, and evolving into a horseshoe vortex system with substantial sediment transport capacity. The resultant scour hole exhibited a circular evolution in the upstream and lateral direction, featuring a prominent berm within. Downstream of the pier, a dune was observed along the centerline of the flume. Stone-like structures exhibited the formation of helices upstream, efficiently creating a scour hole, and a stable vertical vortex downstream of the structure's head. Notably, these structures generated a longitudinal deep section that extended downstream. Dam-like structures, such as the Kdam, showcased a jet-like drop into the tailwater, coupled with two horizontal vortices on either side of the flume, resulting in the erosion of two scour holes. Importantly, all structures exhibited qualitative agreement in bed morphology and flow velocity fields with literature values. Quantitative comparison of scour hole dimensions (depth, area and volume) revealed the Triangular Pier (TP) structure as the most promising variant, rendering this structure the focus for further investigation. Additionally, a secondary finding indicated good agreement between experiments and simulations regarding hydrodynamic observations, with the LES model standing out for highly three-dimensional turbulent flows over the RNG approach. Concerning backwater rise, pier- and stone-like structures exhibited a 7-15 % increase in upstream water level compared to the uniform flow case, while a remarkable 30 % increase was observed with the Kdam. The simulations suggested an influence of blockage ratio, scouring and submergence on the drag coefficient of the structures. However, uncertainties in determining backwater rise were evident, urging further investigations for clarification and refinement in this aspect.

The subsequent series of experiments delved into additional considerations crucial for a pilot site, relying solely on physical model experiments. This comprehensive exploration included three distinct sets: The first set specifically focused on the influence of natural materials on the scouring process and backwater rise. This set comprised three subsets investigating the impact of edge design, surface roughness and porosity. Notably, the edge design proved relevant only for emergent structures, with scour depth decreasing by approximately 20 % for round edges. Submerged structures like the Deflected Groyne (DG) proved insensitivity to round edges. Surface roughness tests on the Double Wing Deflector (DWD), the structure with the largest area in streamwise direction, indicated an insensitivity of the scour process to surface roughness, however a significant increase of up to 50 % backwater rise for high surface roughness. Porosity emerged as the most important factor, with scour depth decreasing by up to 87 % for high porosity, rendering porous structures unsuitable for implementation. The second set of experiments examined the influence of debris accumulations, exploring parameters such as upstream and downstream length, width, and submergence of the debris. The greatest impact on scour depth was observed with submergence, resulting in a 20 % increase. Additionally, the presence of debris led to an approximate 10 % higher backwater rise compared to the case without debris. The final set of experiments aimed to combine a deep pool habitat with a shelter, addressing concerns about the potential accumulation of fish in individual pools attracting terrestrial predators. The deep pool was augmented with a shelter mimicking a dead wood structure (tree crown). A challenge was encountered in realistically modeling a shelter within a movable bed experiment, requiring the adaptation of a vegetation modeling approach from aerodynamics. Various tests with different foliages and arrangements were conducted for the TP, DG, and DWD structures. Shelters installed downstream of the scour hole did not affect the scour hole upstream of the structures, but an additional scour hole developed locally around the shelter. An observed increase of more than 50 % in backwater rise, however, limited the practical application in river restoration projects.

Based on the measured bed morphology and the simulated hydrodynamics, a hydromorphological evaluation regarding the suitability as deep pool habitat was performed. As evident from this dissertation, pier-, stone- and dam-like structures all meet the criteria for target depth and area of deep pools. Additionally, the distribution of suitable areas around the structures regarding the water depth criterion was analyzed. The availability of areas where the water depth was within the target values around the structures was dependent on the type of the structure: Stone-like structures created smaller yet deeper scour holes, and dam-like structures generated larger and shallower scour holes. However, to finally assess the suitability of these in-stream structures for the creation of fish habitats, the hydrodynamics need to be considered as well. Implementing a traffic-light rating system and a vortex strength assessment underscored the significance of comprehending the flow velocity distribution within the scour holes. Suitable areas could be found at the berm inside and in the lateral zones of the pier-like structures. At stone-like structures the suitable areas were located upstream of the head of the structures. Dam-like structures showed two suitable zones at the riverbanks. Combining suitable areas regarding both water depth and flow velocities revealed that all structures can

provide zones of suitable habitat conditions as a deep pool habitat, except from the DWD. Additionally, an adapted specific power density concept from fish passage hydraulics applied as an order-of-magnitude estimation suggested comparable turbulence levels in deep pool habitats and designed fish passes. This comprehensive evaluation not only serves as a foundation for future biological assessments but emphasizes the positive impact of deep pool habitats on overall river beta diversity, contributing to an increase of water depth, flow velocity and possibly sediment variability.

In considering practical applications for restoration projects, various critical factors emerged and should be considered in further investigations. Non-ideal approach flow conditions are recognized, signaling the need for additional experimental work, particularly concerning stone- and dam-like structures. The significance of bed material characteristics, such as mean sediment diameter and uniformity, in shaping scour depth and spatial distribution is highlighted and needs further experimental consideration. Challenges arising from discharge variations are highlighted, prompting further investigations for stone- and dam-like structures as they emerge above the water level with decreasing discharges. Simulations for pier-like structures at lower discharge could proof a consistent flow velocity field and a suitability as deep pool habitat throughout the entire scour hole. The importance of monitoring the in-stream structures under unsteady conditions during flood events and after drought seasons to assess their impact on possible sedimentation processes is emphasized. Additionally, potential adaptations to the geometry of the structure are assessed via variation of the width and height of a pier-like structure, uncovering a potential decrease of backwater rise, however at the cost of decreased scour depth. The utilization of a 2D numerical model for flood neutrality proof are discussed and new lines for research are proposed for an approach for adaptation of hydrodynamic simulations from 3D to 2D. Moreover, an expansion of the methodology to explore diverse habitat types and their synergistic interactions is proposed, offering a versatile framework for comprehensive river restoration measures.

The main contributions of this research are:

- The employed hybrid model approach, combining a physical model experiment with a movable bed to acquire bed morphology and a 3D numerical model for flow velocity fields, can be confirmed as a suitable, effective and efficient methodology.

- All examined structures can attain the required scour depth, rendering them a suitable measure to create deep pool habitats. Best performance is achieved with the triangular pier.

- The flow field within the scour is characterized by prominent vortex structures, and for pier- and stone-like structures, helices are observed. These helices efficiently entrain and transport significant sediment loads, resulting in the formation of the deepest scours. In contrast, the flow field in the dam-like structure is distinct, featuring a jet-like scour that descends into the tailwater. While two vortex systems at the sidewalls contribute to the deepest scour, no helical motions were observed.

- The maximum scour depth showed a high sensitivity to the porosity of the structure, resulting in a reduction of up to 87 % for structures with high porosity.

- The average backwater rise was measured for the idealized structures ranging from 7 to 15 % for pier- and stone-like structures. A backwater rise of up to 30 % was observed for dam-like structures, prohibiting their application in restricted areas. Debris and especially the shelter increased the backwater rise up to 50 %, whereas porous structures tended to decrease backwater rise.

- The application of the hydromorphological criteria on the generated scours revealed that the scour depth could be reached for all variants except the porous ones. Solely taking the mean flow velocity fields as a basis for the evaluation of suitable hydrodynamic conditions was questionable, as helical motions and turbulent fluctuations were not visible here. Streamlines and standard deviations gave crucial additional insights into the hydrodynamic characteristics inside of the scour. An integral approach based on the specific power density revealed comparable turbulence levels in the deep pool habitats and designed fish passes. It is to be discussed whether additional turbulence parameters need to be included in the biological evaluation.

In summary, all structures investigated in this dissertation, including their variants except the porous ones, met the required target values for scour depth. Consequently, the construction of porous structures for the establishment of deep pool habitats is not recommended. While the flow velocity fields identified zones suitable for deep pool habitat conditions, a more in-depth analysis revealed the need for additional hydrodynamic information for a comprehensive biological evaluation. While this work was based on ecological requirements specifically derived from the habitat preferences of the fish species barbel, it is important to note that the resulting benefit is not limited to this species: the in-stream structures under investigation show the potential to enhance the overall beta diversity within the river reach. Further, in view of the scarcity of biological studies in this domain it is strongly recommended to invest in more fundamental research in collaboration with biologists. The quantification of favorable ecological and hydromorphological conditions for deep pool habitats, coupled with an improved assessment of water level elevations during flood events, significantly increases the predictability and safety of the investigated in-stream structures.

Bibliography

Aarts, Bram G W and Piet H Nienhuis (2003). *Fish zonations and guilds as the basis for assessment of ecological integrity of large rivers*, pp. 157–178. DOI: 10.1023/A:1024638 726162.

Adam, Beate et al. (2014). *Merkblatt DWA-M 509 - Fischaufstiegsanlagen und fischpassierbare Bauwerke Gestaltung, Bemessung, Qualitätssicherung*. DWA Deutsche Vereinigung für Wasserwirtschaft, Abwasser und Abfall e. V. ISBN: 9783942964913.

Addy, Stephen and Mark Wilkinson (2016). An assessment of engineered log jam structures in response to a flood event in an upland gravel-bed river. In: *Earth Surface Processes and Landforms* 41 (12), pp. 1658–1670. ISSN: 10969837. DOI: 10.1002/esp.3936.

Akhlaghi, Ebrahim et al. (2020). Assessment the Effects of Different Parameters to Rate Scour around Single Piers and Pile Groups: A Review. In: *Archives of Computational Methods in Engineering* 27 (1), pp. 183–197. ISSN: 18861784. DOI: 10.1007/s11831-018-09304-w.

Aksel, Murat et al. (Apr. 2021). A comparative analysis of coherent structures around a pile over rigid-bed and scoured-bottom. In: *Ocean Engineering* 226. ISSN: 00298018. DOI: 10.1016/j.oceaneng.2021.108759.

El-Alfy, Kassem Salah (2006). *Experimental study of backwater rise due to bridge piers as flow obstructions*. In: *Tenth International Water Technology Conference, IWTC10 2006*. Vol. 10, pp. 319–336.

Ambagts, L. R. (June 2019). *Flow over and around submerged groynes - Numerical modelling and analysis of a groyne flume experiment*. masterthesis. Delft University of Technology. URL: http://repository.tudelft.nl/..

Anlauf, Andreas and Bernd Hentschel (2007). *Untersuchungen zur Wirkung verschiedener Buhnenformen auf die Lebensräume in Buhnfeldern der Elbe*. In: *Wasserstraßen - Verkehrswege und Lebensraum in der Kulturlandschaft. Symposium am 11. September 2007 in Bonn*. Bundesministerium für Verkehr, Bau und Stadtentwicklung., pp. 94–100. URL: https://henry.baw.de/items/a8dab730-bc2f-42b2-9367-d2c19faa0f95.

Armanini, Aronne et al. (2010). *Analysis of a fluvial groynes system on hydraulic scale model*. In: *River Flow 2010*. Bundesanst. für Wasserbau, pp. 1177–1184. ISBN: 9783939230007.

Aubrun, Sandrine et al. (Apr. 2005). Physical modelling of a complex forest area in a wind tunnel - Comparison with field data. In: *Agricultural and Forest Meteorology* 129 (3-4), pp. 121–135. ISSN: 01681923. DOI: 10.1016/j.agrformet.2005.01.001.

Azinfar, H and J.A. Kells (Aug. 2008). Backwater Prediction due to the Blockage Caused by a Single, Submerged Spur Dike in an Open Channel. In: *Journal of Hydraulic Engineering* 134 (8), pp. 1153–1157. DOI: 10.1061/ASCE0733-94292008134:81153.

Azinfar, Hussein and James A. Kells (2009). Flow resistance due to a single spur dike in an open channel. In: *Journal of Hydraulic Research* 47 (6), pp. 755–763. ISSN: 00221686. DOI: `10.3826/jhr.2009.3327`.

Baker, R.E. (1986). *Local scour at bridge piers in non-uniform sediment, Report No. 402*. School of Engineering, The University of Auckland, pp. 1–91.

Bănărescu, Petru M. and Nina G. Bogutskaya (2003). *The Freshwater Fishes of Europe, Cyprinidae 2, Part II: Barbus*. Ed. by Petru M. Bănărescu and Nina G. Bogutskaya. Vol. 5/2. Aula-Verlag, p. 454.

Baras, E (1992). Etude des stratégies d'occupation du temps et de l'espace chez lebarbeau fluviatile, Barbus barbus (L.) In: *Cahier d'Ethologie* 12, pp. 125–442.

Baras, Etienne and Benoît Cherry (1990). Seasonal activities of female barbel Barbus barbus (L.) in the River Ourthe (Southern Belgium), as revealed by radio tracking. In: *Aquat. Licing Resour* 3, pp. 283–294.

Becker, Andreas and Johannes Ortlepp (2022). *Fischökologisch funktionsfähige Strukturen in Fließgewässern*. Regierungspräsidiums Tübingen. URL: `https://rp.baden-wue rttemberg.de/fileadmin/RP-Internet/Themenportal/Wasser_und_Boden/ Geschaeftsstelle_Gewaesseroekologie/Landesstudie_Gewaesseroekologie_G. _I._O/_DocumentLibraries/Documents/Fischoekologisch_funktionsfaehige_ Strukturen.pdf`.

Becker, Florian N. et al. (Nov. 2022). Towards a more comprehensive assessment of the intensity of historical European heat waves (1979–2019). In: *Atmospheric Science Letters* 23 (11). ISSN: 1530-261X. DOI: `10.1002/asl.1120`.

Beheshti, Ali Asghar, Behzad Ataie-Ashtiani, and Hamed Dashtpeyma (Apr. 2017). Numerical simulations of turbulent flow around side-by-side circular piles with different spacing ratios. In: *International Journal of River Basin Management* 15 (2), pp. 227–238. ISSN: 18142060. DOI: `10.1080/15715124.2017.1280811`.

Bennett, Sean J, Taner Pirim, and Brian D Barkdoll (Apr. 2002). Using simulated emergent vegetation to alter stream flow direction within a straight experimental channel. In: *Geomorphology* 44 (1-2), pp. 115–126. ISSN: 0169555X. DOI: `10.1016/S0169-555X(01)001 48-9`.

Bertoldi, David A. and J. Sterling Jones (1998). *Time to Scour Experiments as an Indirect Measure of Stream Power Around Bridge Piers*. In: *Proceedings of the International Water Resource Engineering Conference*, pp. 264–269.

Bezzola, G. R. (2002). *VAW Mitteilung 173: Fliesswiderstand und Sohlenstabilität natürlicher Gerinne unter besonderer Berücksichtigung des Einflusses der relativen Überdeckung*.

Bischoff, Antje and Jörg Freyhof (1999). Seasonal shifts in day-time resource use of 0+ barbel, Barbus barbus. In: *Environmental Biology of Fishes* 56, pp. 199–212. DOI: `10.1023/A:1 007552318543`.

Blevins, R. D. (1984). *Applied Fluid Dynamics Handbook*. Van Nostrand Reinhold Company Inc.

Blohm, H.-P., D. Gaumert, and M. Kämmereit (1994). *Leitfaden für die Wieder- und Neuansiedlung von Fischarten. Binnenfischerei in Niedersachsen 3*. Niedersächsisches Lan-

desamt für Oekologie. URL: https://www.laves.niedersachsen.de/startseite/tiere/binnenfischerei/fischartenschutz/-93498.html.

Bond, N. R. and P. S. Lake (2005). Ecological restoration and large-scale ecological disturbance: the effects of drought on the response by fish to a habitat restoration experiment. In: *Restor Ecol* 13, pp. 39–48. DOI: 10.1111/j.1526-100X.2005.00006.x.

Booker, D. J., D. A. Sear, and A. J. Payne (2001). Modelling three-dimensional flow structures and patterns of boundary shear stress in a natural pool–riffle sequence. In: *Earth Surface Processes and Landforms* 26, pp. 553–576. ISSN: 10969837. DOI: 10.1002/esp.210.

Breusers, H. N.C., G. Nicollet, and H. W. Shen (1977). Local Scour Around Cylindrical Piers. In: *Journal of Hydraulic Research* 15 (3), pp. 211–252. ISSN: 00221686. DOI: 10.1080/00221687709499645.

Breusers, H. N.C. and A.J. Raudkivi (1991). *Scouring*. Ed. by H. N. C. Breusers and Arved J. Raudkivi. VIII. Balkema, VIII, 143 S. : graph. Darst. ISBN: 9061919835.

Britton, J. R. and J. Pegg (Oct. 2011). Ecology of European barbel Barbus barbus: Implications for river, fishery, and conservation management. In: *Reviews in Fisheries Science* 19 (4), pp. 321–330. ISSN: 10641262. DOI: 10.1080/10641262.2011.599886.

BSA Flow Software Version 4.10. Installation and User's Guide (2006). Software documentation. Dantec Dynamics. Dantec Dynamics A/S.

Burkow, M. and M. Griebel (2016). A full three dimensional numerical simulation of the sediment transport and the scouring at a rectangular obstacle. In: *Computers and Fluids* 125, pp. 1–10. ISSN: 00457930. DOI: 10.1016/j.compfluid.2015.10.014.

Capone, T. A. and J. A. Kushlan (1991). Fish community structure in dry-season stream pools. In: *Ecology* 72 (3), pp. 983–992. ISSN: 00129658. DOI: 10.2307/1940598.

Cardoso, A. H. and R. Bettess (Apr. 1999). Effects of Time and Channel Geometry on Scour at Bridge Abutments. In: *Journal of Hydraulic Engineering* 125 (4), pp. 388–399. ISSN: 0733-9429. DOI: 10.1061/(ASCE)0733-9429(1999)125:4(388).

Chang, Wen-Yi, Jihn-Sung Lai, and Chin-Lien Yen (2004). Evolution of Scour Depth at Circular Bridge Piers. In: *Journal of Hydraulic Engineering* 130 (9), pp. 905–913. ISSN: 0733-9429. DOI: 10.1061/(asce)0733-9429(2004)130:9(905).

Charbeneau, Randall J and Edward R Holley (Oct. 2001). *Backwater Effects of Piers in Subcritical Flow*. Center for Transportation Research, The University of Texas at Austin.

Chen, Su Chin, Hsun Chuan Chan, and Yu Hsiu Li (July 2012). Observations on flow and local scour around submerged flexible vegetation. In: *Advances in Water Resources* 43, pp. 28–37. ISSN: 03091708. DOI: 10.1016/j.advwatres.2012.03.017.

Chiew, Y.M. and B.W. Melville (1987). Local scour around bridge piers. In: *Journal of Hydraulic Research* 25 (1), pp. 15–26. ISSN: 0972057X. DOI: 10.1080/00221688709499285.

Cismaș, Cristina Ioana, Doru Bănăduc, and Angela Bănăduc (2018). Diversion of fishing pressure on the economically important fish species Barbus barbus (Linnaeus, 1758) to protect the community interest congeneric Barbus meridionalis Risso 1826, based ona decision-support management system. In: *Transylvanian Review of Systematical and Ecological Research* 20.2, pp. 63–74. DOI: 10.2478/trser-2018-0006.

Coleman, Stephen E., Christine S. Lauchlan, and Bruce W. Melville (2003). Clear-water scour development at bridge abutments. In: *Journal of Hydraulic Research* 41 (5), pp. 521–531. ISSN: 00221686. DOI: 10.1080/00221680309499997.

Curran, Joanna Crowe and W. Cully Hession (Nov. 2013). Vegetative impacts on hydraulics and sediment processes across the fluvial system. In: *Journal of Hydrology* 505, pp. 364–376. ISSN: 00221694. DOI: 10.1016/j.jhydrol.2013.10.013.

Dashtpeyma, Hamed (2019). *Turbulence structures in isolated pool-riffle units*. Dissertation. University of Waterloo.

Dey, Subhasish and Rajkumar V. Raikar (Apr. 2007). Characteristics of Horseshoe Vortex in Developing Scour Holes at Piers. In: *Journal of Hydraulic Engineering* 133 (4), pp. 399–413. ISSN: 0733-9429. DOI: 10.1061/(ASCE)0733-9429(2007)133:4(399).

Dey, Subhasish, Rajkumar V. Raikar, and Abhishek Roy (2008). Scour at Submerged Cylindrical Obstacles under Steady Flow. In: *Journal of Hydraulic Engineering* 134 (1), pp. 105–109. DOI: 10.1061/ASCE0733-94292008134:1105.

Dias, Ana Josefa, Cristina Sena Fael, and Francisco Núñez-González (Feb. 2019). *Effect of Debris on the Local Scour at Bridge Piers*. In: *IOP Conference Series: Materials Science and Engineering*. Vol. 471. Institute of Physics Publishing. DOI: 10.1088/1757-899X/471/2/022024.

Dolloff, C. A. (1986). Effects of stream cleaning on juvenile coho salmon and dolly warden in Southeast Alaska. In: *Transactions of the American Fisheries Society* 115, pp. 743–755. DOI: 10.1577/1548-8659(1986)115<743:EOSCOJ>2.0.CO;2.

Dolloff, C. A. and Melvin L. Warren (2003). *Fish Relationships with Large Wood in Small Streams*. In: *American Fisheries Society Symposium 37*, pp. 179–193. URL: https://www.srs.fs.usda.gov/pubs/ja/ja_dolloff002.pdf.

Ebel, G. (2002). *Untersuchungen zur Stabilisierung von Barbenpopulationen – dargestellt am Beispiel eines Mitteldeutschen Fliessgewässers*. Halle: Impress Druckerei.

Ebel, Guntram (1996). Beobachtungen im Helmegebiet zur Reproduktion der Barbe. In: *Naturschutz im Land Sachsen-Anhalt* 33 (1), pp. 21–28.

Ebrahimi, Mohsen et al. (Dec. 2018). Experimental Study on Scour at a Sharp-Nose Bridge Pier with Debris Blockage. In: *Journal of Hydraulic Engineering* 144 (12). ISSN: 0733-9429. DOI: 10.1061/(asce)hy.1943-7900.0001516.

Eiff, Olivier et al. (2019). *Momentum Balance of a glass-plate patch in shallow flow*. In: *Proceedings of the HYDRALAB+ Joint User Meeting*.

Ettema, R. (1976). *Influence of bed material gradation on local scour, Report No. 124*. University of Auckland, pp. 1–226.

Ettema, Robert (1980). *Scour at bridge piers*. University of Auckland, School of Engineering.

Ettema, Robert, George Constantinescu, and Bruce W. Melville (Sept. 2017). Flow-Field Complexity and Design Estimation of Pier-Scour Depth: Sixty Years since Laursen and Toch. In: *Journal of Hydraulic Engineering* 143 (9). ISSN: 0733-9429. DOI: 10.1061/(asce)hy.1943-7900.0001330.

Ettmer, Bernd et al. (2021). *DWA-M 529 Auskolkungen an pfahlartigen Bauwerksgründungen*. Deutsche Vereinigung für Wasserwirtschaft, Abwasser und Abfall e. V. (DWA). ISBN: 978-3-96862-067-1. URL: www.dwa.de.

Euler, Thomas and Jürgen Herget (2012). Controls on local scour and deposition induced by obstacles in fluvial environments. In: *Catena* 91, pp. 35–46. ISSN: 03418162. DOI: 10.1016/j.catena.2010.11.002.

Euler, Thomas and Jurgen Herget (2011). Obstacle-Reynolds-number based analysis of local scour at submerged cylinders. In: *Journal of Hydraulic Research* 49 (2), pp. 267–271. ISSN: 00221686. DOI: 10.1080/00221686.2010.547719.

Euler, Thomas et al. (2014). Influence of inclination and permeability of solitary woody riparian plants on local hydraulic and sedimentary processes. In: *Hydrological Processes* 28 (3), pp. 1358–1371. ISSN: 08856087. DOI: 10.1002/hyp.9655.

Euler, Thomas et al. (2017). Hydromorphological processes at submerged solitary boulder obstacles in streams. In: *Catena* 157, pp. 250–267. ISSN: 03418162. DOI: 10.1016/j.catena.2017.05.028.

Fage, A. and J. Warsap (1929). *The effects of turbulence and surface roughness on the drag of a circular cylinder*. Aeronaut. Res. Counc. London, Rep. and Memo. No. 1283.

Fausch, K. D. (1993). Experimental analysis of microhabitat selection by juvenile steelhead (Oncorhynchus mykiss) and coho salmon (O. kisutch) in a British Columbia stream. In: *Can J Fish Aquat Sci* 50, pp. 1198–1207. DOI: 10.1139/f93-136.

Fichtner, A. et al. (Aug. 2013). Crown size-growth relationships of European beech (Fagus sylvatica L.) are driven by the interplay of disturbance intensity and inter-specific competition. In: *Forest Ecology and Management* 302, pp. 178–184. ISSN: 03781127. DOI: 10.1016/j.foreco.2013.03.027.

Fisher, Andrew and Peter Klingeman (Aug. 1984). *Local scour at fish rocks*. In: *Water for Resource Development*. Ed. by David Schreiber. American Society of Civil Engineers, pp. 286–290.

Flachsbart, O. (1927). Neue Untersuchungen über den Luftwiderstand von Kugeln. In: *Physikalische Zeitschrift* 28 (13), pp. 461–469.

Flammer, G. H., J. P. Tullis, and E. S. Mason (1970). Free Surface Velocity Gradient Flow past Hemisphere. In: *Journal of the Hydraulics Division* 96 (HY7), pp. 1485–1502.

Flow Science, Inc. (2023). *FLOW-3D, Version 2022R2*. Santa Fe, NM. URL: https://www.flow3d.com/.

Franzetti, S., E. Larcan, and P. Mignosa (1982). *Influence of tests duration on the evaluation of ultimate scour around circular piers*. In: *International Conference on the Hydraulic Modelling of Civil Engineering Structures*, pp. 381–396. ISBN: 0906085756.

Friedrich, Heide et al. (Jan. 2022). Physical modelling of large wood (LW) processes relevant for river management: Perspectives from New Zealand and Switzerland. In: *Earth Surface Processes and Landforms* 47 (1), pp. 32–57. ISSN: 0197-9337. DOI: 10.1002/esp.5181.

Gabl, Roman et al. (Mar. 2014). Anregungen zur Qualitätssicherung in der 3-D-numerisches Modellierung mit FLOW-3D. In: *Wasserwirtschaft* 3, pp. 15–20.

Gebhardt, Michael et al. (June 2012). Backwater effects of Jambor weir sill. In: *Journal of Hydraulic Research* 50 (3), pp. 344–349. ISSN: 00221686. DOI: `10.1080/00221686.2012.686712`.

Gehrig, Wilhelm (1954). *Bewegung von festen Stoffen im fließenden Wasser*. Vol. 3. Bundesanstalt für Wasserbau, pp. 51–53. URL: `https://hdl.handle.net/20.500.11970/103223`.

Gerstmeier, R and T Romig (2003). *Die Süsswasserfische Europas, für Naturfreunde und Angler*. 2. Auflage. Franckh-Kosmos Verlags GmbH & Co.

Grimaldi, Carmelo et al. (2009). Countermeasures against Local Scouring at Bridge Piers: Slot and Combined System of Slot and Bed Sill. In: *Journal of Hydraulic Engineering* 135 (5), pp. 425–431. DOI: `10.1061/ASCEHY.1943-7900.0000035`.

Gromke, Christof (2009). *Einfluss von Bäumen auf die Durchlüftung von innerstädtischen Straßenschluchten*. Dissertation. Karlsruhe: Karlsruhe Institute of Technology. ISBN: 9783866443396.

— (2011). A vegetation modeling concept for building and environmental aerodynamics wind tunnel tests and its application in pollutant dispersion studies. In: *Environmental Pollution* 159 (8-9), pp. 2094–2099. ISSN: 02697491. DOI: `10.1016/j.envpol.2010.11.012`.

— (Sept. 2012). *Modeling vegetation in Wind Engineering wind tunnel studies*. In: *The Seventh International Colloquium on Bluff Body Aerodynamics and Applications*.

— (2018). Wind tunnel model of the forest and its Reynolds number sensitivity. In: *Journal of Wind Engineering and Industrial Aerodynamics* 175, pp. 53–64. ISSN: 01676105. DOI: `10.1016/j.jweia.2018.01.036`.

Gromke, Christof and Bodo Ruck (Aug. 2018). On Wind Forces in the Forest-Edge Region During Extreme-Gust Passages and Their Implications for Damage Patterns. In: *Boundary-Layer Meteorology* 168 (2), pp. 269–288. ISSN: 15731472. DOI: `10.1007/s10546-018-0348-4`.

Gründler, S and E Baier (2018). *Hintergrundinformationen zum Äschensterben am Hochrhein*. URL: `https://sfv-fsp.ch/fileadmin/user_upload/Herausforderungen/Klimaerwaermung/Dossiers/3_180806_DOSSIER_A__schensterben.pdf`.

Gründler, Sämi, Thomas Schläppi, and Sicher Philipp (2019). *Massnahmenkonzept Hitzesommer und Fischerei - Handbuch für Vereine und Angler*. URL: `https://sfv-fsp.ch/fileadmin/user_upload/Herausforderungen/Klimaerwaermung/Massnahmenkonzept/Massnahmenkonzept_Hitzesommer.pdf`.

Grunert, F., D. Benndorf, and K. Klingbeil (1984). Neuere Ergebnisse zum Aufbau von Schutzpflanzungen. In: *Beiträge zur Forstwirtschaft* 3, pp. 108–115.

Guan, D., B. Melville, and H. Friedrich (2015). Live-Bed Scour at Submerged Weirs. In: *Journal of Hydraulic Engineering* 141 (2). ISSN: 0733-9429. DOI: `10.1061/(asce)hy.1943-7900.0000954`.

Guan, Dawei, Bruce Melville, and Heide Friedrich (Mar. 2016). Local scour at submerged weirs in sand-bed channels. In: *Journal of Hydraulic Research* 54 (2), pp. 172–184. ISSN: 00221686. DOI: `10.1080/00221686.2015.1132275`.

Guan, Dawei, Bruce W. Melville, and Heide Friedrich (Jan. 2014). Flow Patterns and Turbulence Structures in a Scour Hole Downstream of a Submerged Weir. In: *Journal of Hydraulic Engineering* 140 (1), pp. 68–76. ISSN: 0733-9429. DOI: `10.1061/(asce)hy.1943-7900.0000803`.

Guan, Dawei et al. (Aug. 2019). Scour Evolution Downstream of Submerged Weirs in Clear Water Scour Conditions. In: *Water* 11 (9), p. 1746. ISSN: 2073-4441. DOI: `10.3390/w11091746`.

Guillén-Ludeña, S. et al. (Sept. 2017). Hydromorphodynamic effects of the width ratio and local tributary widening on discordant confluences. In: *Geomorphology* 293, pp. 289–304. ISSN: 0169555X. DOI: `10.1016/j.geomorph.2017.06.006`.

Haider, Rizwan et al. (2022). Flow Characteristics Around Permeable Spur Dike with Different Staggered Pores at Varying Angles. In: *Arabian Journal for Science and Engineering* 47 (4), pp. 5219–5236. ISSN: 21914281. DOI: `10.1007/s13369-021-06435-4`.

Harada, Morihiro et al. (2013). Characteristics of bed deformation around submerged groins with various angle. In: *Journal of Japan Society of Civil Engineers* 69 (4), pp. I1189–I1194. DOI: `10.2208/jscejhe.69.i_1189`.

Harvey, B. C. and A. J. Stewart (1991). Fish size and habitat depth relationships in headwater streams. In: *Oecologia* 87 (3), pp. 336–342. ISSN: 00298549. DOI: `10.1007/BF00634588`.

Hefti, Daniel (2012). *Wiederherstellung der Fischauf- und-abwanderung bei Wasserkraftwerken. Checkliste Best Practice*. Bundesamt für Umwelt, BAFU.

Heino, Jani and Kimmo T. Tolonen (Nov. 2017). Ecological drivers of multiple facets of beta diversity in a lentic macroinvertebrate metacommunity. In: *Limnology and Oceanography* 62 (6), pp. 2431–2444. ISSN: 19395590. DOI: `10.1002/lno.10577`.

Helfman, G. S. (1981). The advantage to fishes of hovering in shade. In: *Copeia*, pp. 392–400.

Henning, M. and R. Weichert (2020). Hydraulische Parameter von Schlitzpässen in Bemessung und Bestand. In: *BAWMitteilungen Nr. 106 - Hydraulik von Fischaufstiegsanlagen in Schlitzpassbauweise*. URL: `www.baw.de`.

Hentschel, Bernd, Martin Henning, and Thorsten Hüsener (2012). *Morphologie an Buhnenfeldern - Natur- und Laboruntersuchungen*. In: *Wasserbausymposium 2012, der TU München, der ETH Zürich und der TU Graz*. Technische Universität Graz, pp. 403–410. URL: `https://hdl.handle.net/20.500.11970/100817`.

Hockley, F A et al. (2014). Fish responses to flow velocity and turbulence in relation to size, sex and parasite load. In: *J. R. Soc. Interface* 11. DOI: `10.1098/rsif.2013.0814`.

Hoerner, S.F. (1965). *Fluid-Dynamic Drag- theoretical, experimental and statistical information*. published by the author.

Hoffmans, Gijsbertus J. and H. J. Verheij (1997). *Scour manual*. Ed. by H. J. Verheij. Balkema, p. 205. ISBN: 9054106735.

Huang, Cheng-Chang (Aug. 1991). *Local Scour at Isolated Obstacles on River Beds*. Dissertation. Oregon State University.

Ishigaki, Taisuke and Yasuyuki Baba (2004). *Local scour induced by 3D flow around attracting and deflecting groins*. In: *Proceedings of Second International Conference on Scour and Erosion*. Chiew, Yee-Meng; Lim, Siow-Yong; Cheng, Nian-Sheng.

Ismail, Hassan, Yuncheng Xu, and Xiaofeng Liu (Jan. 2021). Flow and Scour around Idealized Porous Engineered Log Jam Structures. In: *Journal of Hydraulic Engineering* 147 (1). ISSN: 0733-9429. DOI: `10.1061/(asce)hy.1943-7900.0001833`.

IUCN (2016). The IUCN Red List of Threatened Species. In: Version 2016-2. URL: `https://www.iucnredlist.org`.

Järvelä, Juha (June 2004). *Flow resistance in environmental channels : focus on vegetation*. Dissertation. Helsinki: Helsinki University of Technology.

Juez, Carmelo et al. (Nov. 2019). Floodplain Land Cover and Flow Hydrodynamic Control of Overbank Sedimentation in Compound Channel Flows. In: *Water Resources Research* 55 (11), pp. 9072–9091. ISSN: 0043-1397. DOI: `10.1029/2019WR024989`.

Kail, Jochem et al. (2007). The use of large wood in stream restoration: Experiences from 50 projects in Germany and Austria. In: *Journal of Applied Ecology* 44 (6), pp. 1145–1155. ISSN: 00218901. DOI: `10.1111/j.1365-2664.2007.01401.x`.

Kalogianni, Eleni et al. (2020). Wood availability and habitat heterogeneity drive spatiotemporal habitat use by riverine cyprinids under flow intermittence. In: *River Research and Applications* 36 (5), pp. 819–827. ISSN: 1535-1459. DOI: `10.1002/rra.3601`.

Kannen, C, F Seidel, and M J Franca (Nov. 2022). *Discussion of various equilibrium concepts on scouring around hydraulic structures*. In: *River Flow 2022, 11th International Conference on Fluvial Hydraulics*. In Press. CRC Press / Balkema.

Kannen, Christin, Frank Seidel, and Mário J. Franca (submitted in 2023). *Morphodynamics of ecological scours as deep pool habitat for adult barbels*. Manuscript submitted for publication in July 2023. Journal of Ecohydraulics.

Keller, Edward A (1971). Areal Sorting of Bed-Load Material: The Hypothesisof Velocity Reversal. In: *Geol. Soc. Am. Bull.* 82, pp. 753–756. DOI: `10.1130/0016-7606(1971)82[753:ASOBMT]2.0.CO;2`.

Keylock, C. J., G. Constantinescu, and R. J. Hardy (Dec. 2012). The application of computational fluid dynamics to natural river channels: Eddy resolving versus mean flow approaches. In: *Geomorphology* 179, pp. 1–20. ISSN: 0169555X. DOI: `10.1016/j.geomorph.2012.09.006`.

Keylock, Christopher J., Kyoungsik S. Chang, and George S. Constantinescu (Oct. 2016). Large eddy simulation of the velocity-intermittency structure for flow over a field of symmetric dunes. In: *Journal of Fluid Mechanics* 805, pp. 656–685. ISSN: 14697645. DOI: `10.1017/jfm.2016.519`.

Khosronejad, Ali, Seokkoo Kang, and Fotis Sotiropoulos (Mar. 2012). Experimental and computational investigation of local scour around bridge piers. In: *Advances in Water Resources* 37, pp. 73–85. ISSN: 03091708. DOI: `10.1016/j.advwatres.2011.09.013`.

Khosronejad, Ali et al. (2013). Computational and experimental investigation of scour past laboratory models of stream restoration rock structures. In: *Advances in Water Resources* 54, pp. 191–207. ISSN: 03091708. DOI: `10.1016/j.advwatres.2013.01.008`.

Kirkil, G., S. G. Constantinescu, and R. Ettema (May 2008). Coherent Structures in the Flow Field around a Circular Cylinder with Scour Hole. In: *JOURNAL OF HYDRAULIC ENGINEERING* 134 (5), pp. 572–587. DOI: `10.1061/(ASCE)0733-9429(2008)134:5(572)`.

Kitsikoudis, Vasileios et al. (2016). Experimental investigation of channel flow through idealized isolated tree-like vegetation. In: *Environmental Fluid Mechanics* 16 (6), pp. 1283–1308. ISSN: 15731510. DOI: 10.1007/s10652-016-9487-7.

Kolmogorov, A. N. (1941). The local structure of turbulence in incompressible viscous fluid for very large Reynolds numbers. In: *Dokl. Akad. Nauk SSSR* 30 (4).

Kothyari, Umesh C., Willi H. Hager, and Giuseppe Oliveto (Nov. 2007). Generalized Approach for Clear-Water Scour at Bridge Foundation Elements. In: *Journal of Hydraulic Engineering* 133 (11), pp. 1229–1240. ISSN: 0733-9429. DOI: 10.1061/(ASCE)0733-9429(2007)133:11(1229).

Kurdistani, Sahameddin Mahmoudi (2013). *Scour downstream of eco-friendly in-stream structures*. Dissertation. University of Pisa.

Kurylyk, Barret L. et al. (Sept. 2015). Preserving, augmenting, and creating cold-water thermal refugia in rivers: Concepts derived from research on the Miramichi River, New Brunswick (Canada). In: *Ecohydrology* 8 (6), pp. 1095–1108. ISSN: 19360592. DOI: 10.1002/eco.1566.

Labbe, Theodore R and Kurt D Fausch (2000). Dynamics of Intermittent Stream Habitat Regulate Persistence of a Threatened Fish at Multiple Scales. In: *Ecological Applications* 10 (6), pp. 1774–1791. DOI: 10.1890/1051-0761(2000)010[1774:DOISHR]2.0.CO;2.

Lacey, R. W. Jay and André G. Roy (July 2008). Fine-Scale Characterization of the Turbulent Shear Layer of an Instream Pebble Cluster. In: *Journal of Hydraulic Engineering* 134 (7), pp. 925–936. ISSN: 0733-9429. DOI: 10.1061/(ASCE)0733-9429(2008)134:7(925).

Lacey, R. W.Jay et al. (May 2012). The ipos framework: Linking fish swimming performance in altered flows from laboratory experiments to rivers. In: *River Research and Applications* 28 (4), pp. 429–443. ISSN: 15351459. DOI: 10.1002/rra.1584.

Lagasse, Peter F ; Lyle W ; Zevenbergen, and Paul E Clopper (Nov. 2010). *Impacts of Debris on Bridge Pier Scour*. In: *Proceedings 5th International Conference on Scour and Erosion (ICSE-5)*. Ed. by Susan E. Burns et al. American Society of Civil Engineers, pp. 854–863. URL: https://hdl.handle.net/20.500.11970/100218.

Lança, Rui, Cristina Fael, and António Cardoso (2010). *Assessing equilibrium clear water scour around single cylindrical piers*. In: *River Flow 2010*. Ed. by Dittrich et al., pp. 1207–1213. ISBN: 9783939230007.

Lança, Rui et al. (Oct. 2013). Clear-Water Scour at Pile Groups. In: *Journal of Hydraulic Engineering* 139 (10), pp. 1089–1098. ISSN: 0733-9429. DOI: 10.1061/(asce)hy.1943-7900.0000770.

Lane, Stuart N. and Keith S. Richards (1997). Linking river channel form and process: Time, space and causality revisited. In: *Earth Surface Processes and Landforms* 22 (3), pp. 249–260. ISSN: 01979337. DOI: 10.1002/(SICI)1096-9837(199703)22:3<249::AID-ESP752>3.0.CO;2-7.

Larinier, M. et al. (1999). *Passes à poissons : expertise, conception des ouvrages de franchissement*. La Documentation Française. ISBN: 2-11-088083-X.

Laursen, E.M. and A. Toch (1956). *Scour around bridge piers and abutments*. Iowa Highways Research Board, Ames, IA.

LAVES (2011). *Vollzugshinweise zum Schutz von Fischarten in Niedersachsen. – Fischarten des Anhangs II der FFH-Richtlinie und weitere Fischarten mit Priorität für Erhaltungs- und Entwicklungsmaß-nahmen – Barbe (Barbus barbus).* Niedersächsisches Landesamt für Verbraucherschutz und Lebensmittelsicherheit. URL: https://www.nlwkn.niedersac hsen.de/vollzugshinweise-arten-lebensraumtypen/vollzugshinweise-fuer-arten-und-lebensraumtypen-46103.html#fische.

Leibundgut et al. (2002). *Einzugsgebietsbezogene Bewertung der Abfluss- und Stoffdynamik als Grundlage eines Bewertungsverfahrens „Hydrologische Güte" zum operationellen Einsatz im nachhaltigen Flussgebietsmanagement.* Institut für Hydrologie der Universität Freiburg, p. 196.

Lelek, A and S Lusk (1965). Výskyt ryb v závislosti na utváření dna (Occurrence of fishes in relation to the bottom formation). In: *Zool. Listy (Folia Zoologica)* 14 (3), pp. 225–234.

LfU (2005). *Mindestabflüsse in Ausleitungsstrecken Grundlagen, Ermittlung und Beispiele.* 1. Auflage. Landesanstalt für Umweltschutz Baden-Württemberg (LfU). ISBN: 3882512970. URL: https://pudi.lubw.de/detailseite/-/publication/65530.

López, Fabián and Marcelo H. García (May 2001). Mean Flow and Turbulence Structure of Open-Channel Flow through Non-Emergent Vegetation. In: *Journal of Hydraulic Engineering* 127 (5), pp. 392–402. ISSN: 0733-9429. DOI: 10.1061/(ASCE)0733-9429(2001)127:5(392).

LUBW (2019). *Zu warm, zu heiß, zu trocken? - Eine klimatische Einordnung des Jahres 2018 für Baden-Württemberg.* URL: https://pudi.lubw.de/detailseite/-/publication/83210.

Lucas, Martyn C. and Emma Batley (Dec. 1996). Seasonal Movements and Behaviour of Adult Barbel Barbus barbus, a Riverine Cyprinid Fish: Implications for River Management. In: *The Journal of Applied Ecology* 33 (6), p. 1345. ISSN: 00218901. DOI: 10.2307/2404775.

Lupandin, A. I. (2005). Effect of Flow Turbulence on Swimming Speed of Fish. In: *Biology Bulletin* 32 (5), pp. 558–565. DOI: 10.1007/s10525-005-0125-z.

MacVicar, B. and A. Roy (Dec. 2007). Hydrodynamics of a forced riffle pool in a gravel bed river: 1. Mean velocity and turbulence intensity. In: *Water Resources Research* 43 (12). ISSN: 00431397. DOI: 10.1029/2006WR005272.

MacVicar, B. J. and A. G. Roy (2011). Sediment mobility in a forced riffle-pool. In: *Geomorphology* 125 (3), pp. 445–456. ISSN: 0169555X. DOI: 10.1016/j.geomorph.2010.10.031.

MacWilliams, Michael L. et al. (Oct. 2006). Flow convergence routing hypothesis for pool-riffle maintenance in alluvial rivers. In: *Water Resources Research* 42 (10). ISSN: 00431397. DOI: 10.1029/2005WR004391.

Magoulick, Daniel D. and Robert M. Kobza (July 2003). The role of refugia for fishes during drought: A review and synthesis. In: *Freshwater Biology* 48 (7), pp. 1186–1198. ISSN: 00465070. DOI: 10.1046/j.1365-2427.2003.01089.x.

Matthews, William J, Bret C Harvey, and Mary E Power (1994). Spatial and temporal patterns in the fish assemblages of individual pools in a midwestern stream (U.S.A.) In: *Environmental Biology of Fishes* 39, pp. 381–397. DOI: 10.1007/BF00004807.

Matthews, William J. (1998). *Patterns in Freshwater Fish Ecology*. Springer US. ISBN: 978-1-4613-6821-2. DOI: 10.1007/978-1-4615-4066-3.

Maza, Maria et al. (Nov. 2017). Velocity and Drag Evolution From the Leading Edge of a Model Mangrove Forest. In: *Journal of Geophysical Research: Oceans* 122 (11), pp. 9144–9159. ISSN: 21699291. DOI: 10.1002/2017JC012945.

McCoy, Andrew, George Constantinescu, and Larry Weber (May 2007). A numerical investigation of coherent structures and mass exchange processes in channel flow with two lateral submerged groynes. In: *Water Resources Research* 43 (5). ISSN: 00431397. DOI: 10.1029/2006WR005267.

McCrimmon, H. and W. Kwain (1966). Use of overhead cover by rainbow trout exposed to a series of light intensities. In: *Journal of the Fisheries Board of Canada* 23, pp. 983–990.

McIntosh, Bruce A. et al. (2000). Historical changes in pool habitats in the Columbia River Basin. In: *Ecological Applications* 10 (5), pp. 1478–1496. ISSN: 10510761. DOI: 10.1890/1051-0761(2000)010[1478:HCIPHI]2.0.CO;2.

McMahon, Thomas E. and Gordon F. Hartman (1989). Influence of cover complexity and current velocity on winter habitat use by juvenile coho salmon (Oncorhynchus kisutch). In: *Can J. Fish. Aqu. Sci* 46, pp. 1551–1557. DOI: 10.1139/f89-197.

Meftah, M and M Mossa (June 2004). *Experimental study of the scour hole downstream of bed sills*. In: *River Flow 2004*. CRC Press, pp. 585–592. DOI: 10.1201/b16998-76.

Meftah, Mouldi Ben and Michele Mossa (2006). Scour holes downstream of bed sills in low-gradient channels. In: *Journal of Hydraulic Research* 44 (4), pp. 497–509. DOI: 10.1080/00221686.2006.9521701.

Melcher, Andreas H. and Stefan Schmutz (May 2010). The importance of structural features for spawning habitat of nase Chondrostoma nasus (L.) and barbel Barbus barbus (L.) in a pre-Alpine river. In: *River Systems* 19 (1), pp. 33–42. DOI: 10.1127/1868-5749/2010/019-0033.

Melville, Bruce (2008). *The physics of local scour at bridge piers*. In: *Proceedings 4th International Conference on Scour and Erosion (ICSE-4)*. Ed. by H. Sekiguchi, pp. 28–40.

Melville, Bruce W and D M Dongol (1992). Bridge Pier Scour with Debris Accumulation. In: *Journal of Hydraulic Engineering* 118 (9), pp. 1306–1310. DOI: 10.1061/(ASCE)0733-9429(1992)118:8(1306).

Melville, Bruce W. and Yee-Meng Chiew (1999). Time Scale for Local Scour at Bridge Piers. In: *Journal of Hydraulic Engineering* 125 (1), pp. 59–65. ISSN: 0733-9429. DOI: 10.1061/(asce)0733-9429(1999)125:1(59).

Mende, Matthias (Jan. 2014). *Naturnaher Uferschutz mit Lenkbuhnen: Grundlagen, Analytik und Bemessung*. Dissertation. Technischen Universität Carolo-Wilhelmina zu Braunschweig.

Metashape, Agisoft (2020). *Agisoft Metashape*.

Monzyk, F. R., W. E. Kelso, and D. A. Rutherford (2003). *Fish Relationships with Large Wood in Small Streams*. In: *American Fisheries Society Symposium 37*, pp. 179–193.

Morgan, Jacob A., Daniel J. Brogan, and Peter A. Nelson (2016). Application of Structure-from-Motion photogrammetry in laboratory flumes. In: *Geomorphology* 276, pp. 125–143. ISSN: 0169555X. DOI: `10.1016/j.geomorph.2016.10.021`.

Morris, H. M. (1955). Flow in Rough Conduits. In: *Transactions Am. Soc. Civil Engr* 120, pp. 373–410.

Mostafa, Mona Mahmoud et al. (2013). *Experimental Study on Flow Characteristics around Single Groyne with Different Permeability in Compound Channel Floodplain*. URL: `https://www.researchgate.net/publication/258860702`.

Möws, R. and Ka Koll (2014). *Influence of a single submerged groyne on the bed morphology and the flow field*. In: *Proceedings of the International Conference on Fluvial Hydraulics, RIVER FLOW 2014*, pp. 1447–1454. ISBN: 9781138026742. DOI: `10.1201/b17133-193`.

Mueller, Peter and Helmut Kobus (1981). Hydraulische Entwurfs-und Bemessungskriterien für Sohlschwellen. In: *Wasserwirtschaft* 71, pp. 295–298. DOI: `10.18419/opus-566`.

Muhawenimana, V. et al. (Nov. 2019). Spanwise Cylinder Wake Hydrodynamics and Fish Behavior. In: *Water Resources Research* 55 (11), pp. 8569–8582. ISSN: 19447973. DOI: `10.1029/2018WR024217`.

Müller, A., F. Seidel, and F. Nestmann (2020). *The effect of micro groins on riverbed structures – Comparison of the velocity distribution in experiments with fixed and mobile bed*. In: *River Flow 2020 - Proceedings of the 10th Conference on Fluvial Hydraulics*, pp. 635–643. ISBN: 9780367627737. DOI: `10.1201/b22619-90`.

Musall, Mark (2011). *Mehrdimensionale hydrodynamisch-numerische Modelle im praxisorientierten und operationellen Einsatz*. Dissertation. Karlsruhe Institute of Technology. DOI: `10.5445/IR/1000028830`.

Nagayama, Shigeya and Futoshi Nakamura (2010). Fish habitat rehabilitation using wood in the world. In: *Landscape and Ecological Engineering* 6 (2), pp. 289–305. ISSN: 18601871. DOI: `10.1007/s11355-009-0092-5`.

Naudascher, Eduard (1992). *Hydraulik der Gerinne und Gerinnebauwerke*. Springer Vienna. ISBN: 978-3-211-82366-8. DOI: `10.1007/978-3-7091-9222-1`.

Nepf, H. M. (1999). Drag, turbulence, and diffusion in flow through emergent vegetation. In: *Water Resources Research* 35 (2), pp. 479–489. ISSN: 00431397. DOI: `10.1029/1998WR900069`.

Nickelson, T. E. et al. (1992). Effectiveness of selected stream improvement techniques to create suitable summer and winter rearing habitat for juvenile coho salmon (Oncorhynchus kisutch) in Oregon coastal streams. In: *Can J Fish Aquat Sci* 49, pp. 790–794. DOI: `10.1139/f92-088`.

Nicolle, A. and I. Eames (2011). Numerical study of flow through and around a circular array of cylinders. In: *Journal of Fluid Mechanics* 679, pp. 1–31. ISSN: 14697645. DOI: `10.1017/jfm.2011.77`.

Nikuradse, J. (1932). Gesetzmässigkeiten der turbulenten Strömungen in glatten Rohren. In: *Forschungsheft* 356.

Oak, Ashutosh G. (May 1992). *Backwater rise due to a submerged spur*. Dissertation. University of Saskatchewan. URL: `http://hdl.handle.net/10388/etd-01312011-131519`.

Okhravi, Saeid et al. (Mar. 2022). Effects of bed-material gradation on clear water scour at single and group of piles. In: *Journal of Hydrology and Hydromechanics* 70 (1), pp. 114–127. ISSN: 13384333. DOI: 10.2478/johh-2021-0036.

Oliveto, Giuseppe and Willi H. Hager (2002). Temporal Evolution of Clear-Water Pier and Abutment Scour. In: *Journal of Hydraulic Engineering* 128 (9), pp. 811–820. ISSN: 0733-9429. DOI: 10.1061/(asce)0733-9429(2002)128:9(811).

Ovidio, Michaël et al. (2007). Multiyear homing and fidelity to residence areas by individual barbel (Barbus barbus). In: *Belg. J. Zool* 137 (2), pp. 183–190. URL: https://hdl.handle.net/2268/5847.

Pagliara, S. and I. Carnacina (Apr. 2013). *Bridge pier flow field in the presence of debris accumulation.* In: *Proceedings of the Institution of Civil Engineers: Water Management.* Vol. 166, pp. 187–198. DOI: 10.1680/wama.11.00060.

Pagliara, St. and Io. Carnacina (2011a). Influence of Wood Debris Accumulation on Bridge Pier Scour. In: *Journal of Hydraulic Engineering* 137 (2), pp. 254–261. DOI: 10.1061/ASCEHY.1943-7900.0000289.

Pagliara, Stefano and Iacopo Carnacina (2011b). Influence of large woody debris on sediment scour at bridge piers. In: *International Journal of Sediment Research* 26 (2), pp. 121–136. DOI: 10.1016/S1001-6279(11)60081-4.

Pagliara, Stefano, Leila Hassanabadi, and Sahameddin Mahmoudi Kurdistani (2015). Clear Water Scour Downstream of Log Deflectors in Horizontal Channels. In: *Journal of Irrigation and Drainage Engineering* 141 (9), pp. 04015007-1–8. ISSN: 0733-9437. DOI: 10.1061/(asce)ir.1943-4774.0000869.

Pagliara, Stefano and Sahameddin Mahmoudi Kurdistani (2013). Scour downstream of cross-vane structures. In: *Journal of Hydro-environment Research* 7, pp. 236–242. DOI: 10.1016/j.jher.2013.02.002.

Panchan, Ruamruedee et al. (Nov. 2022). Seasonal migration and habitat use of adult barbel (Barbus barbus) and nase (Chondrostoma nasus) along a river stretch of the Austrian Danube River. In: *Environmental Biology of Fishes* 105 (11), pp. 1601–1616. ISSN: 15735133. DOI: 10.1007/s10641-022-01352-3.

Pavlov, D. S., A. I. Lupandin, and M. A. Skorobogatov (2000). The effects of flow turbulence on the behaviour and distribution of fish. In: *. Journal of Ichthyology* 40 (S2), pp. 232–261.

Pelz, G and A Kästle (1989). Ortsbewegungen der Barbe Barbus barbus (L.) - radiotelemetrische Standortbestimmungen in der Nidda (Frankfurt/Main). In: *Fischökologie* 1, pp. 15–28.

Peňáz, Milan et al. (2002). Movements of barbel, Barbus barbus (Pisces: Cyprinidae). In: *Folia Zoologica* 51 (1), pp. 55–66.

Pope, Stephen B. (2011). *Turbulent flows.* 1. publ., 9. print. Cambridge: Cambridge Univ. Press,

Pouilly, M. and Y. Souchon (1994). Physical habitat simulation of barbel (Barbus barbus, L. 1758): Selection of biological models based on predictability criteria. In: *Bulletin Francais de la Peche et de la Pisciculture* (334), pp. 213–225. ISSN: 07672861. DOI: 10.1051/kmae:1994023.

Przybilla, Anja et al. (Sept. 2010). Entraining in trout: A behavioural and hydrodynamic analysis. In: *Journal of Experimental Biology* 213 (17), pp. 2976–2986. ISSN: 00220949. DOI: 10.1242/jeb.041632.

Rahimi, Ebrahim et al. (Apr. 2018). Effect of Debris on Piers Group Scour: An Experimental Study. In: *KSCE Journal of Civil Engineering* 22 (4), pp. 1496–1505. ISSN: 19763808. DOI: 10.1007/s12205-017-2002-y.

Rashak, Budoor M. and Saleh I. Khassaf (2020). Study the local scour around different shapes of single submerged groyne. In: *Journal of Water and Land Development* 47 (1), pp. 1–9. ISSN: 20834535. DOI: 10.24425/jwld.2020.135025.

Raudkivi, Arved J. (1986). Functional trends of scour at bridge piers. In: *Journal of Hydraulic Engineering* 112 (1), pp. 1–13. ISSN: 19437900. DOI: 10.1061/(ASCE)0733-9429(1986)112:1(1).

Raudkivi, Arved J. and Robert Ettema (1983). Clear-water scour at cylindrical piers. In: *Journal of Hydraulic Engineering* 109 (3), pp. 338–350. ISSN: 19437900. DOI: 10.1061/(ASCE)0733-9429(1983)109:3(338).

Ricardo, Ana M., Mário J. Franca, and Rui M. L. Ferreira (2016). Turbulent Flows within Random Arrays of Rigid and Emergent Cylinders with Varying Distribution. In: *Journal of Hydraulic Engineering* 142 (9). ISSN: 0733-9429. DOI: 10.1061/(ASCE)HY.1943-7900.0001151.

Roberson, J. A. and C. T. Crowe (1993). *Engineering Fluid Mechanics*. 5 th. Houghton-Miffin.

Roberts, M, M Promny, and S Vollmers (2014). *Klimaprojektionen für Sedimenthaushalt und Flussbettentwicklung. Schlussbericht KLIWAS-Projekt 4.02. KLIWAS-44/2014.* BfG. DOI: 10.5675/Kliwas_44/2014_4.02.

Schalko, I. et al. (June 2019). Laboratory Flume Experiments on the Formation of Spanwise Large Wood Accumulations: I. Effect on Backwater Rise. In: *Water Resources Research* 55 (6), pp. 4854–4870. ISSN: 19447973. DOI: 10.1029/2018WR024649.

Schalko, Isabella et al. (Sept. 2018). Backwater Rise due to Large Wood Accumulations. In: *Journal of Hydraulic Engineering* 144 (9). ISSN: 0733-9429. DOI: 10.1061/(asce)hy.1943-7900.0001501.

Schlichting, Herrmann and Klaus Gersten (2000). *Boundary-Layer Theory*. Springer Berlin Heidelberg. ISBN: 978-3-642-85831-4. DOI: 10.1007/978-3-642-85829-1.

Schmitz, Friedrich et al. (2016). *Ergebnisse der Bundeswaldinventur 2012*. Bundesministeriumfür Ernährung und Landwirtschaft (BMEL).

Schnauder, Ingo, Christine Anlanger, and Katinka Koll (Mar. 2022). Wake flow patterns and turbulence around naturally deposited and installed trees in a gravel bed river. In: *International Review of Hydrobiology* 107 (1-2), pp. 22–33. ISSN: 1434-2944. DOI: 10.1002/iroh.202102096.

Scurlock, S. Michael, Christopher I. Thornton, and Steven R. Abt (Feb. 2012). Equilibrium Scour Downstream of Three-Dimensional Grade-Control Structures. In: *Journal of Hydraulic Engineering* 138, pp. 167–176. ISSN: 0733-9429. DOI: 10.1061/(asce)hy.1943-7900.0000493.

Seehorn, Monte (1992). *Stream habitat improvement handbook*. USDA Forest Service Southern Region.

Seifert, Kurt (2016). *Praxishandbuch Fischaufstiegsanlagen in Bayern - Hinweise und Empfehlungen zu Planung, Bau und Betrieb*. 2nd ed. Landesfischereiverband Bayern e.V., Bayerisches Landesamt für Umwelt.

Seitz, Lydia (2020). *Development of new methods to apply a multiparameter approach-a first step towards the determination of colmation*. Dissertation. Universität Stuttgart. DOI: 10.18419/opus-11249.

Shamloo, Hamid (1997). *Hydraulics of Simple Habitat Structures in Open Channels*. Dissertation. University of Alberta.

Sheppard, D., M. Odeh, and T Glasser (2004). Large Scale Clear-Water Local Pier Scour Experiments. In: *Journal of Hydraulic Engineering* 130 (10), pp. 957–963. ISSN: 07339429. DOI: 10.1061/(ASCE)0733-9429(2004)130:10(957).

Silva, Ana T. et al. (Mar. 2011). Effects of water velocity and turbulence on the behaviour of Iberian barbel (Luciobarbus bocagei, Steindachner 1864) in an experimental pool-type fishway. In: *River Research and Applications* 27 (3), pp. 360–373. ISSN: 15351459. DOI: 10.1002/rra.1363.

Smagorinsky, Joseph (1963). General circulation experiments with the primitive equations. In: *Monthly Weather. Review* 91 (3), pp. 99–164.

Smith, D. L., E. L. Brannon, and M. Odeh (2005). Response of juvenile rainbow trout to turbulence produced by prismatoidal shapes. In: *Transactions of the American Fisheries Society*, pp. 741–753. DOI: 10.1577/T04-069.1.

Sokoray-Varga, B. and R. Weichert (2020). Analyse turbulenter Strömungsprozesse in Schlitzpässen aus Sicht der Fischpassage. In: *BAWMitteilungen Nr. 106 - Hydraulik von Fischaufstiegsanlagen in Schlitzpassbauweise*. URL: www.baw.de.

Solazzi, M F et al. (2000). Effects of increasing winter rearing habitat on abundance of salmonids in two coastal Oregon streams. In: *Can. J. Fish. Aquat. Sci* 57, pp. 906–914. DOI: 10.1139/f00-030.

Steinmann, P, W Koch, and L Scheuring (1937). Die Wanderungen unserer Süsswasserfische, dargestellt auf Grund von Markierungsversuchen. In: *Z. Fischerei* 35, pp. 369–467.

Stoesser, T., W. Rodi, and G. Jirka (2004). *Large-Eddy Simulations of Flow over Rough Channel Beds*. In: *Soil and Bed Stability - Interaction Effects between Geotechnics and Hydraulic Engineering*. Bundesanstalt für Wasserbau. URL: https://hdl.handle.net/20.500.11970/102176.

Sukhodolov, Alexander, Wim S.J. Uijttewaal, and Christof Engelhardt (Mar. 2002). On the correspondence between morphological and hydrodynamical patterns of groyne fields. In: *Earth Surface Processes and Landforms* 27, pp. 289–305. ISSN: 01979337. DOI: 10.1002/esp.319.

Sundbaum, Karl and Ingemar Näslund (1998). Effects of woody debris on the growth and behaviour of brown trout in experimental stream channels. In: *Canadian Journal of Zoology* 76 (1), pp. 56–61. ISSN: 0008-4301. DOI: 10.1139/z97-174.

Suribabu, C R et al. (2011). Backwater Rise and Drag Characteristics of Bridge Piers under Sub-critical Flow Conditions. In: *European Water* 36, pp. 27–35. URL: `https://www.ewra.net/ew/pdf/EW_2011_36_03.pdf`.

Thompson, Douglas M. (2018). *Pool–Riffle Sequences*. Elsevier. DOI: `10.1016/b978-0-12-409548-9.11029-2`.

Trinci, Giuditta et al. (May 2017). Life in turbulent flows: interactions between hydrodynamics and aquatic organisms in rivers. In: *WIREs Water* 4 (3). ISSN: 2049-1948. DOI: `10.1002/wat2.1213`.

Trinci, Giuditta et al. (Jan. 2023). Turbulence signatures of natural river morphology in four dimensions. In: *River Research and Applications* 39 (1), pp. 122–133. ISSN: 15351467. DOI: `10.1002/rra.4071`.

Tritico, H M, A J Cotel, and J N Clarke (Aug. 2007). Development, testing and demonstration of a portable submersible miniature particle imaging velocimetry device. In: *Measurement Science and Technology* 18 (8), pp. 2555–2562. ISSN: 0957-0233. DOI: `10.1088/0957-0233/18/8/031`.

Tritico, H. M. and A. J. Cotel (July 2010). The effects of turbulent eddies on the stability and critical swimming speed of creek chub (Semotilus atromaculatus). In: *Journal of Experimental Biology* 213 (13), pp. 2284–2293. ISSN: 00220949. DOI: `10.1242/jeb.041806`.

Tritico, Hans M. and Rollin H. Hotchkiss (Aug. 2005). Unobstructed and Obstructed Turbulent Flow in Gravel Bed Rivers. In: *Journal of Hydraulic Engineering* 131 (8), pp. 635–645. ISSN: 0733-9429. DOI: `10.1061/(ASCE)0733-9429(2005)131:8(635)`.

Tuomisto, Hanna (Feb. 2010). A diversity of beta diversities: Straightening up a concept gone awry. Part 1. Defining beta diversity as a function of alpha and gamma diversity. In: *Ecography* 33 (1), pp. 2–22. ISSN: 09067590. DOI: `10.1111/j.1600-0587.2009.05880.x`.

Umeda, Shinya, Tatsuo Yamazaki, and Hajime Ishida (Nov. 2008). *Time Evolution of Scour and Deposition Around a Cylindrical Pier in Steady Flow*. In: *Proceeding 4th International Conference on Scour and Erosion (ICSE-4)*. Ed. by Hideo Sekiguchi. The Japanese Geotechnical Society, pp. 140–146. URL: `https://hdl.handle.net/20.500.11970/100107`.

Umweltbundesamt (2016). *Gewässertypen Deutschlands, LAWA-Fließgewässertypen, Bewirtschaftungskarte: Fließgewässertypenkarte*. URL: `https://gewaesser-bewertung.de/files/typenkarte_fliessgewaesser_bewirtschaftungskarte_april2016.pdf`.

Valdimarsson, S. K. and N. B. Metcalfe (1998). Shelter selection in juvenile Atlantic salmon, or why do salmon seek shelter in winter? In: *Journal of Fish Biology* 52, pp. 42–49. DOI: `10.1111/j.1095-8649.1998.tb01551.x`.

Vardakas, Leonidas et al. (Dec. 2017). Defining critical habitat conditions for the conservation of three endemic and endangered cyprinids in a Mediterranean intermittent river before the onset of drought. In: *Aquatic Conservation: Marine and Freshwater Ecosystems* 27 (6), pp. 1270–1280. ISSN: 10990755. DOI: `10.1002/aqc.2735`.

Venditti, Jeremy G. et al. (Sept. 2014). Flow in bedrock canyons. In: *Nature* 513 (7519), pp. 534–537. ISSN: 14764687. DOI: `10.1038/nature13779`.

Ventres-Pake, Roby et al. (2020). Integrating Large Wood Jams into Hydraulic Models: Evaluating a Porous Plate Modeling Method. In: *Journal of the American Water Resources Association* 56 (2), pp. 333–347. ISSN: 17521688. DOI: 10.1111/1752-1688.12818.

Vitale Gewässer (Oct. 2021). *Vitale Gewässer in Baden-Württemberg: Bausteckbrief 2 - Fischunterstand im Vorland in Restriktionsstrecken*. Ed. by LUBW Landesanstalt für Umwelt Baden-Württemberg WBW Fortbildungsgesellschaft für Gewässerentwicklung mbH. URL: https://pd.lubw.de/10266.

Wang, Lu, Bruce W. Melville, and Dawei Guan (Mar. 2018). Effects of Upstream Weir Slope on Local Scour at Submerged Weirs. In: *Journal of Hydraulic Engineering* 144 (3). ISSN: 0733-9429. DOI: 10.1061/(asce)hy.1943-7900.0001431.

Wang, Lu et al. (Aug. 2018). Local Scour at Downstream Sloped Submerged Weirs. In: *Journal of Hydraulic Engineering* 144 (8). ISSN: 0733-9429. DOI: 10.1061/(asce)hy.1943-7900.0001492.

Wang, Lu et al. (Dec. 2019). Scour Estimation Downstream of Submerged Weirs. In: *Journal of Hydraulic Engineering* 145 (12). ISSN: 0733-9429. DOI: 10.1061/(ASCE)HY.1943-7900.0001654.

Watkins, M. S., S. Doherty, and G. H. Copp (May 1997). Microhabitat use by 0+ and older fishes in a small English chalk stream. In: *Journal of Fish Biology* 50 (5), pp. 1010–1024. ISSN: 0022-1112. DOI: 10.1111/j.1095-8649.1997.tb01626.x.

Weichert, Roman (2006). *Bed morpholgy and stability of steep open channels*. Dissertation. Versuchsanstalt für Wasserbau, Hydrologie und Glaziologie der Eidgenössischen Technischen Hochschule Zürich.

Weitbrecht, Volker (Feb. 2004). *Influence of dead-water zones on the dispersive mass-transport in rivers*. Dissertation. Karlsruhe Institute of Technology. ISBN: 3937300074.

WFD (2014). *The EU Water Framework Directive*. DOI: doi/10.2779/75229.

White, C. M., V. S. R. Somandepalli, and M. G. Mungal (Jan. 2004). The turbulence structure of drag-reduced boundary layer flow. In: *Experiments in Fluids* 36 (1), pp. 62–69. ISSN: 0723-4864. DOI: 10.1007/s00348-003-0630-0.

Whittaker, R. H. (July 1960). Vegetation of the Siskiyou Mountains, Oregon and California. In: *Ecological Monographs* 30 (3), pp. 279–338. ISSN: 0012-9615. DOI: 10.2307/1943563.

Wohl, Ellen (2019). Forgotten Legacies: Understanding and Mitigating Historical Human Alterations of River Corridors. In: *Water Resources Research* 55 (7), pp. 5181–5201. ISSN: 19447973. DOI: 10.1029/2018WR024433.

Wohl, Ellen et al. (Apr. 2019). The natural wood regime in rivers. In: *BioScience* 69 (4), pp. 259–273. ISSN: 15253244. DOI: 10.1093/biosci/biz013.

Wright, Justin P. and Alexander S. Flecker (2004). Deforesting the riverscape: The effects of wood on fish diversity in a Venezuelan piedmont stream. In: *Biological Conservation* 120 (3), pp. 439–447. ISSN: 00063207. DOI: 10.1016/j.biocon.2004.02.022.

Wu, S. and N. Rajaratnam (July 1996). Submerged Flow Regimes of Rectangular Sharp-Crested Weirs. In: *Journal of Hydraulic Engineering* 122 (7), pp. 412–414. DOI: 10.1061/(ASCE)0733-9429(1996)122:7(412).

Wunder, Sina, Boris Lehmann, and Franz Nestmann (2011). Determination of the drag coefficients of emergent and just submerged willows. In: *International Journal of River Basin Management* 9 (3-4), pp. 231–236. ISSN: 18142060. DOI: 10.1080/15715124.2011.637 499.

Yagci, Oral et al. (2016). Scour patterns around isolated vegetation elements. In: *Advances in Water Resources* 97, pp. 251–265. ISSN: 03091708. DOI: 10.1016/j.advwatres.201 6.10.002.

Yagci, Oral et al. (Oct. 2017). Clear water scour around a finite array of cylinders. In: *Applied Ocean Research* 68, pp. 114–129. ISSN: 01411187. DOI: 10.1016/j.apor.2017.08.014.

Yarnell, David (Nov. 1934). *Bridge Piers as Channel Obstructions*. United States Department of Agriculture. DOI: 10.22004/ag.econ.164465.

Yeo, Hong Koo et al. (2006). Variations of Flow Thalweg Alignment and Separation Region around a Groyne. In: *Journal of Korea Water Resources Association* 39 (4), pp. 313–320. DOI: 10.3741/JKWRA.2006.39.4.313.

Zanke, U. (1982). *Grundlagen der Sedimentbewegung : mit 13 Tabellen.* XII. Springer, 402 S.

Zeng, Jie and George Constantinescu (June 2017). Flow and coherent structures around circular cylinders in shallow water. In: *Physics of Fluids* 29 (6). ISSN: 10897666. DOI: 10.1063/1.4984926.

Zevenbergen, Lyle W. et al. (2006). *Effects of Debris on Bridge Pier Scour*. In: *Proceedings 3rd International Conference on Scour and Erosion (ICSE-3)*. Ed. by H.J. Verheij and Gijs J. Hoffmans. CURNET, pp. 741–749. URL: https://hdl.handle.net/20.500.11970/1 00091.

Zhang, Hao and Hajime Nakagawa (2009). *Characteristics of local flow and bed deformation at impermeable and permeable spur dykes*. DOI: 10.2208/jscejam.69.I_489.

Zhang, Nuosha, Ian Rutherfurd, and Marco Ghisalberti (2020). Effect of instream logs on bank erosion potential: a flume study with a single log. In: *Journal of Ecohydraulics* 5 (1), pp. 43–56. ISSN: 24705365. DOI: 10.1080/24705357.2019.1634499.

Zika, Ulrike and Armin Peter (2002). The introduction of woody debris into a channelized stream: Effect on trout populations and habitat. In: *River Research and Applications* 18 (4), pp. 355–366. ISSN: 15351459. DOI: 10.1002/rra.677.

Zong, Lijun and Heidi Nepf (2012). Vortex development behind a finite porous obstruction in a channel. In: *Journal of Fluid Mechanics* 691, pp. 368–391. ISSN: 14697645. DOI: 10.1017/jfm.2011.479.

Zscheischler, Jakob et al. (June 2020). A typology of compound weather and climate events. In: *Nature Reviews Earth & Environment* 1 (7), pp. 333–347. ISSN: 2662-138X. DOI: 10.1038/s43017-020-0060-z.

List of Figures

List of Tables

Appendix A

Programs and tools

A.1   Data Analysis

- MATLAB R2019b

- Python with the numpy and scipy libraries

- ArcGis Desktop 10.6.

- Autodesk AutoCAD 2019

- CloudCompare 2.12.4

- Agisoft Metashape 2020

A.2   Numerical simulation

- FLOW-3D® HYDRO (Version 2022R2; 2022; https://www.flow3d.com; Flow Science, Inc.)

- FLOW-3D® POST 22.1.0.

A.3   Graphics and illustrations

- Corel Draw Graphics Suite 2019

- Mindjet MindManager 2019

A.4   Textediting

- ChatGPT, Version 3.5. https://chat.openai.com/

- DeepL

Appendix B

Additional data

B.1 Hydromorphology: Idealized Structures
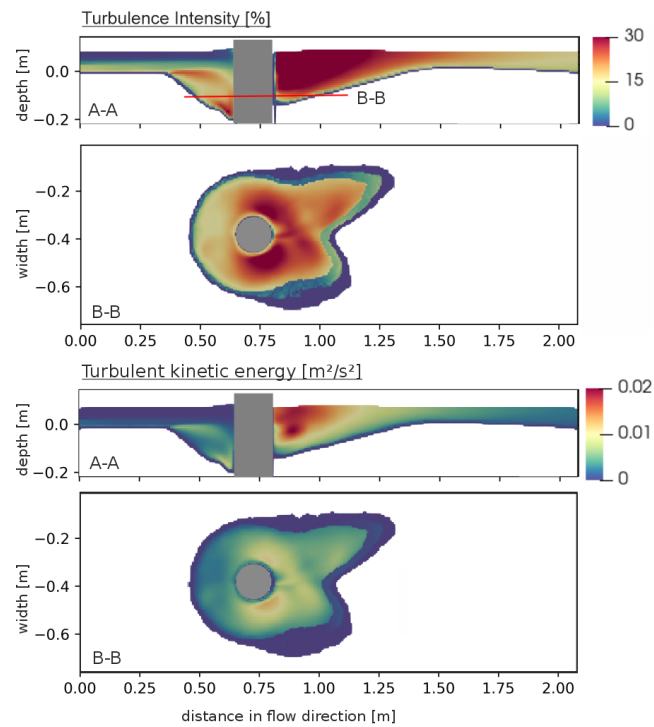
Figure B.1: Turbulence intensity and turbulent kinetic energy for y = 0.39 m (A-A) and z = 0.08 m (B-B) around the CP.
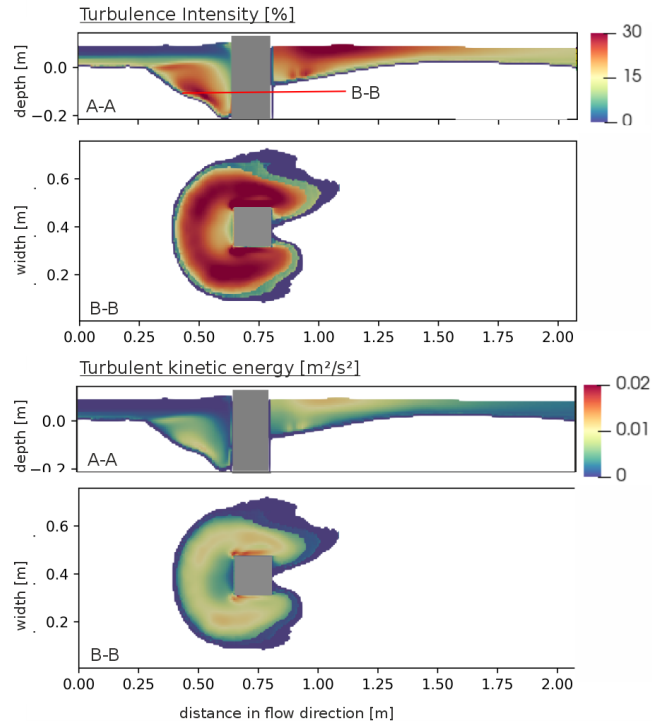
Figure B.2: Turbulence intensity and turbulent kinetic energy for y = 0.39 m (A-A) and z = 0.08 m (B-B) around the RP.
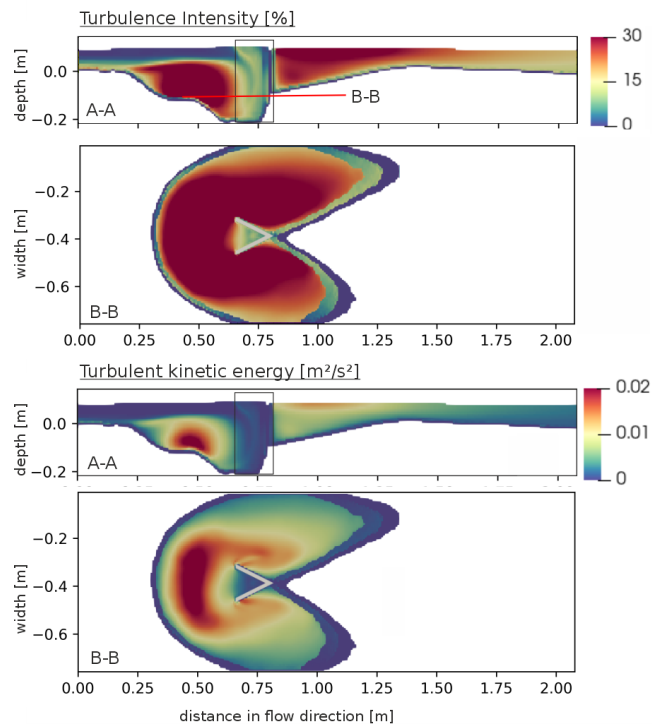
Figure B.3: Turbulence intensity and turbulent kinetic energy for y = 0.39 m (A-A) and z = 0.08 m (B-B) around the TP.
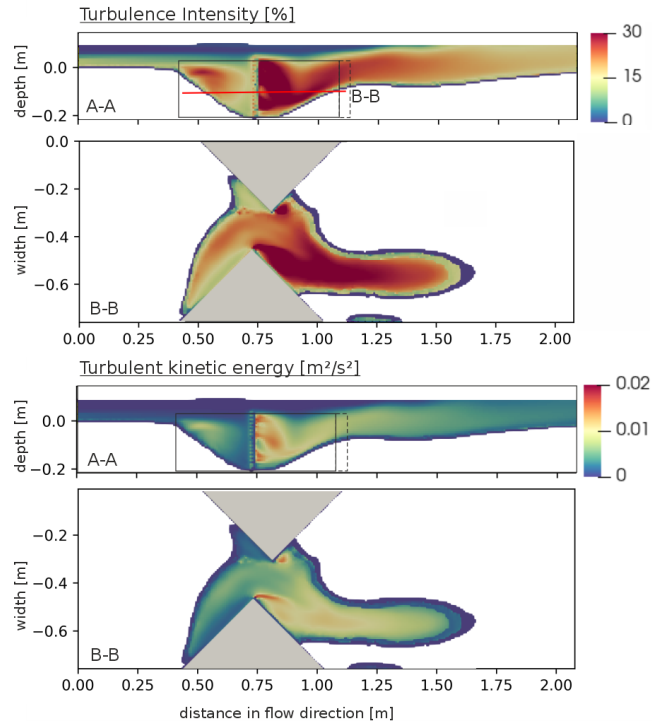
Figure B.4: Turbulence intensity and turbulent kinetic energy for y = 0.39 m (A-A) and z = 0.08 m (B-B) around the DWD.
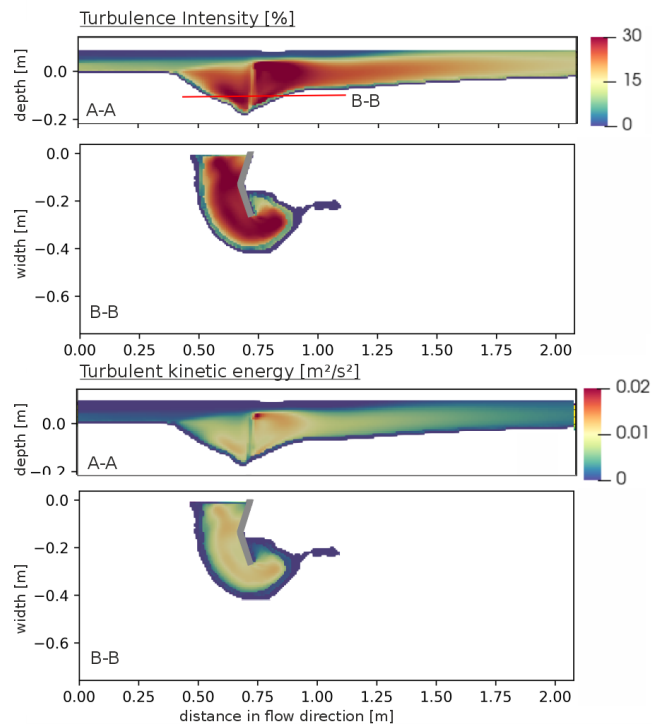
Figure B.5: Turbulence intensity and turbulent kinetic energy for y = 0.39 m (A-A) and z = 0.08 m (B-B) around the DG.
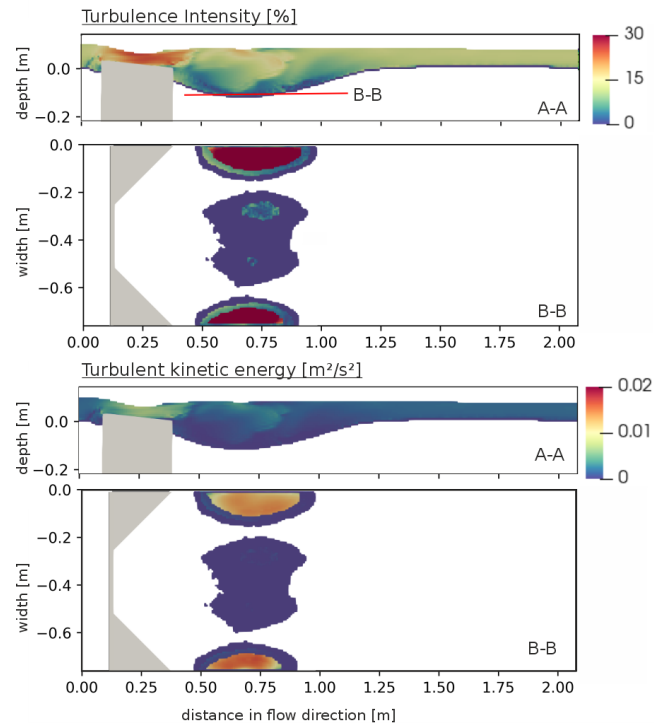
Figure B.6: Turbulence intensity and turbulent kinetic energy for y = 0.39 m (A-A) and z = 0.08 m (B-B) around the Kdam.

B.2 Hydromorphology: Natural materials, debris and shelter

B.2.1 Influence of Natural Materials

Influence of Porosity

Table B.1: Scour dimensions (scour depth d_s, length of scour hole l_{ds}, distance of dune l_{dune} of different structures for different porosities (SVF) of the TP.

			d_s	l_{ds}	l_{dune}
Source	structure type	porosity	d_s/D	x/D	x/D
Linear Structures					
Zhang and Nakagawa (2009)	groyne	nonporous	-1,2	-3	2
		SVF = 0.5	-0,4	-0,6	1
own study	DG	nonporous	-1	-3	6
	TP	nonporous	>-1	-3	∼3
		SVF = 1.00	>-1	-3	∼3
		SVF = 0.49	0	0	1
		SVF = 0.30	0	0	1
ausgefüllte structures					
Ismail, Xu and Liu (2021)	rectangular pier	nonporous	-1	-2	3
		SVF = 0.29	-0,5	-1	2

269

Influence of Surface Roughness
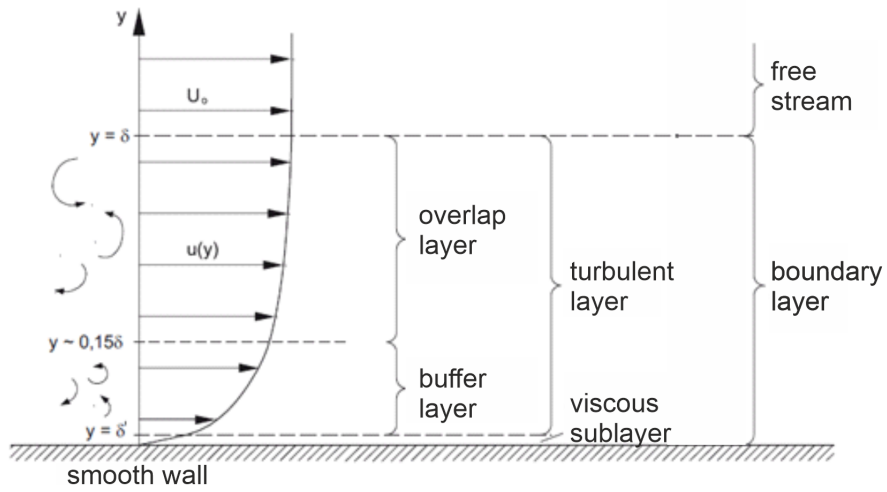
	zone	law	validity range
law-of-the-wall	viscous sublayer	$\frac{u}{u_*} = \frac{y}{l_v}$	$0 < \frac{y}{l_v} < 5$
	buffer zone		$5 < \frac{y}{l_v} < 30$
	inner turbulent zone	$\frac{u}{u_*} = 2.5ln\frac{y}{l_v} + 5.5$	$30 < \frac{y}{l_v} < 500$
outer zone	outer turbulent zone	$\frac{U_o-u}{u_*} = -2.5ln\frac{y}{\delta} + 2.75cos^2\left(\frac{\pi y}{2\delta}\right)$	$\frac{y}{l_v} > 500$ $0.15 < \frac{y}{\delta} < 1$

Figure B.7: Boundary layer zones, velocity laws and respective validity ranges.

B.2.2   Influence of Debris
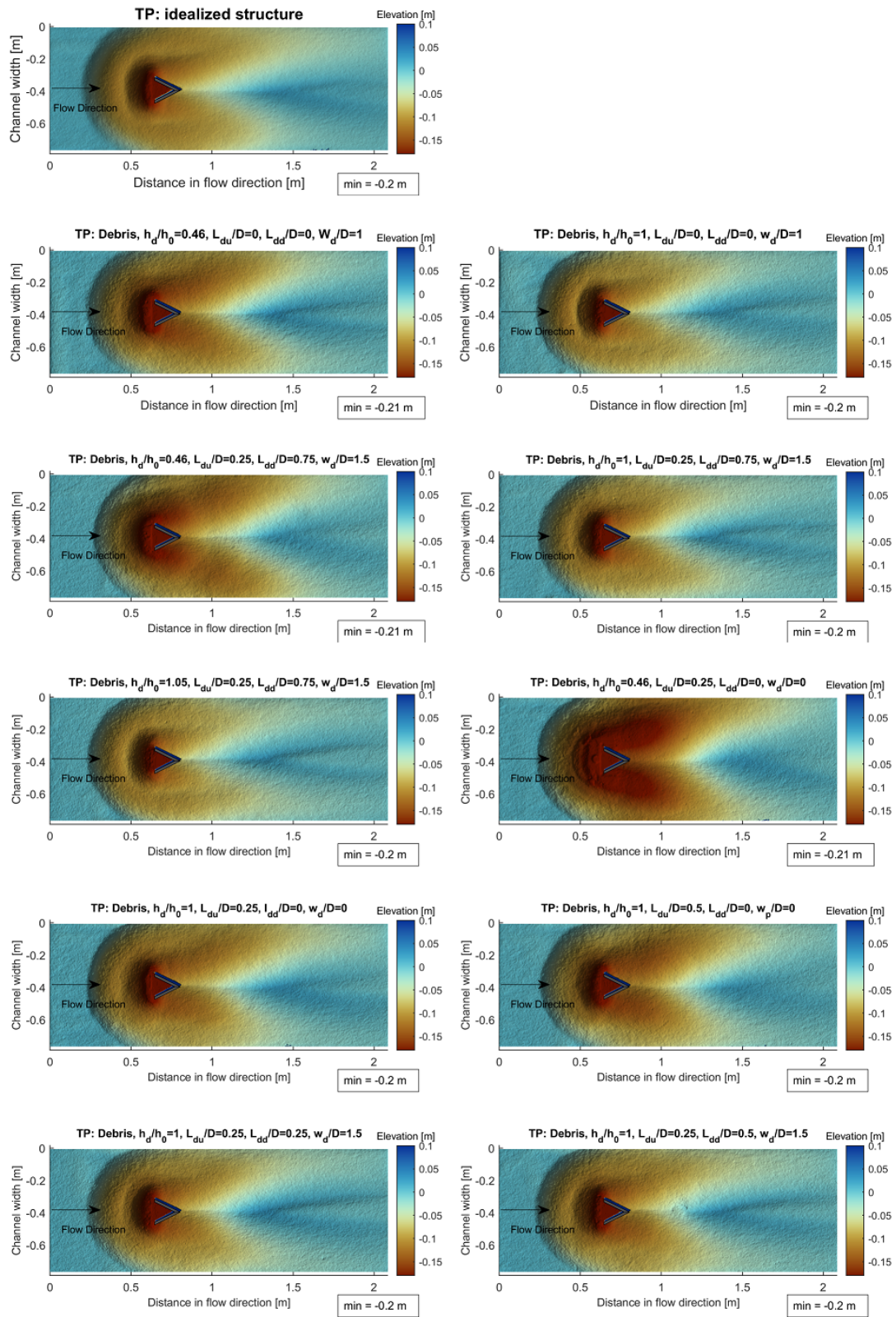
Figure B.8: Equilibrium bed morphologies for different dimensions and arrangements of debris around a TP.
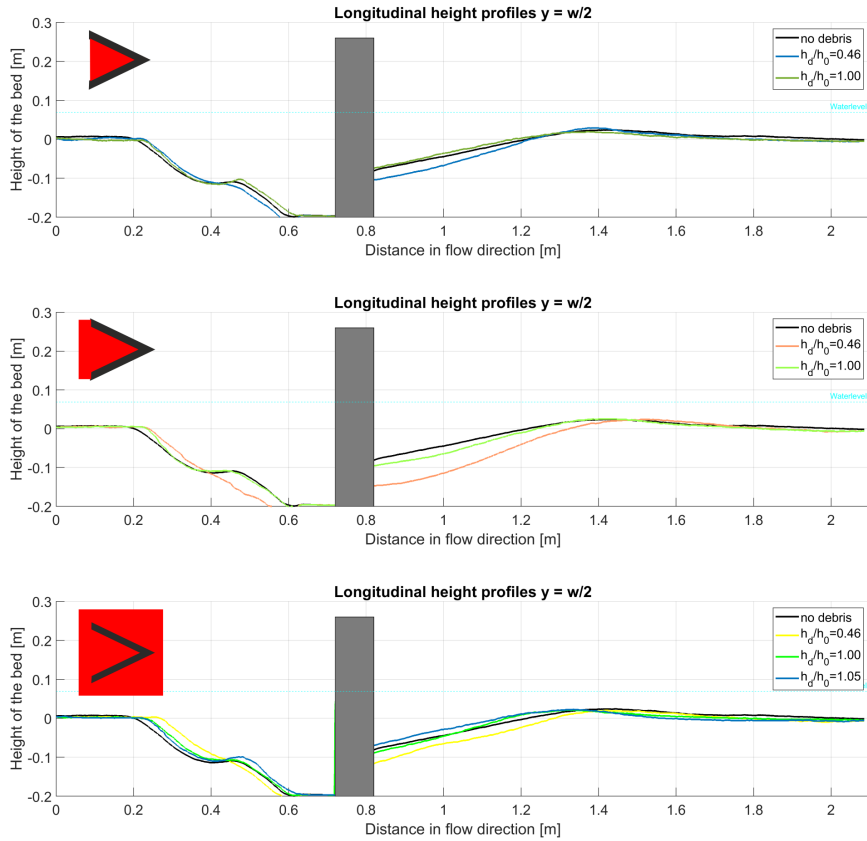
Figure B.9: Longitudinal heightprofiles along the center line of the flume for an idealized TP with and without debris accumulation for submergence levels of h_d/h_0 = 0.46 and 1.00 for different debris dimensions.
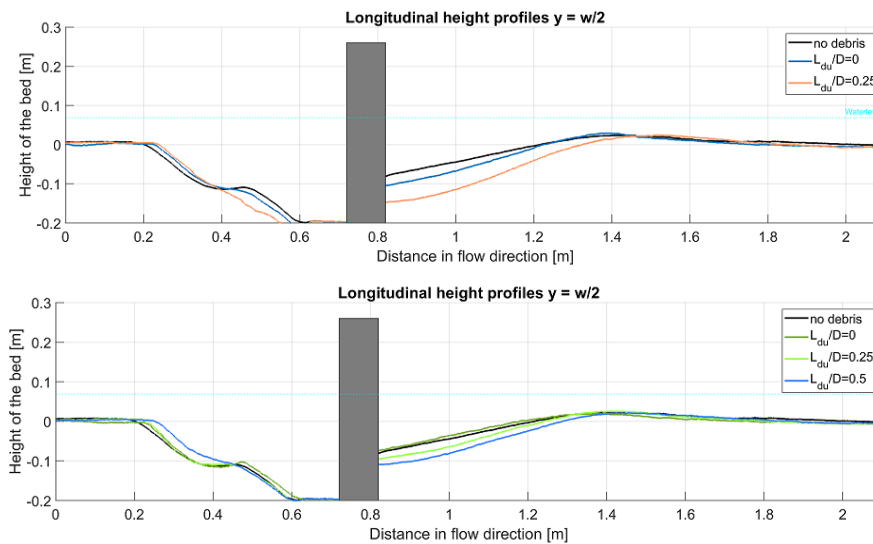
Figure B.10: Longitudinal heightprofiles along the center line of the flume for an idealized TP with and without debris accumulation for different upstream lengths L_{du}.
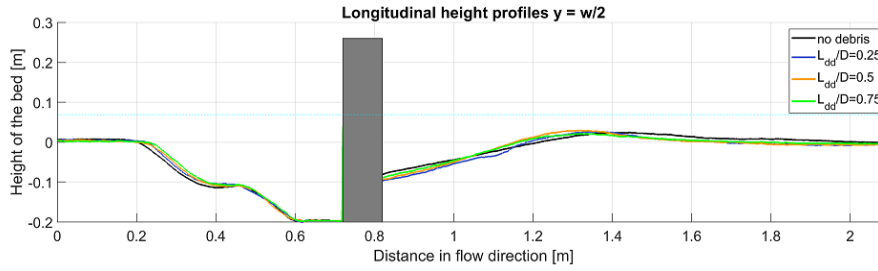
Figure B.11: Longitudinal heightprofiles along the center line of the flume for an idealized TP with and without debris accumulation for different downstream lengths L_{dd}.

B.2.3 Influence of Shelters

Table B.2: Dimensions of a median beech tree (*Fagus sylvatica*) according to Fichtner et al. (2013)

	Natural beech tree	Model beech tree (1:25)
Tree age	122 years	
stem diameter	0.5 m	2 cm
height	33 m	132 cm
radius tree crown	5 m	20 cm
length tree crown	14 m	56 cm
position tree crown	19 m	76 cm
surface tree crown	370 m²	5920 cm²
projected surface tree crown	112 m²	1792 cm²
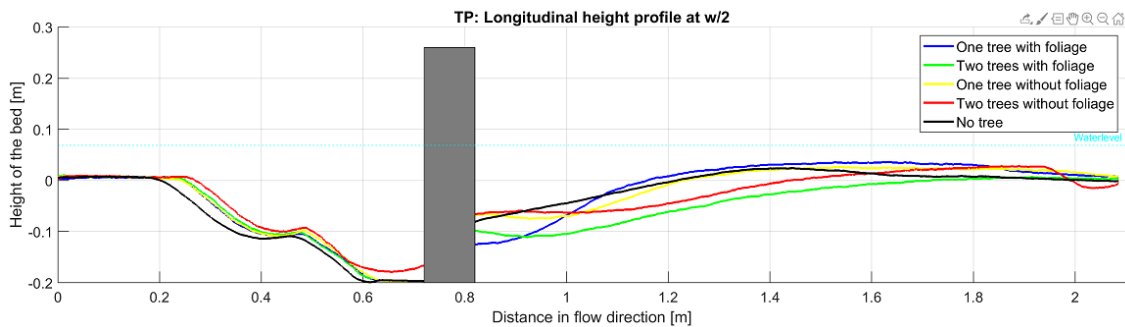
Figure B.12: Longitudinal height profiles of a pier-like structure (TP) with different variations of tree-like shelters in comparison with the case without a shelter in the centre line of the flume.
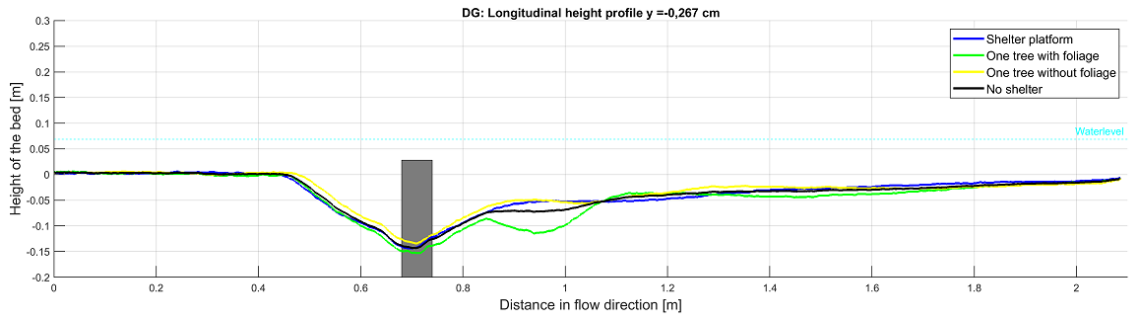
Figure B.13: Longitudinal height profiles of a stone-like structure (DG) with different variations of shelters in comparison with the case without a shelter in the centre line of the flume.

B.3 Hydromorphological evaluation of the structures

B.3.1 Influence of edge design
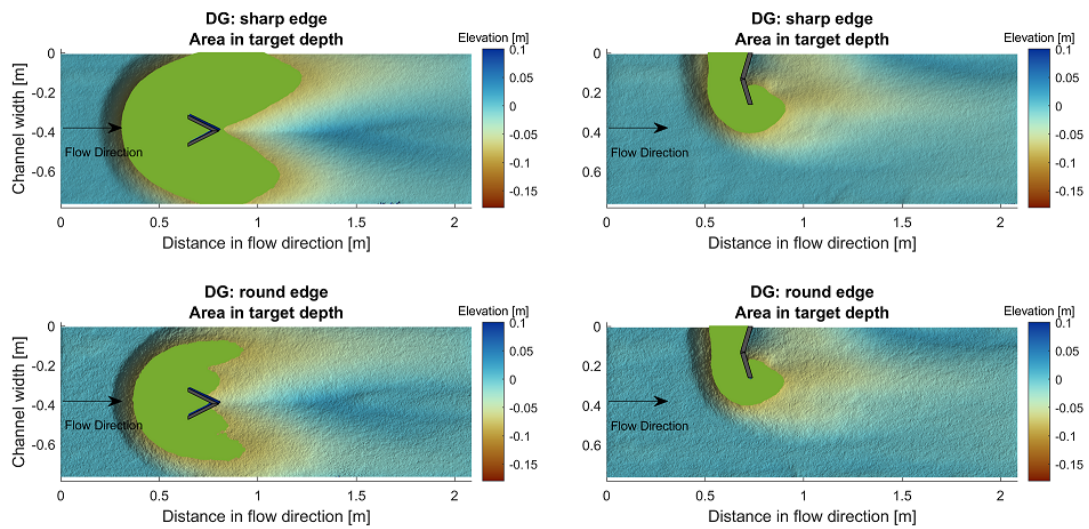
Figure B.14: Distribution of the area of the scour in the target depth of 8 cm for different edge designs, which is considered a suitable depth for a deep pool habitat, according to the application of LSGÖ guidelines and when reduced to the physical model scale. This means the indicated areas (in green) are possible suitable habitats if the flow field is suitable accordingly.

Table B.3: Area at elevation zero A_0, area at the target depth of 8 cm in model and in natural scale $A_{target\ model/nature}$, relative and volume below target depth in model and in natural scale $V_{target\ model/nature}$, and total volume of the scour below an elevation of zero V_{tot} for different edge designs of the TP and the DG.

	TP Sharp edge	TP Round edge	DG Sharp edge	DG Round edge
$A_{target\ model}$ [m²]	0.47	0.23	0.10	0.09
A_0 [m²]	1.19	1.18	1.02	0.99
A_{target}/A_0 [-]	0.40	0.19	0.0944	0.0891
$A_{target\ nature}$ [m²]	295		60	
$V_{target\ model}$ [m³]	0.0158	0.0055	0.0042	0.0039
V_{tot} [m³]	0.0818	0.0614	0.0386	0.0374
V_{target}/V_{tot} [-]	0.19	0.09	0.11	0.10
$V_{target\ nature}$ [m³]	247		67	
theoretical quantitative habitat potential (No of fish)	37050		10050	
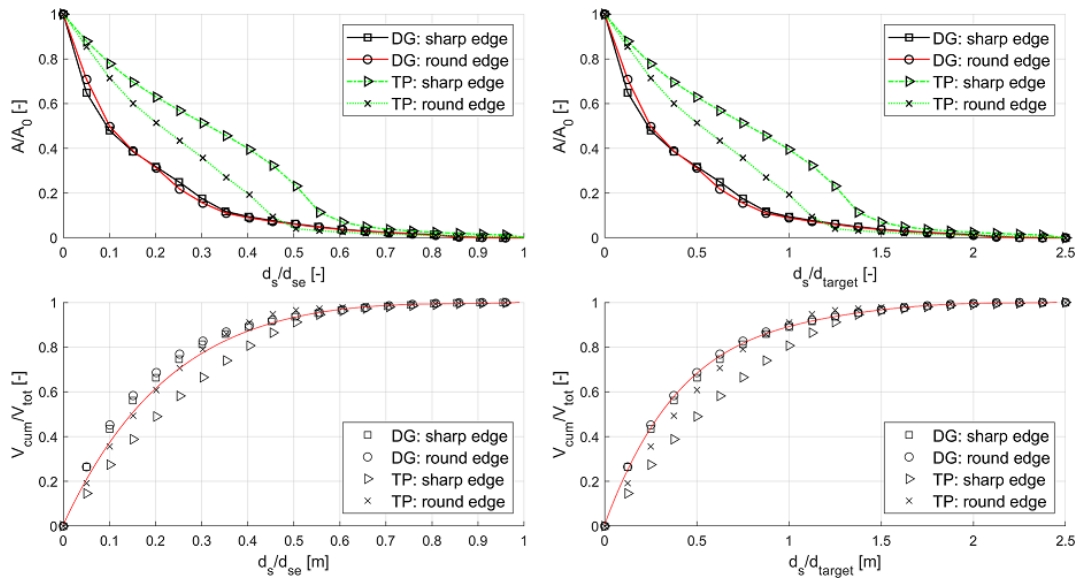
Figure B.15: a) Relative area A/A0 over relative scour depth ds/dse, b) relative area A/A_0 over relative scour depth d_s/d_{target}, c) relative volume V_{cum}/V_{tot} over relative scour depth d_s/d_{se}, d) relative volume V_{cum}/V_{tot} over relative scour depth d_s/d_{target} for different edge designs of the TP and DG.

B.3.2   Influence of surface roughness
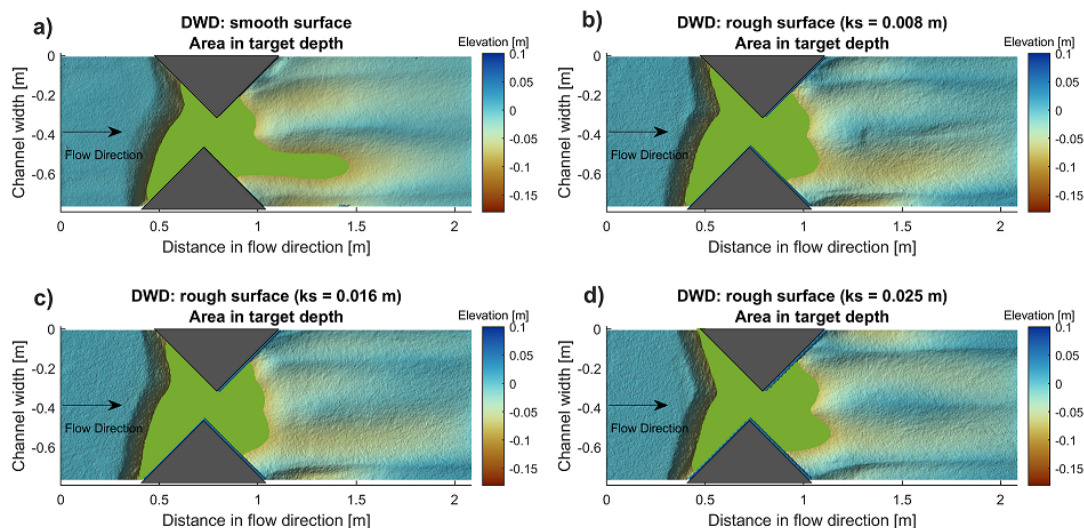
Figure B.16: Distribution of the area of the scour in the target depth of 8 cm for different surface roughnesses, which is considered a suitable depth for a deep pool habitat, according to the application of LSGÖ guidelines and when reduced to the physical model scale. This means the indicated areas (in green) are possible suitable habitats if the flow field is suitable accordingly.

Table B.4: Area at elevation zero A_0, area at the target depth of 8 cm in model and in natural scale $A_{target\ model/nature}$, relative and volume below target depth in model and in natural scale$V_{target\ model/nature}$, and total volume of the scour below an elevation of zero V_{tot} for different surface roughnesses.

	DWD	DWD	DWD	DWD
Version	smooth	Rough $k_s = 8\ mm$	Rough $k_s = 16\ mm$	Rough $k_s = 25\ mm$
$A_{target\ model}$ [m²]	0.21	0.2	0.2	0.21
A_0 [m²]	1.10	1.04	1.05	1.04
A_{target}/A_0 [-]	0.19	0.19	0.19	0.2
$A_{target\ nature}$ [m²]	130	125	125	131
$V_{target\ model}$ [m³]	0.0087	0.0113	0.0122	0.0117
V_{tot} [m³]	0.0588	0.056	0.0567	0.0555
V_{target}/V_{tot} [-]	0.15	0.2	0.22	0.21
$V_{target\ nature}$ [m³]	136	177	191	183
theoretical quantitative habitat potential (No of fish)	20400	26484	28594	27422
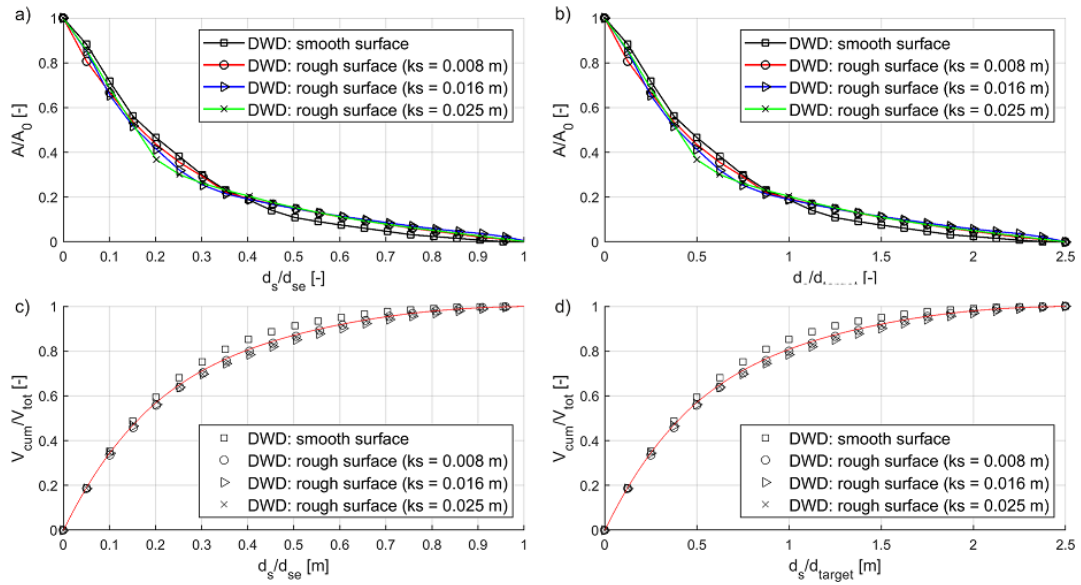
Figure B.17: a) Relative area A/A_0 over relative scour depth d_s/d_{se}, b) relative area A/A_0 over relative scour depth d_s/d_{target}, c) relative volume V_{cum}/V_{tot} over relative scour depth d_s/d_{se}, d) relative volume V_{cum}/V_{tot} over relative scour depth d_s/d_{target} for different surface roughnesses.

B.3.3   Influence of porosity
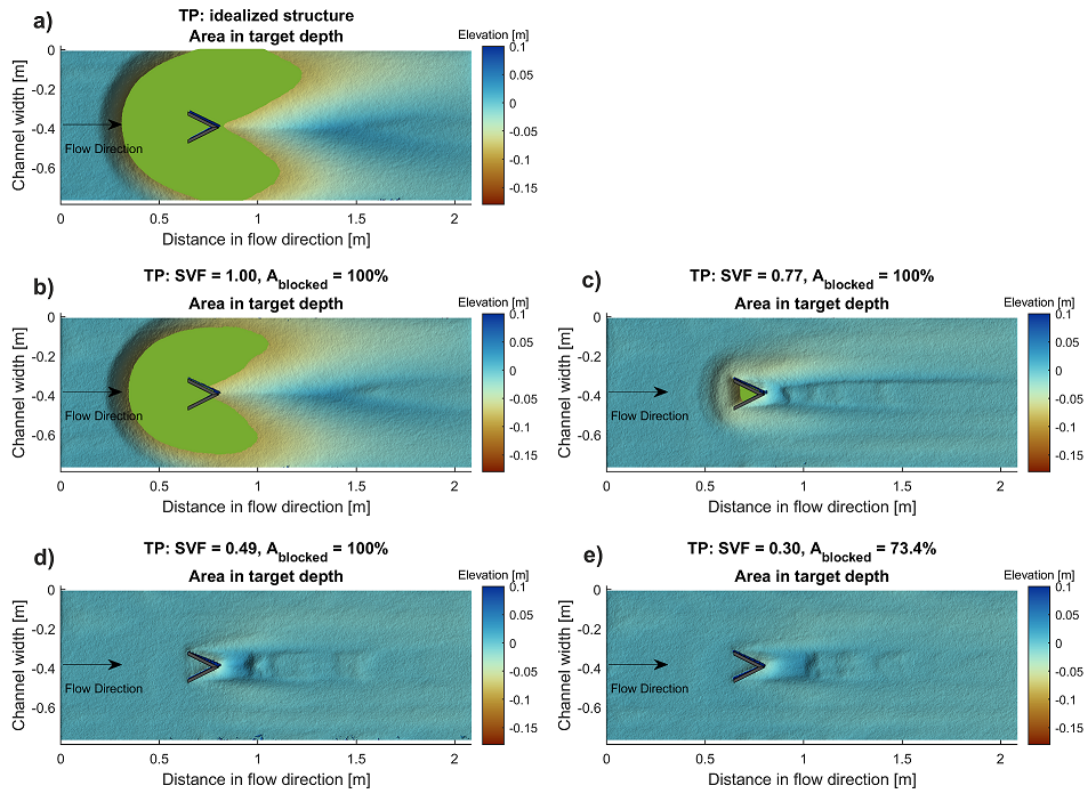
Figure B.18: Distribution of the area of the scour in the target depth of 8 cm for different porosities, which is considered a suitable depth for a deep pool habitat, according to the application of LSGÖ guidelines and when reduced to the physical model scale. This means the indicated areas (in green) are possible suitable habitats if the flow field is suitable accordingly.

Table B.5: Area at elevation zero A_0, area at the target depth of 8 cm in model and in natural scale $A_{target\ model/nature}$, relative and volume below target depth in model and in natural scale$V_{target\ model/nature}$, and total volume of the scour below an elevation of zero V_{tot} for different porosities of the TP.

	TP	TP	TP	TP
Version	idealized structure	SVF = 1.00	SVF = 0.77	SVF = 0.49
$A_{target\ model}$ [m²]	0.47	0.31	0.004	0
A_0 [m²]	1.19	1.23	1.08	0.99
A_{target}/A_0 [-]	0.4	0.25	0.0044	0
$A_{target\ nature}$ [m²]	295	194	3	0
$V_{target\ model}$ [m³]	0.0158	0.0079	0	0
V_{tot} [m³]	0.0818	0.0676	0.0171	0.0555
V_{target}/V_{tot} [-]	0.19	0.12	0.0046	0.21
$V_{target\ nature}$ [m³]	247	123	1	183
theoretical quantitative habitat potential (No of fish)	37050	18516	184	27422
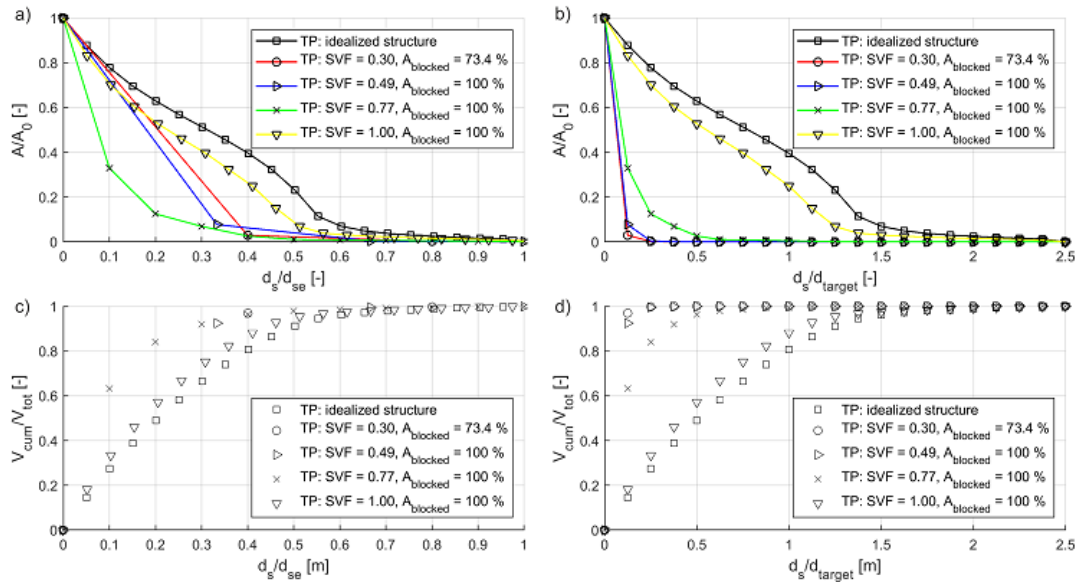
Figure B.19: a) Relative area A/A_0 over relative scour depth d_s/d_{se}, b) relative area A/A_0 over relative scour depth d_s/d_{target}, c) relative volume V_{cum}/V_{tot} over relative scour depth d_s/d_{se}, d) relative volume V_{cum}/V_{tot} over relative scour depth d_s/d_{target} for different porosities of the TP.

B.3.4   Influence of coverage and shelter
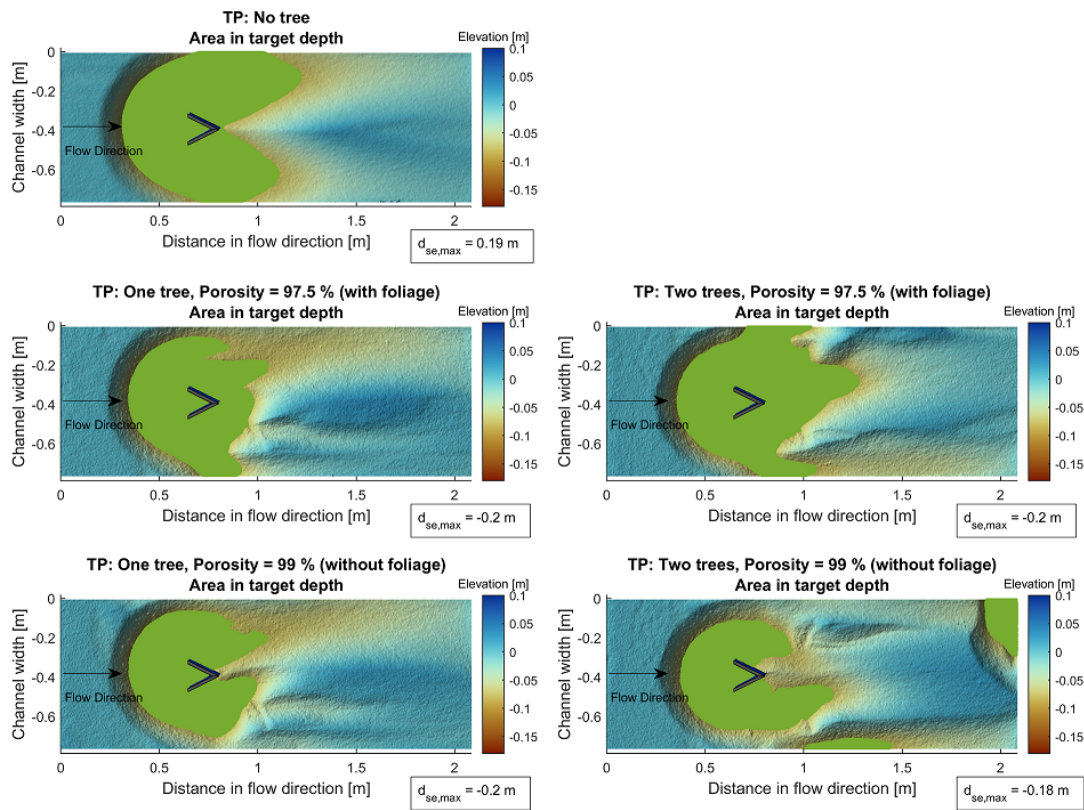
Figure B.20: Influence of different tree-like shelters on the distribution of suitable area in target depth around the pier-like deep pool habitat structure (TP).
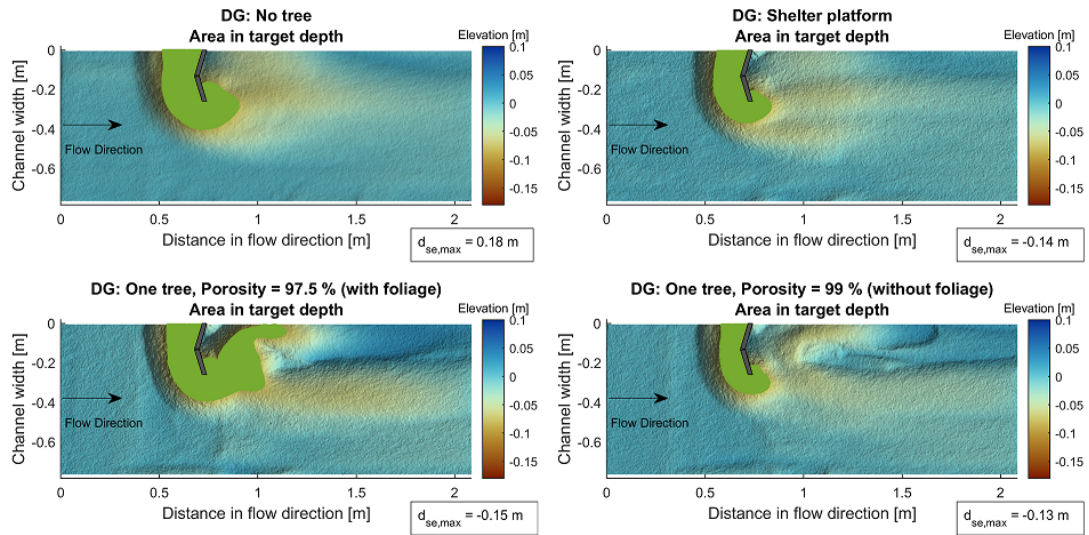
Figure B.21: Influence of different tree- and platform-like shelters on the distribution of suitable area in target depth around the stone-like deep pool habitat structure (DG).
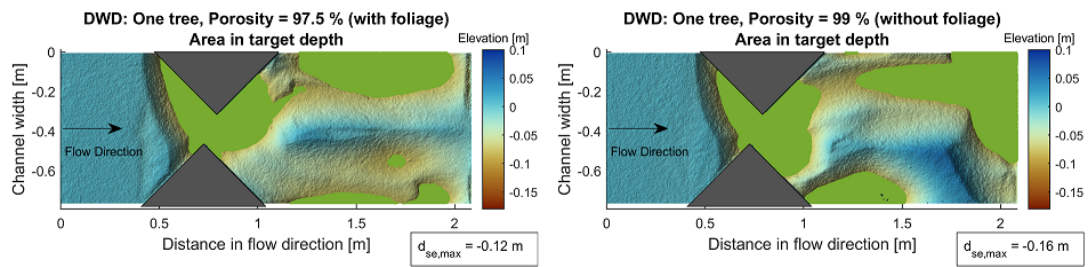
Figure B.22: Influence of different tree-like shelters on the distribution of suitable area in target depth around the stone-like deep pool habitat structure (DWD).

Table B.6: Area at elevation zero A_0, area at the target depth of 8 cm in model and in natural scale $A_{targetmodel/nature}$, relative and volume below target depth in model and in natural scale $V_{targetmodel/nature}$, and total volume of the scour below an elevation of zero V_0 for different shelters.

(a) Pier-like structure TP

	TP				
Version	No tree	One tree	Two trees	One tree	Two trees
Foliage status	none	With	With	Without	Without
$A_{targetmodel}$ [m²]	0.47	0.33	0.42	0.29	0.32
A_0 [m²]	1.19	1.03	1.19	1.06	1.1
A_{target}/A_0 [-]	0.40	0.32	0.35	0.28	0.29
$A_{targetnature}$ [m²]	295	206	263	181	200
$V_{targetmodel}$ [m³]	0.0158	0.0122	0.0148	0.0095	0.0088
V_{tot} [m³]	0.0818	0.0689	0.0769	0.0660	0.0679
V_{target}/V_{tot}	0.19	0.18	0.19	0.14	0.13
$V_{targetnature}$ [m³]	247	191	231	148	138
theoretical quantitative habitat potential (No of fish)	37050	28594	34688	22266	20625

(b) Stone-like structure DG

	DG			
Version	No shelter	platform	One tree	One tree
Foliage status	none	none	With	Without
$A_{targetmodel}$ [m²]	0.10	0.063	0.1385	0.05
A_0 [m²]	1.02	1.02	1.1	0.9797
A_{target}/A_0 [-]	0.0944	0.0619	0.1255	0.0511
$A_{targetnature}$ [m²]	60	39	87	31
$V_{targetmodel}$ [m³]	0.0042	0.0025	0.0048	0.0018
V_{tot} [m³]	0.0386	0.0326	0.0449	0.0322
V_{target}/V_{tot}	0.11	0.0771	0.1073	0.0558
$V_{targetnature}$ [m³]	67	39	75	28
theoretical quantitative habitat potential (No of fish)	10050	5859	11250	4219

(c) Stone-like structure DWD

	DWD		
Version	No tree	One tree	One tree
Foliage status		With	Without
$A_{targetmodel}$ [m²]	0.21	0.33	0.41
A_0 [m²]	1.10	1.05	0.93
A_{target}/A_0 [-]	0.19	0.31	0.44
$A_{targetnature}$ [m²]	130	206	256
$V_{targetmodel}$ [m³]	0.0087	0.0143	0.0194
V_{tot} [m³]	0.0588	0.0766	0.0775
V_{target}/V_{tot}	0.15	0.19	0.25
$V_{targetnature}$ [m³]	136	223	303
theoretical quantitative habitat potential (No of fish)	20400	33516	45469
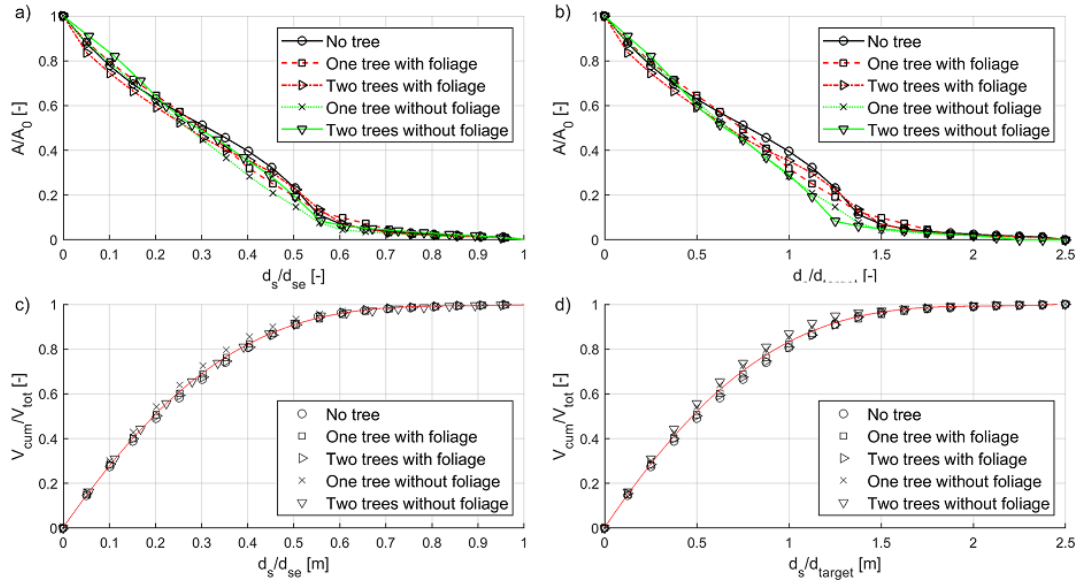
Figure B.23: Comparison of the pier-like structure TP for different tree-like shelters with a shelter-less case for a) Relative area A/A_0 over relative scour depth d_s/d_{se}, b) relative area A/A_0 over relative scour depth d_s/d_{target}, c) relative volume V_{cum}/V_{tot} over relative scour depth d_s/d_{se}, d) relative volume V_{cum}/V_{tot} over relative scour depth d_s/d_{target}.
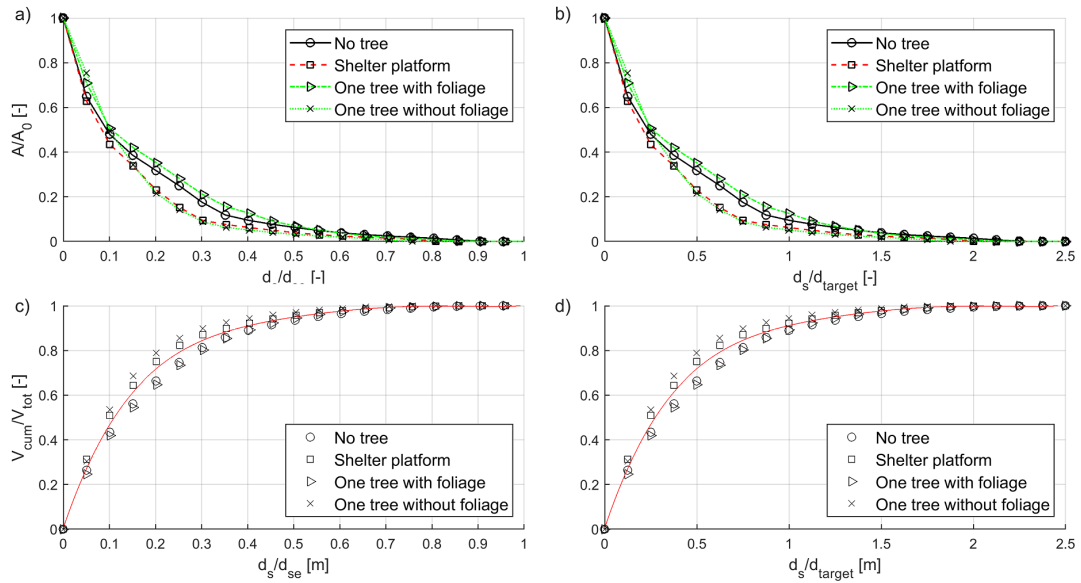
Figure B.24: Comparison of the stone-like structure DG for different tree-like shelters with a shelter-less case for a) Relative area A/A_0 over relative scour depth d_s/d_{se}, b) relative area A/A_0 over relative scour depth d_s/d_{target}, c) relative volume V_{cum}/V_{tot} over relative scour depth d_s/d_{se}, d) relative volume V_{cum}/V_{tot} over relative scour depth d_s/d_{target}.
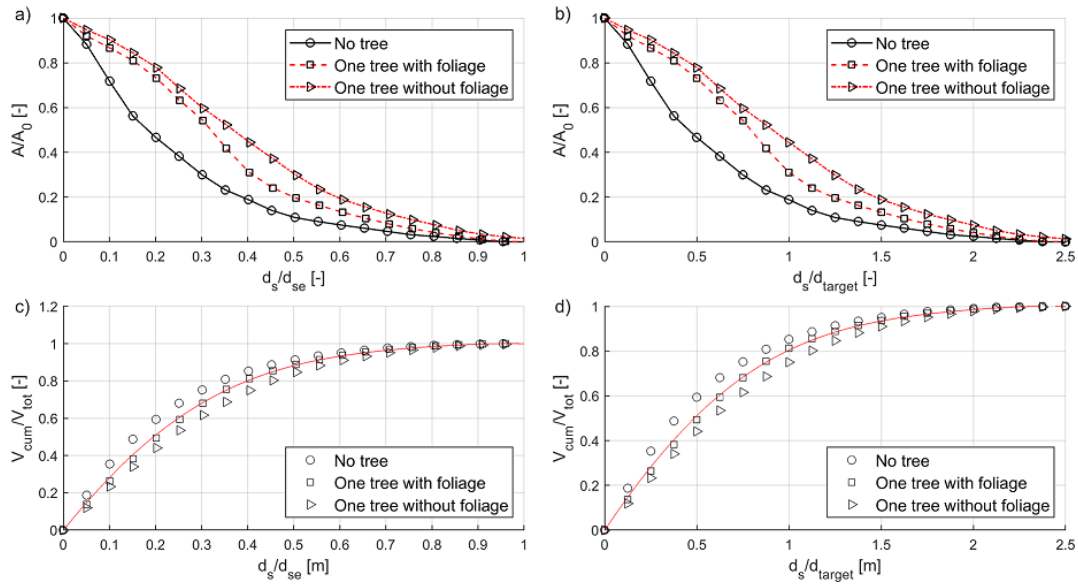
Figure B.25: Comparison of the stone-like structure DWD for different tree-like shelters with a shelter-less case for a) Relative area A/A_0 over relative scour depth d_s/d_{se}, b) relative area A/A_0 over relative scour depth d_s/d_{target}, c) relative volume V_{cum}/V_{tot} over relative scour depth d_s/d_{se}, d) relative volume V_{cum}/V_{tot} over relative scour depth d_s/d_{target}

B.4 Comparison of the geometry of the scour holes for different structures
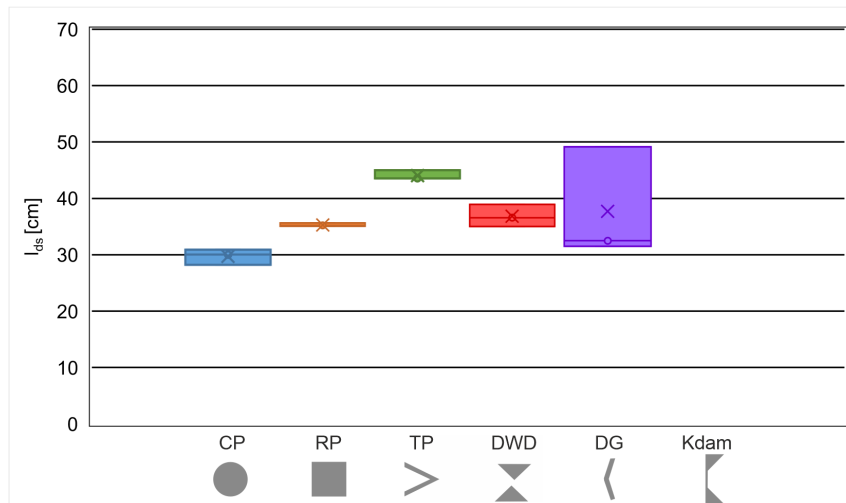
Figure B.26: Comparison of the length of the scour hole of pier-, stone- and dam-like structures.
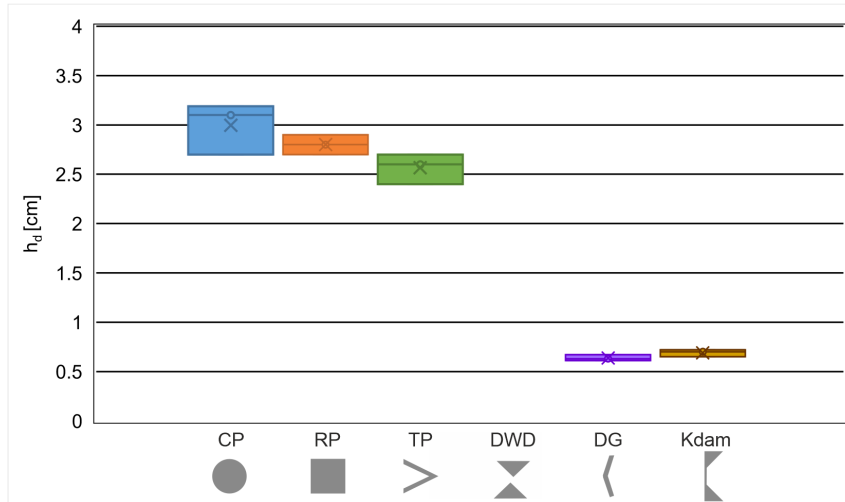
Figure B.27: Comparison of the height of the dune of pier-, stone- and dam-like structures.
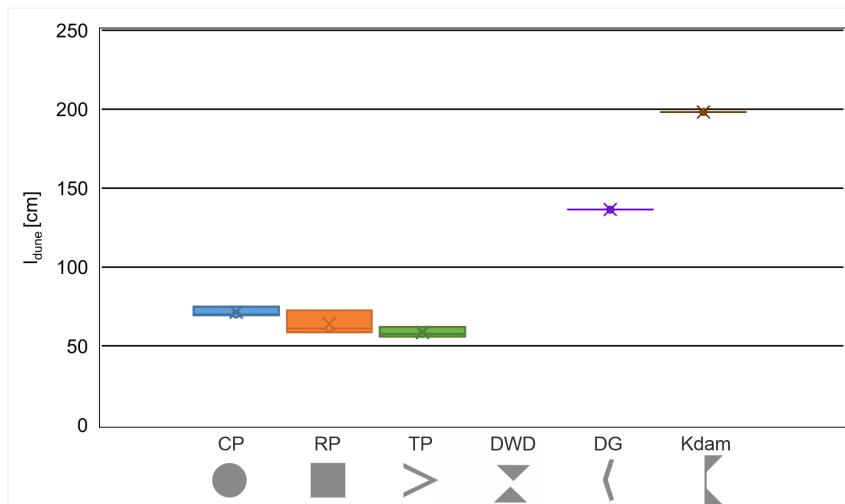
Figure B.28: Comparison of the distance of the dune of pier-, stone- and dam-like structures.

Appendix C

Publications

Kannen, Christin (2019, 14.-16.08.). *Hydraulische und hydrodynamische Analyse des geplanten Sektorwehres am Platzspitz in Zürich* [conference presentation]. JUWI Treffen, Karlsruhe, Deutschland.

Kannen, Christin; Seidel, Frank; Lang, Cornelia; Schulz, Philipp. *Hydraulische und hydrodynamische Analyse des geplanten Sektorwehres am Platzspitz in Zürich*. Bundesanstalt für Wasserbau (Hg.) (2019): 21. Treffen junger WissenschaftlerInnen. Kolloquium 14. bis 16. August 2019. Karlsruhe: Bundesanstalt für Wasserbau.

Kannen, Christin; Seidel, Frank; Nestmann, Franz (2020). *Experimental and numerical methods in investigations of sustainable deep scours as fish habitat*. In Carrillo, J. M.; Fenrich, E.; Ferras, D.; Wieprecht, S. (Eds.), Proceedings of the 1st IAHR Young Professional Congress, (p.188-189) 17.-18.11.2020.

Kannen, Christin; Seidel, Frank; Nestmann, Franz (2020). *Hydraulik und Morphodynamik von Strukturen zur Initiation nachhaltiger tiefer Gewässerzüge – ein künftiges Instrument zur Schaffung von Übersommerungshabitaten?* Wertermittlungsforum 2/2020, 38. Jahrgang, Sachverständigen-Kuratorium für LANDWIRTSCHAFT, FORSTWIRTSCHAFT, GARTENBAU, LANDESPFLEGE, WEINBAU, BINNENFISCHEREI, PFERDE (Hrsg.).

Kannen, Christin (2022, 21.-22.03.). *Hydraulik und Morphodynamik von Strukturen zur Initiation nachhaltiger tiefer Gewässerzüge – ein künftiges Instrument zur Schaffung von Übersommerungshabitaten?* [conference presentation]. 31. SVK-Fischereitagung, Künzell, Deutschland.

Müller, A. C. T., Kannen, C., Seidel, F., and Franca, M. J.: *Use of nature-based solutions for the enhancement of river habitats – transfer of practical experience to scientifically optimized solutions*, EGU General Assembly 2022, Vienna, Austria, 23–27 May 2022, EGU22-4742, https://doi.org/10.5194/egusphere-egu22-4742, 2022.

Kannen, Christin; Seidel, Frank; Franca, Mário J. (2022). *Discussion of various equilibrium*

concepts on scouring around hydraulic structures [conference presentation and paper]. River-flow 2022, Kingston and Ottawa, Canada (online). In press.

Theresa C. van Hateren, Harro J. Jongen, Hadeel Al-Zawaidah, Joris G.W. Beemster, Judith Boekee, Linda Bogerd, Sijia Gao, Christin Kannen, Ilja van Meerveld, Sjoukje I. de Lange, Felicia Linke, Rose B. Pinto, Janneke O.E. Remmers, Jessica Ruijsch, Steven R. Rusli, Roeland C. van de Vijsel, Jerom P.M. Aerts, Sehouevi M.D. Agoungbome, Markus Anys, Sara Blanco Ramírez, Tim van Emmerik, Luca Gallitelli, Gabriela Chiquito Gesualdo, Wendy Gonzalez Otero, Sarah Hanus, Zixiao He, Svenja Hoffmeister, Ruben O. Imhoff, Tim Kerlin, Sumit M. Meshram, Judith Meyer, Aline Meyer Oliveira, Andreas C.T. Müller, Remko Nijzink, Mirjam Scheller, Louise Schreyers, Dhruv Sehgal, Paolo F. Tasseron, Adriaan J. Teuling, Michele Trevisson, Kryss Waldschläger, Bas Walraven, Chanoknun Wannasin, Jan Wienhöfer, Mar J. Zander, Shulin Zhang, Jingwei Zhou, Judith Y. Zomer, Bob W. Zwartendijk (2023) *Where should hydrology go? An early-career perspective on the next IAHS Scientific Decade: 2023–2032*, Hydrological Sciences Journal, 68:4, 529-541, DOI: 10.1080/02626667.2023.2170754

Seidel, Frank; Kannen, Christin; Grafmüller Thomas, Oberle, Peter (2023, 28.-30.06.). *Wasserbauliche Untersuchungen zum Rückhalteraum IMO mittels hybrider Modellierung* [Konferenzbeitrag]. 21. Wasserbau-Symposium der Wasserbauinstitute TU München, TU Graz und ETH Zürich, Wallgau, Deutschland.

Kannen, Christin; Seidel, Frank; Franca, Mário J. (2023, 21.-25.08.). *Ecological benefits of bridge pier scours* [conference presentation]. IAHR World Congress, Wien, Österreich.

Kannen, Christin; Seidel, Frank; Franca, Mário J. (submitted in 2023) *Morphodynamics of ecological scours as deep pool habitats for adult barbels.* Journal of Ecohydraulics.